Institutional Repository - Research Portal
Dépôt Institutionnel - Portail de la Recherche

researchportal.unamur.be

University of Namur

THESIS / THÈSE

DOCTOR OF SCIENCES

First analysis of the spectra obtained from the NOMAD instrument on-board ESA's Trace Gas Orbiter

Trompet, Loïc

Award date:
2023

Awarding institution:
University of Namur

Link to publication

General rights
Copyright and moral rights for the publications made accessible in the public portal are retained by the authors and/or other copyright owners and it is a condition of accessing publications that users recognise and abide by the legal requirements associated with these rights.

- Users may download and print one copy of any publication from the public portal for the purpose of private study or research.
- You may not further distribute the material or use it for any profit-making activity or commercial gain
- You may freely distribute the URL identifying the publication in the public portal ?

Take down policy
If you believe that this document breaches copyright please contact us providing details, and we will remove access to the work immediately and investigate your claim.

Download date: 17. May. 2024

Université de Namur
61, Rue de Bruxelles, B-5000, Namur

Faculté des Sciences

Département de Physique
Laboratoire Lasers et Spectroscopies

First analysis of the spectra obtained from the NOMAD instrument on-board ESA's Trace Gas Orbiter

Dissertation présentée en vue de
l'obtention du grade de
Docteur en Sciences

Loïc Trompet

Namur, 2023

Université de Namur
61, Rue de Bruxelles, B-5000, Namur

Faculté des Sciences

Département de Physique
Laboratoire Lasers et Spectroscopies

First analysis of the spectra obtained from the NOMAD instrument on-board ESA's Trace Gas Orbiter

Dissertation présentée en vue de l'obtention du grade de Docteur en Sciences

Loïc Trompet

Namur, 2023

Promotrices:

Prof. Muriel Lepère, Université de Namur (Belgique)

Dr Ir Ann Carine Vandaele, Institut royal d'Aéronomie Spatiale de Belgique (Belgique)

Membres du jury:

Dr Miguël Dhyne, Université de Namur (Belgique)

Prof. Jean-Claude Gérard, Université de Liège (Belgique)

Prof. Luc Henrard, président du jury, Université de Namur (Belgique)

Dr Miguel Ángel López-Valverde, Instituto de Astrofísica de Andalucía (Espagne)

Première analyse des spectres obtenus par l'instrument NOMAD à bord du Trace Gas Orbiter de l'ESA

Dissertation présentée en vue de l'obtention du grade de Docteur en Sciences

Loïc Trompet

Namur, 2023

Résumé

Depuis avril 2018, l'instrument Nadir and Occultation for Mars Discovery (NOMAD) embarqué à bord du Trace Gas Orbiter de l'ESA enregistre en continu des mesures de l'atmosphère de Mars. L'objectif principal était de confirmer la présence de méthane, un possible indicateur de vie sur Mars. Des mesures de NOMAD, aucune trace de méthane n'a encore pu être trouvée, mais ces mesures permettent de déduire de nombreux autres constituants de l'atmosphère de Mars.

Ce travail se concentre sur la déduction de profils verticaux (tranches de l'atmosphère pour une gamme d'altitudes) de la densité et de la température du dioxyde de carbone à partir du canal d'occultation solaire (SO) de NOMAD. Ce canal comprend un réseau échelle pour la dispersion de la lumière couplé à un filtre accordable acousto-optique (AOTF). Une attention particulière a été portée à l'étalonnage spectral. Les profils de densité et de température du dioxyde de carbone sont nécessaires pour déduire la densité d'autres espèces telles que l'eau et le monoxyde de carbone. En télédétection, cette déduction est appelée "restitution" (retrieval) et est un problème inverse, nécessitant la régularisation des profils "restitués". Dans ce travail, la régularisation est effectuée avec la méthode de Tikhonov et un affinement de cette régularisation est obtenu avec la méthode d'estimation de l'erreur attendue.

Jusqu'à 1848 profils de densité et de température du dioxyde de carbone ont été obtenus entre le 21 avril 2018 et le 26 décembre 2022. Les profils de densité de dioxyde de carbone sont directement extraits des spectres de NOMAD-SO, tandis que la température est extraite de ces derniers et de l'équation d'équilibre hydrostatique.

Les profils de température obtenus sont comparés aux simulations d'un modèle de circulation générale GEM-Mars ainsi qu'à celles d'autres instruments sondant l'atmosphère de Mars. Les données de GEM-Mars sont en moyenne supérieures de 5 K, mais la moyenne des différences absolues est de 12 K. Un total de 117 profils colocalisés a été trouvé avec ceux de l'instrument Mars Climate Sounder (MCS). La moyenne des différences avec le MCS est de 0.1 K alors que la moyenne des différences absolues est de 8.5 K. Ces chiffres peuvent s'expliquer par les variabilités naturelles des profils de température pour les différences en temps et localisation des profils, et s'explique également par de possibles différences restantes dans les résolutions verticales des deux ensembles de données. Un total de 64 profils sont comparés aux profils simultanés du canal proche infrarouge (NIR) de l'Atmospheric Chemistry Suite (ACS) et la moyenne des différences est de 4.7 K et la moyennes des différences absolues est de 6.7 K.

Ce manuscrit présente les variations saisonnières, latitudinales, longitudinales et diurnes de la densité et de la température du CO_2 au terminateur de Mars, en se concentrant sur la mésosphère (qui s'étend de 50 à 100 km). Des tendances spécifiques ont été identifiées, telles que le cycle saisonnier du CO_2, la variation avec les cellules de Hadley (circulation), les réchauffements polaires et les poches chaudes et froides. Ces dernières portent parfois la marque de la présence de nuages de glace CO_2 et leur présence est rapportée dans ce manuscrit. Certaines couches chaudes sont présentes dans l'hémisphère nord à l'aube et au crépuscule et elles ont des amplitudes particulièrement élevées dans l'hémisphère sud à l'aube, mais sont absentes dans l'hémisphère sud au crépuscule. De fortes variations longitudinales sont également rapportées. Elles sont probablement liées aux marées atmosphériques. Cet ensemble de données couvre deux années martiennes et les tendances sont très similaires entre ces deux années.

Samenvatting

Sinds april 2018 registreert het Nadir and Occultation for Mars Discovery (NOMAD) instrument aan boord van ESA's Trace Gas Orbiter continu metingen van de atmosfeer van Mars. Het belangrijkste doel was om de aanwezigheid van methaan, een mogelijke indicator van leven op Mars, te bevestigen. In de metingen van NOMAD is nog geen teken van methaan gevonden, maar er kunnen wel veel andere bestanddelen van de atmosfeer van Mars worden afgeleid.

Dit werk richt zich op de afleiding van verticale profielen (laagjes van de atmosfeer voor een reeks hoogtes) van de dichtheid en temperatuur van kooldioxide uit het SO-kanaal (Solar Occultation) van NOMAD. Dit kanaal bestaat uit een echelle diffractieroster voor de lichtdispersie gekoppeld aan een akoestisch-optisch afstembaar filter. Bijzondere aandacht is besteed aan de spectrale kalibratie. De profielen van de kooldioxidedichtheid en -temperatuur zijn nodig om de dichtheid van andere soorten zoals water en koolmonoxide af te leiden. In teledetectie wordt deze afleiding een "retrieval"genoemd en is het een invers probleem, waarbij de afgeleide profielen moeten worden geregulariseerd. De regularisatie wordt in dit werk uitgevoerd met de Tikhonov-methode en de beste fijnafstemming van deze regularisatie wordt bereikt met de Expected Error Estimation-methode.

Er zijn 1848 profielen van kooldioxidedichtheid en -temperatuur afgeleid voor de periode van 21 april 2018 tot 26 december 2022. Dichtheidsprofielen van kooldioxide zijn rechtstreeks verkregen uit de spectra van NOMAD-SO, terwijl de temperatuur is verkregen uit de spectra van NOMAD-SO en de vergelijking voor hydrostatische evenwicht.

De gevonden temperatuurprofielen werden vergeleken met simulaties van het algemene circulatiemodel GEM-Mars en van andere instrumenten die de atmosfeer van Mars onderzoeken. De dataset van GEM-Mars is gemiddeld 5 K hoger, maar het gemiddelde absolute verschil is 12 K. Er zijn in totaal 117 profielen gevonden die in plaats en tijd overeenstemmen met data van het Mars Climate Sounder (MCS) instrument. Het gemiddelde verschil met de MCS is 0.1 K, terwijl het gemiddelde absolute verschil 8.5 K is. Deze getallen kunnen worden verklaard door natuurlijke variabiliteit van temperatuurprofielen met de verschillen in tijd en locatie van de profielen en ook door mogelijke resterende verschillen in de verticale resolutie van beide datasets. In totaal zijn 64 profielen vergeleken met gelijktijdige profielen van het nabij-infrarood (NIR) kanaal van de Atmospheric Chemistry Suite (ACS) en het gemiddelde verschil is 4.7 K en het gemiddelde absolute verschil is 6.7 K.

Dit manuscript bevat de seizoens-, breedte-, lengte- en dagschommelingen van de dichtheid en de temperatuur van CO_2. Specifieke trends zijn geïdentificeerd, zoals de seizoenscyclus van CO_2, de variatie met Hadley circulatiecellen, de polaire opwarming en warme en koude lagen. Deze laatste vertonen soms de aanwezigheid van CO_2 ijswolken en hun locaties worden gerapporteerd. Sommige warme lagen zijn zowel bij zonsopgang als bij zonsondergang aanwezig op het noordelijk halfrond en hebben bijzonder hoge amplitudes op het zuidelijk halfrond bij zonsopgang, maar zijn afwezig op het zuidelijk halfrond bij zonsondergang. Er worden ook sterke longitudinale variaties gerapporteerd. Deze zijn waarschijnlijk gerelateerd aan atmosferische getijden. Deze dataset bestrijkt twee Marsjaren en de trends zijn van jaar tot jaar zeer vergelijkbaar.

Abstract

Since April 2018, the Nadir and Occultation for Mars Discovery (NOMAD) instrument on board ESA's Trace Gas Orbiter has been continuously recording measurements of the atmosphere of Mars. The main goal was to confirm the presence of methane, a possible indicator of life on Mars. From the measurements of NOMAD, no sign of methane has yet been found but many other constituents of the atmosphere of Mars can be derived.

This work focuses on the deduction of vertical profiles (slices of the atmosphere for a range of altitudes) of carbon dioxide density and temperature from the Solar Occultation (SO) channel of NOMAD. This channel comprises an echelle grating for the light dispersion coupled with an acousto-optic tunable filter. Particular attention has been dedicated to the spectral calibration. The profiles of carbon dioxide density and temperature are necessary for the deduction of the density of other species such as water and carbon monoxide. In remote sensing, this deduction is called a "retrieval" and is an inverse problem, involving the regularisation of the retrieved profiles. The regularisation is performed in this work with the Tikhonov method and the best fine-tuning of this regularisation is achieved with the Expected Error Estimation method.

Up to 1848 profiles of carbon dioxide density and temperature have been retrieved from April, 21st 2018 until December 26th 2022. Carbon dioxide density profiles are directly retrieved from the spectra of NOMAD-SO while temperature is retrieved from the latter and the hydrostatic equilibrium equation.

The retrieved temperature profiles are compared to simulations from the general circulation model GEM-Mars as well as from other instruments probing the atmosphere of Mars. The dataset from GEM-Mars is on average 5 K higher but the average absolute difference is 12 K. A total of 117 co-located profiles were found with the Mars Climate Sounder (MCS) instrument. The average difference with the MCS is 0.1 K while the average absolute difference is 8.5 K. Those numbers can be explained by natural variabilities temperature profiles with the ranges in time and location of the profiles and explained as well by possible remaining differences in the vertical resolution of both datasets. A total of 64 profiles are compared to simultaneous profiles from the near-infrared (NIR) channel from the Atmospheric Chemistry Suite (ACS) and the average difference is 4.7 K and the average absolute difference is 6.7 K.

This manuscript contains the seasonal, latitudinal, longitudinal, and diurnal variations of CO_2 density and temperature at the terminator of Mars, focusing on the mesosphere (extending from 50 to 100 km). Specific trends have been identified, such as the CO_2 seasonal cycle, the variation with Hadley circulation cells, the polar warmings, and warm and cold pockets. The latter sometimes bear the presence of CO_2 ice clouds and their locations are reported. Some warm layers are present in the Northern hemisphere at both dawn and dusk and have particularly high amplitudes in the Southern hemisphere at dawn but are absent in the Southern hemisphere at dusk. Strong longitudinal variations are also reported. They are probably related to atmospheric tides. This dataset covers two Martian years and the trends are very similar between those two years.

Remerciements

Je suis particulièrement reconnaissant envers Dr Ir Ann Carine Vandaele pour m'avoir permis de travailler dans ce domaine passionnant qu'est l'étude des atmosphères planétaires, pour m'avoir donné l'opportunité de réaliser cette thèse, pour m'avoir donné de précieux conseils ainsi que la motivation qui m'ont permis d'achever cette thèse et pour les corrections suggérées à ce manuscrit. Je suis particulièrement reconnaissant envers Pr Dr Muriel Lepère de m'avoir accueilli au sein de l'équipe de l'unité de recherche Lasers et Spectroscopie (LLS) de l'UNamur pour les conseils ainsi que la motivation qui m'ont permis d'achever cette thèse et en particulier pour le temps passé à m'avoir aidé à améliorer mes présentations.

Je suis reconnaissant envers les membres de mon jury : Dr Miguel Dhyne et Pr Dr Jean-Claude Gérard pour avoir accepté de faire partie de mon comité d'accompagnement. Je suis reconnaissant envers Dr Miguel Ángel López Valverde pour les nombreuses suggestions données durant les différentes réunions de NOMAD concernant mon travail dont il est un expert. Je suis reconnaissant envers Pr Dr Luc Henrard pour avoir accepté d'être président de mon jury de thèse. Je remercie tous les membres de mon jury de thèse pour avoir lu ce manuscrit et pour les commentaires et pour les corrections suggérées.

Je remercie particulièrement mes collègues Dr Ian Thomas et Dr Shohei Aoki pour leurs conseils avisés tout au long de ce travail et pour leurs relectures de ce manuscrit. Je remercie particulièrement Dr Séverine Robert, ma voisine de bureau, pour avoir toujours répondu à toutes mes questions concernant l'institut, la spectroscopie, les transferts radiatifs et ASIMUT. Je remercie Dr Frank Daerden et Dr Lori Neary pour leurs réponses à mes questions sur l'atmosphère de Mars. Je remercie mes collègues qui ont relu mon manuscrit et ont pu me fournir quelques commentaires et/ou corrections : Dr Sébastien Viscardy, Dr Filip Vanhellemont, Dr Arianna Piccialli, Miriam Cisneros, et Zachary Flimon. Je remercie l'ensemble de l'unité de recherche en atmosphères planétaires de l'IASB dont font partie également : Dr Yannick Willame, Dr Arnaud Mahieux, Dr Cédric Depiesse, Dr Alexis Libert. Je remercie l'équipe du LLS et en particulier Dr Bastien Vispoel, Olivier Browet, Dr Sylvain Léonis et Jean Clément pour leurs réponses à mes questions concernant la spectroscopie moléculaire. Je remercie Dr Geronimo Villanueva, Dr Giuliano Liuzzi et Adrian Brines pour leurs conseils durant les réunions NOMAD et pour leurs efforts entrepris pour la calibration de NOMAD-SO, dont ce travail a largement bénéficié. Je remercie d'autres collègues rencontrés avant ou durant mon parcours de thèse et qui m'ont aidé dans la réalisation de ce travail. Parmi eux, je remercie Roland Clairquin, Dr Eduard Neefs, Bojan Ristic, Sophie Berkenbosch, Bram Beeckman, Nuno Peirera, Dr Didier Fussen, Dr Emmanuel Dekemper, Philippe Demoulin, Frédéric Counerotte, Yves Geunes, Tim Ooms, Vincent Letocard, Arnaud Lefèvbre, Fabienne Leclere, Philippe Drochmans, Johan Bulcke, Dr Ozgur Karatekin, Dr Luca Ruiz Lozano. Je remercie le programme de recherche et d'innovation Horizon 2020 de l'Union Européenne pour le financement apporté pour les projets ROADMAP (ROle and impAct of Dust and clouds in the Martian AtmosPhere - bourse No 101004052), Europlanet-2020 et Europlanet-2024 (bourses No 654208 et No 871149).

Enfin, et non des moindres, je suis particulièrement reconnaissant envers mon épouse, Katsia, pour son soutien, essentiel, tout au long de ce travail.

Contents

1 Introduction 15

2 Mars 19
- 2.1 Atmospheric parameters . . . 21
  - 2.1.1 Gravitational acceleration . . . 21
  - 2.1.2 Hydrostatic equilibrium . . . 24
  - 2.1.3 Lapse rate . . . 26
  - 2.1.4 Pressure . . . 27
  - 2.1.5 Temperature and thermal structure . . . 29
  - 2.1.6 Homopause . . . 30
- 2.2 Methane on Mars . . . 31
- 2.3 Summary . . . 31

3 Molecular spectroscopy and radiative transfer for solar occultation 33
- 3.1 Molecular spectroscopy . . . 33
  - 3.1.1 Rovibrational transitions . . . 34
  - 3.1.2 Spectral line intensity . . . 37
  - 3.1.3 Spectral line shape . . . 40
- 3.2 Solar occultation . . . 41
  - 3.2.1 Solar spectrum in the mid-infrared spectral range . . . 42
  - 3.2.2 Absorption . . . 42
  - 3.2.3 Scattering . . . 47
- 3.3 summary . . . 47

4 Inverse problems 49
- 4.1 Slant column profile inversion . . . 49
  - 4.1.1 Non-linear least square solution . . . 49
  - 4.1.2 Optimal Estimation Method . . . 50
  - 4.1.3 Uncertainties . . . 51
  - 4.1.4 Information content . . . 51
  - 4.1.5 ASIMUT-ALVL radiative transfer code . . . 52
- 4.2 Density profile inversion . . . 52
  - 4.2.1 Linear least square solution . . . 52
  - 4.2.2 Tikhonov regularisation . . . 54
  - 4.2.3 Similarity to the Optimal Estimation Method . . . 56
  - 4.2.4 Iterated Tikhonov regularisation . . . 59
  - 4.2.5 Regularization parameter selection . . . 60
  - 4.2.6 Vertical resolution . . . 62

4.3 Summary . . . 62

5 The NOMAD instrument 63
5.1 NOMAD-SO description . . . 65
  5.1.1 Echelle grating . . . 65
  5.1.2 Acousto-optic tunable filter . . . 66
  5.1.3 Detector . . . 66
  5.1.4 Measurements . . . 67
  5.1.5 Data processing . . . 68
5.2 NOMAD-SO model . . . 69
  5.2.1 Wavenumber calibration . . . 70
  5.2.2 Instrument Line Shape . . . 76
  5.2.3 AOTF transfer function . . . 78
  5.2.4 Blaze function . . . 80
  5.2.5 NOMAD-SO transfer function . . . 81
5.3 Carbon dioxide lines in NOMAD-SO spectral range . . . 82
  5.3.1 Saturation . . . 84
5.4 summary . . . 89

6 NOMAD-SO calibration 91
6.1 Background subtraction . . . 91
6.2 Transmittance calibration . . . 92
  6.2.1 Uncertainties on transmittance . . . 95
  6.2.2 Selection of the Sun region . . . 97
  6.2.3 Signal to noise ratio . . . 99
6.3 summary . . . 99

7 Detection limits 101
7.1 summary . . . 105

8 Carbon dioxide and temperature retrievals from NOMAD-SO spectra 107
8.1 Retrieval of vertical profiles of carbon dioxide density . . . 107
  8.1.1 Spectral inversion . . . 107
  8.1.2 Vertical inversion . . . 109
  8.1.3 Bins profile combination . . . 115
8.2 Retrieval of vertical profiles of pressure and temperature . . . 117
  8.2.1 Introduction . . . 117
  8.2.2 Deriving simpler formulae . . . 117
  8.2.3 Synthetic test . . . 119
  8.2.4 Choice of the initial pressure . . . 123
  8.2.5 Uncertainties on the temperature profile . . . 124
8.3 Iteration over the retrieved temperature profile . . . 127
8.4 Uncertainties on the profiles . . . 131
8.5 Vertical resolution . . . 131
8.6 Combination of the pressure and temperature profiles with GEM-Mars simulated data . . . 131
8.7 summary . . . 135

9 Comparisons **137**
9.1 Comparison to simulations from the GEM-Mars general circulation model 137
9.2 Comparison to other instruments sounding the atmosphere of Mars 142
9.2.1 Comparison to MRO-MCS 142
9.2.2 Comparison to TGO-ACS-MIR 146
9.2.3 Comparison to TGO-ACS-NIR 148
9.3 summary 149

10 Mars climatology - Thermal structure at the terminator **151**
10.1 Coverage 151
10.2 Seasonal variations 154
10.3 Inter-annual variations 160
10.4 Latitudinal variations 162
10.5 Longitudinal variations 170
10.6 CO_2 condensation temperature limit 172
10.7 Mesospheric inversion layers 174
10.8 summary 179

11 Conclusions and outlook **181**

A Recall on simple linear regression **183**

B Analytical integration of the hydrostatic equilibrium equation **185**

C Derivation of the scale height from a linear interpolation on the natural logarithm of the density **187**

Chapter 1

Introduction

Related to one of the most important challenges in the present time, climate change, understanding the physical and chemical atmospheric processes is necessary for accurate forecasting on short and long timescales. Studying the atmosphere of other planets helps to improve our knowledge of those atmospheric processes. Venus and Mars - the two planets with orbits closest to the Earth - are the most probed planets after the Earth. New results from those atmospheres have never stopped to surprise us. Our understanding of those atmospheres has been widespread for a few decades thanks to sending instruments on landers, rovers, and remote sensing from spacecrafts.

The very hot and high pressure found at the surface of Venus is very different from the one found on our mostly temperate Earth atmosphere, and both are very different from the so cold and low pressures found in the atmosphere of Mars. In addition, Venus is constantly wrapped with a cloud mainly composed of sulfuric acid (Krasnopolsky and Parshev, 1981). Hopefully, no such structure can be found in the Earth's atmosphere, and neither on Mars. The Earth is wrapped in an ozone layer protecting the surface from dangerous ultraviolet radiation. The atmosphere of Mars has some traces of ozone (Piccialli et al., 2022), but not with any similar quantity that would protect the surface from dangerous ultraviolet radiations. An important other difference is the greenhouse warming in these atmospheres: it is highly efficient for Venus, sufficiently efficient for the Earth, and almost inexistent for Mars due to its too-thin atmosphere nowadays.

However, scientists have many reasons to think that Mars and the Earth were not much different at their first stages, billions of years ago with probably an efficient greenhouse warming or local warming due to large meteor impacts Haberle (2015). Several pieces of evidence of past water flowing on the surface of Mars are still present, such as river valley networks, and lake beds, and Mars might have had an ocean. Why did those neighbour planets evolve in such different states?

Many other fascinating questions concerning Mars are unsolved. The most intriguing question is probably the possible presence of life, probably below the surface, hidden from the deadly radiation, and where liquid water could be stable. Nowadays, Mars seems very inhospitable but between three and four billion years ago Mars had a sufficiently thick atmosphere, and liquid water could have flown on its surface. A possible indicator of this life could be methane. Most of the methane present in the Earth's atmosphere is produced by biological activities. Methane could be an indirect indicator of life. Several of the measurements of methane in the atmosphere of Mars (Krasnopolsky et al., 2004; Formisano et al., 2004; Geminale et al., 2008; Mumma et al., 2009; Geminale et al., 2011; Webster et al., 2015; Giuranna et al., 2019) are controversial (Zahnle et al., 2011; Zahnle, 2015) and the well-known signature of methane is absent in NOMAD-SO measurements (Korablev et al., 2019).

Other important challenges that will solve wider questions concern temperature variations, homopause location, atmospheric tides, or gravity waves, etc. These phenomena still need to be better constrained within general circulation models and in particular in the upper layers, i.e. the mesosphere and thermosphere. The middle atmosphere (50-100 km) contains an important latitudinal variability due to circulation with the Hadley cells. In the winter hemisphere, polar warming results from adiabatic compression due to the downward flux produced by the Hadley cell (McDunn et al., 2013). Other important local variabilities are found due to thermal tides (England et al., 2019), gravity waves (Nakagawa et al., 2020b).

Temperature is also important to model properly the spectral signature of other constituents such as water and carbon monoxide. The simultaneous derivation of temperature is thus necessary to quantify accurately the density of those species.

Remote sensing is one of the most efficient ways to collect information about the atmosphere. The aim is to determine indirectly, or "retrieve", atmospheric parameters from measurements, translating their presence and/or state. Remote sensing has a clear advantage over *in situ* measurements as the latter makes very local measurements while the former can cover wide spatial ranges. Retrieving atmospheric parameters from remote sensing measurements is not straightforward and has a cost. It is an ill-posed problem in regards to Hadamard's criteria[1] (Hadamard, 1923; Kirsch, 1996; Doicu et al., 2010b). In particular, any variation in the measurements will have an important impact on the retrieved atmospheric parameter. In this work, the presence of this ill-posedness is translated to the presence of high frequency features in the retrieved data. This work aims at fine-tuning the "retrievals" to remove those artefact while keeping the real variations.

At the time of writing this manuscript, the mesosphere of Mars is sounded by mainly five instruments which are, in order of arrival around Mars: the infrared channel of the SPectroscopy for the Investigation of the Characteristics of the Atmosphere of Mars (SPICAM) spectrometer (Korablev et al., 2006) on board Mars Express (MEx), the Mars Climate Sounder (MCS) (Kleinböhl et al., 2009) on board Mars Reconnaissance Orbiter (MRO), the Imaging UltraViolet Spectrograph (IUVS) and the Extreme UltraViolet Monitor (EUVM) both on-board Mars Atmosphere and Volatile Evolution (MAVEN), the Atmospheric Chemistry Suite (ACS) and the Nadir and Occultation for Mars Discoveries (NOMAD) both on board the Trace Gas Orbiter (TGO). The SPICAM dataset is rather sparse and dedicated to water retrieval. The MCS dataset covers a wide range in time and sounds mainly the local solar times around 3 h and 15 h and thus the day side and the night side. The IUVS dataset covers the night side. The EUVM, ACS, and NOMAD datasets cover the less well-known region separating the day side and the night side: the terminator.

The main goal of this work is the derivation of vertical profiles of carbon dioxide number density at the terminator from measurements made by the NOMAD instrument. Carbon dioxide constitutes around 95% of the atmosphere of Mars and is thus a good indicator of seasonal, latitudinal, diurnal, and longitudinal variations of the atmosphere. The carbon dioxide density is also a good proxy of the total density which is necessary to quantify the volume mixing ratio of other species. A vertical profile of temperature is derived from the carbon dioxide density thanks to the hydrostatic law.

This manuscript is split into eleven chapters: After this general introduction, the atmosphere of Mars and some atmospheric constraints are introduced in chapter 2. Before describing the instrument, its instrument function in chapter 5 and its calibration in chapter 6, chapter 3 and chapter 4 provide the necessary background to understand, respectively, the measurements and the regularisation to apply on the retrievals. Chapter 7 describes a method to directly infer the detection limits from the measurements and that method was applied to infer the detection limits for methane. Chapter 8 describes in detail the retrieval algorithm and the assessment of the errors. Chapter 9 contains some comparisons of the obtained dataset to other measurements and simulations from a general circulation model. Chapter 10 gathers all the results of the inter-annual, seasonal, latitudinal, and longitudinal variations analysed from the retrieved dataset focusing on the mesosphere at the terminator. This chapter also contains an analysis of some extreme temperature values spotted in this dataset. Finally, the conclusions and outlook are summarised in chapter 11.

---

[1] A problem is said "well-posed" if it has a unique and stable solution and "ill-posed" otherwise.

Chapter 2

Mars

Mars is named the red planet due to its rust colour. Its surface shows deep canyons, craters, and the highest volcanoes in our solar system. The topography of Mars is very different in both hemispheres as seen in image 2.1: the Northern hemisphere is flatter and less elevated than the Southern hemisphere. The zero elevation is defined as the equipotential surface (gravitational plus rotational) whose average value at the equator is equal to the mean radius of 3396.2±0.16 km (Smith et al., 2001). The highest surface point is Olympus Mons in the northern hemisphere culminating at 21.2 km altitude (Lat 18.5°, Lon -133° - the first meridian is defined by the Airy-0 crater) and the lowest point is in the southern hemisphere at the Hellas impact crater at -8.2 km (Lat -42°, Lon 70° - 2000 km of diameter). Mars is dry today but there are pieces of evidence that water once flowed on its surface such as valleys and deltas dug by rivers.

Its rotation axis is currently tilted by 25.2° to its revolution axis and there are thus seasonal variations of its atmosphere. Seasons on Mars are defined by a value known as the solar longitude (L_S), where 0 degrees indicates the start of the northern hemisphere spring equinox. Mars orbit around the Sun is elliptical and its aphelion and perihelion (respectively farthest and closest positions to the Sun) occur at respectively L_S 71° and 251°. Southern summers are hotter than northern summers as the perihelion is very close to the southern hemisphere summer solstice (270°). A Martian year (MY) lasts 687 (terrestrial) days. We commonly find in the literature that the first Martian year starts on April, 11th 1955 as defined in Clancy et al. (2000). This work focuses then on MY 34, 35, and 36 which started respectively on May the 5th 2017, March the 23th 2019, and February the 7th 2021. MY 36 ended on December the 26th 2022. A Martian day, called a sol, lasts approximatively 40 minutes longer than a terrestrial day. More information is gathered in table 2.1.

Two natural satellites are orbiting Mars: Phobos and Deimos. They are in a synchronous orbit, always showing the same face to Mars. Phobos is bigger than Deimos and is the closest to Mars with a semi-major axis of 9377 km (23450 km for Deimos).

Carbon dioxide constitutes more than 95% (95.32% following Owen et al. (1977); Franz et al. (2017), or 96.0% following Mahaffy et al. (2012)) of the atmosphere of Mars and its presence was first reported by Gerard P. Kuiper in 1947 from observations in the infrared spectral region (Kuiper, 1947). The main other gases are Argon (2.1%), dinitrogen (2.8%), dioxygen (0.17%) and carbon monoxide (0.075%) (Franz et al., 2017), and their mixing ratio change with the CO_2 seasonal cycle on Mars (Daerden et al., 2019).

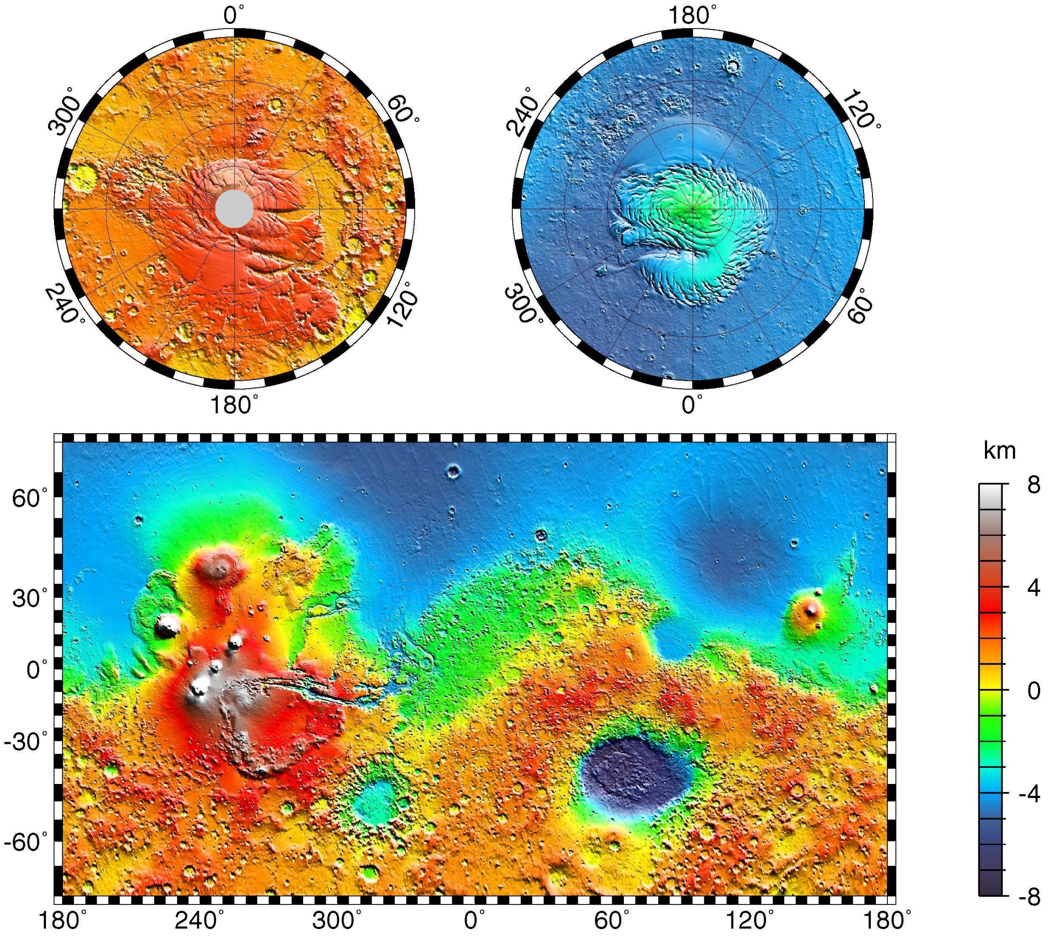
0°
60°
120°
180°
240°
300°
180°
120°
60°
0°
300°
240°
60°
30°
0°
-30°
-60°
180°
240°
300°
0°
60°
120°
180°
km
8
4
0
-4
-8

Figure 2.1: Topography of Mars from Mars Orbiter Laser Altimeter on board Mars Global Surveyor (image from NASA/JPL, downloaded at https://www.planetary.org/space-images/mars-orbiter-laser-altimeter). O the upper panels, the Southern hemisphere is on the left and the Northern hemisphere is on the right.

	Earth	Mars
Mean equatorial radius (km)	6378	3396
Mass (kg)	5.97×10^{24}	6.24×10^{23}
Gravity at surface (m/s^2)	9.81	3.72
Obliquity (°)	23.4	25.2
Revolution on obliquity (h:m:s)	24:00:00	24:39:35
Axial precession (terrestrial year)	26 000	175 000
Perihelion (U.A.)	0.983	1.384
Aphelion (U.A.)	1.017	1.664
Revolution on orbit (terrestrial day)	365.25	687
Minimal surface temperature (°C)	-93	-143
Averaged surface temperature (°C)	15	-63
Maximal surface temperature (°C)	57	20

Table 2.1: Earth and Mars main parameters comparison (Haberle et al., 2017).

2.1 Atmospheric parameters

The important atmospheric parameters such as density, pressure, and temperature are related by the ideal gas law but also by the hydrostatic equilibrium equation where the knowledge of gravity at Mars is important. The next section 2.1.1 is thus about the gravitational acceleration at Mars and the following section 2.1.2 is about the hydrostatic equilibrium.

2.1.1 Gravitational acceleration

Assuming that Mars is a perfect spherical body, the gravitational acceleration at any distance r (besides the radius of Mars) from the centre of Mars is given by

$$g(r) = \frac{G\,M}{r^2} \tag{2.1}$$

where G is the universal constant of acceleration, and M is the mass of Mars ($2.5 \times 10^{16}\,kg$). At the surface of Mars, the averaged gravitational acceleration is $g_0 = 3.721\,m/s^2$.[1] From equation 2.1, we can also determine the gravitational acceleration at any altitude z as

$$g(z) = g_0 \left(\frac{r_M}{r_M + z}\right)^2 \tag{2.2}$$

where r_M is the averaged Mars radius (averaged distance of Mars radius to the surface) and $g_0 = g(r = r_M)$ is the averaged gravitational acceleration at the averaged Mars radius. The parameter $g(z)$ varies with latitude and longitude as Mars is not spherical (see figure 2.1) and it even varies with the CO_2 cycle[2], and the position of other bodies, mainly the Sun and Phobos. Mars gravity is commonly modelled with spherical harmonics (Smith et al., 2009). Hirt et al. (2012) derived gravitational acceleration values between $3.66\,m/s^2$ and $3.74\,m/s^2$ from their Mars Gravity Model 2011. They also derived a value of $3.70875\,m/s^2$ for the equator and $3.73190\,m/s^2$ for the pole from the Mars Geodetic Reference System. Thus a difference of maximum 1.5 % (to be compared with the uncertainties in section 8.2.5). In this section, we will describe a more recent model called GMM3 (Genova et al., 2016).

---

[1] Or $371.1\,Gal$. The gravimetry community uses galileo units with 1 Gal = 1 cm/s^2.

[2] A large amount of atmospheric CO_2 condensates and sublimates following the seasons. See section 2.1.4.

The acceleration g is equal to the gradient of the gravitational potential U, but we are interested only in the vertical coordinate r (Kaula, William, 2000)

$$g_r = -\frac{\partial U}{\partial r} \tag{2.3}$$

where we passed from rectangular to spherical coordinates for the last equality and where the geopotential is

$$U(r,\lambda,\phi) = \frac{GM}{r}\left[1+\sum_{l=2}^{n} u_l(r,\lambda,\phi)\right] \tag{2.4}$$

with

$$u_l(r,\lambda,\phi) = \left(\frac{r_M}{r}\right)^l \sum_{m=0}^{l}\left[\bar{C}_{lm}\cos(m\lambda)+\bar{S}_{lm}\sin(m\lambda)\right]\bar{P}_{lm}(\sin\phi) \tag{2.5}$$

where the $\bar{C}_{lm}$ and $\bar{S}_{lm}$ are the normalized spherical harmonic coefficients. I choose the 'GMM3' model (Goddard Mars Model 3) (Genova et al., 2016) produced by the Goddard Space Flight Center (one of NASA's space flight complex). They derived these coefficients from small fluctuations of the orbits from the MGS, Mars Odyssey, and MRO orbiters up to a degree 120 which corresponds to a surface resolution lower than $90\,km$. The $\bar{P}_{lm}(.)$ are the normalized associated Legendre functions which are related to the unnormalized associated Legendre functions $P_{lm}(.)$ by the following normalization factor

$$\bar{P}_{lm}(x) = (-1)^m\sqrt{\frac{(l+\frac{1}{2})(l-m)!}{(l+m)!}}P_{lm}(x) \tag{2.6}$$

and where the $P_{lm}(.)$ functions are computed with the *scipy.specials.lpmn* function (Virtanen et al., 2020).

The $\bar{C}_{lm}$ coefficients for $l = 2,3,4,5$ are varying with time and take into account the redistribution of mass due to the CO_2 cycle (an important part of CO_2 sublimate or condense at the poles following the seasons). The variation of those coefficients is given by (Lemoine et al., 2006)

$$\Delta\bar{C}_{lm} = \sum_{k=0}^{3} A_k\cos\left(\frac{2k\pi}{T}\Delta t\right) + B_k\sin\left(\frac{2k\pi}{T}\Delta t\right) \tag{2.7}$$

where Δt is the elapsed time since 01/01/2000 at 00:00:00 UTC, T is the orbital period of Mars and the values of the coefficients A_k and B_k are provided in Genova et al. (2016, table 3).

With the mathematical model in 2.4, we find

$$\begin{aligned} g_r(r,\lambda,\phi) &= \frac{GM}{r^2}\left[1+\sum_{l=2}^{n} u_l(r,\lambda,\phi)+\sum_{l=2}^{n} l\,u_l(r,\lambda,\phi)\right] \\ &= \frac{GM}{r^2}\left[1+\sum_{l=2}^{n}(1+l)\,u_l(r,\lambda,\phi))\right] \end{aligned} \tag{2.8}$$

Figure 2.2 shows the relative error on g_0 as computed by equation 2.3 and 2.1. This bias is always between 0.055% and 0.085% depending on the latitude and longitude, while no noticeable change in this bias occurs with seasons. The values are only positive because g_0 in 2.1 is set to $3.711 m/s^2$ which is lower than the averaged value used in the GMM3 model.

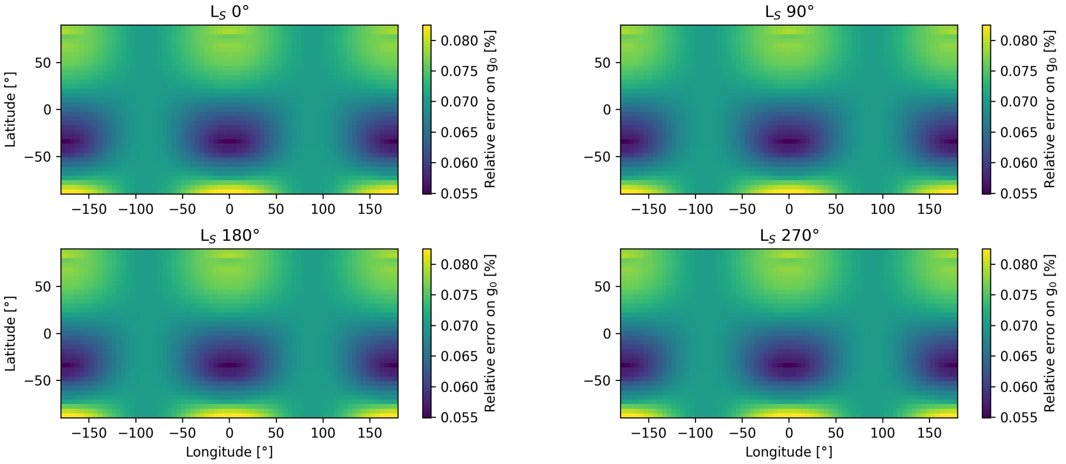

Figure 2.2: Relative error on g_0 as computed by equation 2.3 and 2.1 as a function of longitude and latitude at solstices (L$_S$ 90° and 270°) and equinoxes (L$_S$ 0° and 180°).

The uncertainties on the parameters from GMM3 are provided as well. An upper bound over the uncertainties on the acceleration due to gravity is computed as ((Taylor, 1997, eq. 3.48), considering no uncertainties on r, λ and ϕ and independent parameters)

$$\delta g_r \leq \left|\frac{\partial g_r}{\partial GM}\right| \delta GM + \sum_{l=2}^{n}\sum_{m=0}^{l}\left|\frac{\partial g_r}{\partial \bar{C}_{lm}}\right| \delta \bar{C}_{lm} + \sum_{l=2}^{n}\sum_{m=0}^{l}\left|\frac{\partial g_r}{\partial \bar{S}_{lm}}\right| \delta \bar{S}_{lm} \tag{2.9}$$

The uncertainties over the temporal coefficients A_k and B_k are neglected here as they are three orders of magnitude lower than the other coefficients. With the equation 2.8,

$$\left|\frac{\partial g_r}{\partial GM}\right| \delta GM = \frac{1}{r^2}\left|1 + \sum_{l=2}^{n}(1+l)\, u_l(r,\lambda,\phi)\right|, \tag{2.10}$$

$$\sum_{m=0}^{l}\left|\frac{\partial g_r}{\partial \bar{C}_{lm}}\right| \delta \bar{C}_{lm} = \frac{GM}{r^2}(1+l)\left(\frac{r_M}{r}\right)^l \sum_{m=0}^{l}\delta \bar{C}_{lm}\left|\cos(m\lambda)\bar{P}_{lm}(\sin\phi)\right|, \tag{2.11}$$

$$\sum_{m=0}^{l}\left|\frac{\partial g_r}{\partial \bar{C}_{lm}}\right| \delta \bar{S}_{lm} = \frac{GM}{r^2}(1+l)\left(\frac{r_M}{r}\right)^l \sum_{m=0}^{l}\delta \bar{S}_{lm}\left|\sin(m\lambda)\bar{P}_{lm}(\sin\phi)\right|. \tag{2.12}$$

This is an upper bound as the uncertainties over the coefficients $\bar{C}_{lm}$ and $\bar{S}_{lm}$ might compensate each other in the error propagation.

The uncertainties $\delta\bar{C}_{lm}$ and $\delta\bar{S}_{lm}$ coefficients are five orders of magnitude lower than the coefficients themselves and δGM is eight orders of magnitude lower than GM. The uncertainties δg_r for the data plotted on figure 2.2 are between 10^{-8} and $10^{-6}\ m/s^2$. The level of uncertainties over g ($\delta g/g$) computed with the GMM3 model is thus much lower than the level of uncertainties over the retrieved densities (see 8.4) and are taken into account in the computation of the uncertainties over the pressure and temperature profiles.

There is still a small correction to apply on g due to the rotation of Mars on itself. The apparent gravity g' takes into account the centrifugal force (Petty, 2008, p. 89) which is a function of the latitude λ

$$g' = g - \Omega^2\, z\, \cos^2 |\lambda| \tag{2.13}$$

where Ω is the angular velocity of Mars and equals 2π per $88642\,s$. This correction is $0.017\,m/s^2$ at the equator.

2.1.2 Hydrostatic equilibrium

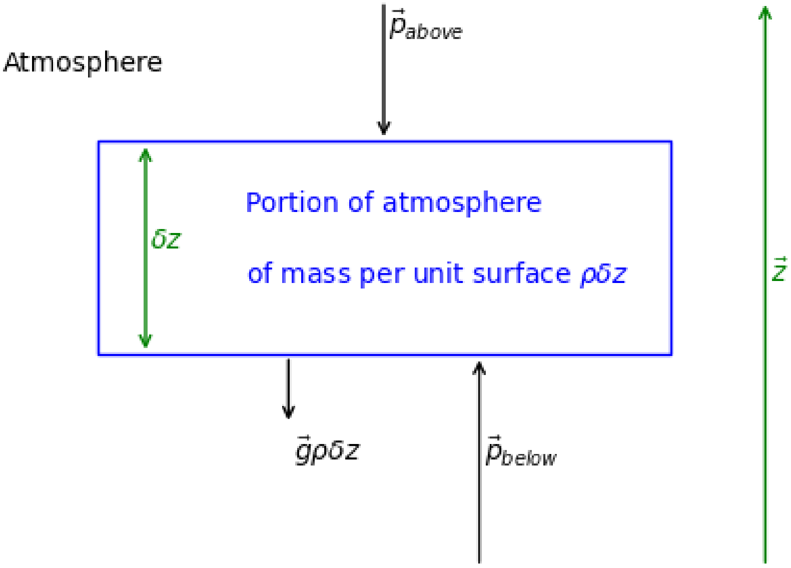

Figure 2.3: Representation of the vertical forces (black) acting on a portion of the atmosphere (blue) in hydrostatic equilibrium.

Figure 2.3 represents a portion of the atmosphere of volumetric mass density ρ which is not accelerated and submitted to gravity and the pressure around it. This means that the forces acting on it are balanced, i.e. this portion of air is in hydrostatic equilibrium. There is no horizontal pressure gradient so the pressure is balanced on both sides of the portion of the atmosphere. But the pressure exerted on the upper side is lower than the pressure exerted on the lower side and the difference of pressure from the bottom to the top of the portion of the atmosphere is noted $\vec{\delta p} = \vec{p}_{below} + \vec{p}_{above}$ and thus $\vec{\delta p}$ point upwards. In amplitude we have $\delta p = p_{below} - p_{above}$. Summing the forces for an arbitrary small layer δz on the vertical gives $\vec{\delta p} + \vec{g}\rho\delta z = 0$ where g is the gravitational acceleration. In amplitude form, as $\vec{\delta p}$ points upwards and $\vec{g}$ points downwards,

$$\delta p \;=\; -g\rho\delta z \tag{2.14}$$

simply stating that, at hydrostatic equilibrium, the difference of pressure along a layer of width δz equals the weight of that layer. For an infinitely small layer δz, we derive from 2.14 the hydrostatic equilibrium equation

$$\frac{\partial p}{\partial z} = -\rho\, g. \tag{2.15}$$

If we consider pressures p_1 and p_2 at altitudes z_1 and z_2 respectively, the integral of equation 2.15 is

$$p_1 - p_2 = \int_{z_1}^{z_2} \rho(z) g(z) \mathrm{d}z. \tag{2.16}$$

where $p_1 - p_2$ is positive if $z_1 < z_2$. The pressure p at an altitude z is equal to the integral of the density multiplied by the gravitational acceleration from z to space

$$p(z) = \int_{z}^{z_{space}} \rho(z) g(z)\, \mathrm{d}z \tag{2.17}$$

where z_{space} is the altitude at which the density of the atmosphere is negligible (see Figure 8.5).

In this work, pressure can sometimes be reported in millibar ($mbar$) equivalent to hectopascale (hPa) or $100 kg/m/s^2$. We derive the CO_2 number density n in molecules/cm^3 that we convert afterwards as volume mass density in kg/cm^3 as $\rho = n\, m_a$ where the atomic mass $m_a(kg) = m_m/N_A/1 \times 10^3$ where N_A is the Avogadro constant and m_m is the molar mass. An average value of CO_2 molar mass over their isotopologues and weighted by their terrestrial abundances is 44.01 g/mol. The same value is used in this work and the error to Mars isotopic abundances is lower than 0.001 g/mol.

The pressure retrieved is only the partial pressure for CO_2. Carbon dioxide in the conditions of the atmosphere of Mars can be considered an ideal gas. The corrections from the Van der Waals equation are around 0.1% on Mars surface[3] while the uncertainties on the retrieved profiles are around 1%. This correction is reduced with increasing altitudes. When computing the temperature from the ideal gas law as

$$T = \frac{p_{CO_2}/\mathcal{R}_{CO_2}}{k_B n_{CO_2}/\mathcal{R}_{CO_2}} = \frac{p_{CO_2}}{k_B n_{CO_2}} \tag{2.18}$$

the temperature computed is independent from the CO_2 volume mixing ratio ($\mathcal{R}_{CO_2}$).

Scale Height

From equation 2.14 and the ideal gas law, $\rho = \frac{m_a\, p}{k_B\, T}$, where m_a is the averaged atomic mass over all molecules in the atmosphere and k_B is Boltzmann's constant ($1.380649 \times 10^{-23}\, J/K^4$.), we find

$$\frac{\delta p}{p} = \frac{\delta z}{\frac{k_B\, T}{m_a\, g}}. \tag{2.19}$$

The denominator on the right-hand side of 2.19 has units of meter and is called the scale height

$$h = \frac{k_B\, T}{m_a\, g}. \tag{2.20}$$

---

[3] Computed only for carbon dioxide. The Van der Waals constants are $a = 3.64 \times 10^{-}1\, m^6 Pa/mol$ (intermolecular attraction) and $b = 4.267 \times 10^{-}5\, m^3/mol$ (excluded volume).

[4] Considered exact since 2019 (Bipm, 2018)

The parameters t, g, and m_a are varying with the altitude z but g is varying very slowly, a gradient over T is limited by the dry adiabatic lapse rate and m_a can be considered as constant below the homopause (∼120 km) where the atmospheric constituents are well mixed. An often reported scale height value for the atmosphere of Mars (below the homopause) is 11.1 km considering a mean temperature of 210 K. This value is higher for Mars than for Earth (8.5 km) as the ratio of temperature over gravity (T/g) is higher for Mars (T is around 1.4 times lower but g is around 2.6 times lower for Mars than for Earth).

If we consider a constant scale height with altitudes, the integration of 2.19 gives the barometric equation

$$p(z) = p_0 \, \exp\left(\frac{z_0 - z}{h}\right) \tag{2.21}$$

where the pressure is divided (multiplied) by a factor e every 11.1 km upwards (downwards).

For Mars, the value of the gravity varies by 12% when passing from 0 to 200 km altitude, or by 0.6% when we go up by one scale height ($11.1\,km$). On a few kilometres, we might assume a constant scale height which is equivalent to assuming an isothermal atmosphere. From 2.19 and $p = n\,k_B\,T$, we then derive

$$n(z) = n_0 \, \exp\left(\frac{z_0 - z}{h}\right). \tag{2.22}$$

The assumptions of a constant temperature or scale height are acceptable approximations on a few kilometres, where g, T and h can somewhat be considered constant.

2.1.3 Lapse rate

The lapse rate is the negative of the vertical temperature gradient

$$\Gamma = -\frac{dT}{dz}. \tag{2.23}$$

An important value for the lapse rate can be derived considering a dry adiabatic parcel of air. The first law of thermodynamics is

$$dq = 0 = c_p \mathrm{d}T - \frac{\mathrm{d}p}{\rho} \tag{2.24}$$

where c_p is the specific heat capacity. Replacing $\mathrm{d}p$ with the hydrostatic equilibrium equation 2.14, we find the theoretical value for the dry adiabatic lapse rate (DALR)

$$\Gamma_d = \frac{g}{c_p} \tag{2.25}$$

which is around $4.3\,K/km$ for Mars. If the parcel moves upwards and the 'environmental' lapse rate is superadiabatic (higher than the DALR), then the parcel will be surrounded by colder air and it will continue to move upwards. If, on the contrary, the parcel is surrounded by warmer air, the parcel will stop and return downward. The first case is an unstable process while the second is stable. In reality, the DALR is $2.5\,K/km$ just above the boundary layer (Haberle et al., 2017).

This parameter is important in the troposphere (first 50 km altitude) of Mars where convection can occur. When the lapse rate is smaller than the adiabatic lapse rate, no convection occurs and the atmosphere is stable.

For a constant lapse rate, we have

$$T(z) = T_0 - \Gamma(z - z_0) \tag{2.26}$$

with a temperature T_0 at an altitude z_0. The integration of equation 2.17 as

$$\int_{p_0}^{p} \frac{\mathrm{d}p'}{p'} = -\frac{m_a\, g}{k_B} \int_{z_0}^{z} \frac{\mathrm{d}z'}{T(z')}, \tag{2.27}$$

we then find

$$\ln\left(\frac{p}{p_0}\right) = \frac{m_a\, g}{k_B}\frac{1}{\Gamma} \ln\left(\frac{T(z)}{T_0}\right) \tag{2.28}$$

and finally

$$p(z) = p_0 \left[\frac{T(z)}{T_0}\right]^{\frac{m_a\, g}{k_B\, \Gamma}}. \tag{2.29}$$

The pressure is always decreasing with altitudes whatever the value of Γ: the ratio $T(z)/T_0$ is lower than one if the temperature decreases ($\Gamma > 0$) and the exponent in 2.29 is negative if the temperature increases ($\Gamma < 0$). Of course, for $\Gamma = 0$, the integral in 2.27 gives 2.21 and not 2.29.

With the ideal gas law and 2.29 we find a similar equation for the density

$$n(z) = n_0 \left[\frac{t(z)}{t_0}\right]^{\frac{m_a\, g}{k_B\, \Gamma} - 1}. \tag{2.30}$$

The power in 2.29 is the ratio of the autoconvective lapse rate over the environmental lapse rate (Petty, 2008). The autoconvective lapse rate is defined as

$$\Gamma_a = \frac{g}{k_B/m_a} \tag{2.31}$$

and is 19.8 K/km for Mars. A lapse rate higher than that value can occur close to the surface where heated air expands producing a density inversion and a convection process (Petty, 2008).

2.1.4 Pressure

The average pressure at 0 km (as defined in Smith et al. (2001)) is 6 mbar, a value ∼150 times lower than for Earth. Carbon dioxide constitutes more than 95% of the atmosphere of Mars and its main variations are similar to those of the pressure. During the Southern winter, which coincides with the aphelion of Mars (when Mars is the farthest from the Sun on its elliptical orbit), the temperature can be so low that a large amount of CO_2 condensates at the pole. The surface pressure decreases by almost 30% to its value in Southern summer. This important variation of pressure was first recorded from entries of landers with Mars 6 (Kerzhanovich, 1977) the Viking Landers (Nier and McElroy, 1977; Seiff and Kirk, 1977) measurements (see figure 2.4). The difference of surface pressure between the two landers are due to a difference in height of the landed surface, Viking lander 2 being 900 m lower in altitude. Along a Martian year, there are two maxima happening at solstices and two minima happening at equinoxes. The carbon dioxide volume mixing ratio varies then by a maximum of 0.5% (Forget et al., 2007; Hourdin et al., 1995).

More measurement of pressure and measurements where performed with Pathfinder (Magalhses et al., 1999), the Mars Exploration Rovers (Withers and Smith, 2006) and from accelerometers during the aerobreaking phases of Mars Global Surveyor (MGS) (Keating et al., 1998), Mars Odyssey (ODY) (Withers, 2006) and Mars Reconnaissance Orbiter (Tolson et al., 2008).

The European orbiter Mars Express (MEx) contained several instruments capable of sounding the density and pressure. The Spectroscopy for Investigation of Characteristics of the Atmosphere of Mars (SPICAM) instrument had two channels (Bertaux et al., 2005), one working in the IR and the other one in the UV. Both channel was sensitive to some CO_2 spectral signature up to around 100 km altitude. The IR channel was mainly dedicated to infer the water vapour volume mixing ratio (Fedorova et al., 2006, 2009) but the UV channel was used to infer the CO_2 seasonal, latitudinal and diurnal variations (Forget et al., 2009). Concerning the mesosphere, they found a similar seasonal variation of CO_2 density that was explained by an increase of the scale height in the lower atmosphere as its temperature was increasing with the dust loading. The IR channel was used to compare the retrieved CO_2 density during MY 28 and 32. They found stronger seasonal variations in MY 28 which involved a global dust storm (Fedorova et al., 2018).

Three other instruments onboard MEx can monitor the density and/or the pressure. The Observatoire pour la Minéralogie, l'Eau, les Glaces et l'Activité (OMEGA) imaging spectrometer retrieves the surface pressure from nadir measurements (Forget et al., 2007). The Planetary Fourier Spectrometer (PFS) (Giuranna et al., 2021)[5] and the Mars Radio Science (MaRS) experiment (Pätzold et al., 2016) are able to retrieve the CO_2 density.

Nowadays, the CO_2 density is monitored in the thermosphere from Imaging Ultraviolet Spectrograph (IUVS) (Evans et al., 2023) and Neutral Gas and Ion Mass Spectrometer (NGIMS) (Stone et al., 2022) onboard Mars Atmosphere and Volatile Evolution (MAVEN) (Jakosky et al., 2015) and from the troposphere to the thermosphere with the Atmospheric Chemistry Suite (ACS) (Belyaev et al., 2022) and the Nadir and Occultation for Mars Discovery (NOMAD) (López Valverde et al., 2022; Trompet et al., 2023a,b) onboard the Trace Gas Orbiter (TGO) (Vago et al., 2015).

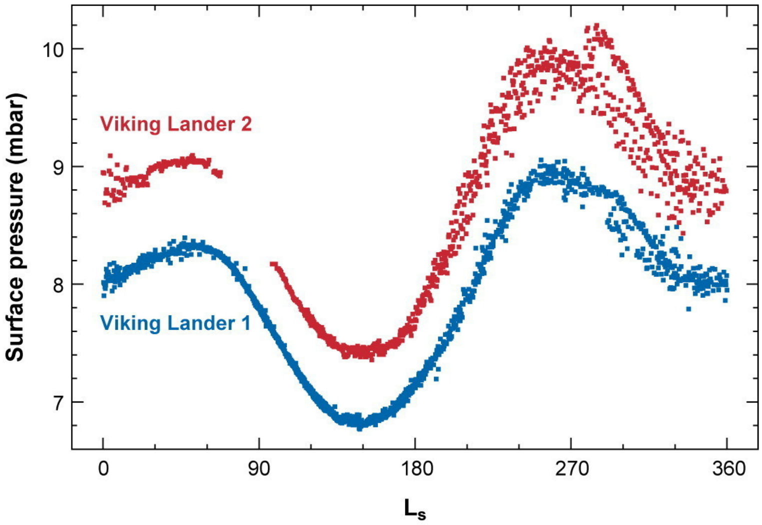

Figure 2.4: Viking Landers pressure curves measured on the landed surface (image downloaded from https://www.planetary.org/space-images/atmospheric-pressure-data-viking-landers).

---

[5] CO_2 density can be retrieved from PFS measurements but, to the best of my knowledge, their retrieved densities have not been published.

2.1.5 Temperature and thermal structure

The temperature of the atmosphere of Mars is much lower than for the Earth. The annual average solar irradiance of Mars is about half of that of the Earth and its atmosphere is much thinner, inhibiting a greenhouse effect. The averaged surface temperature is approximatively 215 K with an extremum of 150 K at the poles during winter and 300 K at the southern subtropic when Mars is close to perihelion.

The thermal structure (i.e. the globally averaged temperature profile) is divided into three main layers (Haberle et al., 2017) represented in Figure 2.5:

- the troposphere extends from the surface up to approximately 60 km, mainly controlled by the surface temperature and where the temperature decreases with altitude,
- the mesosphere extends from ∼50 to ∼100 km where the average temperature stays approximatively constant but there are large zonal variations due to vertically propagating gravity waves, planetary waves, and tides.
- the thermosphere where the temperature increases with altitudes mainly due to extreme UV (EUV) absorption.

There is mainly convection close to the surface of Mars. Radiation in the middle atmosphere and conduction in the higher part of the atmosphere.

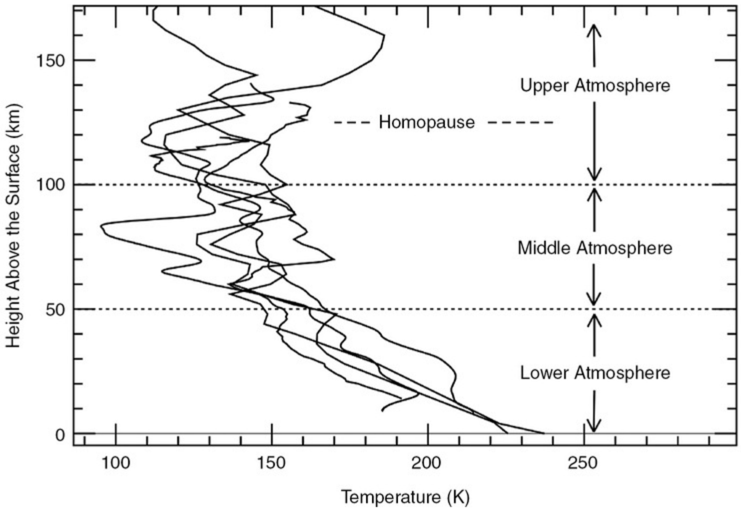

Figure 2.5: In situ measurements of temperature from different landers. The lower, middle and upper atmospheres correspond respectively to the troposphere, mesosphere and thermosphere. Image credits: Haberle et al. (2017)

In the troposphere (0-50 km) the temperature changes with the solar local time and following the dust loading.

The mesosphere (50-100 km) has an averaged constant temperature but the presence of planetary waves produces local variations. As the waves propagate upwards, their amplitude increases, the lapse rate becomes superadiabatic and the wave finally breaks (North et al., 2014).

A planetary boundary layer (PBL) can be considered as a fourth layer. The PBL lays in the first kilometers of altitude close to the surface. The temperature is highly dependent on the surface temperature. Surface heating can further decrease the gradient of temperature during the day or invert the temperature gradient at night due to a colder surface. The PBL is also dependent on the topography. Low surface thermal inertia and such a thin atmosphere produce high-temperature variation between the day and night sides. But with solar occultation measurements in the infrared, the PBL is rarely probed due to strong absorption by dust.

In the planetary boundary layer, the lapse rate is superadiabatic during the day and negative during the night. These strong temperature variations produce atmospheric thermal tides (Haberle et al., 2017) which are said to be migrating if they are Sun-synchronous and non-migrating otherwise.

There are four main temporal trends in the thermal structure of Mars: semi-diurnal, diurnal, seasonal, and inter-annual (Haberle et al., 2017). These variations are mainly due to solar irradiation and heating due to dust storms (Smith, 2008). The seasonal and diurnal variations of temperature are related to the position of Mars along its orbit and the rotation of Mars around itself. Thermal tides with a semi-diurnal variation of temperature appear due to the absorption of infrared radiation from the warm surface during the day. Variation of temperature depends as well on the topography, albedo, and thermal inertia. Inter-annual changes can be seen during the dust storm seasons with some larger regional or global dust storms. Starting on May, 30th 2018, the last global dust storm (GDS) to date covered the whole planet after a few weeks (Montabone et al., 2020) with a substantial increase of the temperature in the troposphere and the thermosphere (Belyaev et al., 2022; López Valverde et al., 2022).

The main difference with Earth's atmosphere is the absence of a stratosphere between the troposphere and the mesosphere where, on Earth, the temperature is increasing due to the presence of an ozone layer absorbing UV radiation. The atmosphere of Mars contains also ozone but in quantity far too small to initiate a substantial modification in the thermal structure of the atmosphere.

The troposphere of the Earth is ∼12 km (about four times smaller than for Mars) with a lapse rate of ∼6.5 K/km. For both atmospheres, the environmental lapse rate is smaller than the DALR. For Earth, this is due to latent heat released from the condensation of water vapor while for Mars, it is the absorption of the solar light by dust which heats the atmosphere.

2.1.6 Homopause

The homosphere is the region of the atmosphere where its gaseous constituents are well mixed by turbulent processes and all these constituents keep a constant volume mixing ratio (VMR) with altitude. For higher altitudes, diffusion starts to predominate over turbulence and the constituents follow equation 2.19 with their atomic mass. This region is called the heterosphere and the VMR of lighter molecules increases with altitude more rapidly than for heavy molecules. The separation between those two regions is called the homopause but is not happening at one specific altitude as the atmosphere continuously passes from mainly turbulent to diffusion processes.

Mahaffy et al. (2015) suggest that the altitude of the homopause should be close to 130 km as they report similar VMR values for the main constituents derived with NGIMS/Maven and those reported by Mahaffy et al. (2012) from on-ground measurements with SAM/Curiosity. More recently, Belyaev et al. (2022) reported a seasonally varying homopause at 90-100 km at aphelion and 120-130 km at perihelion with short-term variations that seem to be related to the dust activity.

2.2 Methane on Mars

Several teams have claimed detection of methane in the atmosphere of Mars but the too-low signal-to-noise (SNR) of their data could not be considered a clear confirmation of methane presence. The first detection of methane was reported in (Krasnopolsky et al., 2004) from measurements made in 1999 using the Fourier Transform Spectrometer Canada-France-Hawaii Telescope. The methane VMR retrieved was 10±3 part per billion (ppb). In 2003, the PFS instrument on board the Mars Express spacecraft detected methane with a VMR ranging from 0 to 35 ppb (Formisano et al., 2004). Mumma et al. (2009) detected several ppb of methane from ground-based measurements in 2003 and 2006 from plumes that were attributed to ground releases. Since 2013, the TLS-SAM instrument on the rover Curiosity reported measurements of methane in the Gale crater (Webster et al., 2013, 2015, 2018, 2020, 2021). Recently, one more result in favor of methane in the atmosphere of Mars is the PFS detection of methane one day after detection from TLS-SAM on-board the Curiosity rover. PFS found 15.5±2.5 ppb while TLS-SAM found 5.78±2.27 ppb of methane the day before. A spot tracking mode was performed (Giuranna et al., 2019) to bin 280 spectra to increase the signal to noise ratio. Different possible processes can be a source of methane: biotic/abiotic or released from clathrates (Yung et al., 2018). On Earth, most of the atmospheric methane has biotic origins. Methane can also be absorbed and released from surface rocks with rates dependent on temperatures. If methane is present in the atmosphere of Mars, several atmospheric processes should reduce its presence: ultraviolet photolysis and reactions with OH and OD (D for Deuterium isotope). The release of methane, if present in the atmosphere of Mars, has been proposed to be seasonal considering possible regolith adsorption/diffusion (Moores et al., 2019; Etiope and Oehler, 2019) or seasonal biologic activities. Nevertheless, methane should be well mixed in the atmosphere up to 60 km of altitude after a few months. Furthermore, GCMs (General Circulation Models) simulations predict a methane lifetime of 300 years in the atmosphere of Mars (Lefèvre and Forget, 2009). The confirmation of methane detection and its quantification was the main aim of TGO and it was first an important topic for this thesis. The first results based on ACS and NOMAD solar occultation spectra do not provide any clear detection of methane in the range of values detected by the other instruments.

2.3 Summary

After providing basic information about Mars, this chapter introduced the state of the atmosphere of Mars. Important seasonal effects are induced on Mars due to its obliquity. In addition, the high eccentricity of its orbit produces an important discrepancy between the seasons in the Northern and Southern hemispheres as the Northern summer solstice is happening close to aphelion (Mars is the farthest from the Sun) and thus Southern summer solstice is happening close to perihelion (Mars is the closets from the Sun). We first reviewed the hydrostatic law and a model for gravity around Mars. The knowledge of the latter is important for an accurate description of the former. The hydrostatic equilibrium equation is very helpful as it directly relates differences in pressure with height as a function of the density. Some important atmospheric parameters - the pressure and thermal structure - were then described. Mars has an important seasonal cycle of pressure and the thermal structure contains three altitude regions: the troposphere (ending at ∼50 km), the mesosphere (∼50-100 km), and the thermosphere (starting at ∼100 km). Finally, the search for methane was summarized. The next chapter continues the introduction by explaining the main concepts necessary to understand the measurements.

Chapter 3

Molecular spectroscopy and radiative transfer for solar occultation

For solar occultation, the radiative transfer equation simplifies to the Beer-Lambert law (section 3.2). The energy transmitted through the atmosphere depends on the number of species along the line of sight and their absorption coefficients (section 3.1). The following sections recall the principal notions on these interactions for infrared radiations.

3.1 Molecular spectroscopy

Molecules can absorb, emit, or scatter specific quantum of electromagnetic radiations - called photons - and molecular spectroscopy is the study of those interactions. Absorption or emission of a photon changes the energy state of a molecule. In spectroscopy, we do not measure directly its energy state but we can measure the radiant energy emitted or absorbed. A spectrum is this radiant energy as a function of the energy range of the photon, which is called a spectral range.

In solar occultation measurements, the radiant energy emitted by molecules in the atmosphere can be neglected with respect to the radiant energy emitted by the Sun and absorbed by the molecules. In this work, scattering will not be considered as their spectral signatures are much broader than those due to absorption by molecules[1].

From quantum mechanics, we know that the energy states of a molecule can only have specific values that are dependent on the symmetry of the molecule. NOMAD spans two different spectral ranges:

- The infrared range where this transition translated a change in the rotation of the molecule and/or a change in the vibration of its atoms to each other. Those transitions are thus called rovibrational: the energy state passes from a rotational level belonging to a vibrational level to another rotational level belonging to another vibrational level. This spectral range is usually expressed in wavenumber ν in cm^{-1} associated with the wave of the photon. This is not an energy unit but is associated with energy by the Plank-Einstein relation:

---

[1] In the lower part of the atmosphere, where a lot of dust is present, scattering is the main process involved in the extinction of the radiance emitted by the Sun. This lower part is carefully avoided in this work (see section 8.1.1.

$E = \nu hc$ where E is the energy in electron-volt eV or Joule (J), h is Planck's constant ($4.135667696 \times 10^{-15}\, eV\, s$ or $6.62607015 \times 10^{-34} J\, s$) and c is the speed of light in vacuum ($299792458\, m/s$). In the following, we will continue to express energies in cm^{-1} and remember the Plank-Einstein relation.

- The ultraviolet-visible range where an electronic transition occurs. This spectral range is used to derive ozone density profiles (Khayat et al., 2021; Patel et al., 2021; Piccialli et al., 2022) as well as aerosols(Willame, 2015). The UV-visible spectral range is usually expressed in wavelength $\lambda = \frac{1}{\nu}$.

As this work focused on the NOMAD-SO infrared channel, only the rovibrational transitions are described hereafter. The HITRAN database (Gordon et al., 2022) provides the precise positions of the transitions for the molecules and spectral ranges we are interested in. Detailed theoretical background on molecular spectroscopy will be found in (Bernath, 2005; Hollas, 2004; Herzberg and Crawford, 1946).

3.1.1 Rovibrational transitions

The theoretical computation of the rotational and vibrational energy levels of a molecule requires solving the Schrödinger's equation and deriving a set of wave functions ψ_i associated with a set of eigenvalues E_i (see, for instance, Bernath (2005, chap. 4&7)) which are the molecular energy levels. Only the results concerning these energy levels are summarized in this section.

The total energy of a molecule is approximated by the sum of the electronic energy, the translational energy, the rotational energy, and the vibrational energy. This is a consequence of the Born-Oppenheimer approximation stating that the nuclei and electron wave functions can be set apart as the nuclei are much heavier than the electrons.

The infrared molecular transitions involve rotational and vibrational energy levels depending on the symmetry of the molecule. The electronic energy being unchanged, the total energy is the sum of the vibrational E_v and the rotational energies E_r.

$$E = E_r + E_v \tag{3.1}$$

and is also called the rovibrational energy.

The energy levels for a diatomic molecule are similar to linear molecules such as CO_2 and are briefly recalled in this section. The rotational energy of each vibrational state for a diatomic molecule is well approximated by

$$E_r(J) = BJ(J+1) - DJ^2(J+1)^2 + ... \tag{3.2}$$

where B is the rotational constant, D is the centrifugal distortion constant and J is the angular quantum number specifying the rotational energy level and is a strictly positive integer. The left-hand side is a series with each following term decreasing by several orders of magnitude.

The B and D parameters are both slightly decreasing as the vibrational energy level increases but a good approximation to the rotational constant is still

$$B(I) = \frac{h}{8\pi^2 Ic} \tag{3.3}$$

where I is the moment of inertia $I = \sum_i m_i r_i^2$ computed for all atoms i. For a molecule with only two atoms, we have $I = \mu\, r_0^2$ with μ the reduced mass and r_0 the bond length. The parameters B and E_r are thus in units of the inverse of a length (usually in cm^{-1}).

The vibrational energy levels are well approximated by

$$E_v(v) = \nu_e\,(v + \frac{1}{2}) \,-\, \nu_e\,\chi_e\,(v + \frac{1}{2})^2 \,+\, ... \tag{3.4}$$

where χ_e is the anharmonicity coefficients, v is a positive integer called the vibrational quantum number and ν_e is the vibrational wavenumber in cm^{-1}. For diatomic molecules, ν_e is inversely proportional to the square root of the reduced mass of the molecule.

The vibrational transitions involve energies of the order of $1000\,cm^{-1}$, much higher than the rotational transitions with energies of $1 - 10\,cm^{-1}$. Purely rotational transitions are thus spread in the microwave spectral range.

Neglecting the second terms in 3.2 and 3.4 the rovibrational energy levels are

$$E(v, J) \;=\; \nu_e\,(v + \frac{1}{2}) \;+\; BJ(J+1) \tag{3.5}$$

where vibrational transitions are $\Delta v = \pm 1, \pm 2, \pm 3, etc.$[2].

Not all transitions of the J number are allowed. There must be a permanent dipole moment and there is a selection rule allowing only transition as $\Delta J = \pm 1$. For polyatomic molecules, a change in the dipole moment can be perpendicular to the direction of the molecular axis and $\Delta J = 0$ is allowed in this case.

Those different transitions are called P, Q, and R branches respectively for lower ($\Delta J = -1$), equal ($\Delta J = 0$), or higher ($\Delta J = +1$) rotational quantum number with respect to the initial energy level. Those three branches form a complete vibrational band. For a Q branch, as J remains the same, these transitions appear in a narrow spectral range around ν. For an R branch, the spacing between rotational levels is $E(v+1, J+1) - E(v, J) \approx\; \nu\,(v + 1 + \frac{1}{2}) + B(J+1)(J+2) - \,\nu\,(v + \frac{1}{2}) \,-\, BJ(J+1) = \nu + 2B(J+1)$ and the spacing between adjacent transitions on a spectrum is $\sim 2B$. For a P branch, the spacing between rotational levels is $E(v+1, J-1) - E(r, J) \approx \nu \,-\, 2B(J+1)$ and the spacing between adjacent transitions on a spectrum is $\sim -2B$. For CO_2 with two identical oxygen isotopes, only even J levels are allowed and the spacing between lines is $\sim 4B$. For increasing wavenumber (in cm^{-1}) we see first the P branch with first the transition for higher J levels, then the Q branch if allowed, and then the R branch with first lower J levels.

There are some noticeable differences for isotopologues (for example, see the CO_2 isotopologues lines in figure 5.14). As the moment of inertia I increases

- the vibrational wavenumber ν_e (as well as $\nu_e\chi_e$) decreases and the transition appears at a lower wavenumber,
- the rotational constant B decreases and the spacings between adjacent rotational transitions decrease.

The next two subsections provides more details concerning the rovibrational transitions of the carbon dioxide molecule in the infrared spectral range.

Carbon dioxide rovibrational transitions

Carbon dioxide is a linear triatomic centrosymmetric molecule belonging to the point group $D_{\infty h}$. The rotational energy of linear molecules is well described by the expression 3.2 used for diatomic molecules.

---

[2] For an harmonic oscillator, there is a selection rule $|\Delta v| = 1$. More information will be found in Herzberg (1950) pp. 79-80 or Hollas (2004) section 6.1.1). In fact, $|\Delta v| > 1$ is possible only if we consider the anharmonicity of the vibration.

A molecule has $3N-6$ normal modes of vibration where N is the number of atoms and where 6 degree of freedom are removed as they describe translational and purely rotational movements. A linear molecule has $3N-5$ normal modes of vibration as the rotation around the molecular axis is degenerated. Figure 3.1 represents the fundamental vibrational modes for carbon dioxide :

- the symmetric stretching mode ν_1 at 1353.6 cm^{-1},
- the bending mode ν_2 at 672.6 cm^{-1} which is doubly degenerated,
- the asymmetric stretching mode ν_3 at 2349 cm^{-1}.

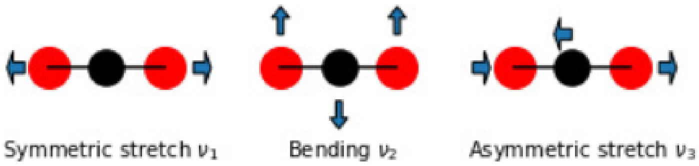

Figure 3.1: Representation of the three fundamental vibration modes of CO_2. The black and red circles represent respectively the carbon and oxygen atoms.

The symmetric stretching mode involves a modification of the dipole only for non-symmetrical molecules so this mode is active only for CO_2 isotopologues containing different oxygen isotopes. The $2\nu_1$ mode is present in the NOMAD-SO spectral range and is an interesting mode to derive the densities for $^{16}O^{12}C^{18}O$ and $^{16}O^{12}C^{17}O$ as this spectral range is free from any line from the main isotopologue $^{12}C^{16}O_2$.

In the following, we will refer to CO_2 isotopologues with the three digit provided in table 3.1.

Iso.	Code	Abundance (Earth)	Abundance (Mars)
$^{12}C^{16}O_2$	626	0.98420	0.98338
$^{16}O^{13}C^{16}O$	636	0.01106	0.01162
$^{16}O^{12}C^{18}O$	628	0.00395	0.00419
$^{16}O^{12}C^{17}O$	627	0.00073	0.00078
$^{16}O^{13}C^{18}O$	638	0.00002	0.00002

Table 3.1: The five most important isotopologues for CO_2 with their three digit code and their abundances for Earth and Mars (Shved, 2016).

The rotational levels are alternatively symmetric for even (*gerade* in German) J noted g and antisymmetric for odd (*ungerade* in German) J noted u. For a centrosymmetric CO_2 molecule containing oxygen atoms with zero-spin nuclei, only even J levels are allowed (Herzberg and Crawford, 1946, chap. IV) and the spacing between adjacent lines is ~4B instead of ~2B. Therefore, the spacing between adjacent lines for $^{12}C^{16}O_2$ and $^{13}C^{16}O_2$ are larger than for $^{16}O^{12}C^{18}O$ for which odd J levels are allowed.

The main CO_2 transition are described in (Herzberg and Crawford, 1946) and (Courtoy, 1957). In the following, we use the transitions recorded in the HITRAN database (Gordon et al., 2017) and use the AFGL notation code as defined in Rothman and Young (1981); Esplin et al. (1988); Mcclatchey et al. (1973). The energy levels are described by five numbers $\nu_1 \nu_2 l \nu_3 r$ where l is the angular momentum associated with the bending mode and r is the ranking index. The last number is necessary as there is a Fermi resonance between the modes ν_1 and ν_2. The quantum number l can either be $\nu_2, \nu_2 - 2, \nu_2 - 4, ..., 1$ or 0 and r can either be $1, 2, ...\nu_1 + 1$ and specifies the level in the Fermi resonating group. A ranking index of 1 means that the state is not involved in Fermi resonance and higher values correspond to lower energies (Mcclatchey et al., 1973).

As the molecule rotates, there is a Coriolis interaction between the ν_2 and ν_3 modes and the energy levels split for symmetric or antisymmetric wave functions referenced respectively by a letter e or f (Esplin et al., 1988). This is known as the l-type doubling and must not be confused with the g/u notation.

3.1.2 Spectral line intensity

The derivation of the spectral line intensity S is detailed in (Šimečková et al., 2006). The intensity of a transition line at thermodynamic equilibrium depends on the Einstein A-coefficients and on the population of the energy levels which follows a Boltzmann distribution. The resulting expression is

$$S_{21}(t) = I_a \, \frac{A_{21}}{8\,\pi\,c\,\nu^2} \frac{g_2 \exp\left(\frac{-c_2\,E_1}{T}\right)\left(1 - \exp\left(\frac{-c_2\,\nu}{T}\right)\right)}{Q(T)} \tag{3.6}$$

where $c_2 = h\,c/k_B$ is the second radiation constant, E_1 is the lower state energy, g_2 is the statistical weight of the upper state, I_a is the abundance, usually provided for the Earth and Q is the total internal partition sum function

$$Q(t) = \sum_k g_k \, exp\left(-\frac{c_2\,E_k}{T}\right) \tag{3.7}$$

where the sum is on all rovibrational states k.

The last factor $(1 - \exp(-c_2\,\nu/T))$, called the induced emission term, can be neglected in the infrared (Gamache et al., 2022).

The peaks of intensity of all lines are a function of the temperature as seen in Figure 3.2 for transitions involving $2\nu_1 + \nu 2$. But the lines with high J number of the P and R branch are much more sensitive to temperature variations.

To get rid of the abundance factor in 3.6, it is written considering a ratio with respect to a reference temperature $T_{ref} = 296\,K$,

$$S(T) = S(T_{ref})\frac{Q(T_{ref})}{Q(T)} \exp\left(-c_2\,E_1\left(\frac{1}{T} - \frac{1}{T_{ref}}\right)\right)\frac{(1 - \exp(-c_2\,\nu/T))}{(1 - \exp(-c_2\,\nu/T_{ref}))} \tag{3.8}$$

where, in this work, $S(T_{ref})$, $Q(T_{ref})$, $Q(T)$ and E_1 are taken from the HITRAN database (Gordon et al., 2017). The intensities of other molecules can be compared in Figure 3.3.

Local Thermodynamic Equilibrium

An assumption used in this work is that the atmosphere of Mars is in local thermodynamic equilibrium (LTE). This assumption is valid when collision are frequent enough so that the kinetic temperature of the molecules corresponds to the population of the vibrational energy states.

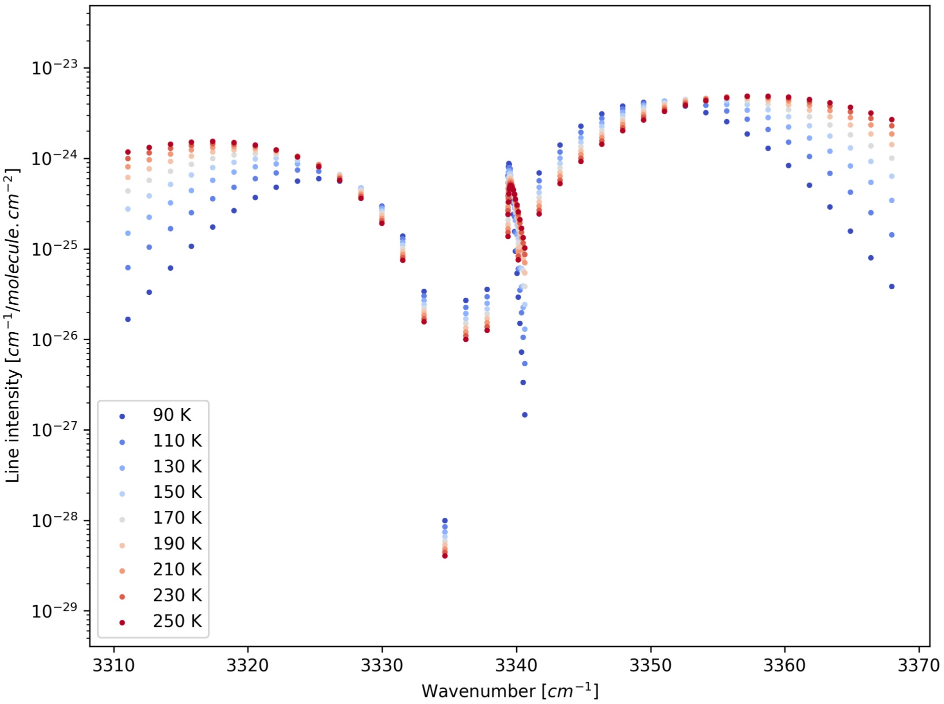

Figure 3.2: The intensity of the lines for transition $2\nu_1 + \nu 2$ (AFGL code 21102-00001) of CO_2 as a function of temperature and computed with equation 3.8. This band contains a Q branch around $3340\,cm^{-1}$.

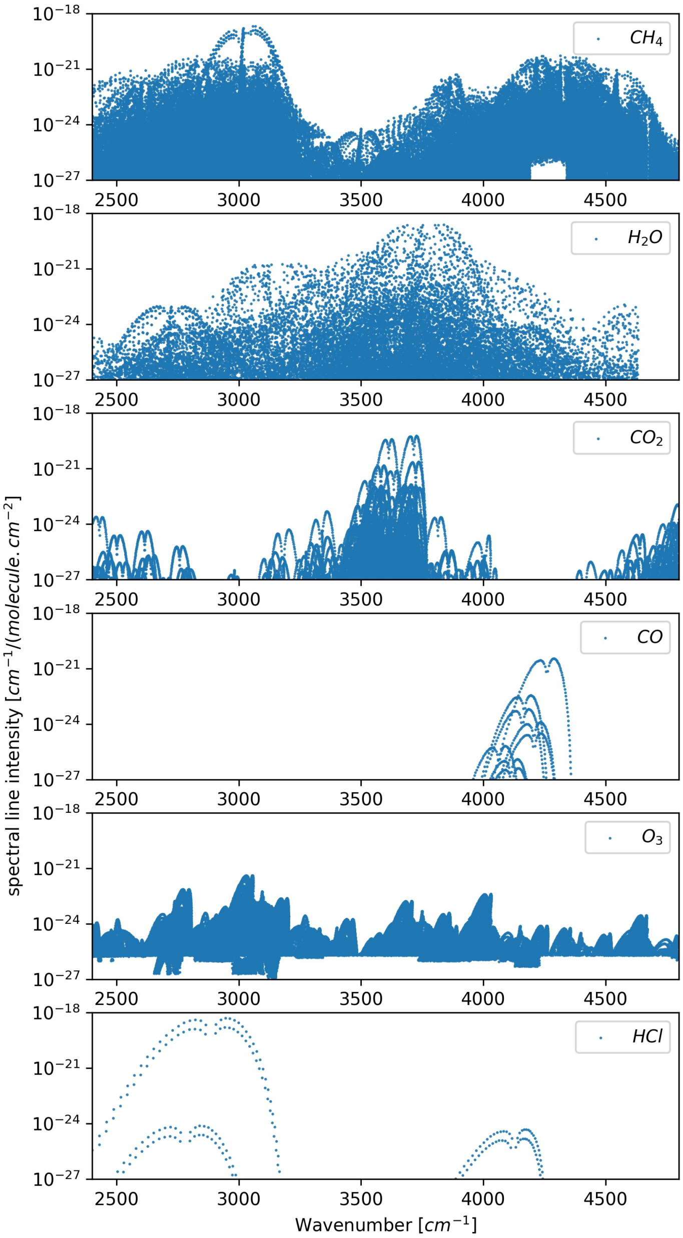

Figure 3.3: The intensity of lines of different molecules reported in Mars atmosphere and in the mid-infrared. The values are taken from the HITRAN database.

At high altitudes, when the mean time between molecular collision starts to be lower than the radiative lifetime of the vibrational states, the populations of those states do not anymore follow the Boltzmann law and the intensities of the transition depart from the formula 3.8.

As presented in section 3.1.1, most of the spectral lines fitted in this work correspond to transitions from the ground state which are less affected than hot bands by non-LTE processes (Edwards et al., 1998).

The partition functions needed in formula 3.8 and provided by HITRAN are those for LTE case.

A non-LTE population of levels in the first hot bands in the spectral range corresponding to diffraction order 165 might lead to a difference of up to 0.005 in transmittance at a tangent altitude of 130 km (López-Valverde et al., 2018).

3.1.3 Spectral line shape

In practice, a transition line does not appear at a single wavenumber corresponding to the transition energy but several processes produce a broadening of the line:

- **Doppler broadening**: the gas molecules are moving in different directions and their average velocity is proportional to the temperature (provided that the gas is in local-thermodynamic equilibrium). The velocities are given by the Maxwell-Boltzmann distribution and the Doppler broadening function is therefore a Gaussian following a normal distribution

  $$\Phi_D(\nu, \nu_0, T, m) = \frac{1}{\alpha_D\sqrt{2\pi}} \exp - \frac{(\nu - \nu_0)^2}{2\alpha_D^2} \tag{3.9}$$

  where ν_0 is the wavenumber of the transition and the Half-Width at Half-Maximum (HWHM) is

  $$\alpha_D(\nu_0, T, m) = \frac{\nu_0}{c}\sqrt{\frac{k_B T}{m}} \tag{3.10}$$

  where m is the molecule mass.

- **collisional broadening**: when pressure is important enough and a non-negligible amount of molecules come close enough, their energy levels are perturbed and this is translated by a line broadening as well as a line displacement (smaller than the broadening). This broadening is modelled by a Lorentzian

  $$\Phi_C(\nu, \nu_0, p, T) = \frac{1}{\pi} \frac{\gamma_C(p, T)}{\gamma_C^2(p, T) + (\nu - \nu_0 - \delta_C(p))^2} \tag{3.11}$$

  where δ_C is the collisional shift of the centre of the line and γ_C is the collisional broadening HWHM

  $$\gamma_C(p, T) = \left(\frac{T_{ref}}{T}\right)^{n_{air}} \left[\gamma_{air}(p_{top}, T_{ref})(p - p_{self}) + \gamma_{self}(p_{top}, T_{ref})p_{self}\right] \tag{3.12}$$

  where n_{air} is the coefficient of the temperature dependence of the air-broadened half-width, γ_{air} (with the Martian air) is the air-broadened half width at half maximum, γ_{self} is the self-broadened half width at half maximum, p_{self} is the partial pressure of the gas and for CO_2 in Mars homosphere, $p_{self} \approx 0.95\,p$. In HITRAN, the values of n_{air} and γ_{air} are provided for standard Earth air. The values for Mars are derived as explained in Robert et al. (2016); Vandaele et al. (2008) with some values derived from Sung and Varanasi (2005).

- **natural broadening**: the Heisenberg uncertainty principle tells us that the transition energy between two states cannot be known with infinite precision. Nevertheless, in our case, the natural broadening is negligible with respect to the previous processes.

Doppler broadening depends on temperature (and the molecule mass) and collisional broadening depends on the pressure and temperature of the medium. The relative importance of these two broadenings can be estimated by comparing their Full-Width at Half-Maximum (FWHM) which are $FWHM_D = 2\sqrt{2\ln 2}\alpha_D$ and $FWHM_C = 2\gamma_C$.

The Voigt profile combines the Doppler broadening and the collisional broadening:

$$\Phi_V(\nu,\nu_0,p,T,m) = A\frac{y}{\pi}\int_{-\infty}^{+\infty}\frac{\exp -u^2}{y^2+(x-u)^2}du \tag{3.13}$$

with

$$\begin{aligned} A(\nu_0,T,m) &= \frac{S\sqrt{\ln 2}}{\alpha_D(\nu_0,T,m)\sqrt{\pi}}, \\ y(\nu_0,p,T,m) &= \sqrt{\ln 2}\frac{\gamma_C(p,T)}{\alpha_D(\nu_0,T,m)}, \\ x(\nu,\nu_0,p,T,m) &= \sqrt{\ln 2}\frac{\nu-\nu_0-\delta_C(p)}{\alpha_D(\nu_0,T,m)}. \end{aligned} \tag{3.14}$$

In practice, the Voigt profile must be approximated and, in this work, we use the Faddeeva approximation (Wells, 1999).

The spectra treated in this work have a resolution of around $0.15\,cm^{-1}$ and the Voigt profile is a well-enough accurate model for the line shape. At low resolution, the Voigt profile deviates from the experimental profile and we must consider more elaborated line shape profiles like the Rautian (Rautian and Sobel'man, 1967) or Galatry (Galatry, 1961) models that take into account the dependence between the Doppler effect and the pressure effect.

The spectral absorption coefficient are eventually computed as

$$\sigma(\nu,p,T) \;=\; S_{ij}(T)\,\Phi(\nu,\nu_0,p,T,m). \tag{3.15}$$

3.2 Solar occultation

A solar occultation consists of recording the spectral signature of species absorbing the Sun light. Occultation by stars from the ground have been used since a long while (Pannekoek, 1903; Hays and Roble, 1968). But satellite have the advantage of getting rid of the Earth atmosphere and provide a better SNR. The latter is much improved thanks to using the Sun as source but the atmosphere probed is restricted to the terminator.

The first solar occultation measurements from a satellite was performed in 1979 with SAGE I to study the Earth atmosphere (McCormick, 1987) and the first one scanning the Martian atmosphere was performed a decade later with PHOBOS-2 (Blamont et al., 1989). Further solar occultations of the Martian atmosphere were performed with the IR channel of the SPICAM instrument onboard Mars Express to provide carbon dioxide and water density, and temperature profiles. More recently, solar occultations have been performed with two instruments onboard the Trace Gas Orbiter (TGO): the Atmospheric Chemistry Suite (ACS) and the NOMAD instruments.

An occultation measurement consists in recording the remaining radiance passing through the atmosphere and along the line of sight as drawn in figure 3.4. The radiative transfer equation reduces to the Beer-Lambert law, meaning that we consider only absorption and can neglect refraction and scattering. As the atmosphere of Mars is thin and has a low pressure even at low altitudes, refraction is neglected as well.

3.2.1 Solar spectrum in the mid-infrared spectral range

In theory, a transmittance spectrum should not contain any remaining features from the source as they would cancel in the ratio I/I_0. In practice, the instrument function, and mainly the pixel to wavenumber calibration (see section 5.2.1), might slightly change between the recording of the solar and atmospheric spectra letting some residual of the solar lines in the transmittance spectrum. Those residuals are small, and have a characteristic "N" shape and we can verify that they correspond to solar lines thanks to solar spectra like those presented in Hase et al. (2010); Meftah et al. (2018). Table 3.2 gives an overview of the most important solar lines in the mid-infrared range[3]. The solar spectrum used in this work is a combination of ACE data (Hase et al., 2010) which covers the whole NOMAD-SO spectral range and SOLSPEC data which starts at $3300cm^{-1}$ (Meftah et al., 2018).

Diffraction order	Wavenumber $[cm^{-1}]$	Species
126	2837.83	Si
130	2927.05 2928.08	Si Na
134	3014.97	Si
140	3154.42	Si
141	3172.87	Si
142	3197.95 3209.44 3210.67	Si Mg Si
151	3414.35	Ca
156	3520.43	Si & C
162	3650.93	Si
168	3787.88	Mg

Table 3.2: Main solar lines in the NOMAD-SO spectral range.

Those solar lines are also interesting while working with calibration measurements to derive some instrumental parameters (see section 5.2.3) or the pixel to wavenumber calibration. We still need to keep in mind that the intensity of the solar lines varies following the position on the solar disk and following the solar activity cycle of 11 years.

3.2.2 Absorption

The Beer-Lambert law states that the variation of intensity of a radiation dI passing through a medium is proportional to the initial intensity I_0 multiplied by the density of the medium, the absorption coefficient of the medium, and the distance travelled in the medium. Applied to a solar occultation at a tangent altitude z_{tg}, we find

---

[3] None of them are present in the spectral ranges (diffraction orders) used in this work.

$$dI(\nu, z_{tg}) \;=\; I_0(\nu) \sum_{gas\, i} \int \sigma_i(\nu, p(r), T(r)) n_i(r) dr \tag{3.16}$$

where n_i is the number density of the gas i, σ_i is the spectral absorption coefficients at wavelength ν of the gas i and dr is the distance travelled along the line of sight.

Another form of the Beer-Lambert law is found by integrating 3.16

$$\mathcal{T}(\nu, z_{tg}) = \frac{I(\nu, z_{tg})}{I_0(\nu)} = e^{-\tau(\nu, z_{tg})} \tag{3.17}$$

where τ is the optical depth, I is the remaining radiance after passing through the atmosphere and $\mathcal{T}$ is the transmittance. The optical depth is a function of density, pressure, and temperature. In practice, the Beer-Lambert law is not valid any more for high optical depths. In the following, this analysis will be restricted to optical depth small enough so that the Beer-Lambert law is valid and more information on the way this restriction is implemented is provided in section 5.3.1.

Both densities and absorption coefficients are functions of the vertical altitude z and not of the altitudes along the line of sight (LoS) r. We can apply a change of variable using Pythagoras formula $z^2 = r^2 + z_{tg}^2$ where z and z_{tg} are given with respect to Mars centre (see Figure 3.4). Considering that the line of sight does not move during the measurement of a spectrum, it follows that

$$dr = \frac{z}{\sqrt{z^2 - z_{tg}^2}} dz. \tag{3.18}$$

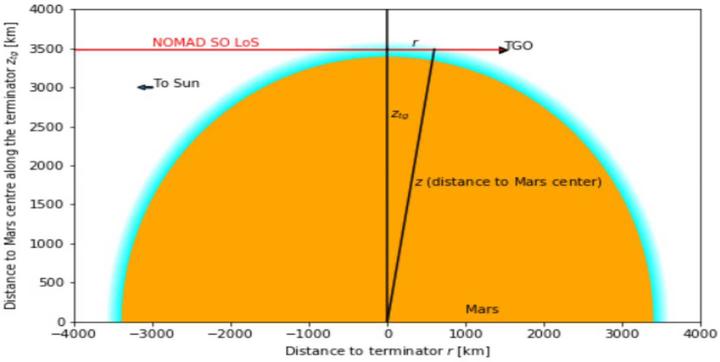
NOMAD SO LoS
r
TGO
To Sun
z_{tg}
z (distance to Mars center)
Mars
Distance to Mars centre along the terminator z_{tg} [km]
Distance to terminator r [km]
4000
3500
3000
2500
2000
1500
1000
500
0
−4000
−3000
−2000
−1000
0
1000
2000
3000
4000

Figure 3.4: Geometry of an occultation.

The optical depth is computed as the integration along the LoS of the absorption coefficients σ of the gas composing the atmosphere multiplied by the density:

$$\begin{aligned} \tau(\nu, z_{tg}, p, T) &= \sum_{gas\, i} \left(\int_{-z_{space}}^{z_{space}} \sigma_i(\nu, p(z), T(z))\, n_i(z)\, \frac{z}{\sqrt{z^2 - z_{tg}^2}}\, \mathrm{d}z \right) \\ &= 2 \sum_{gas\, i} \left(\int_{z_{tg}}^{z_{space}} \sigma_i(\nu, p(z), T(z))\, n_i(z)\, \frac{z}{\sqrt{z^2 - z_{tg}^2}}\, \mathrm{d}z \right) \end{aligned} \tag{3.19}$$

where z_{space} is the altitude above which the remaining density is negligible[4]. The second equality remains only if we consider that the gradient of pressure and temperature on both sides of the terminator is negligible.

The total column density of one gas along the LoS is called the slant column density:

$$c(z_{tg}) = 2\int_{z_{tg}}^{z_{space}} n(z)\frac{z}{\sqrt{z^2 - z_{tg}^2}}\,\mathrm{d}z. \tag{3.20}$$

The slant column profile is the vertical projection of a two-dimensional circularly symmetric function of the local density. This relation is known as the Abel[5] transform (Abel, 1826). As we will see in chapter 4, this is a Fredholm integral equation of the first kind (Press et al., 2007) and is an ill-posed problem.

In practice, c and n are vectors with discrete values of the continuous functions $c(z)$ and $n(z)$. We make also the approximation of an atmosphere split into spherically symmetrical layers as in figure 3.5. That assumption of layers within which the density is constant is commonly used in occultation retrievals. We consider only vertical variations of the atmospheric state and no horizontal variations. In each of those layers, the density, pressure, and temperature are assumed to be constant. The density in one layer is then set to the average density within the layer.

From equation 3.20 we have the following matrix notation

$$\boldsymbol{c} = \boldsymbol{K}\,\boldsymbol{n} \tag{3.21}$$

where $\boldsymbol{K}$ is the Abel transform matrix. Figure 3.5 describes how the atmosphere is discretised and the elements K_{ij} are computed as

$$K_{ij} = 2\int_{zmid_{j-1}}^{zmid_{j+1}} f(r)\frac{r}{\sqrt{r^2 - z_i^2}}\mathrm{d}r. \tag{3.22}$$

where $zmid$ are either

$$zmid_j = \begin{cases} (z_j + z_{j-1})/2 & \text{if j in [0, N-1],} \\ z_j + (z_j - z_{j-1})/2 & \text{if j = N.} \end{cases} \tag{3.23}$$

If the layers are small enough (in practice, less than 1 km), we can make the approximation of a constant density within the layer and $f(r) = 1$. Equation 3.22 simplifies to

$$K_{ij} = \sqrt{zmid_{j+1}^2 - z_i^2} - \sqrt{zmid_{j-1}^2 - z_i^2}. \tag{3.24}$$

The K matrix is an upper quasi-triangular matrix (see Figure 3.7) not necessarily square with the most important values on the diagonal and continuously decreasing on the off-diagonal.

We approximated the altitude where the mean density occurs in the middle of the layer. This is not true but with sufficiently small layers, we can consider that this altitude corresponds to the middle altitudes of each layer *zmid*. Using the GEM-Mars averaged CO_2 density profile and computing the column profile for different discretisation, we get the figure 3.6. A discretisation of 1 km step leads to a relative error smaller than 2%.

---

[4] A precise altitude at which the remaining density can be considered as negligible will be derived in section 8.1.2 and summarized in Figure 8.5.

[5] Niels Henrik Abel (5 August 1802 – 6 April 1829), Norwegian mathematician

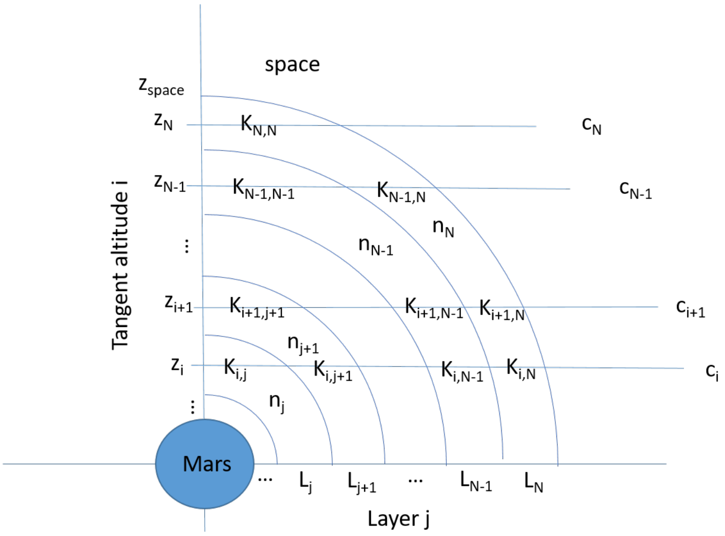
space
z_{space}
z_N
$K_{N,N}$
c_N
z_{N-1}
$K_{N-1,N-1}$
$K_{N-1,N}$
c_{N-1}
n_N
n_{N-1}
Tangent altitude i
⋮
z_{i+1}
$K_{i+1,j+1}$
$K_{i+1,N-1}$
$K_{i+1,N}$
c_{i+1}
n_{j+1}
z_i
$K_{i,j}$
$K_{i,j+1}$
$K_{i,N-1}$
$K_{i,N}$
c_i
⋮
n_j
Mars
...
L_j
L_{j+1}
...
L_{N-1}
L_N
Layer j

Figure 3.5: Discretization of the atmosphere for the Abel transform.

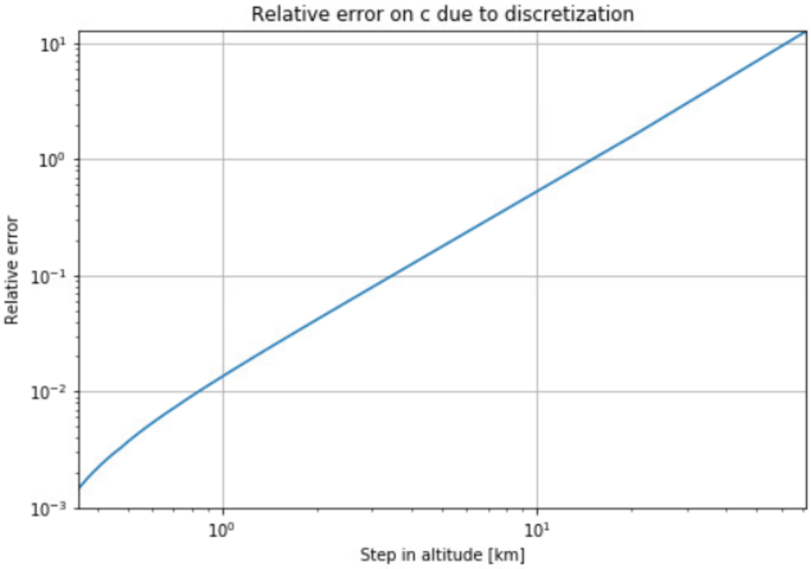

Figure 3.6: Relative error on c due to the discretisation of the atmosphere. The density used here is the GEM-Mars averaged CO_2 density profile from version a585.

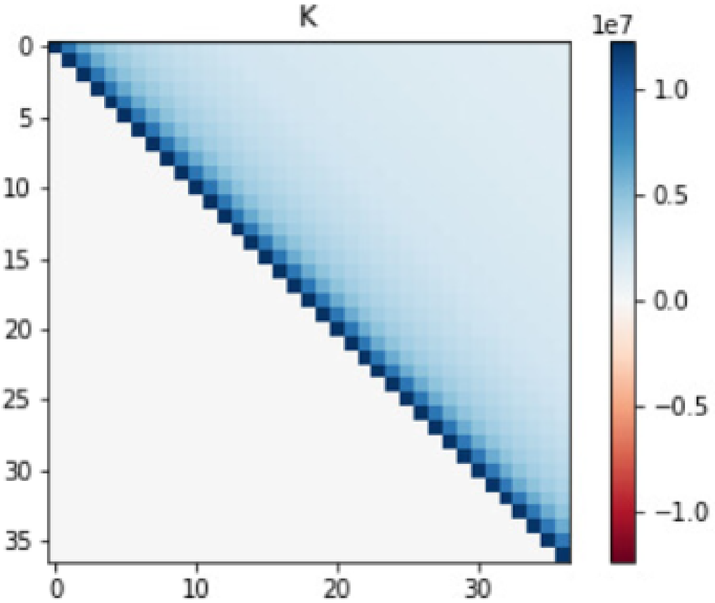

Figure 3.7: Example of K matrix where the y-axis corresponds to the i index and the x-axis corresponds to the j index. Those index correspond to around 60 km for index 0 to around 100 km for index 36. The colour bar provides the values of the matrix in meter. We see that the K matrix is an upper triangular matrix with values decreasing with off-diagonal terms.

3.2.3 Scattering

In the computation of the optical depth in equation 3.19, we should also take into account the scattering of the Sunlight along the slant path. The consequence of scattering on the infrared spectra is a broad decrease of the signal at all wavelength with still a more important decrease at higher wavenumbers. In this work, we will avoid any spectrum that might contain an important amount of spectral signature of dust, water ice clouds, or carbon dioxide ice clouds by not processing spectra that have a mean signal half of Sun spectra. Retrieving those features involves Mie theory for scattering. Nevertheless, we still need to consider the scattering due to the molecules of the atmosphere which involves the Rayleigh theory which applies when the size of the scattering particles is much smaller than the wavelength of the scattered light.

The Rayleigh scattering cross-sections are directly proportional to the fourth power of the wavenumber and is thus more important for UV and visible spectral range than for the infrared. In practice, the scattering cross sections are computed from the formula in Sneep and Ubachs (2005) (already implemented in the radiative transfer code ASIMUT, see section 4.1.5).

3.3 summary

This chapter is an overview of the theory of radiative transfer in the infrared for solar occultations. The first section recalled the necessary background on the spectral signature of molecules with particular attention brought to carbon dioxide. In the second section, the Beer-Lambert law is recalled. This law involves the transmittance as a function of absorption coefficients, the path along the line of sight, and the density. Deriving the density from the transmittance involves the inverse of the Abel transform which leads to inverse problems. The theory for inverse problems is thus described in the next chapter.

Chapter 4

Inverse problems

Our problem consists in finding a vertical profile of number density for selected species from the transmittance in equations 3.17 and 3.19. This problem is ill-posed and non-linear. The main cause of the ill-posedness is that the solution, i.e. the local density at the terminator, is unstable to small variations in the measurements, i.e. the molecular lines in the spectra.

The retrieval implemented in this work is made in two main steps:

- First, for each transmittance spectrum, we adjust a factor to the optical depth in equation 3.17 to fit our forward model to the spectrum. The initial slant column if multiplied by this factor to find the fitted slant column. This task is done using the ASIMUT program where the optimal estimation method is implemented (see section 4.1.2).
- Second, we treat the ill-posed problem: the slant column profile is directly inverted into a local density profile with a Tikhonov regularisation (see section 4.2). The main role of this regularisation is to reduce as much as possible the amplification of noise due to the ill-posedness of the problem while keeping the real physical variations of the profile.

The advantage of this inversion in two steps is the possibility to fine-tune the Tikhonov regularisation as the second part involves only linear algebra.

The notation used in this section is similar to Rodgers (2000) which is the most commonly used inverse method for atmospheric science.

4.1 Slant column profile inversion

In this first step of the inversion, we derive slant column values for each transmittance spectrum of the solar occultation with the radiative transfer code ASIMUT-ALVL (Vandaele et al., 2006) where the regularisation is done in a Bayesian framework.

4.1.1 Non-linear least square solution

In this case, the measurements are the transmittance $\mathcal{T}$ and the solution is the true density profile n to be derived with equation 3.17. This equation is formalised here as

$$\boldsymbol{y} = \boldsymbol{F}(\hat{\boldsymbol{x}}, \boldsymbol{b}) + \boldsymbol{\epsilon} \tag{4.1}$$

where $\boldsymbol{F}$ is the forward model containing the exponential of the inverse of the optical depth. This forward model depends on the true solution $\hat{\boldsymbol{x}}$ (the density profile) and model parameters like instrumental and spectroscopic characteristics gathered in $\boldsymbol{b}$, and $\boldsymbol{y}$ are the measurements. In practice, there is always some noise affecting the transmittance spectra translated in the $\boldsymbol{\epsilon}$ term. The forward model is a non-linear function of $\boldsymbol{x}$ so a direct inversion would be quite difficult. Instead, we will adjust the retrieved solution to fit as well as possible the measurements using the forward model. The theoretical solution can be found by iterating over the solution $\boldsymbol{x}$ using for example a Gauss-Newton iteration algorithm weighted on the uncertainties as

$$\boldsymbol{x_{i+1}} = \boldsymbol{x_i} + \left(\boldsymbol{J_i^T S_\epsilon^{-1} J_i}\right)^{-1} \boldsymbol{J_i^T S_\epsilon^{-1}} \left(\boldsymbol{y} - \boldsymbol{F(x_i)}\right) \tag{4.2}$$

where $\boldsymbol{S_\epsilon}$ is the covariance matrix over the measurement state and $\boldsymbol{J_i}$ is the Jacobian of the forward model at the solution $\boldsymbol{x_i}$.

This method iteratively changes the solution $\boldsymbol{x}$ to match the measurements. We still call it an 'inversion' but that should not be confused with a 'direct inversion' of the forward model (that would require some approximation for this non-linear problem).

4.1.2 Optimal Estimation Method

Also known as statistical regularisation or climatological regularisation, this method is often used for Earth atmosphere parameter retrievals for which an *a priori* is pretty well known. It is also sometimes used for the Mars atmosphere for which some GCM can provide some results for a precise time and geometry. The general theory over this regularisation method is described in Rodgers (2000); Tarantola (2005). The solution for a linear problem is (Rodgers, 2000, eq. 4.3)[1],

$$\boldsymbol{x} = (\boldsymbol{K^T S_\epsilon^{-1} K} + \boldsymbol{S_a^{-1}})^{-1} \left(\boldsymbol{K^T S_\epsilon^{-1} y} + \boldsymbol{S_a^{-1} K x_a}\right) \tag{4.3}$$

where $\boldsymbol{S_\epsilon}$ is the covariance matrix over the measurement state and should not be confused with the covariance matrix $\boldsymbol{S_e}$ of an ensemble of state about the mean state:

$$\boldsymbol{S_e} = \mathbb{E}\{(\boldsymbol{x} - \overline{\boldsymbol{x}})(\boldsymbol{x} - \overline{\boldsymbol{x}})\} \tag{4.4}$$

If the *a priori* $\boldsymbol{x_a}$ is set to the null vector, the formula 4.3 is similar to 4.15 for the Tikhonov regularisation described in section 4.2.2 and they are both compared in section 4.2.3.

The Gauss-Newton iterative algorithm for the non-linear least square problem weighted with the uncertainties over the measurements is given by this expression

$$\begin{aligned} \boldsymbol{x_{i+1}} &= \boldsymbol{x_a} + \left(\boldsymbol{J_i^T S_\epsilon^{-1} J_i} + \boldsymbol{S_a^{-1}}\right)^{-1} \boldsymbol{J_i^T S_\epsilon^{-1}} \left(\boldsymbol{y} - \boldsymbol{F(x_i)} + \boldsymbol{J_i(x_i - x_a)}\right) \\ &= \boldsymbol{x_a} + \boldsymbol{G} \left(\boldsymbol{y} - \boldsymbol{F(x_i)} + \boldsymbol{J(x_i - x_a)}\right) \end{aligned} \tag{4.5}$$

where the $\boldsymbol{S_a}$ matrix is called the covariance matrix over the *a priori* (Rodgers, 2000, eq. 2.23 & 5.9)

$$\boldsymbol{S_a} = \mathbb{E}\{(\boldsymbol{\hat{x}} - \boldsymbol{x_a})(\boldsymbol{\hat{x}} - \boldsymbol{x_a})\}. \tag{4.6}$$

This iterative algorithm stops when the following convergence criteria are satisfied ((Rodgers, 2000, eq. 5.29 and 5.33))

$$\begin{aligned} (\boldsymbol{x_i} - \boldsymbol{x_{i-1}})^{\boldsymbol{T}} \boldsymbol{S_i^{-1}} (\boldsymbol{x_i} - \boldsymbol{x_{i-1}}) &< 10^{-2}\, n, \\ (\boldsymbol{y_i} - \boldsymbol{y_{i-1}})^{\boldsymbol{T}} \boldsymbol{S_\epsilon^{-1}} (\boldsymbol{y_i} - \boldsymbol{y_{i-1}}) &< 10^{-3}\, m. \end{aligned} \tag{4.7}$$

Rodgers (2000) does not explain in detail how to build the $\boldsymbol{S_a}$ matrix. Of course, its diagonal elements should be at least of the order of $\boldsymbol{J}^T \boldsymbol{S_\epsilon^{-1} J}$ to have an impact on the retrieval. When we have some good reasons to think that the *a priori* $\boldsymbol{x_a}$ is close to the true solution $\boldsymbol{\hat{x}}$, we can see this problem as a modification of the *a priori* with a $\boldsymbol{S_a}$ matrix that allows some modifications to that *a priori* to better fit the measurements. This works if the *a priori* information represents a good knowledge of the parameter state to be retrieved. Usually, three kinds of matrices are proposed: a diagonal matrix or some sort of diagonal matrix but with values on the off-diagonal terms which decrease with a Gaussian, an exponential, or a tent function. If the *a priori* is taken from a GCM, we might construct this matrix with the variability over the *a priori* as provided by the GCM.

---

[1] In the linear case, $\boldsymbol{J} = \boldsymbol{K}$.

In our case, we want to derive a slant column c from a transmittance spectrum. To simplify the problem, ASIMUT does not fit c directly but a factor f multiplying c and we rewrite eq. 3.17 as

$$\mathcal{T}(\nu, z_{tg}) = e^{-f\,\tau(\nu, z_{tg}, p, T, n)}. \tag{4.8}$$

The Jacobian of $\mathcal{T}$ with respect to f is then $-\tau\mathcal{T}$. The baseline of the spectra is fitted at the same time with a fourth-order polynomial. It is important to use multiplication when deriving the baseline as an addition can introduce a biased factor f if the baseline is lower than 1.

In this work, the slant columns are computed individually for each transmittance spectrum with an *a priori* covariance value $S_a = 0.81\, x_a^2$. The inverse of this term, which appears in the formula 4.5, is small with respect to the term $\boldsymbol{J}^T \boldsymbol{S_\epsilon}^{-1} \boldsymbol{J}$. The impact of the regularisation applied here is weak[2]. This value of 0.81 correspond to a confidence up to 90% on the *a priori* value. The aim is to avoid implausible values that might appear at too high altitudes when the lines in the spectra are too weak to be correctly fitted or lower in the atmosphere when some aerosols strongly reduce the signal.

4.1.3 Uncertainties

The uncertainties over the slant column profile are computed here from the square root over the diagonal of the covariance matrix of the slant column profile which is computed as (Rodgers, 2000, eq. 5.30)

$$\boldsymbol{S_i} = (\boldsymbol{J_i^T S_\epsilon^{-1} J_i + S_a^{-1}})^{-1} \tag{4.9}$$

if the solution $\boldsymbol{x_i}$ has converged.

Some caution must be taken, we see that the covariance matrix is a function of the $\boldsymbol{S_a}$ matrix which is usually provided by the user. Its value can then be artificially reduced by giving small covariance values. This is not the case in this work as we provide a value of 81% of the *a priori*.

Also, this formula considers only the first moment (first derivatives) that can provide an approximated value for weakly non-linear problems. When saturation occurs, we should take into account additional terms involving higher derivatives. By comparing the values using the formula 4.9 with a Monte Carlo method, the first method provides uncertainty values that are three times lower than with the second method.

4.1.4 Information content

An important operator describing the retrieval is the averaging kernel defined in the n-space as

$$\boldsymbol{A} = \boldsymbol{G}\boldsymbol{K} \tag{4.10}$$

---

[2] The importance of this Sa value at this step of the retrieval is low because I select the retrieved slant column values with a degree of freedom higher than 0.99 (see section 4.1.4)

where $\boldsymbol{G}$ is the gain matrix (or generalized inverse of $\boldsymbol{K}$) and $\boldsymbol{K}$ is either the linear forward model in the linear case or the Jacobian of the final iteration step in the non-linear case.

From equations 4.5 and 4.9, we can also see the average kernel as the ratio of the covariance matrix for the regularised solution $\boldsymbol{S}$ to the covariance matrix of the unregularised solution $\boldsymbol{S_0}$

$$\boldsymbol{A} = \boldsymbol{S}\,\boldsymbol{S_0^{-1}} \tag{4.11}$$

The same operator but in the measurement-space is computed as

$$\boldsymbol{A_y} = \boldsymbol{K}\,\boldsymbol{G}. \tag{4.12}$$

Both operators contain the same information while A is, by far, the most used one in literature as well as the most useful as we usually need to check the spatial resolution of the solution related to the width of the averaging kernels. In the non-regularised least square case where no regularisation is applied, $\boldsymbol{A}$ is the identity matrix. The $\boldsymbol{A}$ matrix gets further away from the identity matrix as more information from the *a priori* is used to the derived solution. In information theory, the trace of A gives the number of degrees of freedom for the signal and the trace of $(\boldsymbol{A} - \boldsymbol{I_n})$ gives the number of degrees of freedom for noise (Rodgers, 2000).

4.1.5 ASIMUT-ALVL radiative transfer code

In this work, the slant columns are derived with the ASIMUT-ALVL radiative transfer code (Vandaele et al., 2006) developed at BIRA-IASB. ASIMUT fits a simulated spectrum to a measured one using a Gauss-Newton algorithm as a non-linear least square method with an analytical computation of the Jacobian. ASIMUT can retrieve densities for different geometries and different instrument types. ASIMUT can regularise any solution using the Optimal Estimation Method (Rodgers, 2000) through an *a priori* profile and its covariance matrix controlling the level of regularisation.

ASIMUT uses the onion peeling scheme to split the atmosphere into spherically homogenous layers and uses the Curtis-Godson approximation for the density, pressure and temperature vertical profiles. The contribution from each layer depending on varying vertical density, pressure, and temperature profiles are approximated with a single homogenous path with mean density, pressure, and temperature profiles that would give the same contribution to the transmittance spectrum (Curtis, A, 1952; Godson, 1953; Goody and Yung, 1989; Kleinböhl et al., 2009).

ASIMUT is able to simulate a gradient of temperature to avoid the hypothesis of a symmetric temperature profile from both side of the terminator as explained in section 3.2.2 (equation 3.19). This feature is not used in this work and is left for a further study.

4.2 Density profile inversion

We have derived some slant column profiles in the previous section and we now derive the corresponding local number density profile.

4.2.1 Linear least square solution

In practice, there is always some noise affecting the data, and equation 3.21 needs to be rewritten as

$$\boldsymbol{c} = \boldsymbol{K}\,\boldsymbol{\hat{n}} + \boldsymbol{e_c} \tag{4.13}$$

where $\boldsymbol{e_c}$ represents the error on the slant column $\boldsymbol{c}$ and $\boldsymbol{\hat{n}}$ is the true density profile to be distinguished from the retrieved density profile $\boldsymbol{n}$.

Our problem consists to inverse the matrix $\boldsymbol{K}$ to derive the solution $\boldsymbol{n}$ from $\boldsymbol{c}$. Even if $\boldsymbol{c}$ is not the actual measurement, in literature, it is a common practice to say that the quantity to be retrieved belongs in the "solution" space and the quantity to invert belongs in the "measurement" space. So we say that $\boldsymbol{n}$ is in the (solution) n-space in units of cm^{-3} and $\boldsymbol{c}$ is in the (measurement) c-space in units of cm^{-2}.

The Abel transform $\boldsymbol{K}$ defined in chapter 3 is not necessarily square but its Gram matrix $\boldsymbol{K}^T\boldsymbol{K}$ is square (also symmetric and positive semi-definite) by construction. The theoretical solution for $\boldsymbol{n}$ in equation 3.21 is then found by multiplying that equation by $(\boldsymbol{K}^T\boldsymbol{K})^{-1}\boldsymbol{K}^T$. As $\boldsymbol{K}$ is the Abel transform matrix, the pseudo inverse is then also an upper triangular matrix with two main diagonals.

Our problem consists to find the minimum of the linear least square problem $\left\| \boldsymbol{S_c^{-\frac{1}{2}}} \left(\boldsymbol{c} - \boldsymbol{K}\boldsymbol{n}\right) \right\|_2^2$. The solution of the local number density profile $\boldsymbol{n}$ is

$$\begin{aligned} \boldsymbol{\hat{n}} &= \left(\boldsymbol{K}^T\boldsymbol{S_c^{-1}}\boldsymbol{K}\right)^{-1}\boldsymbol{K}^T\boldsymbol{S_c^{-1}}\boldsymbol{c} \\ &= \boldsymbol{G_0}\,\boldsymbol{c} \end{aligned} \tag{4.14}$$

where $\boldsymbol{S_c}$ is the covariance matrix on the slant columns and $\boldsymbol{G_0}$ can be seen as a pseudo-inverse matrix of $\boldsymbol{K}$. The $\boldsymbol{G_0}$ matrix is approximatively bidiagonal (see figure 4.1) and thus is not continuous, a symptom of ill-posed problems.

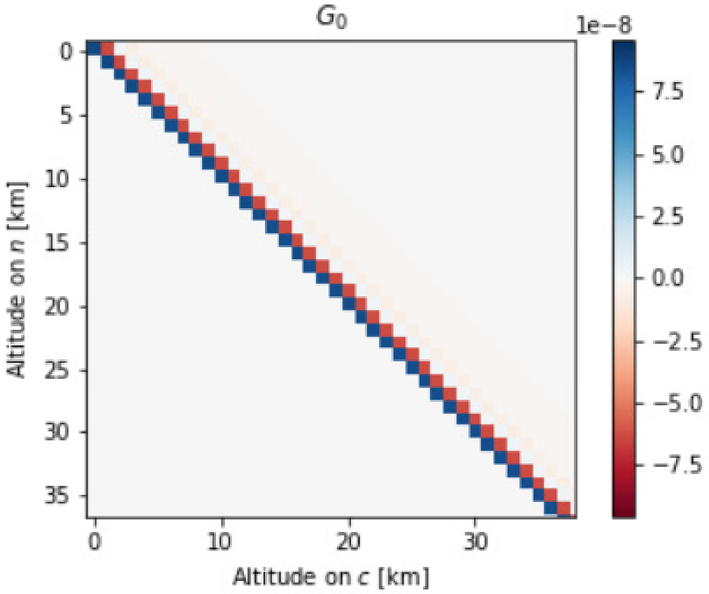

Figure 4.1: Example of $\boldsymbol{G_0}$ matrix.

Some examples of results are shown in figures 4.2 and 4.3. First, a local density profile is taken from GEM-Mars GCM[3] (Daerden et al., 2019). This profile plotted in blue on the upper right panel is a CO_2 density profile averaged over all local times, seasons, and latitudes (Erwin et al., 2018). This profile is then converted to a slant density profile using equation 3.21 (blue curve on the upper left panel). Some noise is added by considering a normal distribution centred on the profile and a standard deviation of 0.1 or 0.01 (orange curve). A local density profile is finally retrieved using equation 4.14 (orange curve on the upper left panel). Comparing the errors to the true profile (lower panels of figure 4.2), we see that they have been amplified by a factor of ∼5 after the retrieval. A well-known effect of ill-conditioned matrices.

---

[3] version a585

A parameter that gives a hint about the well-posedness of a matrix is the condition number which is here computed as the ratio of the highest singular value to the smallest one. For the $\boldsymbol{K}$ matrix of this example, the condition number has a high value around 550 (and the value is the same for the corresponding $\boldsymbol{G_0}$ matrix).

The same values of amplification of the noise are found whatever the initial error on the slant column profile as can be seen in figure 4.3.

The amplification of the noise is also related to the discretisation of the profile. If we further increase the altitude step, the condition number of $\boldsymbol{K}$ increases as well and so does the amplification of the errors.

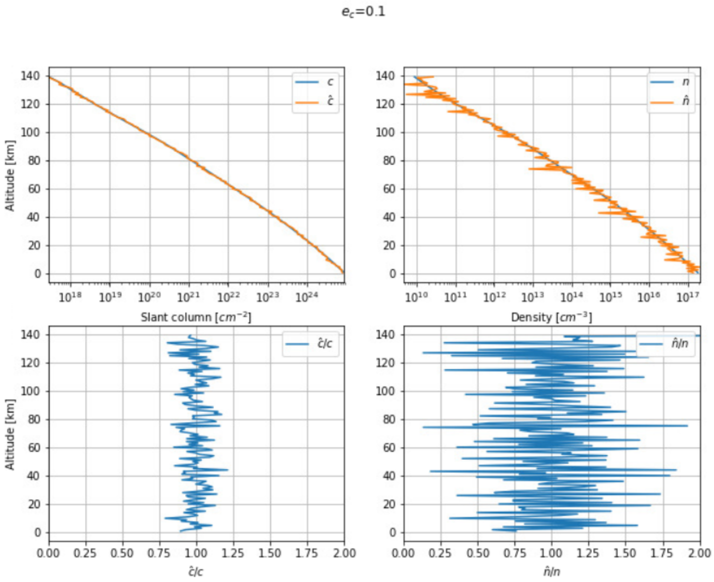

Figure 4.2: Example of slant columns (upper left panel) and local densities (upper right panel). From the local density $\boldsymbol{n}$, a slant column $\boldsymbol{c}$ is computed. Some random noise is added from a Gaussian distribution with $\sigma = 0.1$ to get $\hat{\boldsymbol{c}}$ (see the ratio $\hat{\boldsymbol{c}}/\boldsymbol{c}$ in the lower left panel). A local density $\hat{\boldsymbol{n}}$ is retrieved from $\hat{\boldsymbol{c}}$ using the non-regularised least square formula (see the ratio $\hat{\boldsymbol{n}}/\boldsymbol{n}$ in the lower right panel).

4.2.2 Tikhonov regularisation

A first attempt to solve an ill-posed problem with this regularisation method was carried on by Phillips (1962). Later Andrey Tikhonov developed the mathematical theory of this linear regularisation method, first in a paper (Tikhonov, 1963), and later in a book with Vasiliy Arsenin (Tikhonov and Arsenin, 1977). At the same time, Sean Twomey made an in-depth description

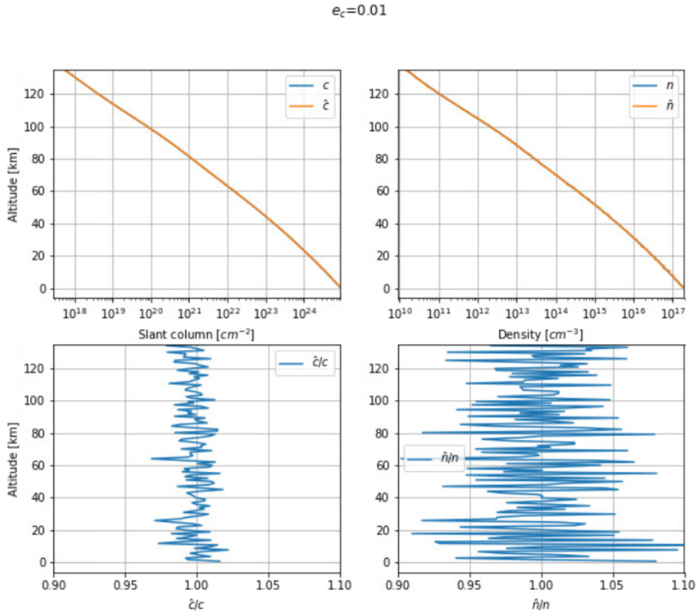

Figure 4.3: Same as figure 4.2 but with added noise by considering a standard deviation of 0.01.

of the method in Twomey (1963, 1977) for atmospheric parameter retrievals. For these reasons, what we call here the Tikhonov regularisation might be found in the literature as any combination of the names Phillips-Tikhonov-Twomey. In machine learning, this method is also known as the "ridge regression" method.

This regularisation method is quite similar to the one developed in Backus and Gilbert (1970) but Tikhonov's method regularises with respect to the smoothness of the solution while Backus and Gilbert (1970) regularise with respect to the variance of the solution, meaning that they do not seek for a smoother solution but for a more stable solution.

The idea behind Tikhonov's method is to add a constraint to the least square problem in favor of a smoother solution. The least-square solution consisted then to find the minimum of the penalized least square problem $\left\|\boldsymbol{S_c}^{-\frac{1}{2}}(\boldsymbol{c}-\boldsymbol{Kn})\right\|_2^2 + \lambda\left\|\boldsymbol{Ln}\right\|_2^2$ where λ is the regularisation parameter and $\boldsymbol{L}$ is the regularisation matrix which can either be the identity matrix, a discrete approximation of a differential operator or even a combination of them Eriksson (2000).

The solution to the regularisation least square problem is

$$\hat{\boldsymbol{n}} = (\boldsymbol{K}^T\boldsymbol{S_c^{-1}}\boldsymbol{K}+\boldsymbol{R})^{-1}\boldsymbol{K}^T\boldsymbol{S_c^{-1}}\,\boldsymbol{c} \tag{4.15}$$

where $\boldsymbol{R} = \lambda\boldsymbol{L}^T\boldsymbol{L}$ and $\boldsymbol{L}^T\boldsymbol{L}$ is the Gram matrix of $\boldsymbol{L}$.

The choice of the $\boldsymbol{L}$ matrix has different effects on the retrieved solution: an identity matrix $\boldsymbol{I}$ allows control of the magnitude of the solution while the first $\boldsymbol{L_1}$ and second $\boldsymbol{L_2}$ derivative operators control the smoothness of the solution. There are still some differences in using $\boldsymbol{L_1}$ or $\boldsymbol{L_2}$. The second one better removes spurious peaks caused by noise.

For a regular grid step, $\boldsymbol{L_2}$ is simply:

$$\boldsymbol{L_2} = \begin{pmatrix} -1 & 1 & 0 & 0 & ... & 0 \\ 1 & -2 & 1 & 0 & ... & 0 \\ 0 & 1 & -2 & 1 & ... & 0 \\ ... & ... & ... & ... & ... & ... \\ 0 & ... & 0 & 1 & -2 & 1 \\ 0 & ... & 0 & 0 & -1 & 1 \end{pmatrix} \tag{4.16}$$

The first and last lines of the matrix are here chosen as a first differential but they can be replaced as well with $(2\ -1)$ or $(0\,0)$.

This matrix needs to be slightly modified if the altitude steps are not regular and the values are derived following the algorithm of Fornberg (1988).

The retrieved solution is a density profile varying exponentially with altitudes. The density profile spans a wide range of orders. Thus, in equation 4.15, we would prefer to have a regularisation scaled to each altitude. Quémerais et al. (2006) propose to use λ proportional to the inverse of the uncertainties on the estimated density ($1/e_n$). This way of defining λ assumes that the uncertainties are directly proportional to the densities. Otherwise, densities with higher relative uncertainties will be less regularised. In our case, when the line starts to appear, the noise is important and decreases in the very first altitudes until it increases again due to the density increases.

As we can already guess, the level of regularisation required should be proportional to the level of noise on the densities. We thus modify the regularisation term as $\boldsymbol{R} = \lambda \boldsymbol{L}^T \boldsymbol{S_n^{-1}} \boldsymbol{L}$ and $\boldsymbol{S_n}$ needs to be a diagonal matrix. When λ is increased, the uncertainties increase but the vertical resolution decreases.

The Tikhonov regularisation is applied here only once but we will see in section 4.2.4 that applying several times the Tikhonov method improves the result.

4.2.3 Similarity to the Optimal Estimation Method

Equations 4.15 and 4.3 are equivalent if all values of $\boldsymbol{x_a}$ are zeros and if we state

$$\lambda \boldsymbol{L}^T \boldsymbol{L} = \boldsymbol{R} = \boldsymbol{S_a^{-1}}. \tag{4.17}$$

Tikhonov (1963) developed the mathematical background to regularise an ill-posed inverse problem by choosing $\boldsymbol{L}$ as a differential operator (or a combination of a differential operator, also called Sobolev's norm). Rodgers (2000) developed very similar tools but in a Bayesian background and defined the regularisation term as a covariance matrix. This work uses both regularisation and we want to compare those two views on regularisation.

The two methods were already compared in Steck (2002) where he proposed four different ways to find the best λ: a) considering the number of degrees of freedom, b) considering the retrieval noise error, c) considering the forward model error, d) considering the total error (Steck (2002) considered only the smoothing error and the noise uncertainty). That last method is the expected error estimation described in the section 4.2.5.

The same regularisation could have been done using only the Optimal Estimation Method. By choosing a convenient (or a Sobolev's sum of) differential operator and the problem of finding λ remains.

In OEM theory, Rodgers (2000, sect. 2.6) proposes as example to construct $\boldsymbol{S_a}$ as a Markovian covariance matrix

$$S_{a_{ij}} = \sigma_a^2 e^{-|i-j|\frac{\delta z}{h}} \tag{4.18}$$

where i and j are different layers of the atmosphere, δz is the layers spacing, σ_a is "a variance" (Rodgers, 2000, 10.3.3.2) and h is a parameter related to the scale height. For example, Irwin et al. (2008) suggest using 1.5 times the scale height for h. The formula 4.18 is followed in several radiative transfer inversion codes (Vandaele et al., 2006; Irwin et al., 2008; Eriksson et al., 2005) in a slightly modified form allowing for different altitude z:

$$S_{a_{ij}} = \sigma_a^2 e^{-\frac{1}{h}|z(i)-z(j)|} \tag{4.19}$$

The choice of σ_a is important to compute a properly regularised inversion. This formulation is nice as it somewhat reminds the barometric equation 2.21.

As Rodgers (2000, Eq. B71) showed, the inverse of expression 4.18 which is a Markovian covariance matrix is known to be a tridiagonal matrix of the form

$$\boldsymbol{S_a}^{-1} = \sigma_a^{-2}\frac{1}{1-\alpha^2}\begin{pmatrix} 1+\alpha^2 & -\alpha & 0 & \cdots & 0 & 0 \\ -\alpha & 1+\alpha^2 & -\alpha & \cdots & 0 & 0 \\ \vdots & \vdots & \ddots & \vdots & \vdots & \vdots \\ 0 & 0 & 0 & \cdots & 1+\alpha^2 & -\alpha \\ 0 & 0 & 0 & \cdots & -\alpha & 1+\alpha^2 \end{pmatrix} \tag{4.20}$$

where $\alpha = e^{-dz/h}$. The Cholesky factorization of the previous matrix gives

$$\boldsymbol{L} = \begin{pmatrix} 1 & -\alpha & 0 & \cdots & 0 & 0 \\ 0 & 1 & -\alpha & \cdots & 0 & 0 \\ \vdots & \vdots & \ddots & \vdots & \vdots & \vdots \\ 0 & 0 & 0 & \cdots & 1 & -\alpha \\ 0 & 0 & 0 & \cdots & 0 & 1 \end{pmatrix} \tag{4.21}$$

which is close to being a combination of an identity matrix and a first differential operator.

In the case for varying altitude steps (eq. 4.19) the inverse can be well approximated by $\frac{1}{\lambda(1-(\overline{dz}/h)^2)}\boldsymbol{L}^T\boldsymbol{L}$ where

$$\boldsymbol{L} = \begin{pmatrix} 1 & e^{(-|z_1-z_0|/h)} & 0 & \cdots & 0 & 0 \\ 0 & 1 & e^{(-|z_2-z_1|/h)} & \cdots & 0 & 0 \\ \vdots & \vdots & \ddots & \vdots & \vdots & \vdots \\ 0 & 0 & 0 & \cdots & 1 & e^{(-|z_n-z_{n-1}|/h)} \\ 0 & 0 & 0 & \cdots & 0 & 1 \end{pmatrix} \tag{4.22}$$

if $h < n\overline{dz}/10$ where n is the number of altitudes.

Some authors also propose a Gaussian (Xu et al., 2020) that fits better with a probability distribution function, or also a linearly decreasing correlation function (Eriksson et al., 2005). While the use of an identity matrix in $\boldsymbol{S_a}$ is obvious and translates our confidence in the *a priori*, it is good to keep in mind that the off-diagonal terms are there to smooth a retrieved profile which is altered by the noise in the measurement. We will prefer to keep the Tikhonov form of the regularisation term with a combination of differential operators as their effects are well known and one can manage easily the level of smoothing required. This way also avoids the inversion of the $\boldsymbol{S_a}$ matrix.

We can compute as well the inverse matrices for $\boldsymbol{L_1^T L_1}$, $\boldsymbol{L_2^T L_2}$, $\boldsymbol{L_1^T L_1 + L_2^T L_2}$, $\boldsymbol{I + L_2^T L_2}$, and $\boldsymbol{I + L_1^T L_1 + L_2^T L_2}$ but we cannot compute an inverse for singular matrices like $\boldsymbol{L_1^T L_1}$. Figure 4.4 provides the shape of the middle row of the $\boldsymbol{S_a}$ matrix corresponding to different differential operators.

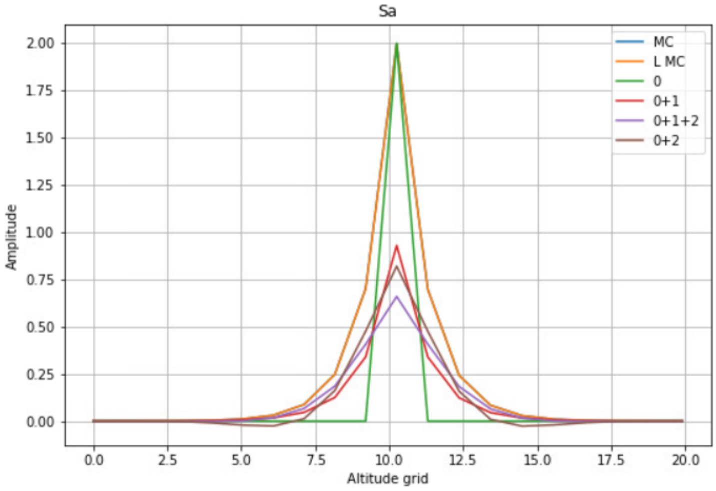

Figure 4.4: Values for the middle row of the $\boldsymbol{S_a}$ matrix obtained by inverting different combinations of differential operators. The orange and blue curves are the Markovian covariance matrices. The green curve is the identity matrix. The red, purple and brown curves correspond, respectively, to the $\boldsymbol{L_0} + \boldsymbol{L_1}$, $\boldsymbol{L_0} + \boldsymbol{L_1} + \boldsymbol{L_2}$ and $\boldsymbol{L_0} + \boldsymbol{L_2}$ differential operators.

The $\boldsymbol{S_a}$ from equations 4.18 or 4.19 are very close to an identity matrix added with a square of a first derivative.

Another interesting study on those different regularisation matrices is Xu et al. (2020) which showed that $\boldsymbol{L_1}$ better smooths the solution than $\boldsymbol{L_2}$ when the *a priori* information is less reliable.

Another method with a very similar formulation than OEM or Tikhonov is the Levenberg-Marquardt algorithm which consists in improving the solution $\boldsymbol{\hat{x}_i}$ with

$$\begin{aligned} \boldsymbol{\hat{x}_i} &= \boldsymbol{\hat{x}_{i-1}} + \left(\boldsymbol{J}^T \boldsymbol{S_c^{-1}} \boldsymbol{J} + \lambda \boldsymbol{D}^T \boldsymbol{D}\right)^{-1} \boldsymbol{J}^T \boldsymbol{S_c^{-1}} \left(\boldsymbol{y} - \boldsymbol{F}(\boldsymbol{\hat{x}_{i-1}})\right) \\ &= \boldsymbol{\hat{x}_{i-1}} + \boldsymbol{G} \left(\boldsymbol{y} - \boldsymbol{F}(\boldsymbol{\hat{x}_{i-1}})\right) \end{aligned} \tag{4.23}$$

where $\boldsymbol{F}$ is the forward model function, $\boldsymbol{J}$ is the corresponding Jacobian matrix over the retrieved parameters and evaluated in $\boldsymbol{x_{i-1}}$. The positive parameter λ controls the trade-off between a Gauss-Newton iteration as λ tends to zero and a steepest-descent iteration as λ tends to infinity. If the first guess is far from the solution, the term $\boldsymbol{J}^T \boldsymbol{S_c^{-1}} \boldsymbol{J}$ might become ill-conditioned and the steepest descent would perform better. This formula was first given in Levenberg (1944) and improved in Marquardt (1963). More information can be found in Moré (1977). The choice of λ was recommended to change at each iteration: if the residual increases, increase λ and forget the retrieved $\boldsymbol{\hat{x}_i}$ otherwise decrease λ. The $\boldsymbol{D}$ matrix must be positive definite and is also recommended to be a diagonal matrix where each diagonal element are scaled as the inverse of the diagonal elements of $\boldsymbol{J}^T \boldsymbol{S_c^{-1}} J$. What appears like a regularisation term $\lambda \boldsymbol{D}^T \boldsymbol{D}$ is more commonly called the 'damping' term in literature.

The interest in reviewing all these methods was to show that they are all equivalent. Indeed, all of them methods try to reduce the presence of noise in the data and they all need fine-tuning of a parameter controlling the regularisation.

4.2.4 Iterated Tikhonov regularisation

Due to the presence of noise in the measurements, applying the Tikhonov regularisation only once often does not provide an enough accurate solution (Doicu et al., 2010a, sect. 3.4). In this case, the iterated Tikhonov regularisation improves the accuracy by applying first a simple weighted least square solution 4.14 without regularisation and then applying successively the Tikhonov regularisation until the desired accuracy is achieved. In the theoretical iterative Tikhonov regularisation, the solution of the next iteration is computed as

$$\boldsymbol{\hat{n}_i} = \boldsymbol{G_i}\,\boldsymbol{c} + (\boldsymbol{I_n} - \boldsymbol{G_i}\,\boldsymbol{K})\boldsymbol{\hat{n}_{i-1}} \tag{4.24}$$

where the step in the solution $\boldsymbol{\hat{n}_i}$ is

$$\begin{aligned} \boldsymbol{p_i} &= \boldsymbol{\hat{n}_i} - \boldsymbol{\hat{n}_{i-1}} \\ &= \boldsymbol{G_i}\,(\boldsymbol{c} \;-\; K\boldsymbol{\hat{n}_{i-1}}) \end{aligned} \tag{4.25}$$

Quémerais et al. (2006) proposes the following algorithm

$$\begin{aligned} \boldsymbol{\hat{n}_i} &= (\boldsymbol{K}^T\boldsymbol{S_c}^{-1}\boldsymbol{K} + \lambda_0\,\boldsymbol{L}^T(\boldsymbol{S_{i-1}^{-1}})_{\boldsymbol{jj}}\boldsymbol{L})^{-1}\boldsymbol{K}^T\boldsymbol{S_c^{-1}}\,\boldsymbol{c} \\ &= \boldsymbol{S_i}\,\boldsymbol{K}^T\,\boldsymbol{S_c^{-1}}\,\boldsymbol{c} \\ &= \boldsymbol{G_i}\,\boldsymbol{c} \end{aligned} \tag{4.26}$$

where the new solution $\boldsymbol{n_i}$ are improved as the covariance matrix $\boldsymbol{S_{i-1}}$ are refined with the following equation

$$\begin{aligned} \boldsymbol{S_{n_i}^{-1}} &= \boldsymbol{K^T S_c^{-1} K} + \lambda_0 \boldsymbol{L^T S_{n_{i-1}}^{-1} L} \\ &= \sum_{j=0}^{i-1} \lambda_0^j (\boldsymbol{L^T})^j \boldsymbol{S_{n_0}^{-1}} (\boldsymbol{L})^j \end{aligned} \tag{4.27}$$

and where the covariance matrix for the non-regularised least square solution is

$$\boldsymbol{S_{n_0}^{-1}} = \boldsymbol{K^T S_c^{-1} K}. \tag{4.28}$$

which is a full matrix as $\boldsymbol{K}$ is an upper triangular matrix. The equation 4.27 can be used only if the solution $\boldsymbol{n_i}$ has converged. The uncertainties on the density profile are the square roots of the diagonal values of the covariance matrix over the solution S_n which are computed from the covariance matrix S_c (Doicu et al., 2010a).

The steps in the solutions are this time

$$\begin{aligned} \boldsymbol{p_i} &= \boldsymbol{\hat{n}_i} - \boldsymbol{\hat{n}_{i-1}} \\ &= (\boldsymbol{S_i} - \boldsymbol{S_{i-1}})\boldsymbol{K}^T\boldsymbol{S_c^{-1}}\,\boldsymbol{c} \end{aligned} \tag{4.29}$$

where equation 4.27 is used for the last equality. The $\boldsymbol{L}$ matrix being a second derivative operator, $\boldsymbol{L}^T\boldsymbol{S_{n_{i-1}}^{-1}}\boldsymbol{L}$ is a pentadiagonal matrix. Also $\boldsymbol{K}$ being an upper triangular matrix, the computed $\boldsymbol{S_i}$ for the next iteration with 4.27 is not a diagonal matrix. Nevertheless, this algorithm works only if only the diagonal values of $\boldsymbol{S_i^{-1}}$ are kept. Those values are the square of the uncertainties on $\boldsymbol{n_i}$. In 4.26, those values play the role of scaling factors to the values of the densities which are much higher at low altitudes.

This iteration scheme cannot be formulated like 4.24 where the solution of the next iteration is a linear function of the solution at the previous step. But in practice, this algorithm provides the desired accuracy faster than 4.24. An important point that must be noted is that the covariance matrix $\boldsymbol{S_{n-1}}$ must always be diagonal or the algorithm will not give the correct solution.

Two convergence criteria are applied:

- the desired accuracy over the solution must be reached

$$\chi_{\boldsymbol{n_i}} = (\boldsymbol{n_i} - \boldsymbol{n_{i-1}})^T \boldsymbol{S^{-1}_{n_{i-1}}} (\boldsymbol{n_i} - \boldsymbol{n_{i-1}}) < 10^{-6}; \tag{4.30}$$

- ensuring that the solution is converging

$$\begin{aligned} \chi_{\boldsymbol{c_i}} = (\boldsymbol{c} - \boldsymbol{K}\boldsymbol{n_i})^T \boldsymbol{S^{-1}_c} (\boldsymbol{c} - \boldsymbol{K}\boldsymbol{n_i}) + \lambda_0 (\boldsymbol{L}\boldsymbol{n_i})^T \boldsymbol{S^{-1}_{n_{i-1}}} (\boldsymbol{L}\boldsymbol{n_i}), \\ \chi_{\boldsymbol{c_i}} - \chi_{\boldsymbol{c_{i-1}}} < 10^{-2}. \end{aligned} \tag{4.31}$$

An improved version of the method from Quémerais et al. (2006) is detailed in the Algorithm 1. It is called *HC* as it is referred in Quémerais et al. (2006) as developed by Alain Hauchecorne and Charles Cot.

Algorithm 1 Improved HC algorithm

```
procedure HC($\boldsymbol{c}, \boldsymbol{e_c}, \boldsymbol{z_c}, \lambda_0$)                ▷ Find $\boldsymbol{n}$ and $\boldsymbol{e_n}$
    $Compute\, \boldsymbol{K}, \boldsymbol{L}\, from\, \boldsymbol{z_c}$
    $\boldsymbol{S_c} = \boldsymbol{e_c^T} \boldsymbol{e_c}$
    $\boldsymbol{S_{n_0}} = \left(\boldsymbol{K}^T \boldsymbol{S_c}^{-1} \boldsymbol{K}\right)^{-1}$
    $\boldsymbol{e_{n_0}} = \sqrt{(\boldsymbol{S_{n_0}})_{jj}}$
    loop over $\boldsymbol{n_i}$ and start at $i = 1$
        $\boldsymbol{S_{n_i}} = \left(\boldsymbol{S^{-1}_{n_0}} + \lambda_0 \boldsymbol{L}^T \boldsymbol{S^{-1}_{n_{i-1}}} \boldsymbol{L}\right)^{-1}$
        $\boldsymbol{G_i} = \boldsymbol{S_{n_i}} \boldsymbol{K}^T \boldsymbol{S^{-1}_c}$
        $\boldsymbol{n_i} = \boldsymbol{G_i}\, \boldsymbol{c}$
        $\boldsymbol{e_{n_i}} = \sqrt{(\boldsymbol{S_{n_i}})_{jj}}$
    end loop
    return $\boldsymbol{n_i}$, $\boldsymbol{e_{n_i}}$
end procedure
```

The convergence is generally achieved after around twelve iterations.

4.2.5 Regularization parameter selection

The regularisation parameter controls the smoothing applied to the retrieved profile. Looking at 4.26 we could take a parameter for which $\lambda = trace(\boldsymbol{S_{n_0}})/trace(\boldsymbol{R})$ as proposed by Twomey (1977). Unfortunately, this regularisation parameter is often too high. Since then, many methods have been proposed and we will compare them.

- The most common method is the L-curve (Hansen, 1992a,b; Hansen and O'Leary, 1993) which consists to draw the logarithm of the square of the Euclidean norm $\|.\|_2$ of the residual

$$\rho(\lambda_0)^2 = \|\boldsymbol{K}\boldsymbol{n}(\lambda_0) - \boldsymbol{c}\|_2^2 \tag{4.32}$$

versus the logarithm of the square of the Euclidean norm of the regularisation term

$$\eta(\lambda_0)^2 = \|\boldsymbol{L}(\boldsymbol{n}(\lambda_0) - \boldsymbol{n_a})\|_2^2 \tag{4.33}$$

the best λ_0 then corresponds to the point of maximum curvature.

- Another method is based on Morozov's discrepancy principle (Morozov, 1966; Doicu et al., 2010a) which seeks λ_0 that satisfies

$$\rho(\lambda_0) \simeq \|\boldsymbol{e_c}\|_2 \,. \tag{4.34}$$

  There is only one λ_0 that can satisfy this equation as ρ is a monotonically increasing function of λ_0. The idea behind this method is that the residual should be of the same order as the level of the uncertainties.

- The formula provided by the generalized cross-validation method (Golub et al., 1979) consists in finding λ_0 that minimizes

$$\frac{\|(\boldsymbol{I_m} - \boldsymbol{A_c}(\lambda_0))\boldsymbol{c}\|_2^2}{[trace(\boldsymbol{I_m} - \boldsymbol{A_c}(\lambda_0))]^2} \tag{4.35}$$

  provided that there is one. In formula 4.35, m is the length of the c vector and $\boldsymbol{A_c}$ is the influence matrix, i.e. the equivalent of the averaging kernels matrix in the slant column space. The numerator is the square of the residual and this formula is the square of the ratio of the residual over the degree of freedom for noise (Rodgers, 2000).

- The maximum likelihood estimation method (Doicu et al., 2010a) fits particularly well with the optimal estimation method and consists in finding the λ_0 that minimizes

$$\frac{\boldsymbol{c}^T(\boldsymbol{I_m} - \boldsymbol{A_c}(\lambda_0))\boldsymbol{c}}{\sqrt[m]{det(\boldsymbol{I_m} - \boldsymbol{A_c}(\lambda_0))}} \tag{4.36}$$

- The quasi-optimality criterion (Doicu et al., 2010a) which consists in finding λ_0 that minimizes

$$\|(\boldsymbol{A}(\lambda_0) - \boldsymbol{I_n})\,\boldsymbol{G}(\lambda_0)\boldsymbol{c}\|^2 \,. \tag{4.37}$$

- The expected error estimation finds the value of λ_0 that minimizes the total expected error. It was used by Steck (2002) and briefly described in Rodgers (2000, chap. 10). The total expected error is the sum of the smoothing error, the retrieval noise error, the forward model error (mainly due to spectroscopic uncertainties), and the instrument model error. Evaluating the total expected error is complicated because evaluating the smoothing error requires knowing the true state, and in practice, we only guess the forward and instrument model error. In this work, I used the approximation of the smoothing error as given in Xu et al. (2016) and neglected the forward and instrument error:

$$\begin{aligned} \|\boldsymbol{e_{tot}}(\lambda_0)\|^2 &= \|\boldsymbol{e_s}(\lambda_0)\|^2 + \|\boldsymbol{e_m}(\lambda_0)\|^2 \\ &= \|(\boldsymbol{A}(\lambda_0) - \boldsymbol{I_n})(\boldsymbol{n}(\lambda_0) - \boldsymbol{n_a})\|^2 + \sigma^2 trace(\boldsymbol{G}(\lambda_0)\boldsymbol{G}(\lambda_0)^T). \end{aligned} \tag{4.38}$$

  where σ is the variance over $\boldsymbol{e_c}$. This function has theoretically a minimum as the smoothing error is an increasing function of λ_0 and the retrieval noise error is a decreasing function of λ_0. In practice, this method shows good performance. Unfortunately, no method is perfect and in very rare cases, the two terms might not be of the same order of magnitude and no clear minimum can be seen.

- The unbiased predictive risk estimation (Doicu et al., 2010a) consists in finding the minimum of

$$\rho(\lambda_0)^2 + 2\sigma^2 trace(\boldsymbol{A_c}(\lambda_0)) - m\sigma^2 \tag{4.39}$$

  which seems very similar to the expected error estimation but its results are definitively not. This method is also known to give undersmoothing (Doicu et al., 2010a).

4.2.6 Vertical resolution

An averaging kernel matrix can be computed like in 4.10 or 4.12. When a regularisation is applied using $\boldsymbol{L_1}$ or $\boldsymbol{L_2}$, the averaging kernel matrix deviates from the identity matrix translating in a decrease in resolution.

There are several ways to compute the vertical resolution of a profile using the averaging kernel matrix $\boldsymbol{A}$ and computing

- the full width at half maximum of each row of $\boldsymbol{A}$ divided by $2\sqrt{2\ln 2}$ if we consider that the averaging kernels are Gaussians,
- the grid width divided by the diagonal elements (König et al., 2019)
- different formulation of the Backus-Gilbert spread (Purser and Huang, 1993).

All these formulations give roughly the same values but the Backus-Gilbert spread has the advantage to be weakly sensitive to the grid used. The original formulation is:

$$s(z) = 12\frac{\int (z - z_i)^2 a_i^2(z)dz}{\left[\int a_i^2(z)dz\right]^2} \tag{4.40}$$

where the normalizing factor 12 has been chosen for rectangular averaging kernels (Conrath, 1972).

Another formula better takes into account the possible negative lobes of the averaging kernels

$$s(z) = 4\frac{\int |(z - z_i)a_i(z)|dz}{\int |a_i(z)|dz} \tag{4.41}$$

Purser and Huang (1993) also proposed a very similar formulation to the 'radius of gyration':

$$s(z) = \left[12\frac{\int (z - z_i)^2 a_i^2(z)dz}{\int a_i^2(z)dz}\right]^{\frac{1}{2}} \tag{4.42}$$

It is also important to keep in mind that those values correspond to resolutions which are smaller than the full width at half maximum.

4.3 Summary

This chapter reviewed the formality in inverse problems as we will need it in the following of this work. We started with the theory that will be necessary for the slant column retrieval from transmittances. The formulation for a non-linear least squares combined with the Optimal Estimation Method for the regularisation was then presented. The second part provided the formulation for linear least squares combined with an iterated Tikhonov method for the regularisation. A similarity to the Optimal Estimation Method is highlighted. This second part contained more details about the regularisation and in particular several ways for a fine-tuning of the regularisation as needed for the local densities retrieval from the slant columns. The instrument and its measurements is presented in the next two chapters now that the necessary background has been reviewed.

Chapter 5

The NOMAD instrument

The science objectives of the NOMAD instrument (Vandaele et al., 2015a) onboard the Trace Gas Orbiter (Vago et al., 2015) are in line with those of the ExoMars mission. NOMAD is dedicated to the detection and characterising of the distribution of trace gases in the atmosphere of Mars. Up to now, the main investigations are on the distribution of water (Aoki et al., 2022a, 2019; Vandaele et al., 2019), the D/H ratio (Villanueva et al., 2021, 2022), carbon monoxide (Yoshida et al., 2022), hydrogen chloride (Aoki et al., 2021), dust (Liuzzi et al., 2019), CO_2 ice clouds (Liuzzi et al., 2021), and ozone (Piccialli et al., 2022). The spectral signature of methane, one of the main targets of TGO was not detected (Korablev et al., 2019; Montmessin et al., 2021; Knutsen et al., 2021). While not being a trace gas as it represents 95% of Mars atmosphere, carbon dioxide is an important species to track the bulk variations of the atmosphere (López Valverde et al., 2022; Aoki et al., 2022b; Trompet et al., 2023b,a). NOMAD is also able to improve spectroscopic theories by characterising previously unobserved emission lines, such as the oxygen green and red lines at, respectively, 577 and 630 nm (Gérard et al., 2020, 2021).

NOMAD is a set of three spectrometers (see figure 5.1):

- SO: an infrared (IR) spectrometer dedicated to solar occultation;
- LNO: an IR spectrometer dedicated to limb and nadir;
- UVIS: an ultraviolet (UV) and visible spectrometer dedicated to limb, nadir, and occultation.

The LNO and UVIS channels contain two apertures, one for solar occultation and the other one for nadir or limb measurements. The SO channel has only one aperture dedicated to occultation measurements. The occultation LoS are represented with yellow lines and the nadir LoS are represented with orange arrows in Figure 5.1. The angle between these two LoS is 67.07°which is approximately the same angular difference between nadir and the limb of Mars, to minimize the length of manoeuvres required to pass from nadir to occultation measurements.

The NOMAD design is described in Neefs et al. (2015) for the IR channels and in Patel et al. (2017) for the UVIS channel. NOMAD optical and radiometric models have been first described in Thomas et al. (2016) for the IR channels and in Vandaele et al. (2015b) for the UVIS channel.

This manuscript focused on the NOMAD-SO channel data and which will be described in more detail in the two following sections. The first section 5.1 describes the SO channel and 5.2 describes its instrumental function.

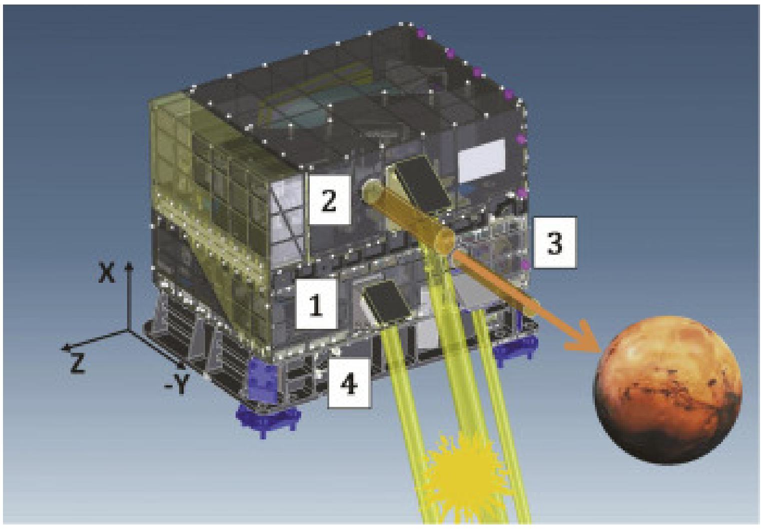

Figure 5.1: The NOMAD instrument (Vandaele et al., 2015a) with (1) the SO channel, (2) the LNO channel; (3) the UVIS channel; (4) the electronics SINBAD.

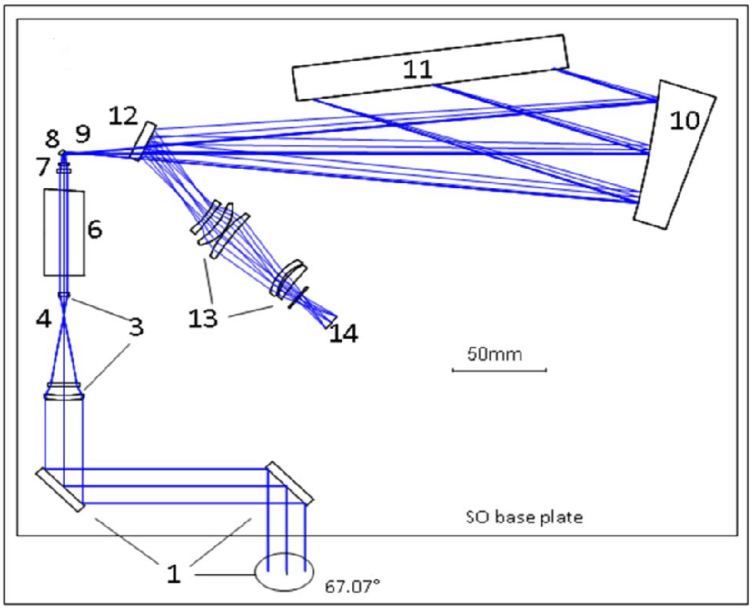
11
10
12
8
9
7
6
4
3
13
14
50mm
SO base plate
1
67.07°

Figure 5.2: NOMAD-SO base plate (Neefs et al., 2015): 1) Entrance consisting of three flat mirrors, 3) AOTF entrance optics, 4) diaphragm, 6) the AOTF, 7) AOTF exit optics, 8) folding mirror, 9) spectrometer entrance slit, 10) off-axis parabolic mirror, 11) the echelle grating, 12) folding mirror, 13) detector optics, 14) the detector.

5.1 NOMAD-SO description

Figure 5.2 represents the base plate of NOMAD-SO. The main optical elements are

- the slit (4) that affects the instrument line shape and the spectral resolution,
- the echelle grating (11) for the dispersion of radiation of wavelengths within each diffraction order (see section 5.1.1),
- the AOTF (6) for the diffraction order selection (see section 5.1.2),
- and the detector (14 - see section 5.1.3).

All measurements are controlled by the NOMAD control unit SINBAD (Neefs et al., 2015; Jerónimo Zafra et al., 2016; Pastor-Morales et al., 2016).

5.1.1 Echelle grating

The spectral range of SO extends from around 2200 to around 4800 $\mathrm{cm^{-1}}$ (2.2 to 4.5 μm). SO is composed of an echelle grating (made of triangular grooves with a very high blaze angle) for the dispersion of the light following the grating equation for near-Littrow configuration:

$$\lambda_c m = 2N \sin \Theta_B \cos i \cos \gamma = 443.3\,\mu m \tag{5.1}$$

where λ_c is the central wavelength in diffraction order m, N is the grating spacing, Θ_B is the blaze angle, i is the off-Littrow angle and γ is the off-blaze angle. For the SO channel, N, Θ_B, i and γ are respectively 248.06 μm, 63.43°, 2.6°and -0.02°from the on-ground calibration (Neefs et al., 2015). The corresponding equation for the central wavenumber ν_c in diffraction order m is

$$\frac{\nu_c}{m} = \frac{1}{2N \sin \Theta_B \cos i \cos \gamma} = 22.56\,cm^{-1} \tag{5.2}$$

With these equations, we can compute that the central wavenumber should be 3722,4 $\mathrm{cm^{-1}}$ (2.6867 μm) for the diffraction order 165 while the actual value (see section 5.2.1) is 3722.9 $\mathrm{cm^{-1}}$. Also, the central wavenumber should be 2616.9 $\mathrm{cm^{-1}}$ (3.8216 μm) for diffraction order 116 while the calibrated value is 2617.3 $\mathrm{cm^{-1}}$. The pixel to wavenumber calibration for diffraction orders (section 5.2.1) is made with a second-degree polynomial due to some small imperfection of the grating which is unavoidable for such small design (Palmer, Jr., 2005). Also, the grating spacing slightly varies with temperature and passes from 248.06 μm at 24.5 °C to 247.92 μm (Neefs et al., 2015) at 0 °C so a refined wavenumber calibration is necessary for each occultation (see section 5.2.1).

An important parameter for grating is the free spectral range (FSR) which is defined as the largest wavelength range in a diffraction order for which there is no superposition of a wavelength from an adjacent order, i.e. $m(\lambda + FSR) = (m+1)\lambda$ (Palmer, Jr., 2005) or

$$FSR_\lambda = \frac{\lambda}{m} = \frac{443.3\,\mu m}{m^2}. \tag{5.3}$$

This equation is inversely proportional to the square of the diffraction order but recomputing the free spectral range in wavenumber leads to a formula independent of the diffraction order

$$FSR_\nu = \frac{\nu}{m} = 22.56\,cm^{-1}. \tag{5.4}$$

and, in wavenumber, the difference between central wavenumbers of adjacent orders is thus a constant. As we will see in section 5.2.4, in practice, the FSR for NOMAD-SO is not a constant and changes as the grating expands or contracts due to variations of the instrument temperature.

5.1.2 Acousto-optic tunable filter

The SO channel is based on an Acousto-Optical Tunable Filter (AOTF) for the diffraction order selection. The transfer function of the AOTF is theoretically a sinc square function (Dekemper, 2014) and the full width at half maximum (FWHM) of the main lobe of the AOTF transfer function is close to the FSR of the grating. Detailed analysis of an AOTF can be found in Yano and Watanabe (1976); Dekemper (2014); Neefs et al. (2015). The NOMAD-SO AOTF is made of an anisotropic crystal of paratellurite in which Bragg diffraction filters the outgoing light. Paratellurite is a birefringent crystal that consists of tellurium dioxide (TeO2) and allows longitudinal and shear strains. The latter ones are needed for the AOTF capability (see Dekemper (2014) for a complete description of this effect). An electrical signal with a frequency A (see section 5.2.3) is transformed by a transducer into an acoustic wave that propagates into the AOTF crystal and interacts with photons following Bragg diffraction and the tuning function (Dekemper, 2014, eq. 4.38 and 4.10) summarized in equation 5.5.

$$A = \nu\, v\, f_A(n_o(\lambda), n_i(\lambda), ...) \tag{5.5}$$

where v is the phase velocity of the shear wave and f_A is a function depending on the ordinary n_o and extraordinary n_e refractive indices as well as different angles which are fixed in our case. The frequency A can well be approximated by a linear function of wavenumber but a more precise approximation of the tuning function requires a second-order term (given in equation 5.13) to take into account the dependence of the refractive indices on wavenumber. For $\mathrm{TeO_2}$ with a temperature of 293 K and a wavenumber between 2900 and 20000 cm^{-1}, Dekemper (2014, eq. 4.39, 4.40) computed the refractive indices as:

$$\begin{aligned} n_o^2(\nu) &= 1 + \frac{3.71789}{1 - 0.19619^2\nu^2} + \frac{0.07544}{1 - 4.61196^2\nu^2}, \\ n_e^2(\nu) &= 1 + \frac{4.33449}{1 - 0.202429^2\nu^2} + \frac{0.14739}{1 - 4.93667^2\nu^2}. \end{aligned} \tag{5.6}$$

Dekemper (2014, eq. 4.46, 4.44, 4.45) derived the theoretical AOTF transfer function f_{AOTF} which is a square of a sinc function with an argument proportional to ν but also non-linearly proportional to the ordinary and extraordinary refractive indices.

The main advantage of this filter is the absence of any mechanical parts. Some drawbacks with AOTFs are that adjacent diffraction orders are still transmitted by the side lobes of the sinc square function. Also, their tuning curves are slightly temperature dependent (Neefs et al., 2015). It is also known that for relatively high driving powers (as required for NOMAD-SO AOTF (Neefs et al., 2015)), the stiffness coefficients and the refractive indices depend on temperature and lead to an asymmetric transfer function (Dekemper, 2014, chap. 4).

5.1.3 Detector

The detector of NOMAD-SO is a two-dimensional array made of photovoltaic mercury cadmium telluride (HgCdTe) pixels with 320 pixels in the spectral direction and 256 pixels in the spatial direction. All 320 pixels of the spectral direction are illuminated. In the spatial direction, the slit length corresponds to 24 lines but the solar disk illuminates only 16 lines. During a measurement, NOMAD-SO performs 12 accumulations of 4 ms integration time and these 16 lines are binned into four spectra. In the following we will call one of those four spectra a 'bin'.

5.1.4 Measurements

The number of solar occultations that can be performed is limited to a maximum of 24 occultations per day as TGO performs 12 orbits per day. TGO is on a quasi-circular orbit at 400 km of altitude. The orbit of the TGO itself slightly rotates.

A solar occultation can either be:

- an ingress as the Sun is setting behind the planet;
- an egress where the Sun is rising out of the atmosphere.

In an ingress case (see for example Figure 23), the measurement starts when NOMAD points to the Sun above the atmosphere. As the LoS gets closer to the surface, the baseline of the spectra drops due to three different causes:

- the extinction by dust or ice clouds,
- the continua of absorption due to the superposition of line wings from strong absorption lines of CO_2 and H_2O,
- refraction but this effect can be neglected due to the low values of density in the atmosphere of Mars.

Solar occultation observations are limited to the terminators, i.e. the plane separating the daylight side to the night side of a planet. The terminator corresponds generally to local times close to 6h or 18h. The important geometrical parameters in solar occultation are the tangent altitude and the β-angle.

- The tangent altitude is the lowest altitude reached by the LoS of the instrument, i.e. it is the intersection between the LoS and the altitude axis perpendicular to that LoS. As the spacecraft moves further in its orbit, several scans with different LoS cross different tangent altitudes, corresponding to different latitudes and longitudes. In Figure 3.4, the tangent altitude is the intersection between the red vertical line (the LoS) and the vertical black line (z_{tg}).
- The β-angle is the angle between the Mars-Sun direction and the current orbital plane of the satellite. Typically, when the β-angle is lower than 63.5°, TGO performs a complete occultation from/to the surface. As the β-angle increases, the range of tangent altitudes and the ranges of latitudes/longitudes covered increase as well. For β-angles between 63.5°and 67°, grazing occultations are performed as the LoS never reaches the surface of the planet. The ingress occultation immediately follows up by the egress occultation. When the beta angle is higher than 67°, the lowest tangent altitude reached by the LoS is 100 km and the NOMAD team decided not to perform solar occultations in that case. There are thus periods where no occultations are possible due to the orbit of the TGO.

An important parameter characterizing the measurements is the Field of View (FOV) which is the projection of the slit of the instrument at the terminator. For NOMAD-SO, the FOV varies between $1.6\,km$ and $1.9\,km$. Another important parameter is the vertical sampling, i.e. the vertical distance between two measurements and which varies a lot with the β-angle: from a dozen of metres to less than a kilometre for, respectively high and low β-angles.

Different measurements are performed with NOMAD-SO:

- Science measurements which are regular ingress or egress occultation and where there are two typical science measurement sequences for NOMAD-SO:

  - scan five diffraction orders and one dark each second;
  - scan six diffraction orders with onboard background subtraction each second.

  The last option is the one giving higher SNR (see figure 5.3) as the background is directly subtracted for each line of the detector. For the first option, the spectra and the darks are first binned and then subtracted in the NOMAD data pipeline (which is the code that converts the incoming raw data into calibrated data for further analysis).

- Solar fullscans where more than a dozen to more than a hundred sequential diffraction orders are scanned while pointing to the Sun.
- Atmospheric fullscans where more than a dozen to more than a hundred sequential diffraction orders are scanned during an occultation. Those measurements give a lower vertical sampling per diffraction order scanned than the regular science measurements.
- Miniscans where the frequency applied to the AOTF is slightly swept across and serves to derive the AOTF function.
- Solar line scans are performed to adjust the pointing.

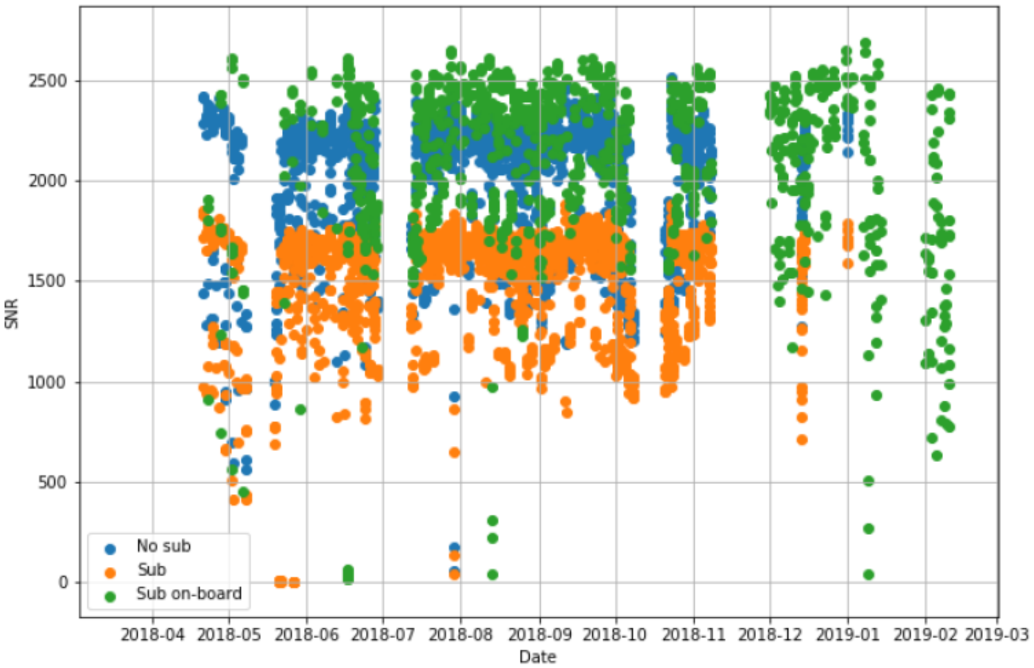

Figure 5.3: Mean SNR in the Sun region for on-board background subtraction (green), background subtraction (orange), and no background subtraction (blue).

5.1.5 Data processing

The NOMAD data calibration pipeline is separated into the following levels:

- 0.0a: Binary files are received from the ESA EDDS (EGOS Data Dissemination System);
- 0.1a: Conversion to Hierarchical Data Format, Version 5, known as HDF5 files. Gathering and sorting of data;
- 0.1d: Data split into one diffraction order per file;
- 0.1e: Bad pixels removal;
- 0.2a: Geometry computation using SPICE kernels and APIs;

The next levels are made for Science measurements (ingress, egress, atmospheric fullscans) only.

- 0.3a: Spectral calibration using coefficients of spectral resolution, pixel-to-wavenumber conversion and coefficients, AOTF-to-wavenumber coefficients (and the reverse), AOTF bandwidth, and blaze function parameters from look-up tables;
- 0.3i: the dark frame is added to the file if it was not subtracted on-board;
- 0.3j: The dark frames are subtracted. Then, observations with the same diffraction order are merged, if the combination of orders was switched during an occultation and if both combinations contained the same diffraction order. For instance, if the orders measured were [121, 134, 165, 168, 190, dark] and [121, 136, 149, 168, 190, dark] then merge [121, 168, and 190]. Merged ingress-egress occultations are split.
- 0.3k: If the ingress and egress occultations were merged (for high beta-angle) then they are split. The merged occultations with short duration, that pass only slightly or not at all behind Mars are called grazings (the filename contains a *'G'* letter as science case (5th parameter of the file name, see next paragraph).
- 1.0a: Transmittance calibration as described in section 6.2. Save all supplementary information on the transmittance calibration. The uncertainties are also computed and added to the file.

The filename contains four to seven parameters: 1) date; 2) time; 3) level; 4) channel; 5) science case; 6) observation type; 7) diffraction order. (example: 20180820_094517_1p0a_SO_1_E_134). All information on the content of NOMAD files can be found in the EAICD[1]. My task for the transmittance calibration started at level 0.3i.

The metaparameters of the observations can be found on the NOMAD-obs database that I maintain and which is hosted at BIRA-IASB and accessible at https://mars.aeronomie.be/en/exomars/obs-overview/index.php. Three different web pages are available, one for each channel of NOMAD. This database is updated every night. There is another database for the retrieved profiles to easily access them. The retrieved profiles are also accessible through the VESPA portal [2].

5.2 NOMAD-SO model

The instrument function described here is described in (Villanueva et al., 2022) and based on the preliminary work in Liuzzi et al. (2019) which relies on the previous work from Mahieux et al. (2008, 2010) made for the SOIR instrument.

---

[1] https://nomad.aeronomie.be/ProjectDir/documents/EXM-NO-ICD-AER-00001-iss3rev0-EAICD_NOMAD_221221.pdf

[2] https://vespa.obspm.fr/planetary/data/

5.2.1 Wavenumber calibration

A first spectral calibration was performed on-ground and a temperature shift of the pixel to wavenumber calibration was already noticed. An in flight spectral calibration was performed later using known solar lines (Liuzzi et al., 2019). The relation between the detector pixel number p (integer from 0 to 319) and the wavenumber ν for each order m is modelled with a polynomial function

$$\frac{\nu}{m} = \sum_i F_i \, p^i. \tag{5.7}$$

The wavenumber calibration changes with the instrument temperature T probably due to the thermal expansion of the grating.

The pixel to wavenumber calibration given in (Liuzzi et al., 2019) uses a second-order polynomial (see table 5.1 for the coefficients) and can still be off by $\sim 0.8\,cm^{-1}$ and this offset changes for each occultation.

The Doppler shift alone cannot explain this shift. The maximum TGO speed with respect to the Sun is around $3.3\,km/s$ and the Doppler shift would then be around $0.036\,cm^{-1}$. An order of magnitude lower than the shift encountered.

To be able to fit the molecular lines correctly we must refine this wavenumber calibration and set each line on its theoretical position. A correction is applied independently to each bin of each dataset. We first need to carefully select some CO_2 lines as provided by HITRAN (Gordon et al., 2017). They must be intense enough, not too saturated and they should not overlap any significant line from other molecules or adjacent orders. If there is no strong CO_2 lines, we then use the most intense solar lines (Hase et al., 2010). For higher diffraction orders (189, 190, 191), CO lines are used.

We need to compute this correction on the NOMAD-SO level 0.3k. The spectra are refined by zero-padding (with a subroutine from ASIMUT (Vandaele et al., 2006)) and sixty points are added within each pixel to accurately find a minimum of the absorption lines. The zero padding technique is an interesting tool when we only seek the position of a line and it takes into account the asymmetric ILS.

The spectra are then normalized by dividing them with a baseline computed with the asymmetric least square method as proposed by Eilers (2003). This method can fit to a curve by de-weighting values that are below the main curve. Two parameters must be specified: a parameter λ controlling the smoothness of the fitted curve and a parameter p controlling the asymmetry of the constraint applied on the data point used for the fit. After several attempts, the best parameters for NOMAD-SO spectra were chosen as $\lambda = 10^9$ and $p = 2.10^{-4}$. An example of the fit of the baseline with this method is shown in Figure 5.4.

The theoretical spectrum must be convolved with the ILS. For each line of each spectrum, we then compute the shift $\Delta\nu$ as the difference and divide it by the diffraction order number. The coefficients can then directly be added to the coefficients in equation 5.7. We do not expect a strong variation of the shift along the spectra and a strong constraint is applied against outliers: all shifts that are further than $0.2\,cm^{-1}$ from the median shift are considered outliers.

These shifts are then fitted with a linear regression along the spectra with

$$\Delta\nu(I) = A_0 + A_1\, z \tag{5.8}$$

where z is the tangent altitude of the spectrum. Figure 5.5 shows an example of this linear regression which takes into account a slight and continuous variation of the shift with spectra due to a variation of the temperature over a long time. For order 140, only a shift is computed as the CO_2 lines are too weak and there is only one strong solar line.

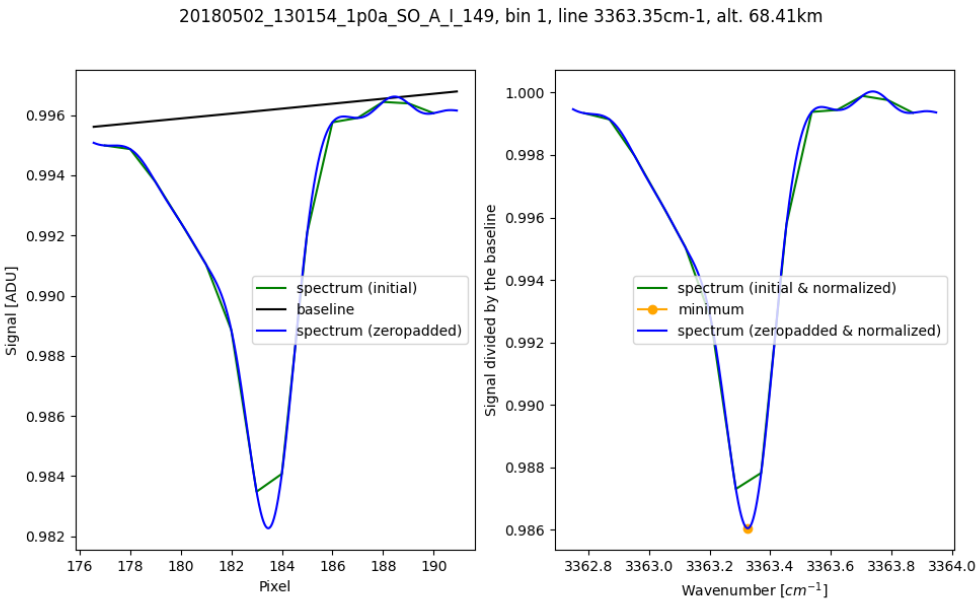

Figure 5.4: Example of refined and normalized line for 20180502_130154_0p3k_SO_A_I_149, bin 1. The initial spectrum is in blue, the refined one with zero padding is in green and the minimum of the line is the orange dot. The black curve in the left panel is the baseline fitted with the asymmetric least-square method. The curves in the right panel have been normalized by dividing the curves in the left panel by the black curve.

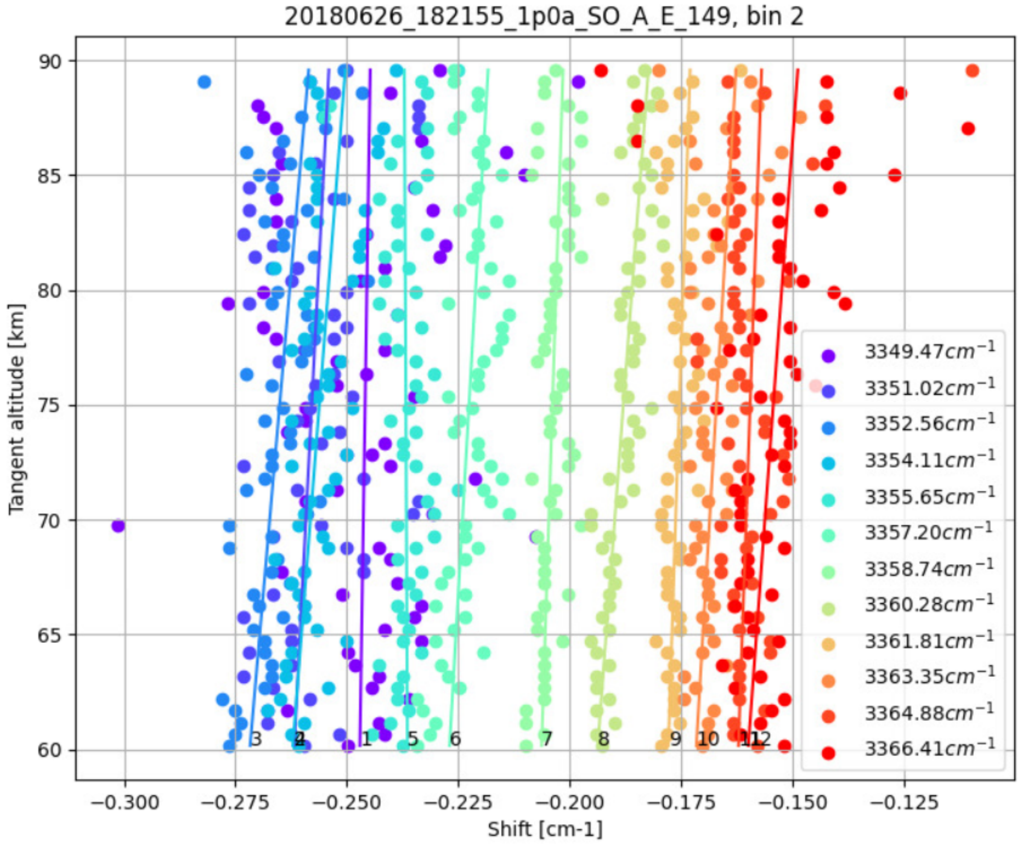

Figure 5.5: Example of fitted wavenumber shift for the CO_2 lines in the dataset 20180626_182155_1p0a_SO_A_E_149, bin 2. The shift computed here is with respect to the previous calibration.

Once the two coefficients of the linear regression are computed for all lines, we then apply another constraint against outliers: all lines with any coefficient different from the median with more than 20% are removed. We then compute another linear regression over the remaining coefficients with respect to pixels as shown in Figure 5.6. An example of the resulting shift can be seen in figure 5.7.

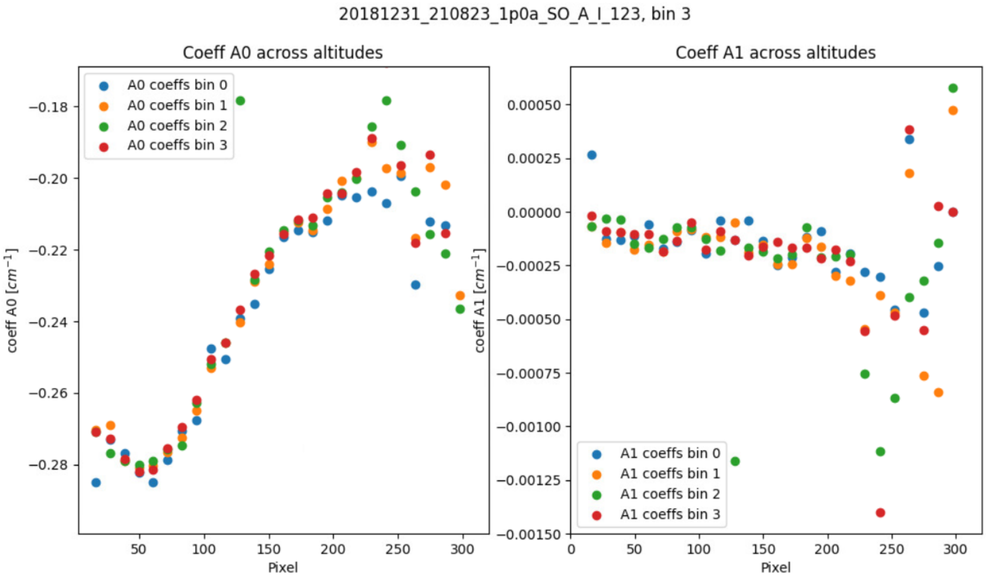

Figure 5.6: Coefficients of the shift with respect to pixels and computed from a linear regression on the coefficients computed along the spectra for 20181231_210823_1p0a_SO_A_I_123.

The spectral calibration is fitted for each occultation individually. I then computed the spectral calibration with as many datasets as possible and with all diffraction orders containing strong and isolated molecular lines: 116, 122, 123, 140, 147, 148, 149, 158, 164, 165, 189, 190, and 191. From the shifts computed with 5.8, I compute an average shift along altitudes (within bounds to avoid too faint or saturated lines) and for each occultation. An example of pixel to wavenumber relation is seen in figure 5.9 for diffraction order 116. We can also see how the lines move along the pixels following the temperature of the instrument.

From figure 5.8 it is obvious that the relation between temperature and pixel number is linear. If, on average, some diffraction orders were scanned at a different temperature, the coefficients would then be biased. To avoid that, I fitted for each molecular line and for all occultations the variation of the pixels with temperature with a simple linear regression (see appendix A)

$$\Delta p_i(t) = A_{i,0} + A_{i,1}\, T. \tag{5.9}$$

for each molecular line i. The $A_{i,0}$ coefficients are the pixels at 0°C. The wavenumber at 0°C was computed in the same way. The uncertainties $\sigma_{A_{i,0}}$ and $\sigma_{A_{i,1}}$ are computed as in appendix A.

The A_1 coefficients found for each line of a diffraction order are very similar. They are averaged with a weighted mean

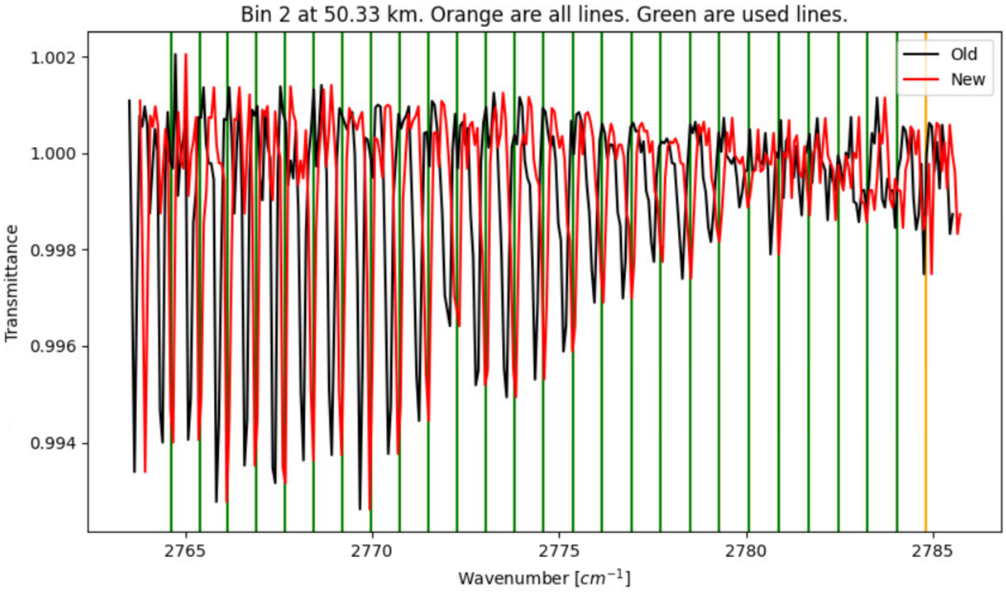

Figure 5.7: Example of corrected spectrum for 20180502_130154_0p3k_SO_A_I_149, bin 1 at 60 km. The initial spectrum is in black, and the new one is in red. The main theoretical CO_2 lines positions are marked with vertical lines. The green lines are those used for the correction.

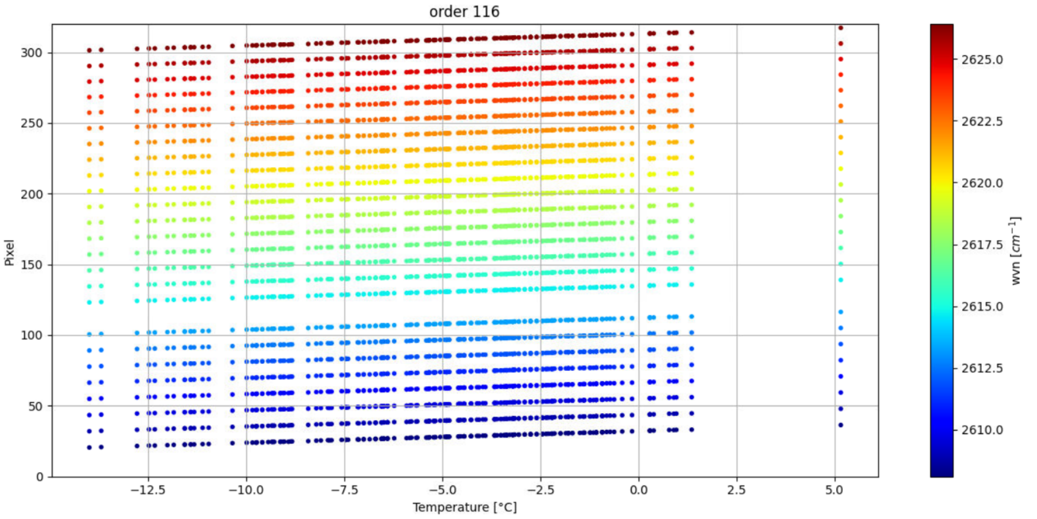

Figure 5.8: Variation of the position of the line on the detector as a function of temperature for diffraction order 116 and all datasets until August 2021.

$$
\begin{aligned}
A_1 &= \frac{\sum A_{i,1}\sigma_{A_{i,1}}}{\sum \sigma_{A_{i,1}}}, \\
\sigma_{A_1} &= \frac{\sum \sigma^2_{A_{i,1}}}{\sum \sigma_{A_{i,1}}}.
\end{aligned}
\tag{5.10}
$$

A mean coefficient amongst all orders is then computed using the same formula as in 5.10 and I found the value $-0.8281 \pm 0.0022\, pixel/°C$.

We have found the variation of pixel to wavenumber with the instrument temperature but we still need to derive the coefficients for the relation pixel to wavenumber considering a temperature of 0°C. From figure 5.9, the relation seems almost linear but looking at the left panel in 5.6 which shows the corrections to apply to the wavenumber as given by Liuzzi et al. (2019), it seems that a higher degree polynomial would improve the fit. For all diffraction orders, the pixel to wavenumber was fitted with different polynomials of different degrees. Looking at the residuals of these fits, there is no improvement after a fourth-degree polynomial. The coefficients were then again averaged across orders their values are given in table 5.1.

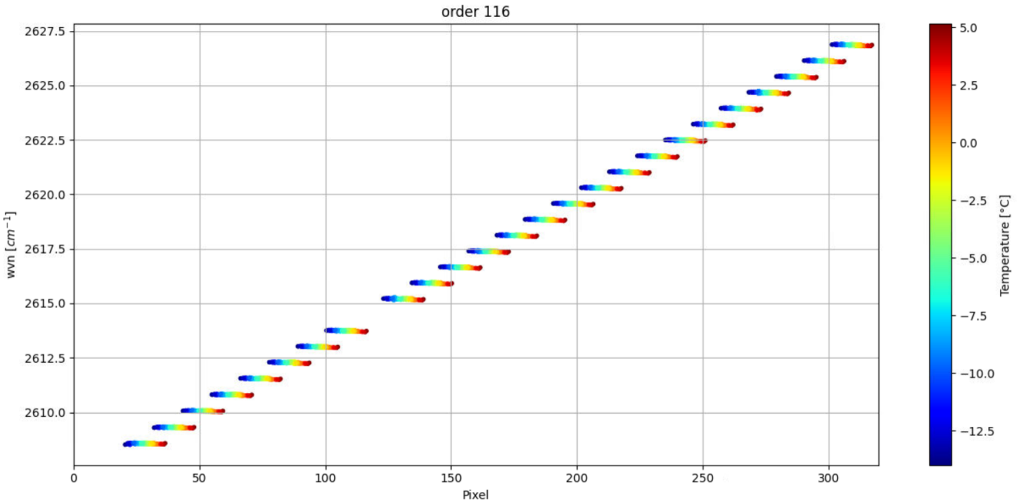

Figure 5.9: Pixel to wavenumber for diffraction order 116 and all datasets until August 2021.

Poly. fit	F_0	F_1	F_2	F_3	F_4
Liuzzi et al. (2019)	22.473	5.560e-4	1.751e-8	0	0
$1^{st} order$	22.469	5.596e-4	0	0	0
$2^{nd} order$	22.470	5.480e-4	3.287e-8	0	0
$3^{rd} order$	22.470	5.600e-4	-4.863e-8	1.597e-10	0
$4^{th} order$	22.469	5.802e-4	-2.531e-7	1.009e-9	-1.230e-12

Table 5.1: Table of coefficients F_i corresponding to different polynomial orders n with i an integer in $[0, n]$. Those coefficients are in units of cm^{-1}.

Figure 5.10 shows the relative difference between the ν/m obtained by the different polynomial fit with respect to the previous values. The differences are very weak but we still note more differences for the first pixels where we have fewer constraints as less strong and isolated lines could be found there. The improvement with the higher order polynomial appears for pixels below 50 where the noise on the spectra are larger, thus keeping a second order polynomial is a good compromise between enough complexity to represent the pixel to wavenumber shift and avoiding unnecessary complexity.

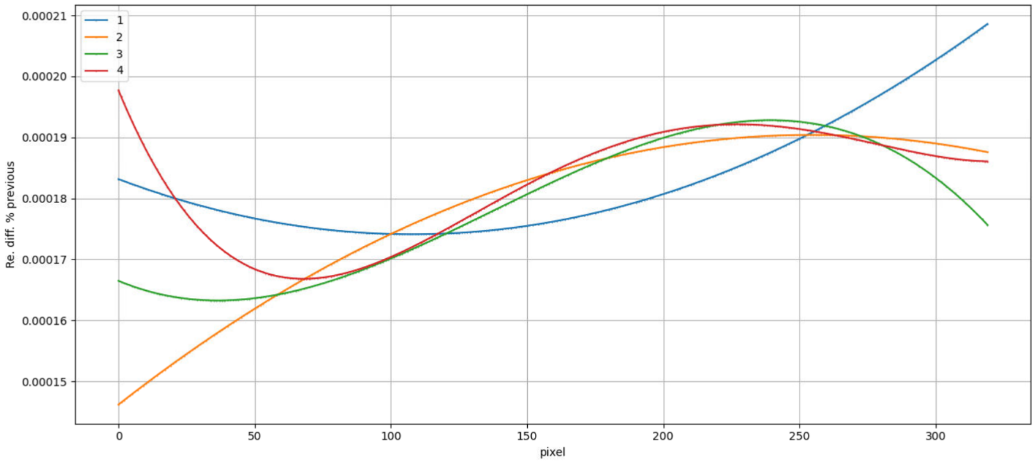

Figure 5.10: Variation of the position of the line on the detector as a function of temperature for diffraction order 116 and all datasets until August 2021.

Spectral sampling

The minimum and maximum spectral sampling within one order is provided in Figure 5.11. The spectral resolution induced by the spectral sampling is twice the spectral sampling. It is smaller than the spectral resolution induced by the blurring due to the width of the slit (see section 5.2.2) and is not taken into account.

5.2.2 Instrument Line Shape

In theory, it would be better to have an infinitely small slit to avoid any blurring of the spectrum. In practice, we need to let enough light enter the instrument to have enough signal arriving to the detector. The width of the slit is a compromise between the incoming light and the blurring of the spectrum. The instrument line shape (ILS) models this blurring. In the case of NOMAD-SO, it is an asymmetric function modelled with a double Gaussian function with parameters varying with diffraction orders and pixels

$$f_{Slit}(m,\nu) = I_{0,2}\exp\left(-\frac{(I_{0,0}-\nu)^2}{2\,I_{0,1}}\right) + I_{1,2}\exp\left(-\frac{(I_{1,0}-\nu)^2}{2\,I_{1,1}}\right). \tag{5.11}$$

where ν is the relative wavenumber to the center where this function is evaluated.

The parameters were reported in Villanueva et al. (2022) and are

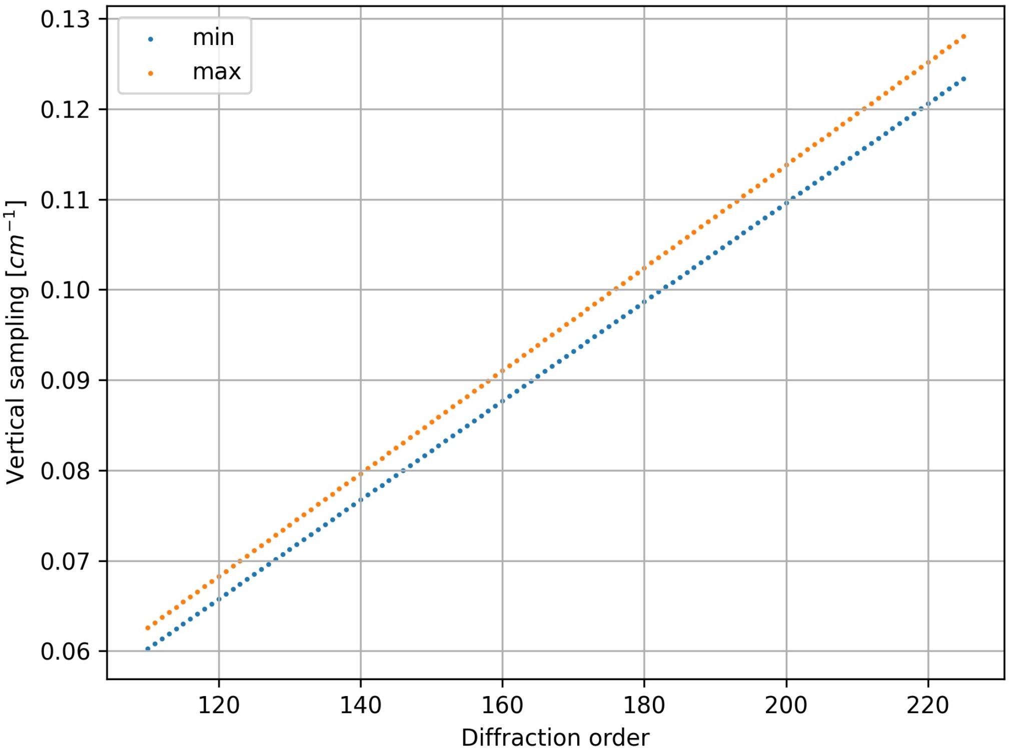

Figure 5.11: Minimum and maximum spectral sampling within diffraction orders.

$$
\begin{aligned}
I_{0,0} &= 0 \\
I_{0,1} &= \frac{wvn_{mid}}{2\sqrt{(2\ln(2))}\,RP} \\
I_{0,2} &= 1 \\
I_{1,0} &= -\left(1.31671485.10^{-3} + 1.71638815.10^{-3}\,pixel - 3.06665339.10^{-6}\,pixel^2\right)\frac{wvn_{mid}}{wvn_{ref}} \\
I_{1,1} &= \frac{wvn_{mid}}{2\sqrt{(2\ln(2))}\,RP} \\
I_{1,2} &= 0.27
\end{aligned}
\tag{5.12}
$$

where wvn_{mid} is the mean pixel of the diffraction order, wvn_{ref} is 3700 cm^{-1}, and RP is the expected resolving power of 17 000. Only the displacement of the second Gaussian ($I_{1,0}$) varies along a spectrum and only this displacement and the resolutions ($I_{0,1}$ and $I_{1,1}$) vary with diffraction orders.

The total vertical resolution is computed as the sum of the resolution and the displacement. We can also compute the spectral resolution from the detector array by considering two times the spectral sampling (Nyquist-Shannon sampling theorem). Both are provided in Figure 5.12. The latter are lower limits to the spectral resolution. The model provides lower spectral resolution for the 60 first pixels but those pixels where not taken into account for its derivation.

5.2.3 AOTF transfer function

The AOTF theoretical transfer function is a sinc square function (Dekemper, 2014) which is the Fourier transform of a rectangular electrode as seen in the direction of optical propagation. Miniscans measurements are dedicated to deriving the AOTF transfer function (f_{AOTF}). During a miniscan, the radio frequency applied to the transducer is increased by small steps of a few kHz, and the center of the f_{AOTF} slightly moves along wavenumbers.

The centre of f_{AOTF}, that we note here ν_0 changes with frequency A applied to the transducer, and the peak of the main lobe of the transfer function is given by (Liuzzi et al., 2019)

$$\nu_0 = G_0 + G_1 A + G_2 A^2 \tag{5.13}$$

where G_0, G_1, G_2 are respectively $305.0604\,cm^{-1}$, $0.1497089\,cm^{-1}$, $1.3408210^{-7}\,cm^{-1}$.

The f_{AOTF} can be derived by fitting the depth of solar lines which varies with the intensity of the f_{AOTF} at the wavenumber corresponding to that line. We need strong solar lines and they must also be isolated from the presence of other lines that would overlap from nearby orders, i.e. at a multiple of the FSR.

The solar lines depth is fitted with respect to the AOTF central wavenumber and the AOTF transfer function is fitted as

$$f_{AOTF}(m,\nu) = sinc^2\left(\frac{\nu - \nu_0}{w}\right) \tag{5.14}$$

where the $sinc(x) = sin(\pi x)/\pi x$, and ν_0 and w are functions of temperature and order.

It has been reported that the centre of the AOTF function slightly varies with the instrument temperature as

$$\nu_0(t) = \nu_0\left(1 - 6.5278.10^{-5}\,T\right). \tag{5.15}$$

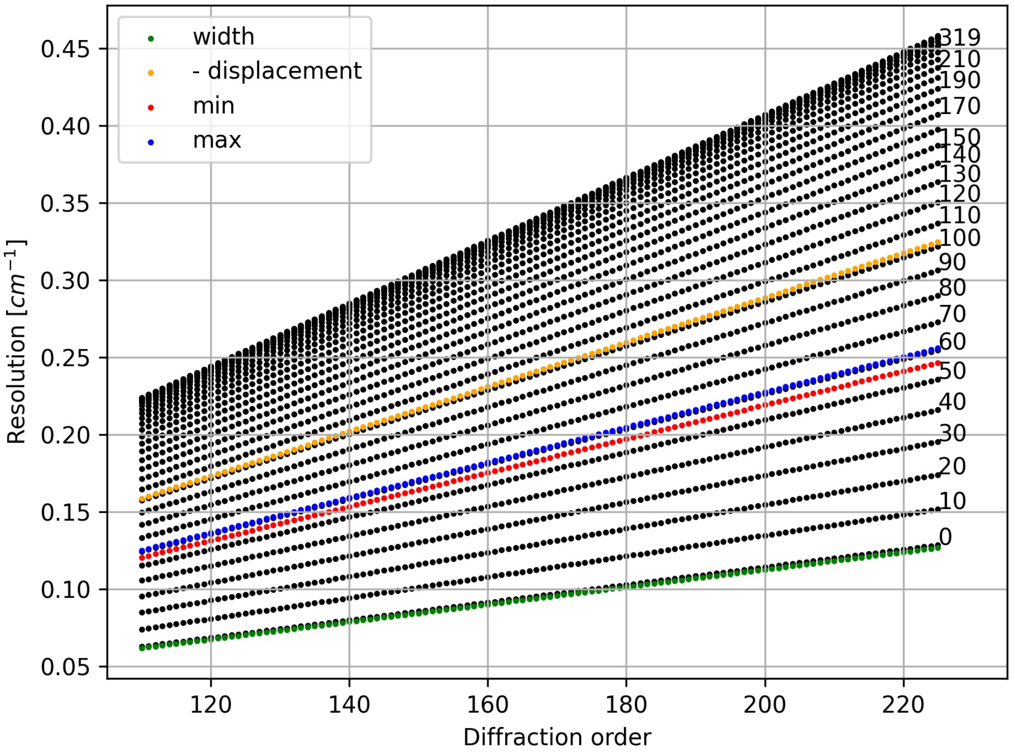

Figure 5.12: Spectral resolution computed from the model 5.11 and 5.12 in black for all diffraction orders and pixels referred on the right of each curve. The minimum and maximum spectral resolution computed from the detector array is provided, respectively, in red and blue. The green, orange and purple curves are the width and the opposite of the displacement for the first and last pixels, respectively.

The best model for the AOTF function has higher side lobes than expected for a $sinc^2$ function. It is as well asymmetrical and has a Gaussian offset with a width of 50 $\text{cm}_{\text{-}1}$. All those parameters and the width varies with diffraction order (Villanueva et al., 2022).

The width w, the sidelobe ratio sl, the asymmetry a and the amplitude of the Gaussian offset o of the AOTF function in equation 5.14 are

$$\begin{aligned}
w(\nu_0) &= 20.1730360 + 7.47648684.10^{-4}\,\nu_0 - 1.66406991.10^{-7}\,\nu_0^2 \\
sl(\nu_0) &= 4.08845247 - 3.30238496.10^{-3}\,\nu_0 + 8.10749274.10^{-7}\,\nu_0^2 \\
a(\nu_0) &= -1.24925395 + 1.29003715.10^{-3}\,\nu_0 - 1.54536176.10^{-7}\,\nu_0^2 \\
o(\nu_0) &= 1.60097815 - 9.63798656.10^{-4}\,\nu_0 + 1.49266526.10^{-7}\,\nu_0^2
\end{aligned} \tag{5.16}$$

The side lobe ratio is applied only further than one width w from the AOTF central wavenumber nu_0 and the asymmetry is applied only at wavenumbers that are one width w lower than nu_0.

5.2.4 Blaze function

The blaze function for a perfect grating, for a diffraction order m with p_0 the centre in pixel and w_p the width, is well approximated by:

$$f_{Blaze}(p, p_0, w_p) = sinc^2(\pi(p - p_0)/w_p) \tag{5.17}$$

where p_0 for order m is given by:

$$p_0(m) = B_0 + B_1 m \tag{5.18}$$

and where B_0 and B_1 are respectively 150.80 and 0.22.

The theoretical formula for the Blaze function is (Engman and Lindblom, 1982; Pyo, 2003; Mahieux, 2011)

$$BF(\nu) = sinc^2\left(\frac{\sigma\nu\cos(\gamma)\cos(\alpha)}{\cos(\alpha_B)}\left(\sin(\alpha_B) - \sin(\beta - \theta_B)\right)\right). \tag{5.19}$$

The incidence angle to the grating normal is simply $\alpha = \theta_B + \alpha_B$. The diffracted angles are then computed from the grating equation $\beta = \arcsin\left(\frac{m}{\sigma\nu\cos(\gamma)} - \sin(\alpha)\right)$.

As we use a high blaze angle, we need to take into account a shadowing due to the presence of the grooves when the diffracted angle β is larger than the incidence angle α. The effective blaze function for $\alpha < \beta$ is

$$EBF = BF\left(\frac{\cos(\beta)}{\cos(\alpha)}\right)^2 \tag{5.20}$$

The effect of this shadowing is a quasi-linear reduction of the intensity of the blaze function from the pixel corresponding to the blaze angle (where $\alpha = \beta$) to the first pixel where the maximum reduction is of 7%. The blaze function is shown in Figure 5.13 for three ranges of diffraction orders. We see that there are some gaps between the wavenumber ranges of lower diffraction orders (110-115) while higher diffraction orders are covering partly their neighbour ones.

The blaze width is equal to the FSR computed at the wavenumber corresponding to the blaze angle. We know that wavenumber changes with temperature following 5.7. Writing it again with the correction due to the temperature shift

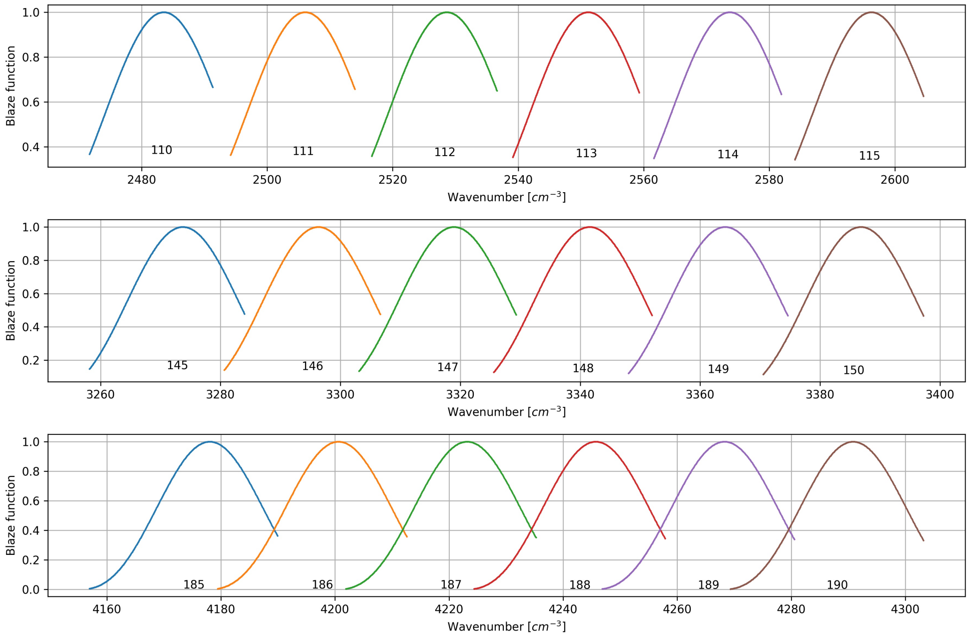

Figure 5.13: Blaze function for different diffraction orders in the range 110-115, 145-150, and 185-190.

$$
\begin{aligned}
\frac{\nu}{m} &= F_0 + F_1(p + G_1T) + F_2(p + G_1T)^2. \\
&= \left(\frac{\nu}{m}\right)_{T=0} + (F_1G_1 + 2F_2G_1p)T + (F_2G_1^2)T^2 \\
&\approx \left(\frac{\nu}{m}\right)_{T=0} - 4.65\,10^{-4}T - 2.25\,10^{-8}T^2.
\end{aligned}
\tag{5.21}
$$

But the temperature variation might be just a shift of the wavenumber on the detector and the blaze function remains the same.

5.2.5 NOMAD-SO transfer function

To model a spectrum recorded by SO, we need to consider all wavenumbers that the AOTF let pass. Typically, this corresponds to five to nine orders if we consider, respectively, two to four adjacent orders. The radiance defined in section 3.2 is affected by the slit modelled as in section 5.2.2. That radiance is then multiplied by the AOTF function selected for the central order m. Then the radiance for each order is multiplied by its Blaze function (formula 5.17). Finally, the orders are summed up on the pixels of the detector.

The transformation of the atmospheric intensities due to NOMAD-SO optical elements is then

$$
\begin{aligned}
&I_{tot}(m, \nu, z_{tg}) = \\
&\sum_{i=m-\Delta m}^{m+\Delta m} f_{AOTF}(A(m), \nu_i) f_{Blaze}(i, \nu_i) \left[f_{Slit}(i, \nu_i) * I(z_{tg}, \nu_i) \right]
\end{aligned}
\tag{5.22}
$$

where Δm is the number of adjacent orders, ν_i is the wavenumber from order i recorded on the same pixel than wavenumber ν from order m ($\nu_i = \nu + FSR_\nu * (i - m)$).

5.3 Carbon dioxide lines in NOMAD-SO spectral range

Figure 5.14 shows the simulated transmittance of CO_2 for the five most abundant CO_2 isotopologues for the whole NOMAD-SO spectral range at an altitude of 5 km, and convolved with the SO ILS (simplified as one Gaussian with a width of $0.15\,cm^{-1}$). The SO diffraction orders where CO_2 lines can be retrieved are 116, 118, 121, 132, 140, 147, 148, 149, 154, 156, 158, 159, 164, 165, 171, and 200. Not all of these orders are dedicated to CO_2 density retrievals. For instance, order 121 is dedicated to water density retrievals but contains some weak CO_2 lines and is one of the most often scanned orders. The next most often scanned orders are 148, 149, 164, and 165 which are usually scanned several times per day.

Table 5.2 summarizes the diffraction orders and the approximated altitudes a which the isotopologues can be retrieved. The upper limit depends on the line strength and the lower limit depends on the saturation of the line (described in section 5.3.1) that occurs two to four scale heights below the upper limit. The lower limit also depends on the presence of dust that might already remove any signal above 40 km, especially during the dusty seasons. The altitude provided in this table varies with the CO_2 cycle as well as with latitudes.

CO_2 iso.	Diffraction order	Altitude [km]
626	140	40-80
	147	60-100
	148	50-90
	149	60-100
	158	100-140
	159	130-170
	164	140-180
	165	140-190
636	154	70-110
	156	100-140
628	116	50-90
	121	20-60
	132	100-140
	171	30-70
627	118	20-80
638	154	60-100

Table 5.2: Diffraction orders and altitude for the retrievals of CO_2 density profiles. The first column provides the isotopologue number as defined in the AFGL notation (Mcclatchey et al., 1973): 626 for $^{12}C^{16}O^2$, 636 for $^{13}C^{16}O^2$, 628 for $^{16}O^{12}C^{18}O$, ...

Table 5.3 provides some useful parameters for the five main CO_2 isotopologues. The Earth and Mars abundances are close and we still use the Earth values for the retrieval. Each isotopologue is retrieved separately. To simplify the notation, in the following, we will use the AFGL notations that were first defined in (Mcclatchey et al., 1973).

Chemical formula	AFGL code	Earth abundance	Mars abundance	Molar mass g/mole
$^{12}C^{16}O_2$	626	0.984204	0.98338	43.98983
$^{13}C^{16}O_2$	636	0.011057	0.01162	44.993185
$^{16}O^{12}C^{18}O$	628	0.003947	0.00419	45.994076
$^{16}O^{12}C^{17}O$	627	$7.339890.10^{-4}$	$7.76.10^{-4}$	44.994045
$^{16}O^{13}C^{18}O$	638	$4.434460.10^{-5}$	$2.43.10^{-5}$	46.997431

Table 5.3: Parameters of the five most abundant CO_2 isotopologues. The Earth abundance are those provided in HITRAN and used in ASIMUT. The Mars abundances are those provide in (Shved, 2016).

In NOMAD-SO spectral range, there are many strong CO_2 bands involving different CO_2 isotopologues. The main transitions bands used in this work are the fundamental ones with the ground state (00001) as a lower level. Table 5.4 provides the main CO_2 bands scanned with NOMAD-SO.

AFGL code	Fundamental mode	Approx. band centre $[cm^{-1}]$	Diff. order (branch)	iso.
20002-00001	$2\nu_1$	2614	116 (P+R)	628
20002-00001	$2\nu_1$	2641	118 (R)	627
01111-00001	$\nu_2 + \nu_3$	2981	132 (P+Q+R)	628
21103-00001	$2\nu_1 + \nu_2$	3181	140 (P)	626
21102-00001	$2\nu_1 + \nu_2$	3340	148 (P+Q+R)	626
10012-00001	$\nu_1 + \nu_3$	3490	155 (P+R)	638
10012-00001	$\nu_1 + \nu_3$	3527	156 (P)	636
10012-00001	$\nu_1 + \nu_3$	3613	160 (P+R)	626
10011-00001	$\nu_1 + \nu_3$	3714	165 (R)	626

Table 5.4: The main CO_2 bands regularly scanned by NOMAD-SO. The AFGL code for CO_2 (Rothman and Young, 1981; Esplin et al., 1988; Mcclatchey et al., 1973) rovibrational energy levels is $\nu_1\nu_2 l\nu_3 r$ (see section 3.1.1). The fundamental modes are those described in Figure 3.1. The diffraction orders correspond to spectral ranges specific to the NOMAD-SO channel and are explained in chapter 5. The last column gives the corresponding CO_2 isotopologue.

The $\nu_2 + \nu_3$ band around 2981 cm^{-1} from the isotopologue 628 was already studied in the atmosphere of Venus with the SOIR instrument on-board VenusExpress (Wilquet et al., 2008). Two of the three channels of NOMAD have strong heritage from the SOIR instrument (see section 5.1).

Order 140 contains the least intense lines of the main isotopologue 626 but most of them saturate (see section 5.3.1) already at an altitude of 40 km. The troposphere (0 to 50 km) is probed with orders 132 and 121. For the latter, the CO_2 628 lines are on the right side of the spectrum covered by more intense lines from order 122. Order 132 contains the Q branch of the ($\nu_2 + \nu_3$) band of the isotopologue 628 well centered in that order as well as a few lines from the P and R branches, and there are no noticeable CO_2 lines contribution from the adjacent orders. Diffraction orders 147 to 149 contain CO_2 lines from the $2\nu_1 + \nu_2$ fundamental band of the main isotopologue (626). This band contains the Q branch of the $2\nu_1 + \nu_2$ band centered in order 148 with an intensity adequate to probe the mesosphere. Diffraction orders 164-165 contain the strong $\nu 1 + \nu 3$ fundamental band of the main isotopologue (626) adequate to probe the upper thermosphere (140-200 km). Diffraction orders 158-159 contain CO_2 lines with intermediate intensities between the mesosphere and the upper thermosphere. Those last orders are more challenging to invert as they contain many bands with almost similar intensity from different isotopologues (see Figure 5.14) as well as from the adjacent orders.

The line intensity for carbon dioxide, water, and carbon monoxide are plotted in Figure 5.15. It is important to notice that water lines are present over the whole spectral range of NOMAD-SO but the water density is considerably varying with seasons and latitudes (Aoki et al., 2022a). This needs to be taken into account for the retrievals.

5.3.1 Saturation

The lower limit of the altitude in table 5.2 is due to the saturation of the lines. The saturation is easily seen when looking at the curve of growth of the molecular lines which is defined as the area covered by the line

$$W = \int_{-\infty}^{\infty} (1 - e^{-\tau(\nu)}) \mathrm{d}\nu. \tag{5.23}$$

The curve of growth of a molecular line has three main parts:

- The "linear" part where the whole line increases with the density: $W \propto n$ for $\tau < 1$.
- The "saturated" part where the line weakly increases with the density: $W \propto \sqrt{\ln(n)}$ for $10 < \tau < 10^3$.
- The "damped" part where the wings of the line increase with the density: $W \propto \sqrt{n}$ for $10^4 < \tau$.

Example of curves of growth [3] for orders 149 and 165 are presented in figures 5.16 and 5.17, respectively. The equivalent width is the area of one line and is usually plotted against the natural logarithm of the density. However, here, it is plotted against altitude which is close to a linear function of the logarithm of the density. To retrieve the density in the saturated part is difficult as the lines grow very weakly when the density increases and any error in the line parameter, the forward model, and the instrument function leads to an important error in the retrieved density.

For order 149, the "linear" part extends from 70 to 100 km, the "saturated" part extends from 40 to 70 km and the "damped" part extends to altitudes lower than 30 km. For order 165, the "linear" part extends from 140 to 180 km, the "saturated" part extends from 70 to 140 km, and the "damped" part extends to altitudes lower than 70 km.

Retrievals in the "damped" part of orders 164 and 165 are possible as an increase in the density is translated into a substantial increase of the wings of the lines. But retrievals in the "damped" part have the additional difficulty that weaker lines begin to be significant.

---

[3] In practice, the baseline of the transmittance spectra is not always perfectly set to one. To correct the baseline of the spectrum we apply a least square fit with a second-order polynomial for the baseline and the asymmetric ILS as described in section 5.2.2 for the line. The spectra are then divided with the baseline retrieved and then the area under the line is numerically integrated.

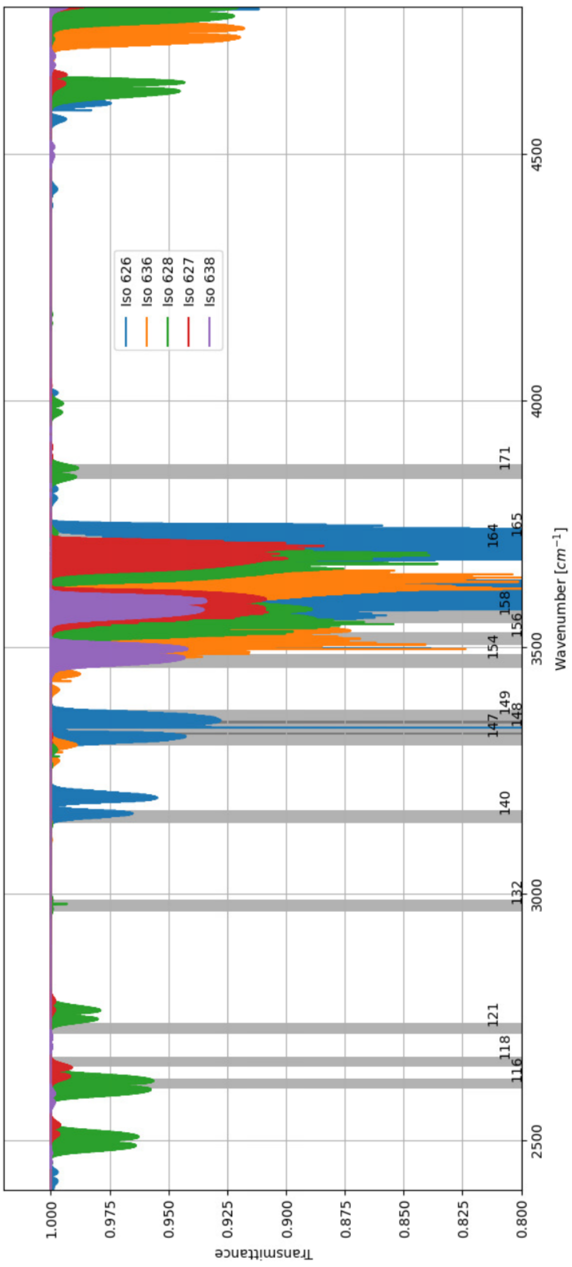

Figure 5.14: Simulated transmittance of CO_2 five main isotopologues at an altitude of 5 km with GEM-Mars version a585 (Erwin et al., 2018) and convolved with an ILS consisting of one Gaussian with a width of $0.15 cm^{-1}$. The spectral range of the main diffraction order where CO_2 density is retrieved are shown in grey.

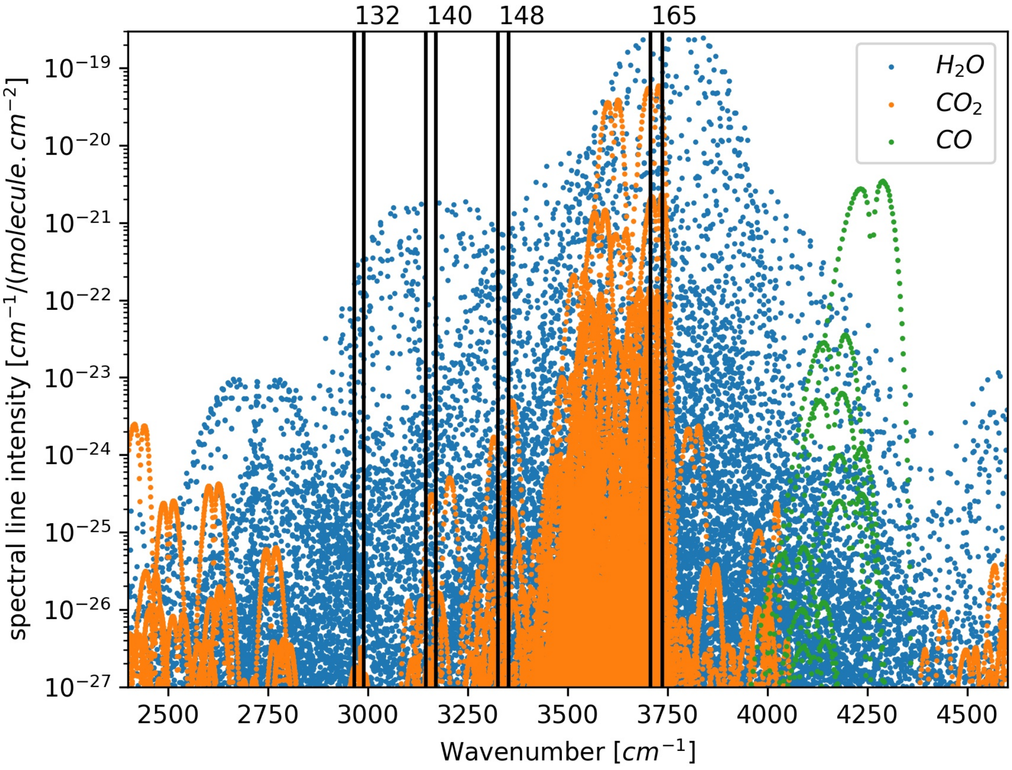

Figure 5.15: Line intensities for CO_2 (orange), H_2O (blue) and CO (green) in NOMAD-SO spectral range. Examples of extension of diffraction orders 132, 140, 148, and 165 are represented in black.

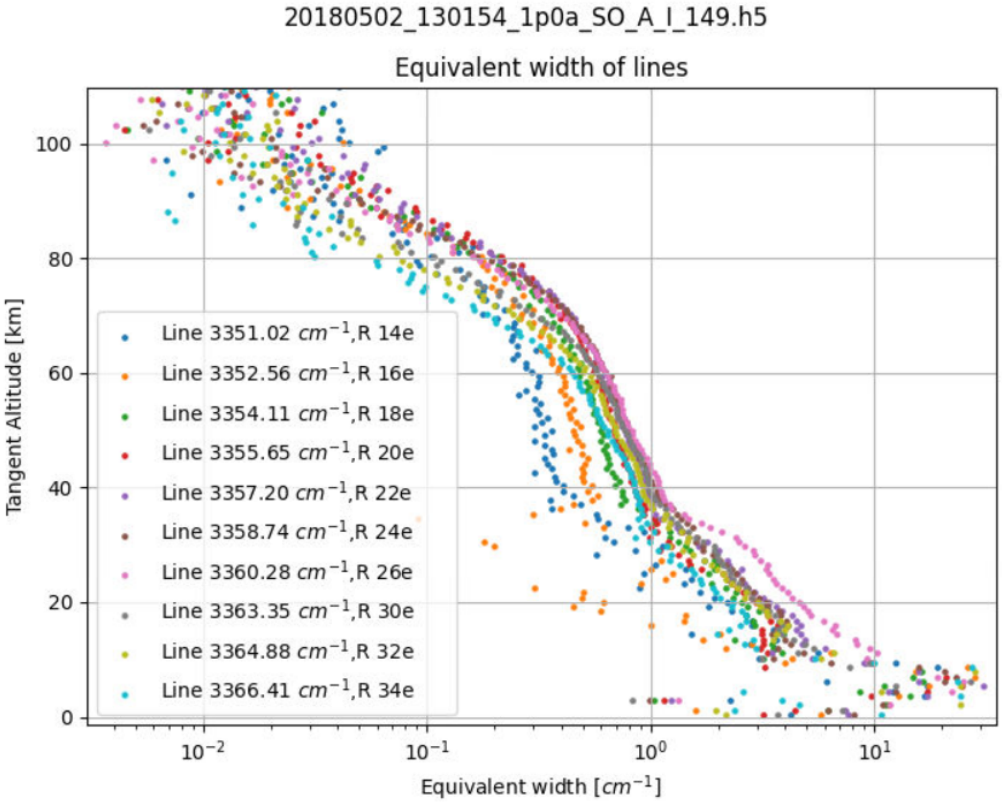

Figure 5.16: Example of curves of growth for order 149 and dataset 20180502_130154_1p0a_SO_A I.

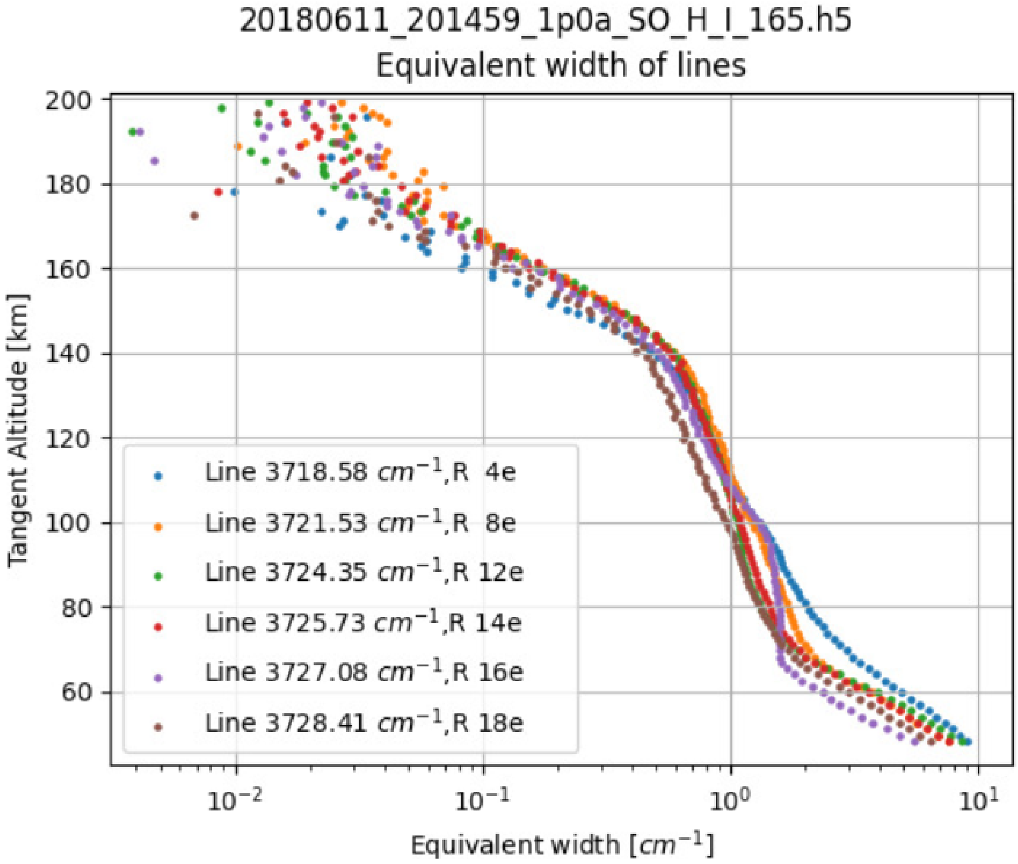

Figure 5.17: Example of curves of growth for order 165 and dataset 20180611_201459_1p0a_SO_H I.

For order 149, we can see also that below 10 km, the equivalent width is decreasing. This effect is due to another artificial effect: as the baseline reduces, the line (normalized to 1) should reach the 0 of transmittance but this is never the case, the line reduces as the baseline decreases.

The saturated part will be dealt with in further work. For the moment, we automatically cut the profiles when the second derivative of the curve of growth (applying also a Savitzky-Golay filter to smooth the noise) reaches zero on average for the most important lines in the diffraction order.

The effect of saturation can be seen in other measurements using occultations and even in the UV spectral range. Montmessin et al. (2017) noticed that the data below 60 km altitude in SPICAM-UV had an important bias as the density profiles were lower than expected. This was attributed to insufficiently accurate CO_2 cross-sections for the temperatures present in the atmosphere of Mars. This increase in the sensitivity of the CO_2 lines to temperature could be attributed to the saturation of the CO_2 lines.

5.4 summary

This analysis focuses on the measurements from the SO channel of the NOMAD instrument. This channel is a spectrometer which diffracts the light with an echelle grating and selects one main diffraction order thanks to an acousto-optic tunable filter (AOTF). SO's transfer function is affected by the instrument line shape (ILS), the blaze function produced by the echelle grating, and the AOTF transfer function. All those functions affect the instrument function described in this chapter. Another important function is the detector's pixel-to-wavenumber conversion. The last section provided the main carbon dioxide lines within the spectral range of the SO channel and described the saturation of those lines. Now that the instrument and its transfer function are known, we will describe the transmittance calibration in the next chapter.

Chapter 6

NOMAD-SO calibration

NOMAD-SO spectra are affected by shot noise, electronics read-out noise, dark current noise, quantization noise, and thermal background (Thomas et al., 2016).

Quantification noise will accumulate while thermal background noise and dark current noise can be removed.

6.1 Background subtraction

When no impulses are applied to the AOTF crystal, no light should be passing through and the recorded signal should be zero. In practice, there are still the detector dark current, and the thermal background (photons from the instrument hitting the detector) and the signal is non-zero. This noise can be removed by simply recording that remaining signal and subtracting it from the spectra.

NOMAD-SO scans six diffraction orders per second (with twelve accumulations of 4 ms integration time) and has two main modes to record the dark current:

1. For each order, half of the accumulations are dedicated to the order and the other half are dedicated to the dark, with the AOTF switched off.

2. SO scans five orders and the dark is recorded as a sixth order.

In the first case, the darks are directly subtracted from the spectra for each line of the detector and are not saved for downlinking. In the second case, the integration time is entirely dedicated to the order and the darks are binned on-board before downlinking. They are then subtracted in the NOMAD calibration pipeline before the transmittance calibration (between levels 0.3a and 1.0a, see section 5.1.5). Before subtraction, the values of the dark are interpolated for the corresponding time stamps.

Figure 6.1 shows an example of a variation of the signal at a given detector pixel obtained while the AOTF is turned on (red - the light can pass through the AOTF) and the background noise obtained when the AOTF is turned off (blue - no light should pass through the AOTF) with respect to tangent altitude. The background noise follows the curve of the signal indicating also the possible presence of a remaining signal of around 1% of the total signal and which is removed from the spectra with the background subtraction. This remaining signal is thought to be due to straylight.

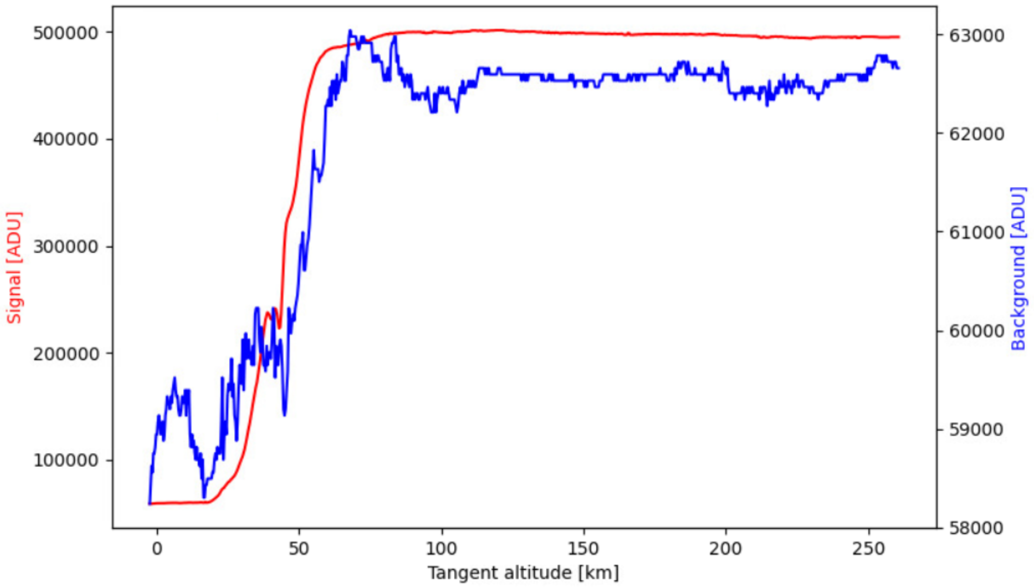

Figure 6.1: Comparison of the variations of the background (blue) and the signal for order 164 (red) at pixel 180 for dataset 20180521_195114_0p3k_SO_A_E_164.

6.2 Transmittance calibration

The transmittance calibration of NOMAD-SO and NOMAD-UVIS solar occultation spectra is based on Trompet et al. (2016). A transmittance calibrated spectrum $\mathcal{T}$ is the ratio of the remaining radiance I to the initial radiance I_0 as in equation 3.17. Transmittance spectra are then free from any instrument artefacts if both signals are recorded by the same instrument and under similar instrumental conditions. During a solar occultation measurement, I corresponds to a radiance spectrum obtained while scanning the atmosphere and I_0 is the reference source spectrum of the Sun. The latter is recorded while the instrument is pointing to the Sun but at a tangent altitude well above the atmosphere.

We define three main regions during a solar occultation (see 6.2):

- The “Sun” region (S) which contains solar spectra recorded while pointing at a tangent altitude well above the atmosphere.
- The “Transmission” (P) region contains spectra of the atmosphere of Mars. They are recorded between the surface and the top of the atmosphere.
- The “Umbra” (U) region contains the data recorded when Mars occults the Sun.

To separate between the S and P regions, a parameter, S_{min}, is set to different values depending on the diffraction order. While this limit can be set to 120 km for most of the orders, we must raise it for orders containing some strong CO_2 lines that can be observed above this altitude. The limits are given in table 6.1.

The black curves in figure 6.3 is an example of the variation of the recorded signal for six pixels. The reference source I_0 needs to be extrapolated while the Line Of Sight (LOS) is passing through the atmosphere as the intensity may change due to limb darkening, i.e. the LOS is

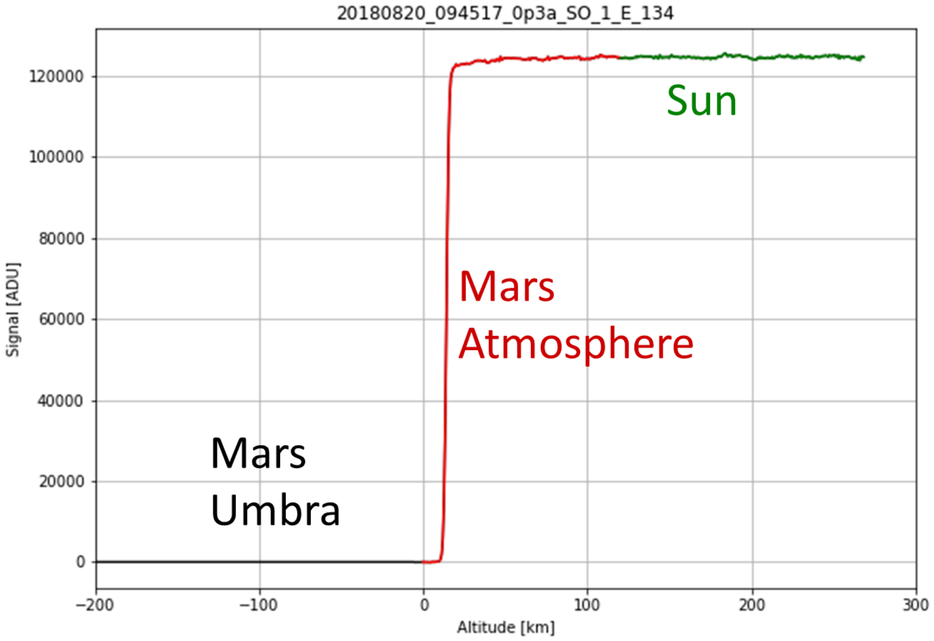

Figure 6.2: Example of the signal recorded on pixel 180, bin 1 for the dataset 20180820_094517_0p3a_SO_A_E_134. For diffraction order 134, the top of the atmosphere is 120 km.

Channel	SO					UVIS
Diffraction order	97-145	146-154	155-157	158-166	167-210	/
S_{min} [km]	120	160	180	200	120	120

Table 6.1: Table of S_{min}: the tangent altitudes separating the atmosphere region T and the Sun region U.

slightly moving on the apparent Solar disk resulting in a change of the signal intensity. The signal will continue to change in the atmosphere region and we assume that the signal varies linearly. We extrapolate its values in the P region using a linear regression over the signal in the S region. We avoid higher-order regressions as they are likely to give some extrapolated values that deviate too far from the curves. Also from figure 6.3, we see that the slope of the curves is different for each pixel in the S region (above 120 km) thus we compute a linear regression per pixel.

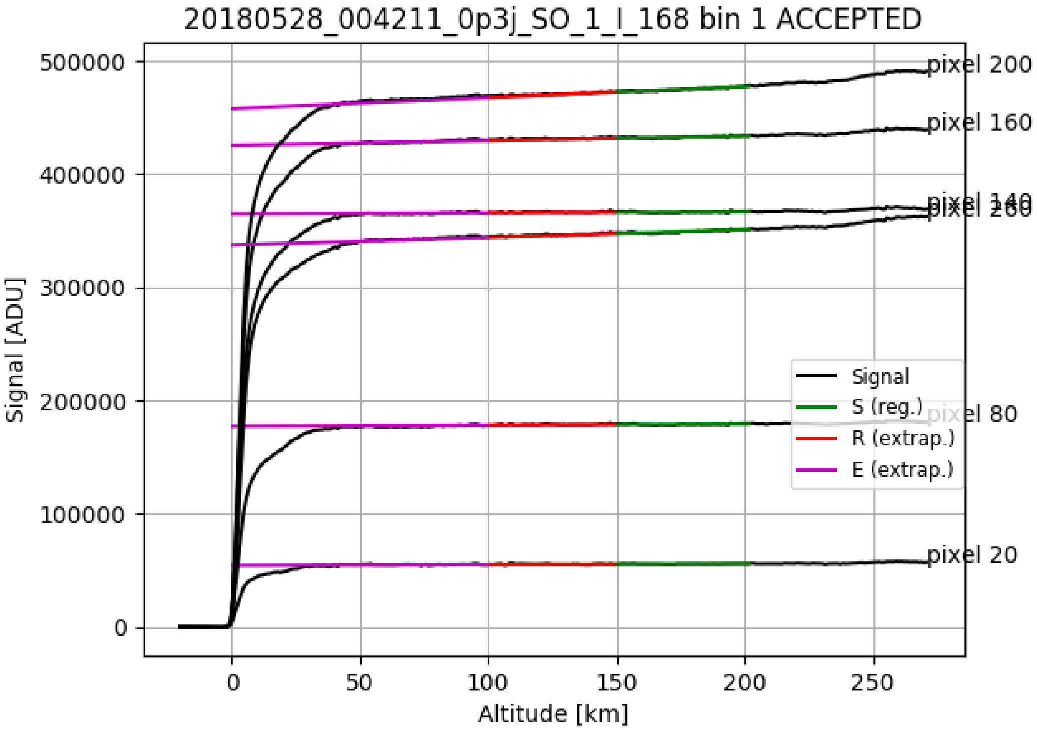

Figure 6.3: Example of variation of the signal over six pixels (numbers 20, 80, 140, 160, 200, 260) for bin 1 of dataset 20180528_004211_0p3j_SO_A_I_168. The linear regression is in green and the extrapolated values are in red and purple.

In the following, we write P_{ij} the value of the signal of the spectrum i and pixel j, and $\hat{P}_{ij}$ is the corresponding value computed from the linear regression on the P_{ij} values in the S region:

$$\hat{P}_{ij} = A_j \, X_i + B_j. \tag{6.1}$$

where A_j and B_j are the coefficients of the linear regression for pixel j and X_i is the time stamp of the spectrum. The transmittance is then computed as

$$\mathcal{T}_{ij} = \frac{P_{ij}}{\hat{P}_{ij}}. \tag{6.2}$$

6.2.1 Uncertainties on transmittance

If we have a closer look at the signal on each pixel for SO data (see figure 6.4), we notice a systematic variation of the signal for all pixels probably due to a voltage fluctuation of the detector. Before computing any uncertainty, we remove these systematics in SO data by subtracting the mean signal for each spectrum from the S, P, and U regions:

$$N_{ij} = P_{ij} - \frac{1}{n_p}\sum_{j=0}^{n_p-1} P_{ij} \tag{6.3}$$

where n_p is the number of pixels (320).

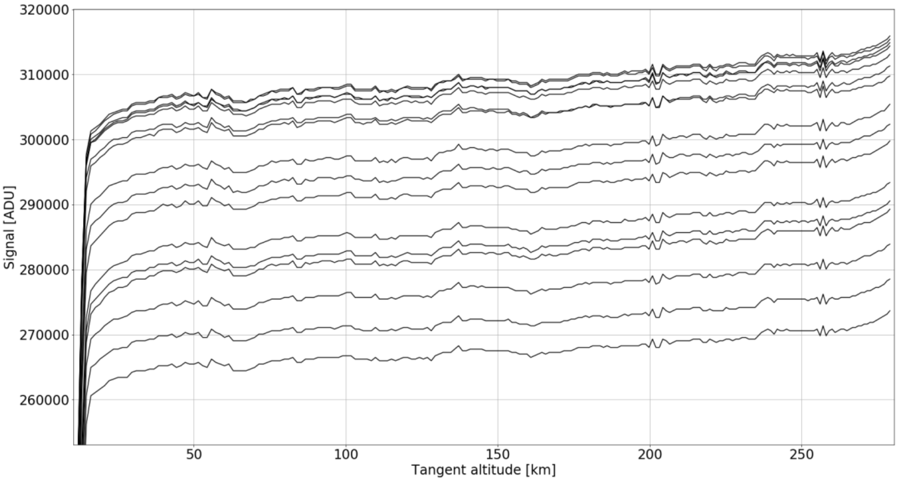

Figure 6.4: Signal for pixels 160 to 240 for dataset 20180607_140558_0p3a_SO_A_I_133.

The uncertainties δU_j is the noise over the Umbra spectra. Provided that we consider enough spectra to be statistically significant, the uncertainties are computed as the (Bessel corrected) standard deviation over the signal for each pixel

$$\delta U_j = \sqrt{\frac{1}{n_u - 1}\sum_{i=0}^{n_u-1}\left(N_{ij} - \frac{1}{n_u}\sum_{j=0}^{n_u-1} N_{ij}\right)^2} \tag{6.4}$$

for $i \in U$ and where n_u is the number of spectra in the u region.

The uncertainties on the fitted values S_{ij} in the S region with the linear regression are computed as (see Taylor (1997, sect. 8.3))

$$\delta F_j = \sqrt{\frac{1}{n_s - 2} \sum_{i=0}^{n_s - 1} \left(N_{ij} - \hat{N}_{ij} \right)^2} \tag{6.5}$$

for $i \in S$ where the $\hat{N}_{ij}$ are the values derived from a linear regression on N_{ij}. This formula is very similar to the usual standard deviation formula but takes into account the slope of the signal for each pixel.

When predicting a particular value, the uncertainties must also take into account the distance from the S region. It can be shown (Casella and Berger, 2002, sect. 11.3) that the uncertainties on the predicted value S_{ij} from a linear regression must be computed as

$$\delta S_{ij} = \delta F_j \sqrt{1 + \frac{1}{n_s} + \frac{(i - \hat{I})^2}{\left(\sum_{k=s_{min}}^{s_{max}} k - \hat{I} \right)^2}} \tag{6.6}$$

where s_{min} and s_{max} are the bounds of the S and $\hat{I}$ is the average of the indexes in S. This uncertainty must be taken into account when we are fitting broad features to retrieve dust or water ice clouds. For retrievals of molecular spectral signature, the fit of the baseline serves only to normalize the spectra and the uncertainties from equation 6.6 would not make sense.

The uncertainties on the atmospheric spectra are computed as

$$\delta P_{ij} = \delta U_j + |\mathcal{T}_{ij}| \left(\delta F_j - \delta U_j \right). \tag{6.7}$$

This last formula estimates the noise in the T region, considering that the transmittance values are close to one near the S region, and zero near the U region. This formula gives back $\delta P_{ij} \approx \delta F_j$ close to the S region and $\delta P_{ij} \approx \delta U_j$ close to the U region. There is a very similar formula in Vandaele et al. (2013) where the only difference is that they were computing the square root over the transmittances. But the transmittance value is between zero and one and thus the square root over the transmittance values was always higher than the transmittance values.

The transmittance $\mathcal{T}_{ij}$ is a function of P_{ij} and S_{ij} which are independent and

$$\begin{aligned} \delta \mathcal{T}_{ij} &= \sqrt{\left(\frac{\partial \mathcal{T}_{ij}}{\partial P_{ij}} \right)^2 \delta P_{ij}^2 + \left(\frac{\partial \mathcal{T}_{ij}}{\partial S_{ij}} \right)^2 \delta S_{ij}^2} \\ &= \mathcal{T}_{ij} \sqrt{\left(\frac{\delta P_{ij}}{P_{ij}} \right)^2 + \left(\frac{\delta S_{ij}}{S_{ij}} \right)^2}. \end{aligned} \tag{6.8}$$

Atmospheric fullscans

Atmospheric fullscans are measurements where NOMAD-SO scans a range of diffraction orders during an occultation. That range extends generally from order 110 to 225. There are only a few spectra per order in the U, T, and S regions and the uncertainties cannot be computed as a standard deviation over those few points. Instead, we consider that the signal is mainly noise as the Sun is hidden behind Mars. For the S region, the signal is mainly due to the intense radiation from the Sun. We then consider that the uncertainties are mainly composed of the shot noise which is proportional to the square root of the signal.

So for atmospheric fullscans, 6.5, 6.6 and 6.4 are replaced with

$$\begin{aligned}\delta S_j &= \sqrt{\left(\frac{1}{n_s}\sum_{i=0}^{n_s} S_{ij}\right)},\\ \delta U_j &= \frac{1}{n_s}\sum_{i=umin}^{umax} S_{ij}.\end{aligned} \tag{6.9}$$

The SNR is thus varying from one in U to the square root over the signal in S. The uncertainties computes with 6.5 is three to four times smaller than the square root over the signal.

6.2.2 Selection of the Sun region

In a perfect measurement, the signal is constant in the S region. In practice, the signal might vary due to, for instance, limb-darkening, detector voltage variation inducing a variation of the pixel sensitivity, instrument function change due to temperature variation, etc. Taking into account all the spectra recorded in the S region may not lead to the correct extrapolated solar spectra.

Looking again at figure 6.3, we see a slight increase of the signal above 250 km mainly for the pixels with the highest values. If this part was taken into account, the linear regression would have a too large slope, and the transmittances would be much higher than 1. We would prefer to restrict the S region to the green part in figure 6.3. We would also prefer to keep the signal as close as possible to the P region and be continuous.

An algorithm to find the best S region for SOIR/VEx is described in Trompet et al. (2016) and has been slightly modified for NOMAD. It is based on the fact that the highest spectra in the T region should not deviate too much from $1 \pm f\delta\mathcal{T}_{ij}$ where f is a positive integer and $\delta\mathcal{T}_{ij}$ are the uncertainties on the transmittance. For these spectra, we know that the solar light is still too weakly absorbed to reduce their baselines. We define two new subregions where this criterion is tested: the Reference (R) region extending 30 km above S_{min} where the tested transmittances must be close to 1. From the five criteria defined in Trompet et al. (2016) we now only use two:

$$\begin{aligned}&\frac{1}{n_r}\sum_{i=s_{min}}^{r_{max}} \left(|1-\mathcal{T}_{ij}| \, < \, f\,\delta\mathcal{T}_{ij}\right),\\ &\frac{1}{n_s-1}\sum_{i=s_{min}}^{s_{max}}\left(P_{ij}-\frac{1}{n_s}\sum_{i=s_{min}}^{s_{max}} P_{ij}\right)^2 \, < \, f\,\sqrt{\frac{1}{n_s}\sum_{i=s_{min}}^{s_{max}} P_{ij}}.\end{aligned} \tag{6.10}$$

where f is a factor set to 2, n_r is the number of spectra in the R region. The factor $f = 2$ was chosen by trial and error as $f = 1$ was rejecting too many pixels while $f = 3$ was accepting too many of them. These criteria are tested on pixels 70 to 300 for SO and on $[n_p/4; 3n_p/4]$ for UVIS to avoid the noisy part of the spectra. The first criterion serves to test the condition mentioned above while the second one serves to avoid the case where the slope of the curves S_{ij} is too large.

The algorithm iterates by removing the highest spectra of the S region. The minimum number of spectra must be twenty to keep statistically significant samples for the uncertainty computation. Otherwise, the dataset is rejected. More than 99.5% of the datasets passed the criteria. The other ones are impossible to calibrate because of a movement of the High Gain Antenna of TGO that perturbed the recorded signal by NOMAD-SO right in the R region.

Figure 6.5 shows an example of a dataset where this algorithm is important. As we see on that figure, the algorithm selected the pixels after the huge decrease of the signal which, in this case, was due to a movement of the High Gain Antenna.

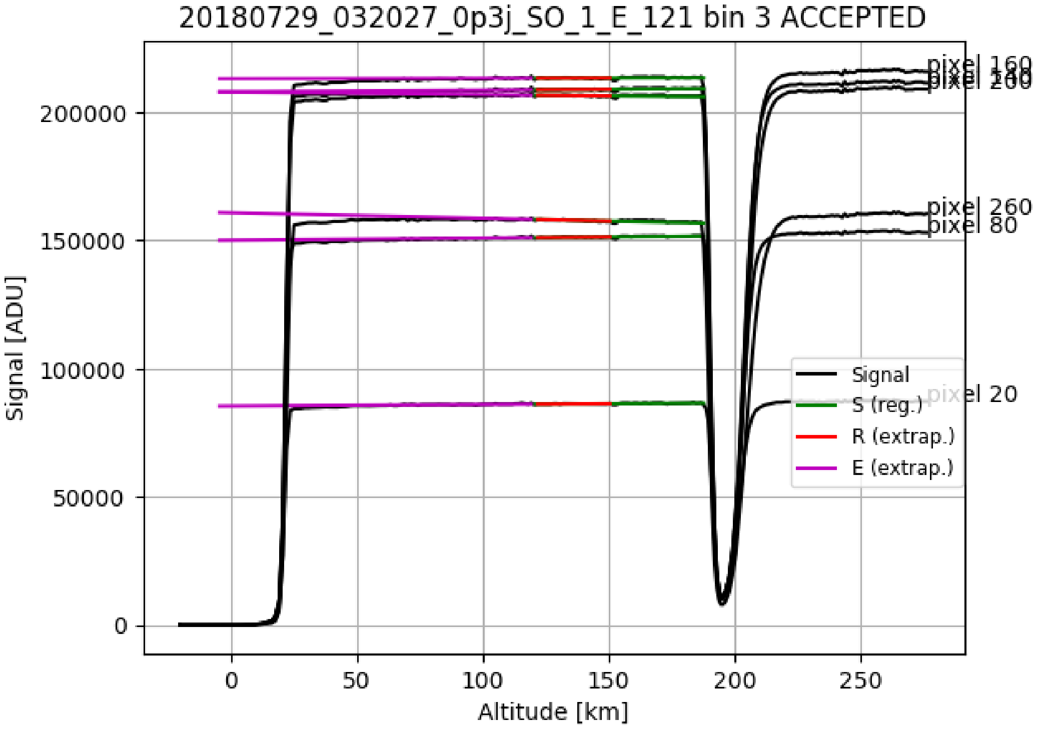

Figure 6.5: Example of occultation (20180729_032027_0p3j_SO_1_I_121 bin 3) where there was a movement of the High Gain Antenna (HGA). The selected solar region for the transmittance calibration is represented in green. The region with the drop in the signal recorded was avoided by the algorithm.

As transmittance is the ratio of the atmospheric spectra to a Sun spectrum, we might thus increase the effect of shot noise on transmittance-calibrated atmospheric spectra. This is avoided by taking enough Sun spectra to compute an averaged Sun reference spectra. Random noise can also be reduced by increasing the integration time but then reducing as well the vertical resolution.

6.2.3 Signal to noise ratio

The signal-to-noise ratio (SNR) is defined as

$$SNR_{ij} = \frac{P_{ij}}{\delta P_{ij}} = \left(\sqrt{\left(\frac{\delta \mathcal{T}_{ij}}{\mathcal{T}_{ij}}\right)^2 - \left(\frac{\delta S_{ij}}{S_{ij}}\right)^2} \right)^{-1} \tag{6.11}$$

where the last part of the equation comes from 6.8 and the SNR is not equal to $\mathcal{T}_{ij}/\delta\mathcal{T}_{ij}$.

Once the background is subtracted from the signal, we expect the SNR to increase with the integration time as for this high level of the signal, the main source of noise should be the shot noise which has a Poisson distribution. We therefore expect an SNR roughly equal to the square root of the signal.

Figure 6.6 shows the mean signal, uncertainty, and SNR in the S region for diffraction order 168. As explained in section 6.1 the spectra with on-board subtracted background (orange) have half the number of accumulations and therefore half the total integration time of the spectra with background subtracted in the pipeline (blue). Nevertheless, as seen in the third subplot, the SNR of the onboard subtracted seems to be higher or similar to the pipeline subtracted spectra.

6.3 summary

This chapter described the transmittance calibration of the spectra of the SO channel. The same calibration was performed for the SOIR spectrometer that was onboard Venus Express and to the UVIS channel of NOMAD. Although calibrating the spectra into transmittance seems rather simple by dividing the atmospheric spectra by a reference Sun spectrum, some difficulties arise in practice due to the presence of many perturbations. An algorithm was set up to select the best Sun spectra. This chapter also provided the computation of the uncertainties on the transmittance spectra which is necessary for the retrievals of atmospheric parameter and for the determination of detection limits that will be described in the next chapter.

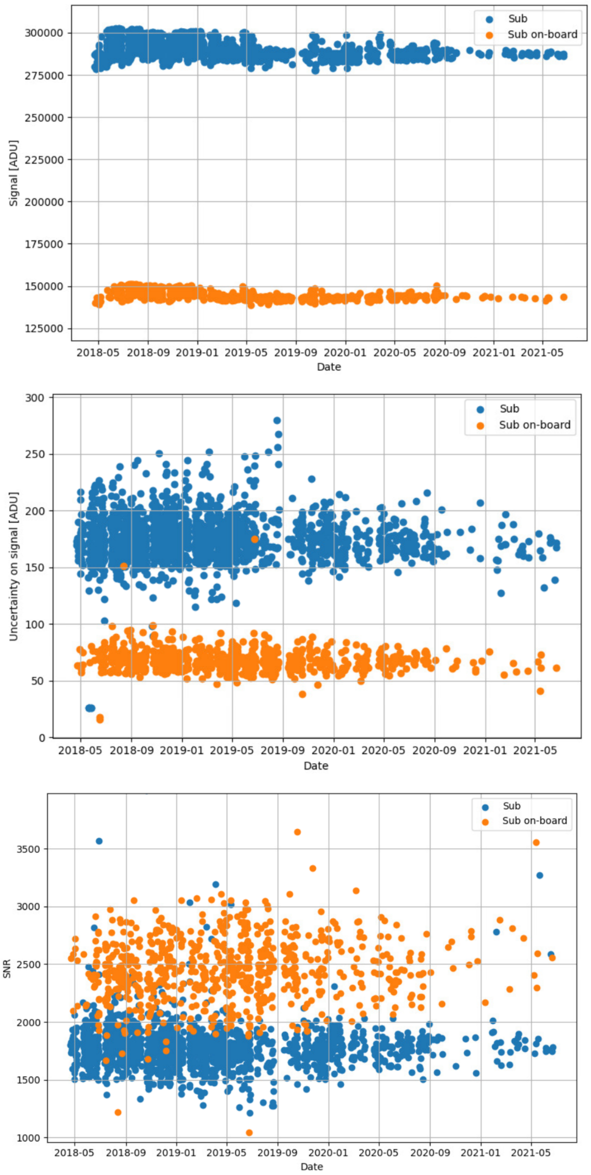

Figure 6.6: Mean signal (top), mean uncertainty on the signal(middle) and mean signal-to-noise ratio (bottom) in the S region for all datasets for diffraction order 168. Orange points are for datasets where the background is subtracted on-board TGO (before binning) while the blue points are for datasets with the background subtracted in the pipeline.

Chapter 7

Detection limits

One of the main objective of the Trace Gas Orbiter and the NOMAD instrument was to retrieve methane. From Robert et al. (2016), we already knew that the best diffraction orders to derive methane were 134 and 136. The first one contains the Q branch and the second one contains the strongest lines (for a temperature corresponding to the atmosphere of Mars) in the R-branch of the ν_3 band of methane. Unfortunately, no methane lines could be seen in NOMAD-SO spectral range either by "eye", trying to combine spectra, or using statistical methods. An example of spectra where the methane spectral signature was expected can be seen in Figure 7.1. A last attempt was performed using independent component analysis[1] to try to isolate the methane spectral signature. A better method was tested in Schmidt et al. (2020) using non-negative matrix factorization and could not find any methane too in NOMAD-SO spectra. This left us with determining the detection limits for methane.

The method to derive the detection limit consists of a direct inversion of the spectrum uncertainties Y_{err} assuming a constant VMR profile. The optical depth due to that CH_4 VMR is then simplified as

$$\begin{aligned} \tau_{CH_4}(\nu, z_{tg}) &= \int_{z_{tg}}^{z_{space}} \sigma_{CH_4}(\nu, p(z), T(z)) n_{CH_4}(z) dz \\ &= \mathcal{R}_{CH_4} \int_{z_{tg}}^{z_{space}} \sigma_{CH_4}(\nu, p(z), T(z)) n_{tot}(z) dz \end{aligned} \tag{7.1}$$

where n_{CH_4} is the CH_4 number density profile, n_{tot} is the total density profile of all species present in the atmosphere of Mars, and σ represents the absorption coefficients depending on the pressure p and the temperature T. The three parameters n_{tot}, p and t were obtained from GEM-Mars (Daerden et al., 2019). We integrated along the line of sight from the tangent altitude of the measurement z_{tg} to the top of atmosphere z_{space} defined as 120 km. We then convolve τ_{CH_4} with the instrument resolution.

This optical depth must be at least equal to the optical depth computed from the spectrum uncertainties

$$\tau_{err}(\nu, z_{tg}) = -ln\left(1 - 3.2\frac{Y_{err}(\nu, z_{tg})}{Y_{bg}(\nu, z_{tg})}\frac{I_{tot}(\nu)}{I_o(\nu)}\right) \tag{7.2}$$

where Y_{bg} is the background, and I_{tot} and I_o are the contributions from the central order radiance and the total radiance obtained when probing the z_{tg} altitude. The factor 3 is a common factor

---

[1] See, for instance, Hyvärinen (2013) for more information on independent component analysis.

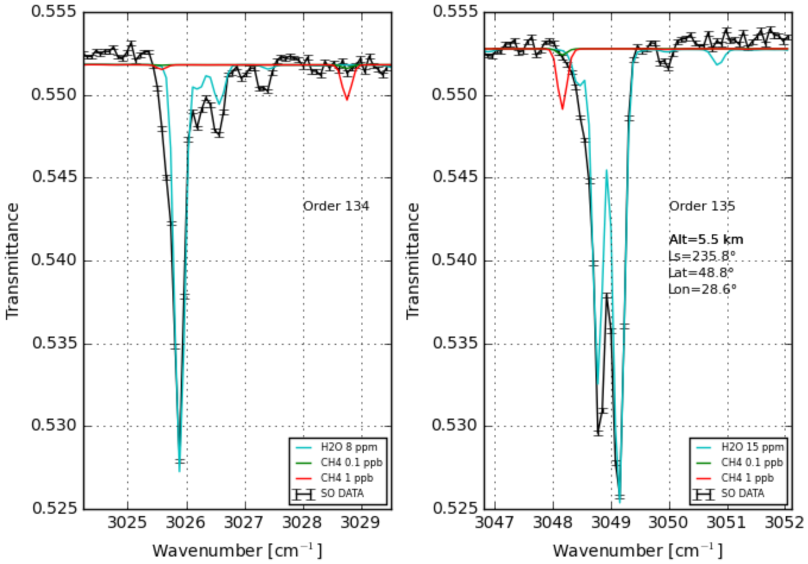

Figure 7.1: Example of NOMAD-SO spectra in black for occultation 20180823_063314_1p0a_SO_A_E, left panel for diffraction order 134 and right panel for diffraction order 135. Simulations of spectra containing 0.1 ppb and 1 ppb of methane are plotted in red and green respectively and a water spectrum in cyan (those spectra are simulated but not fitted to the experimental spectra).

when ones want to retrieve detection limits. Following the standards on detection limits as defined for chemistry, it is good practice to derive a detection limit as 3 times the standard deviation (Long and Winefordner, 1983; Committee, 1987; Shrivastava and Gupta, 2011).

By considering the detection limit as the equality between τ_{CH_4} and τ_{err}, we can then compute the CH_4 VMR detection limit as

$$\mathcal{R}_{CH_4}(z_{tg}) = \min_{\nu} \frac{\tau_{err}}{\int_{z_{tg}}^{z_{space}} \sigma_{CH_4}(\nu, p(z), T(z)) n_{tot}(z) dz} \tag{7.3}$$

The minimum over the wavenumbers corresponds for the strongest CH_4 line. As the uncertainties are more important on the edge of the spectrum, it will also tend to choose a line centered on the spectrum (higher τ_{err} on the side of the spectra).

The elements of path are computed for each tangent altitude of the observed spectra. The absorption coefficients are computed from HITRAN and are different for each layer as the temperature and pressure are different for each layer. For the line shape, we used a simple Doppler-broadened Gaussian line shape. It is sufficient for this detection limit computation as we are interested in the maximum of the intense lines and not the shape of the wings.

A more common method to derive detection limits from remote sensing data consists to fit simulated spectra to the measured ones using regularisation and check if the retrieved values (density or VMR) are significantly higher than the retrieved uncertainties (Korablev et al., 2018). This method here called the "fitting method" is the same as the method described here except that the comparison of the signal to noise is done in the solution (density or VMR) space instead of the measurement space (transmittance) as used here.

The direct inversion method has the advantage of being faster than the fitting method basically because no simulated spectrum is fitted to the measured spectrum. Also, the fitting method can be used with some regularisation. If this is the case, the averaging kernels should be provided too. Otherwise, we do not know if the detection limit is derived from information coming from the *a priori* profile used.

Some detection limits for MY 34 are shown in Figure 7.2. For each occultation, their values vary with height as the lines increase with increasing density and decreasing altitude until aerosols decreases the signal and the values of detection limit increase again. In the upper panel, we recognize that the lowest detection limit for an occultation increase closer to perihelion (L_S 251° - reddish profiles) as there are more dust at higher altitudes. The lowest detection limits are around 60 part per trillion (ppt), a similar value than in Korablev et al. (2019) and the reprocessing of the NOMAD data in Knutsen et al. (2021).

I used the same method as described here to derive the SOIR PH_3 detection limits (Trompet et al., 2021). They are equivalent to those derived with a fitting method when the latter provided detection limits that are not stuck on the *a priori* profile.

The NOMAD-SO methane detection limits found with the method described in (Trompet et al., 2021) are similar to those derived using an inversion in Korablev et al. (2019). The detection limits in the latter consist to provide three times the uncertainties from a fit of methane to the spectra. Nevertheless, one need to be careful if the inversion is done in an Optimal Estimation framework (see section 4.1.2). The results from the inversion can be artificially changed as the uncertainties are then computed as a sum in quadrature over the measurements uncertainties and those on the *a priori*.

Another method to derive detection limits was reported in Piccialli et al. (2022) and consist to determine whether there is a substantial increase of the χ^2 when the spectral signature of the targetted molecule is added in the fit.

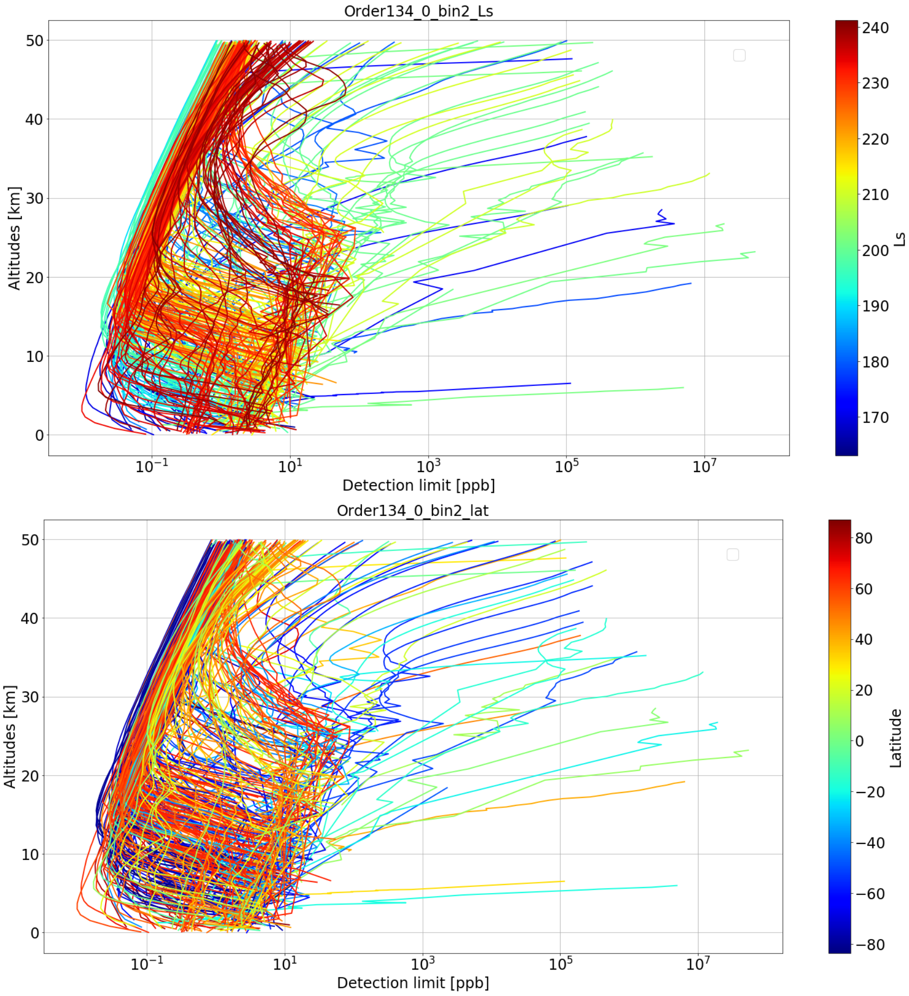

Figure 7.2: Detection limits as a function of altitude for occultations in Martian year 34. The colour bars in the left and right panels represent respectively the solar longitude on the latitude.

7.1 summary

One of the objectives of this work was to retrieve methane. The quantity of retrieved methane could have an important impact on the possibility of past or present life on Mars. Unfortunately, no spectral signature has been found up to now in the spectra of SO. This chapter aims to provide a simple way to derive the detection limits for methane based on the uncertainties in the transmittance spectra defined in the previous chapter. The detection limits decrease with height, as the simulated line decreases, and can be lower than 100 ppt. The lowest detection limits are not found close to the surface but rather around 10 km due to the presence of dust close to the surface. Dust reduces the incoming signal and thus the signal-to-noise ratio.

Chapter 8

Carbon dioxide and temperature retrievals from NOMAD-SO spectra

The retrieval of CO_2 density and temperature is performed in several steps depicted in Figure 8.1. The retrieval of a vertical profile of CO_2 from NOMAD-SO transmittance spectra are described in section 8.1. The retrieval is split into two main parts: a spectral inversion converting a transmittance spectrum to a slant column density, and a vertical inversion converting this slant column to a local density. The pressure and temperature profiles are then derived from the CO_2 density profile as described in section 8.2 assuming hydrostatic equilibrium. Those two profiles are needed in the first step and an iteration is performed as explained in section 8.3.

8.1 Retrieval of vertical profiles of carbon dioxide density

The aim is to derive a CO_2 vertical profile of density from transmittance spectra containing CO_2 lines and acquired from solar occultation. The theory necessary for solar occultation measurements is provided in chapter 3 and can be found as well in Smith and Hunten (1990) or Lenoble (1993).

As the modelling of the instrument function is quite complex, the vertical profiles are not directly inverted from the transmittance spectra but are fitted with a forward model. The fit is performed by first using the forward model to derive slant columns (spectral inversion - section 8.1.1) and then a direct inversion of the slant column with the Abel transform provides the local number density (vertical inversion - section 8.1.2).

8.1.1 Spectral inversion

The necessary background for the spectral inversion was provided in section 4.1. Seven parameters are adjusted:

- a multiplicative factor to the optical depth adjusting the slant column value,
- five coefficients for a fourth-order polynomial fit of the baseline,
- one parameter adjusting a residual shift of the pixel to wavenumber calibration.

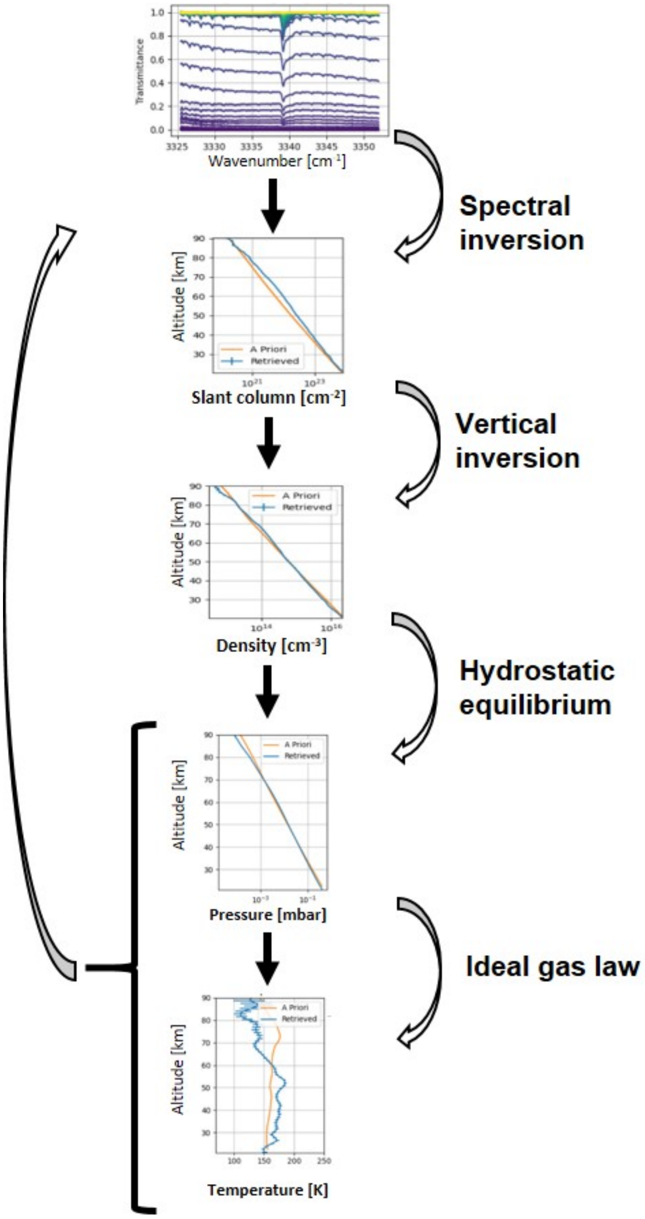
Transmittance
Wavenumber [cm⁻¹]
Spectral inversion
Altitude [km]
A Priori
Retrieved
Slant column [cm⁻²]
Vertical inversion
Altitude [km]
A Priori
Retrieved
Density [cm⁻³]
Hydrostatic equilibrium
Altitude [km]
A Priori
Retrieved
Pressure [mbar]
Ideal gas law
Altitude [km]
A Priori
Retrieved
Temperature [K]

Figure 8.1: Diagram of the retrieval of vertical profiles of CO_2 density, CO_2 partial pressure and temperature. Once retrieved, pressure (computed from the CO_2 partial pressure) and temperature are provided fir another loop on the retrieval until convergence.

The fit of the baselines needs a fourth-order polynomial as several effects produce bendings of the baseline such as aerosols or a variation of the instrument function along an occultation.

To ease the radiative transfer computation, ASIMUT uses the Curtis-Godson approximation (Curtis, A, 1952; Godson, 1953). Another important assumption is that the atmosphere is split into homogeneous layers of density, temperature, and pressure. The maximum equivalent slant path for Mars atmosphere is $\sqrt{2\pi(r_M + z)H} \approx 500\,km$ ($250\,km$ on each side of the terminator) where r_M is Mars radius, z is the altitude and H is the scale height [1]. Considering the homogenous layers, this horizontal extension corresponds to a vertical extent of only 10 km for the Mars radius and to a longitudinal angle of 15°(7.5°on each side of the terminator). From the models, we know that the atmospheric parameters (density, pressure, temperature) can vary by 2%. Considering that this is for the maximum equivalent slant path, this assumption is acceptable.

The forward model takes into account the latest updates on the calibration of the AOTF, blaze function, and ILS (Villanueva et al., 2022). ASIMUT uses a Gauss-Newton iteration scheme for the fit and the Optimal Estimation Method (OEM) for regularisation(Rodgers, 2000). The *a priori* profile is a GEM-Mars profile (Daerden et al., 2019; Neary et al., 2020) averaged over all seasons, latitudes, and local solar times. The variance over the *a priori* is set to 81% meaning that we do not expect the true CO_2 density being further away than 90% of the *a priori* value. Once the slant column has been retrieved from the spectrum, we keep this retrieved value only if the associated DOF is higher than 0.99 and we can consider that there is no regularisation applied in this retrieval. The spectroscopic parameters are taken from HITRAN (Gordon et al., 2022) and self-broadening and broadening by a CO_2 are considered. Example of fitted spectra are provided in figures 8.2, 8.3, and 8.4 for diffraction orders 165, 148 and 132.

Water slant column density is retrieved below 60 km in a second fit to improve the fit of the CO_2 slant column. The *a priori* value is set to a constant VMR of 1 ppm with a variance of 100,000%. An example of the fit of water lines with carbon dioxide lines can be seen in figure 8.4.

As explained in section 5.3.1, the lowest limit in altitude for the retrieval are given by the saturation of the molecular lines. But scattering by aerosols might also give a lower limit as it reduces the baseline of the spectra. The spectra with a baseline lower than 0.5 in transmittance are avoided.

The spectral inversion is the most time-consuming part of the retrieval due to the computation of the absorption coefficients on a fine spectral grid and the convolution with the ILS. Fitting one spectrum takes around one minute. However, this step is parallelized as the fit of each spectrum is independent.

8.1.2 Vertical inversion

In this step, we convert the slant column profile c into a local density profile n by applying the inverse Abel transform. This is an inverse problem and solutions to inverse problems are known to be unstable when uncertainties are present in the measurements. An iterated-Tikhonov method is applied in this work where we use a slightly modified version of the iterated Tikhonov regularisation (see section 4.2.4) and the smoothing parameters are different for each altitude. That algorithm was first described in Quémerais et al. (2006) were they report this algorithm as developed by Hauchecorne and Cot. This algorithm was also used in other works, for instance, in Forget et al. (2009); Sandel et al. (2015); Gröller et al. (2018); Koskinen et al. (2013); Sandel et al. (2015); Snowden et al. (2013).

This algorithm needs between 10 and 15 iterations. The criteria for convergence are given in section 4.2.4.

---

[1] This is related to the Chapman functions, see Chapman (1931)

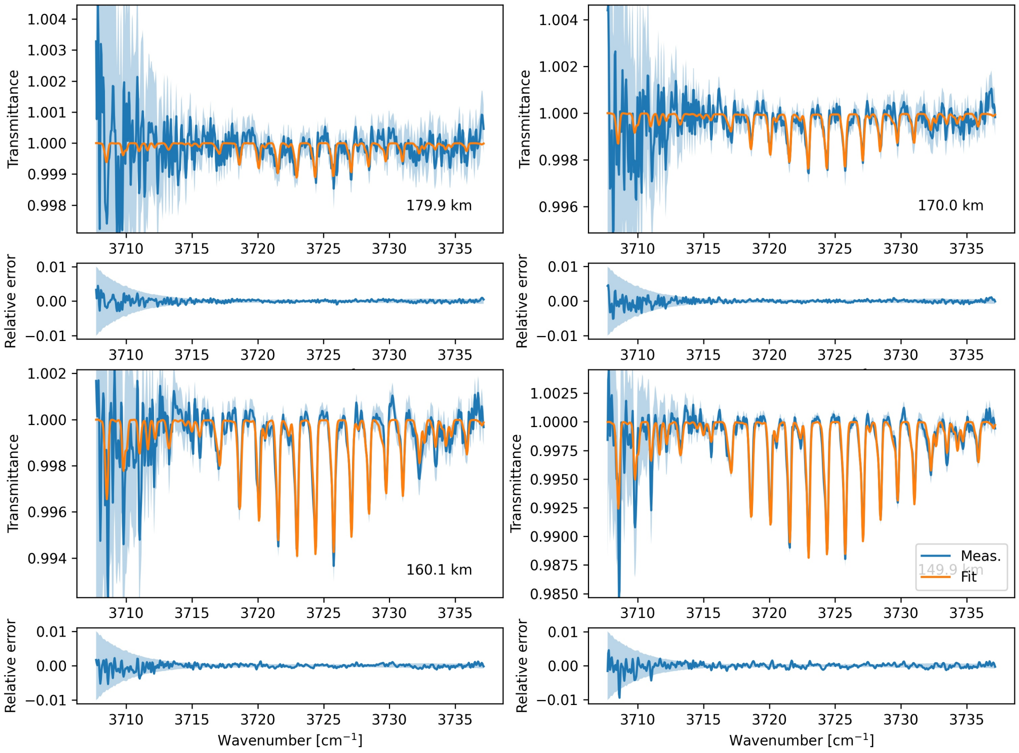

Figure 8.2: Example of fit for order 165, dataset 20200806_074733_1p0a_SO_A I for four altitudes. The residuals are provided in the lower panels and compared to the $1 - \sigma$ standard deviation on the spectra.

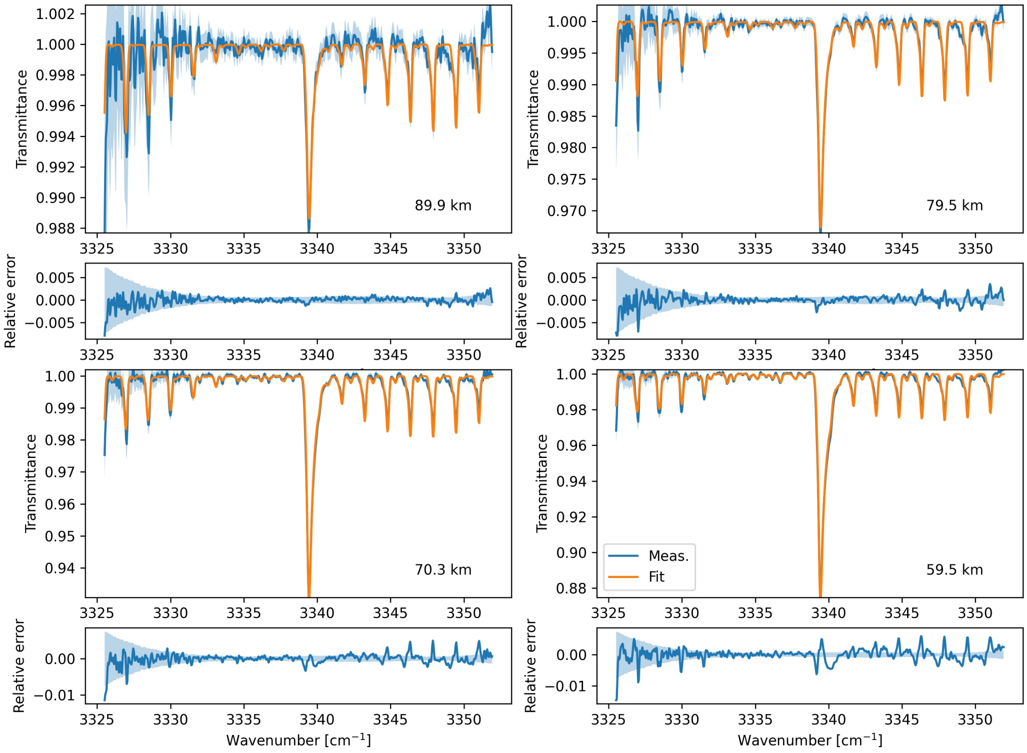

Figure 8.3: Example of fit for order 148, dataset 20200824_020917_1p0a_SO_A I for four altitudes. The residuals are provided in the lower panels and compared to the $1-\sigma$ standard deviation on the spectra.

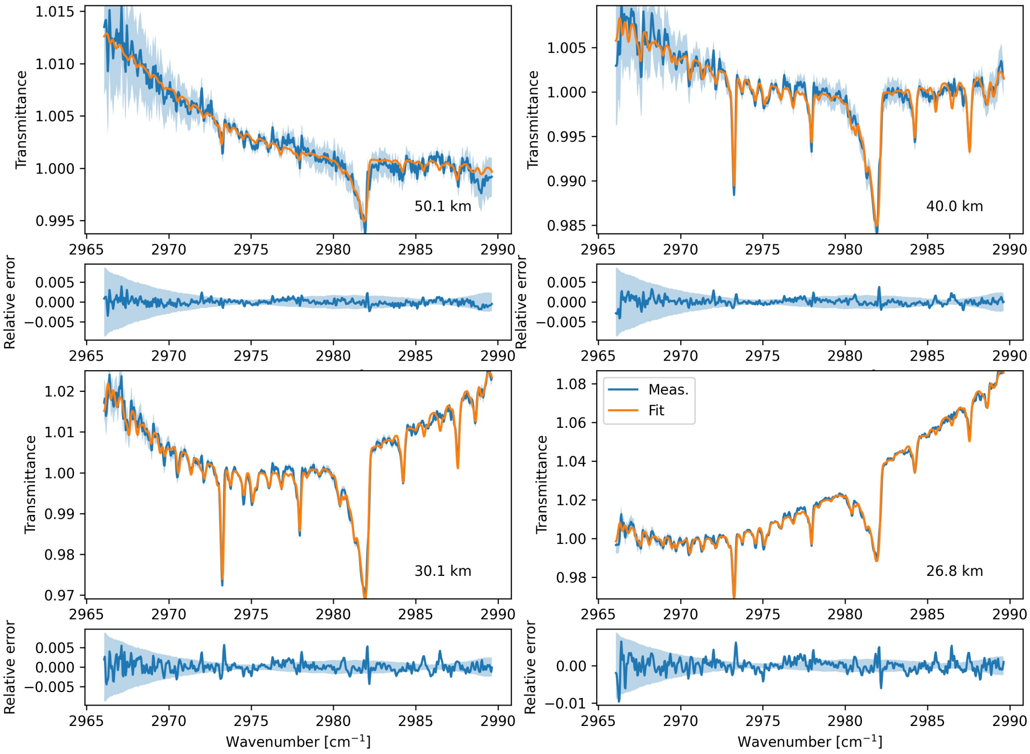

Figure 8.4: Example of fit for order 132, dataset 20200622_155025_1p0a_SO_A I for four altitudes. The residuals are provided in the lower panels and compared to the $1-\sigma$ standard deviation on the spectra. There are also some strong water lines fitted as the water line at $2973.25\,cm^{-1}$.

In that algorithm, we still need to provide a parameter controlling the regularisation. Since the first application of the Tikhonov method, a lot of effort was carried on to find the best regularisation parameter λ (see section 4.2.5). Most of them involve to compare the uncertainties to the smoothing error (Hansen (1992a); Doicu et al. (2010a)). The latter can be computed only after the solution to the inverse problem is found. Thus finding the best smoothing parameter requires first computing the solution for many λ. The best method to derive λ was found to be the Expected Error Estimation (Doicu et al., 2010a; Xu et al., 2016) in section 4.2.5. This method is coupled with a simplex using the Nelder-Mead algorithm (Gao and Han, 2012) to find the best λ.

The altitudes on all plots are with respect to Mars areoid but the computation of the Abel transform needs the altitudes with respect to the center of Mars (as computed from SPICE kernels). The difference between the two depends on the surface elevation of Mars below the tangent point probed. On average, it is 2-3 km.

Correction to the Abel transform equation

In theory, the upper bound of the integral in equation 3.20 should be the limit for space, i.e. when the atmosphere is negligible. In practice, the measurements are bounded on an upper tangent altitude but the remaining density above this last tangent altitude is not negligible. We can compute the altitude at which the atmosphere is negligible by applying the Abel transform. The ratio of the atmosphere considered to the atmosphere neglected is depicted in figure 8.5. Following the line $c_{out}/c_{in} = 10^{-2}$ (error of 1%), we see that we always need to consider 20 km above the last tangent point. For the retrievals, we use a limit of 40 km above the last tangent point which corresponds to an error of 0.1%.

In practice, to consider the altitudes above the last measured tangent altitude, we extrapolate the slant column profile using a similar method as in Thiemann et al. (2018).

The characteristic effect on the density inversion of neglecting the upper part of the atmosphere which is not negligible is an increase of density for the highest altitudes as it can be seen in Quémerais et al. (2006, fig. 15).

Best method for the regularisation parameter selection

We tested seven methods (see section 4.2.5) with a known density profile, called n_{true}, and taken from GEM-Mars version hf-a585. I converted this density profile into a slant column profile and then added some random noise. Seven noise levels extends from 0.1%, 0.5%, 1%, 5%, 10%, 50%, 100%, and a thousand samples for each noise level. For each sample, the HC algorithm is tested with a hundred values of λ_0. It then computed the result for the seven methods which provided their best λ_0 and the corresponding density profile. I then computed the averaged relative error to n_{true}. The results are shown in figure 8.6.

The two best methods are the discrepancy principle and the expected error estimation. Morozov's discrepancy principle seems to work better than the Expected Error Estimation as in this synthetic case we know exactly what the level of error is. For a real case, we approximate the level of error with the uncertainties in the data. Those are slightly overestimated and thus the discrepancy principle is likely to give a too high λ_0. The discrepancy principle is already known to give slightly overestimated λ_0. Thus I decided to keep the expected error estimation as the first method to derive the best λ_0. In practice, it happens that the expected error estimation cannot find a minimum and then the algorithm uses the discrepancy principle. We see also that as the input noise level increases, the retrieved profiles will also have higher noise levels. The Tikhonov method can reduce the noise level but not discard it completely and as the noise increases, its presence also increases in the retrieved profile.

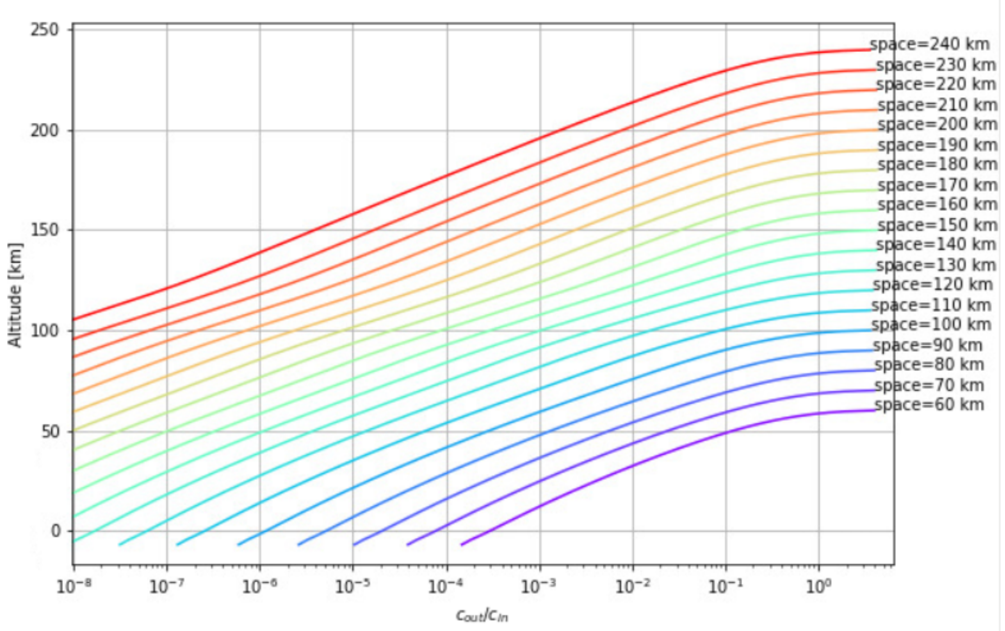

Figure 8.5: Ratio of slant column below the altitude to the slant column above that altitude for different limits of the atmosphere considered (space).

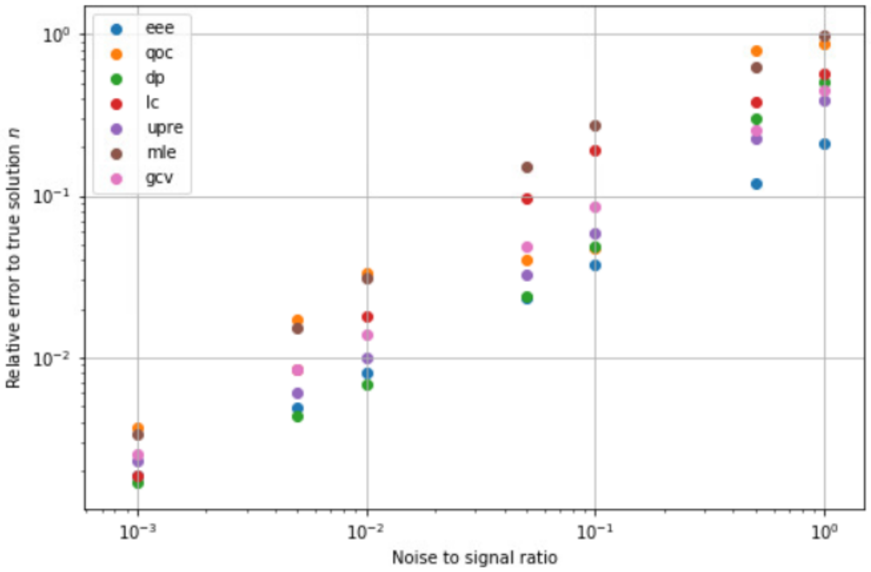

Figure 8.6: Relative error with respect to n_{true} from the synthetic tests for different noise levels.

All methods described above need first to retrieve the local density for different smoothing parameters. Thus the algorithm 1 established in section 4.2.4 has to be recomputed with different values of λ_0. In our case, this is quite fast as we have separated the spectral inversion and the vertical inversion and this is applied only to the vertical inversion. To find the λ_0 leading to a minimum, a first guess computes the algorithm 1 for 100 values of λ_0 between zero and seven using the expected error estimation method and takes the minimum value. Then I refine the computation of the minimum by using a Simplex starting from the previously found minimum. This entire computation of the optimal λ_0 takes one to a maximum of two minutes.

Another method that is worth mentioning is the error consistency method (Ceccherini, 2005) but this method always provides a smoothing parameter at least an order of magnitude too low.

Examples of inverted profiles for different λ_0 for the same occultation is given in Figure 8.7. The differences on the density profiles (first panel) are difficult to see by "eye" but the differences are larger in the temperature profiles (last panel). The best λ_0 was found to be 0.73 from the expected error estimation method. We see that for lower values of λ_0, spurious variations in the profile still remains while higher values deviate from the true variability of the profile.

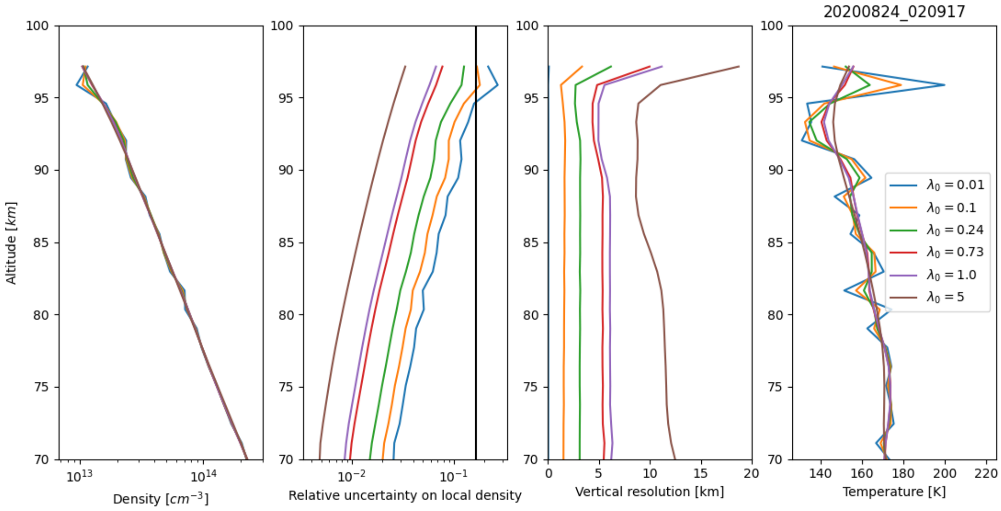

Figure 8.7: Inverted density profile for different λ_0 values for occultation 20200824_020917_1p0a_SO_A_I, diffraction order 148. The best λ_0 is 0.73 from the expected error estimation method. The first panel provides the density profiles and the second panel provides the corresponding relative uncertainties. The vertical line in the second panel corresponds to 1/6. The third panel provides the vertical resolution corresponding to each λ_0 with the Backus-Gilbert spread formula. The last panel represents the corresponding temperature profiles.

8.1.3 Bins profile combination

The density profiles are computed for each bin independently and combined afterward by first interpolating the profiles on the same altitude grid

$$\boldsymbol{x_i} = \boldsymbol{W_i}\,\boldsymbol{y_i} \tag{8.1}$$

with $\boldsymbol{x_i}$ the profile on the altitude grid combining the grids of all bins, $\boldsymbol{y_i}$ is the profile for bin i, and the interpolation matrix $\boldsymbol{W_i}$. The best λ_0 values for each bin are usually very similar. For density and pressure profiles, this linear interpolation is applied on the logarithm of the profile and we then need to compute the exponential of the interpolated profile. There is no loss of information when passing from a coarser to a finer grid. The inverse transformation is the pseudo-inverse of W

$$\boldsymbol{V} = (\boldsymbol{W^T W})^{\boldsymbol{-1}} \boldsymbol{W^T}. \tag{8.2}$$

The Jacobian, gain, and averaging kernels matrices are transformed as (Calisesi et al., 2005)

$$\begin{aligned} \boldsymbol{K_x} &= \boldsymbol{K_z V}, \\ \boldsymbol{G_x} &= \boldsymbol{W G_z}, \\ \boldsymbol{A_x} &= \boldsymbol{W A_z V}. \end{aligned} \tag{8.3}$$

where the x subscript is for the finer grid and the z subscript is for the initial coarser grid. As for the regularisation, we describe the divergence of the product WV from the identity matrix with the averaging kernel for the interpolation $\boldsymbol{A_{interp}} = \boldsymbol{WV}$ König et al. (2019). We then compute the total averaging kernel that also considers the modifications of the vertical resolution due to the different regularisation and interpolation.

$$\boldsymbol{A_{combined}} = \boldsymbol{A_{interp}}\,\boldsymbol{A} = \boldsymbol{W\,V\,G\,K} \tag{8.4}$$

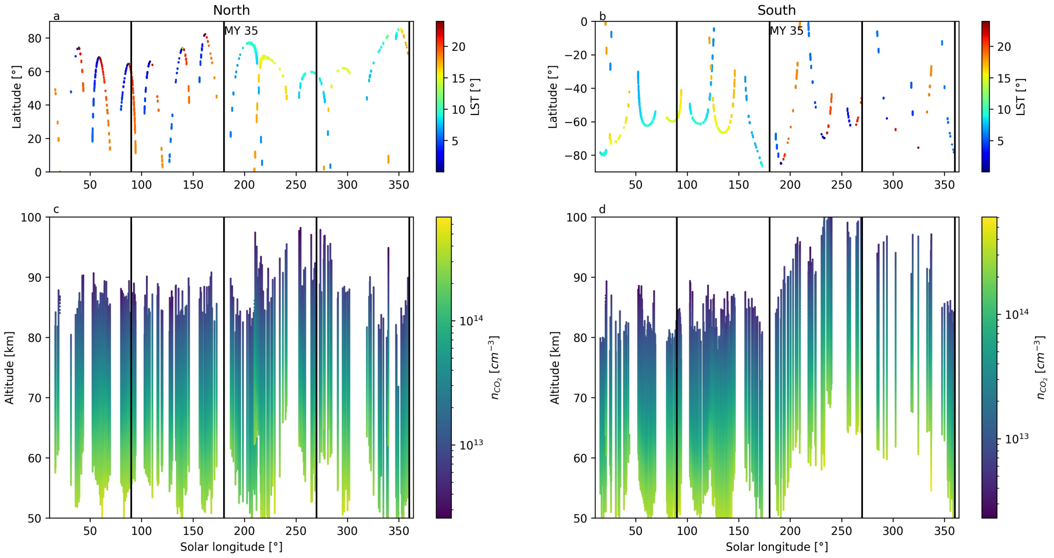

Figure 8.8: Retrieved profiles of CO$_2$ density in MY 35 with NOMAD-SO.

Figure 8.8 shows all the derived CO$_2$ density profiles for MY 35 after recombination of the four bins. We see a typical seasonal variation that will be discussed in section 10.2.

8.2 Retrieval of vertical profiles of pressure and temperature

This section describes the retrieval of temperature from the carbon dioxide profiles. The temperature profiles are characterised by important parameters such as the uncertainties, and the vertical resolution that are treated in sections (8.4) and (8.5) respectively.

8.2.1 Introduction

By using the hydrostatic equilibrium equation (2.16) and the previously retrieved CO_2 density profile, we derive a carbon dioxide partial pressure profile as

$$\begin{aligned} p(z_i) &= p(z_{i+1}) + \int_{z_i}^{z_{i+1}} \rho(z) g(z)\, \mathrm{d}z \\ &= p(z_{i+1}) + \Delta p_i \\ &= p_{top} + \sum_{j=i}^{N} \Delta p_j \end{aligned} \tag{8.5}$$

where the pressure profile is computed as a series of differences of pressure Δp_i. An initial pressure $p_{top} = p(z_N)$ needs to be guessed (see section 8.2.4) and N is the total number of vertical layers. The pressure profile is computed downward in 8.5. This equation can be reformulated in linear algebra as

$$\boldsymbol{p} = \boldsymbol{K_p}\, \boldsymbol{\Delta p} \tag{8.6}$$

where $\boldsymbol{\Delta p}$ is a vector containing the Δp_j elements except the last (first) element which contains p_{top} for the downward (upward) case. The $\boldsymbol{K_p}$ matrix is an upper (lower) triangular matrix of ones (-1 except the first column which is filled with 1) for the downward (upward) case.

Eventually, we derive the temperature profile from the pressure and CO_2 number density profiles by using the ideal gas law.

This method was already used in the 60s for the pitot-static tube experiment, the falling sphere experiment (Jones et al., 1959, eq. 2), (Theon and Nordberg, 1965), the rocket grenade experiment (Horvath et al., 1962, eq. 12). They all argued that the error on the starting value is negligible after 15 km (the Earth scale height is around 8.5 km) and they selected the initial pressure p_{top} as the one that gives the fastest convergence.

This hypothesis of hydrostatic equilibrium might not always be valid. Leclercq et al. (2020) shows that in absence of significant perturbation, this method reproduces the temperature profile, but for higher altitudes, where the perturbation is more significant, this method might not be reliable any more. Unfortunately, they do not provide any correction or alternative method to apply. In this work, I consider the hydrostatic equilibrium for all retrieved temperature profiles.

The integral of Δp_i is usually computed numerically: for instance Snowden et al. (2013) uses the midpoint rule while Mahieux et al. (2015) uses the trapezoidal rule. The numerical integration requires the refinement of the integrand and the values are interpolated by considering a linear variation of the logarithm of the density and equation 2.2.

8.2.2 Deriving simpler formulae

The assumption of a linear logarithm of the density used in all numerical integration of 8.5 is equivalent to equation 2.22 with a constant scale height (see appendix C)

$$h_i = \frac{z_i - z_{i+1}}{\ln\left(\frac{n_{i+1}}{n_i}\right)}. \tag{8.7}$$

By using 2.2 and 2.22, the integral can be summarized as

$$\Delta p_i = m_a\, n_i\, g_0\, r_M^2 \int_{z_i}^{z_{i+1}} \frac{\exp\left((z_i - z)/h_i\right)}{(r_M + z)^2}\, \mathrm{d}z \tag{8.8}$$

Using this formula, an error is introduced as we are using equation 2.22 which is valid only if the scale height and the temperature are constant along altitudes. In our case, this assumption works for steps in altitudes lower or around one kilometre. An analytical formulation of 8.8 can be computed as (see appendix B)

$$\Delta p_i = m_a\, n_i\, g_0\, r_M^2 \exp\left(\frac{r_M + z_i}{h_i}\right) \left[\frac{E_2\left(\frac{r_M+z_i}{h_i}\right)}{r_M + z_i} - \frac{E_2\left(\frac{r_M+z_{i+1}}{h_i}\right)}{r_M + z_{i+1}}\right] \tag{8.9}$$

where E_2 is an exponential integral (see Zhang and Jin (1996, chap. 19) and Press et al. (2007, sect. 6.3)[2]). Zhang and Jin (1996, sect. 19.4) provides an algorithm that gives an approximation of the exponential integral and we use this algorithm via the *scipy.special* module (Virtanen et al., 2020). This algorithm iterates until an accuracy of the machine epsilon is reached. The values of the argument $(r_M + z_i)/h_i$ in our case are typically around 300[3].

Finally, a simpler formulation is obtained if we define the reduced altitudes $a_i = \frac{r_M+z_i}{h_i}$ and $b_i = \frac{r_M+z_{i+1}}{h_i}$:

$$\Delta p_i = m_a\, n_i\, g_0\, r_M^2\, h_i\, \exp(a_i) \left[\frac{E_2(a_i)}{a_i} - \frac{E_2(b_i)}{b_i}\right]. \tag{8.10}$$

This last formula is the one used in the data pipeline but we could consider g as a constant as the gravitational acceleration computed as 2.2 is varying by only 0.012% between 0 and 200 km. Then by computing the integral for n only

$$\Delta p_i = -m_a\, g\, h_i \left[\exp\left(\frac{z_i - z_{i+1}}{h_i}\right) - 1\right]. \tag{8.11}$$

But by using 8.7, an even simpler formula can be derived from the ideal gas law to compute directly the pressure profile:

$$\begin{aligned} p_i &= n_i\, k_B\, t_i \\ &= n_i\, m_a\, g_0\, r_M^2\, h_i \frac{1}{(r_M + z_i)^2} \end{aligned} \tag{8.12}$$

where we used equation 2.20 and 2.2 for the last equality and we did not use the hydrostatic equilibrium equation. This last formula requires much fewer operations than any numerical integration nor formula 8.10 and we call it the 'direct' method. It is also much simpler to derive the uncertainties. The pressure p_i at altitude z_i depends on the density n_i but also on n_{i+1} as h_i is computed by 8.7.

---

[2] The exponential integral is also present in radiative transfer, in the Scharzschild-Milne integral equation (Chandrasekhar, 1960, chap I, eq. 97-98).

[3] It cannot exceed 709.7 otherwise the exponential and E_2 functions return a value no more representable in double precision.

8.2.3 Synthetic test

From equation 8.5, it seems that we could start either from a top altitude and add the Δp_i values or start from the bottom altitude and subtract the Δp_i values. We will call those two cases, respectively, the downward case and the upward case. In practice, the density profile contains a small presence of error (but with more important errors at the extremities of the profile due to lower information at the top and saturation at the bottom). As the density is exponentially decreasing with altitudes, the error propagation through the computation of the series in equation 8.5 leads to much higher error propagation in the upward case. In practice, only the downward case works, still with a bias for the highest altitudes.

Constant scale height

To better see this effect and the differences amongst the different formulae we built a synthetic pressure profile generated with equation 2.21 with $p(z_0 = 0) = 0.58\,hPa$, an altitude grid z with steps of 1 km from 0 to 100 km and a constant scale height of $h = 11.1\,km$. The 'true' temperature profile $\hat{t}$ can be directly derived from the scale height and we will consider only CO_2 for the atomic mass. We then compute the density profile $\hat{p}$ from the ideal gas law. The values of $\Delta\hat{p}$ are then computed as the first (discrete) difference over $\hat{p}$. On another side, we compute Δp from equation 8.9, then p and t from 8.5 and the ideal gas law. Eventually, we compute the relative error on Δp as $\frac{\Delta\hat{p}-\Delta p}{\Delta\hat{p}}$.

We can also use this test to check the number of required interpolated points within each layer i to compute a sufficiently accurate numerical integration. As seen from figure 8.9, by using a trapezoidal rule, thirty interpolated integration points already give a solution with an accuracy of less than 1×10^{-6}. We also see that the curve are independent on the altitude. As this test was made with an altitude step of 1 km the number of integration points must be proportional to the altitude step to keep the same accuracy.

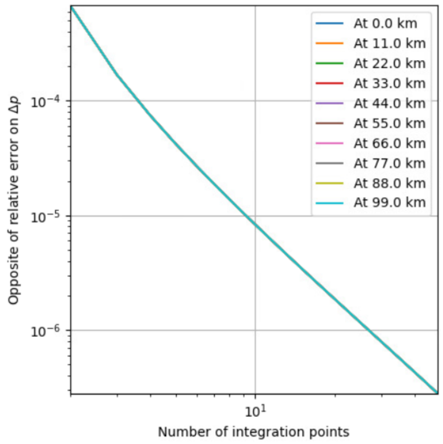

Figure 8.9: Relative error on Δp with respect to the number of points interpolated within each altitude z to compute the numerical integration of 8.5. As the integrand in 8.8 is concave up, the numerical integration slightly overestimates the value of the integral and the relative error is negative. The opposite of the relative error is shown here as we used a logarithmic scale. The curves are the same for all altitudes.

Table 8.1 contains the results for this synthetic test for an altitude of 50 km.

Method	Δp at $z_i = 50\,\mathrm{km}$	Relative error on Δp
True	49.9676654	/
Analytical	49.9676646	1.5×10^{-8}
Numerical	49.9677048	-7.9×10^{-7}
With g=cst	49.9821866	2.9×10^{-4}
Direct	50.2970442	-6.6×10^{-3}

Table 8.1: Relative error on Δp for $z_i = 50\,\mathrm{km}$ from the different methods. The methods are sorted in ascending order of absolute relative error on Δp.

The precision on the numerical integration is improved by considering more segments. On another side, the round-off error[4] is more important depending on its accumulation with the number of operations and, thus, the number of segments. Nevertheless, such low relative errors and their accumulation in 8.5 are negligible with respect to the level of uncertainties in the derived profiles in 8.2.5.

For the analytical integration, we must be cautious with the term $\exp(\frac{r_M+z}{h})$ which cannot be represented any more in double float precision if h is smaller than 5 km considering the mean radius of Mars. The same argument stands for the term with the exponential integrals.

The formula 8.11 provides a relative error around 0.03% since g is not a constant but varies with altitudes. For the direct method 8.12, where we did not use the hydrostatic equilibrium equation, the relative error is -0.66%. This value cannot be explained by any discretisation error and is close to the uncertainties on the pressure and temperature profiles (section 8.2.5). This formula is therefore inadequate for the computation of the pressure from the density.

Error on the density

Figure 8.10 shows the relative error of the profiles derived with the density profile multiplied by values in the range [0.99:1.01] with a step of 0.002 and corresponding to blue to red curves. This figure shows the cumulative sum of errors in both cases. In the upward case, the relative error increases exponentially due to the propagation of error from the higher pressure at the bottom. In the downward case, the propagation of error increases first fast but reaches a constant value after two scale heights as the errors from the higher altitudes can be neglected at higher pressures. If the density profile is too high, the pressure profile will also be too high in the upward case while it will be too low in the downward case as we subtract higher Δp at each layer. Thus the downward case would be better to remove any bias in the temperature profile as it is computed as a ratio between pressure and density (and divided by Boltzmann's constant) and the error in the temperature profile decreases exponentially with lower altitudes. Thus only the downward case gives a stable solution if n contains some noise.

This effect in the propagation of errors explains why the profile needs one to two scale heights before reaching the right pressure when starting from the top. This is due to the relatively high errors for the pressure retrieved for the highest altitude and it needs two scale heights before the pressure is divided by e^2 and the error becomes much smaller than the pressure. In addition to the noise on the density profile, the error on the starting pressure also propagates and becomes negligible as we reach lower altitudes.

---

[4] In double precision, the epsilon machine is around $2.2\,10^{-16}$.

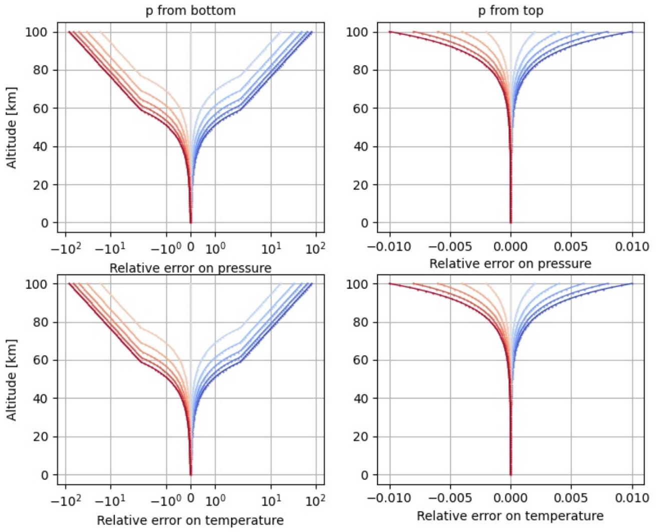

Figure 8.10: Relative error on the derived pressure(up) and temperature (down) profiles for the synthetic case. The left panels are for the upward case and the right panel are for the downward case. The colours are passing from dark blue to dark red corresponding to 0.99 to 1.01 times the density profile by step of 0.001.

Constant lapse rate

We continue our synthetic tests to determine the errors introduced but consider several values for the lapse rate. A non-zero lapse rate brings us further away from a constant scale height or an assumption of a constant temperature in 2.22. To fix the problem for this exercise, I choose $p_0 = 5.8\,Pa$ and $t_0 = 209.8\,K$ at $z_0 = 0\,km$ which are typical mean values for the atmosphere of Mars. Then a temperature profile is computed with 2.26 and the pressure is computed with 2.29.

A constant positive lapse rate through the atmosphere is physically impossible as the temperature would finally reach $0\,K$. The aim is to keep plausible temperature values so we will restrict the difference in altitude to only $40\,km$ which is the length of the profiles retrieved from SO spectra.

Figure 8.11 shows the relative error on the pressure retrieved with 8.5 for this synthetic case.

The presence of this error can be easily understood as on one side we have a pressure computed from a non-constant temperature profile with 2.29. On another side, the integration of Δp is made assuming that the logarithm of the density can be linearly interpolated which requires a constant scale height and thus a (quasi-)constant temperature.

From the formula 2.29, the Binomial Theorem and by considering that $\Gamma(z - z_0) \ll t_0$ then we can derive

$$\begin{aligned} n = \frac{p}{k_B\, t} &= \frac{p_0 \left[1 - \frac{m_a\, g}{k_B\, t_0}(z - z_0)\right]}{k_B\, t} \\ &= \frac{p_0\, k_B\, t_0 + p_0\, k_B\, \Gamma(z - z_0) + p_0\, m_a\, g\, z_0 - p_0\, m_a\, g\, z}{k_B^2\, t\, t_0} \end{aligned} \tag{8.13}$$

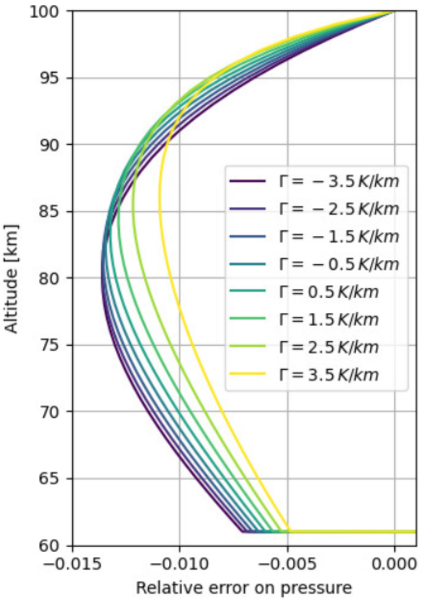

Figure 8.11: Derived pressure profiles for the synthetic case with different values for the lapse rate Γ.

On the other side, to compute Δp with 2.17, we consider n varying with equation 2.22. We consider also that $(z - z_0) \ll h$ which acceptable assumption as h is 11.1 km and the difference in altitude is $\sim 1\,km$. Then we derive also

$$\begin{aligned} n_{\Gamma=0} &= \frac{p_0}{k_B\,t_0}\left[1 + (z_0 - z)\frac{m_a\,g}{k_B\,t}\right] \\ &= \frac{p_0\,k_B\,t_0 + p_0\,m_a\,g\,z_0 - p_0\,m_a\,g\,z}{k_B^2\,t\,t_0} \end{aligned} \tag{8.14}$$

where we already see that 8.14 is equal to 8.13 if $\Gamma = 0$, the difference increases as Γ is further away from 0. The absolute error between those two expressions is

$$\epsilon_n(z) = \frac{p_0\,\Gamma(z - z_0)}{k_B\,t(z)\,t_0} = n_0\,\frac{\Gamma(z - z_0)}{t_0 - \Gamma(z - z_0)} \tag{8.15}$$

using 2.26 for the second equality. The relative error induced by this assumption is a function of the lapse rate Γ, the difference in altitude $z - z_0$, and is inversely proportional to the temperature t_0.

For NOMAD-SO measurements, the altitude step for only one bin ranges from $100\,m$ to $1.6\,km$, respectively for low to high β-angles. If we consider all four bins, then these values have to be divided by four. This error will be larger at the middle of the altitude step, where the interpolated density value is the most distant from the known density values. So we restrict this error analysis to a maximum altitude difference $(z - z0)$ of $0.8\,km$ (half of $1.6\,km$). Given the values of p_0 and t_0 given above and a lapse rate of $3.5\,K/km$, the relative error are the same as the ones shown in figure 8.11.

8.2.4 Choice of the initial pressure

For diffraction orders dedicated to altitudes below 130 km, the pressure profiles from GEM-Mars give a reasonably close guess of the pressure at top of the SO retrieved profile and a pressure value combining the retrieved density and the temperature from GEM-Mars is $p = n_{SO}\, k_B\, t_{GEM}$. For higher altitudes (mainly for NOMAD-SO diffraction orders 164, 165), we need to derive the pressure at the top altitude and we need to keep in mind that the pressure retrieved in this work is only the partial pressure for CO_2. From the ideal gas law, we can write

$$\frac{1}{p}\frac{dp}{dz} = \frac{1}{n}\frac{dn}{dz} + \frac{1}{t}\frac{dt}{dz}. \tag{8.16}$$

Replacing $\mathrm{d}t/\mathrm{d}z$ and $\mathrm{d}p/\mathrm{d}z$ with the adiabatic lapse rate 2.23, the hydrostatic equilibrium equation 8.5 respectively and replacing t with the ideal gas law, we find

$$-\frac{g(z)\, m\, n(z)}{p(z)} = \frac{1}{n(z)}\frac{dn(z)}{dz} - \Gamma\frac{n(z)\, k_B}{p(z)}, \tag{8.17}$$

where m is the average atomic mass of the atmosphere. Above the homopause ($\sim 120\, km$), m is a function of altitude but we will consider it as approximatively constant.

Rearranging the terms to isolate p, we have

$$p(z) = n^2(z)\left(\frac{dn(z)}{dz}\right)^{-1}(\Gamma\, k_B - g(z)\, m). \tag{8.18}$$

If we bring out the k_B factor in the last term and remember the definition of the autoconvective lapse rate 2.31, we find that the pressure can be expressed as a function of the difference between the environmental lapse rate and the autoconvective lapse rate

$$p(z) = k_B\, n^2(z)\left(\frac{dn(z)}{dz}\right)^{-1}(\Gamma - \Gamma_a). \tag{8.19}$$

Replacing Γ as a ratio α of the DALR from equation 2.25 (with a value between -1 and 1), we finally write

$$p(z) = g(z)n^2(z)\left(\alpha\frac{k_B}{c_p} - m\right)\left(\frac{dn(z)}{dz}\right)^{-1} \tag{8.20}$$

The specific heat capacity at constant pressure c_p is related to the heat capacity at constant pressure C_p as $c_p = C_p/m$ and the heat capacity is related to the heat capacity ratio γ as $C_p = (\gamma/\gamma - 1)k_B$. For CO_2, the heat capacity ratio is usually reported as 1.3 for 293 K and 1013.25 hPa. That value is not a constant and decreases with temperature (and changes also with pressure but very slightly). So γ should also be a function of altitude but we will approximate it as a constant for the range of temperature spanned in the atmosphere of Mars ($\sim$ 150 to $\sim 250\, K$).

By using $n = n_{CO_2}/vmr_{CO_2}$

$$p(z) = g(z)n^2(z)m\left(\alpha\frac{\gamma - 1}{\gamma} - 1\right)\left(\frac{dn(z)}{dz}\right)^{-1} \tag{8.21}$$

This formula is used for altitudes above 150 km as this is the limit of the profiles provided by GEM-Mars. The temperature gradient in the thermosphere will be considered as small enough and we will take $\alpha = 0$. Another approximation is necessary for the gradient over the density $dn(z)/dz$. Most usually, that gradient is computed from the three-four highest values from the density profile retrieved (Snowden et al., 2013; Mahieux et al., 2015) but this has shown bad results as the highest values are those corresponding to the thinnest lines (and thus lowest information content). Instead, we use equation 2.22 to compute the derivative and 8.21 becomes

$$\begin{aligned} p(z) &= h(z)\, g(z)\, n(z)\, m \left(1 - \alpha \frac{\gamma - 1}{\gamma}\right) \\ &= n(z)\, k_B\, t(z) \left(1 - \alpha \frac{\gamma - 1}{\gamma}\right) \end{aligned} \tag{8.22}$$

and we find back the ideal gas law if we choose $\alpha = 0$.

The sensitivity of temperature profiles to the choice of this parameter is assessed by recomputing the temperature profiles with P_{top} varying by a factor up to 20%. We could notice that 10 km below z_{top} the profile variation due to that parameter is below the uncertainty level.

Another formula is

$$p(z) = n(z)\, k_B\, t(z) \left(1 + \frac{k_B}{m\, g(z)} \frac{dt}{dz}\right) \tag{8.23}$$

where the second term in the parenthesis slightly corrects the pressure taking into account the temperature gradient directly computed from the smoothed version of the GEM-Mars profile (Erwin et al., 2018).

Uncertainties on the initial pressure

The error on this initial pressure introduces is difficult to assess as it depends on the true temperature profile and lapse rate values.

$$\delta p_{top} = \sqrt{\left(\frac{p_{top}}{n} \delta n\right)^2 + \left(\frac{p_{top}}{t} \delta t\right)^2 + \left(n\, k_B\, t\, \frac{\gamma - 1}{\gamma} \delta \alpha\right)^2} \tag{8.24}$$

The variability on the temperature provided by GEM-Mars is around 20%, the uncertainty on the gravitational acceleration is neglected, the uncertainties on the density are around 1% (depending on the spectral lines intensity) and the uncertainty over α can be important depending on the region of the atmosphere. But still, α is expected to be close to 0 above 160 km.

We will consider an uncertainty of 20% and take $\delta p_{top} = 0.2\, p_{top}$.

8.2.5 Uncertainties on the temperature profile

The uncertainties on the temperature δt can be derived in two different ways:

- the Monte Carlo method: by computing the temperature profile for all many density profiles computed within the uncertainties and then taking the standard deviation,
- the first moment method: the covariances are forward propagated (see for example Taylor (1997)).

By Monte Carlo analysis

The propagation of the uncertainties δn over the density n to uncertainties δp over pressure p computed by 8.5 with a Monte Carlo analysis follows three steps:

1. A number nt of random density profiles are computed following a normal distribution with a mean n and a standard deviation δn.

2. Then, nt pressure profiles are computed using 8.5.
3. Finally, an uncertainty pressure profile δp is computed as the standard deviation over all the nt pressure profiles.

First, we need to know which number of profiles for δn gives a converged solution for the uncertainties over t. The improvement in the solution accuracy with the increase of the number of samples is slow with a relative error on the uncertainties around 10^{-3} for 2000 samples and 10^{-4} for 20000 samples (see figure 8.12).

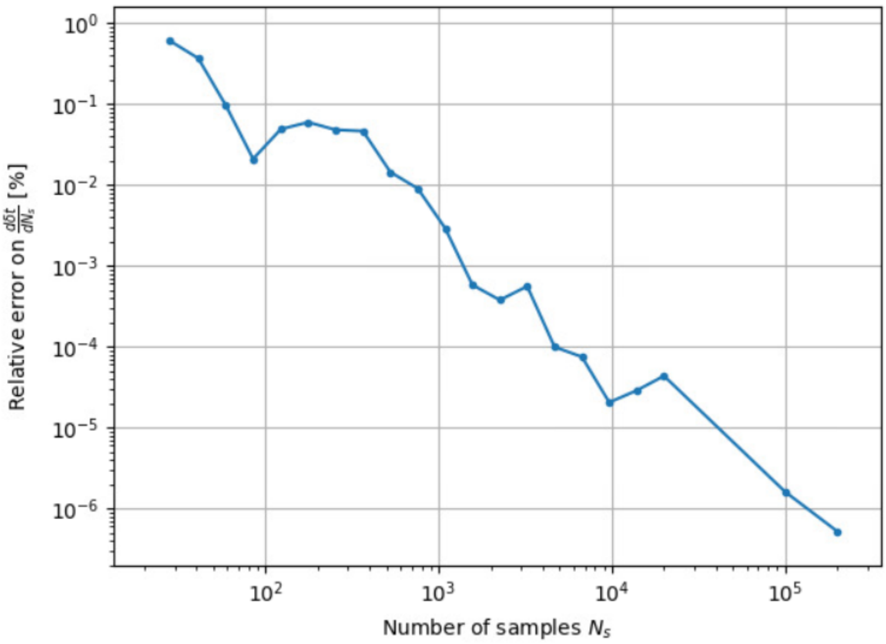

Figure 8.12: Convergence of the $\delta t/t$ values computed with the Monte Carlo method to the number of samples N_s.

By forward propagation of the covariances

To compute the uncertainties over the $\delta\Delta p_j(n_j, n_{j+1})$ elements with $j = 0, ..., N$, we consider only the uncertainties n_j and n_{j+1} which are not independent due to the regularisation (section 4.2). The covariance terms $\sigma_{n_j n_{j+1}}$ are provided by the covariance matrix computed with 4.27 and then compute

$$\delta\Delta p_j(n_j, n_{j+1}) \approx \sqrt{\left(\frac{\partial\Delta p_j}{\partial n_j}\right)^2 \delta n_j^2 + \left(\frac{\partial\Delta p_j}{\partial n_{j+1}}\right)^2 \delta n_{j+1}^2 + 2\frac{\partial\Delta p_j}{\partial n_j}\frac{\partial\Delta p_j}{\partial n}\sigma_{n_j n_{j+1}}}. \tag{8.25}$$

Or in matrix notation, we derive the covariance matrix as

$$\boldsymbol{S_{\Delta p}} = \boldsymbol{J_{\Delta p}}\,\boldsymbol{S_n}\,\boldsymbol{J_{\Delta p}^T}. \tag{8.26}$$

where $J_{\Delta p}$ is a bi-diagonal matrix containing the $\partial \Delta p_i / \partial n_i$ elements on the diagonal and the $\partial \Delta p_i / \partial n_{i+1}$ on the first diagonal above. The $S_{\Delta p}$ matrix is thus a tridiagonal matrix. The uncertainties over the Δp_i are the square roots of the diagonal elements in $S_{\Delta p}$.

From formula 8.9 and knowing that $E_2'(x) = -E_1(x)$, we derive the expression for the partial derivative to n_j

$$\begin{aligned}\frac{\partial \Delta p_j}{\partial n_j} =& \frac{\Delta p_j}{n_j} - \frac{\Delta p_j}{n_j} \frac{r_M + z_j}{(z_{j+1} - z_j)} \\ &+ \frac{m_a\, g_0\, r_M^2}{(z_{j+1} - z_j)} \exp\left(\frac{r_M + z_j}{h_j}\right) \left[E_1\left(\frac{r_M + z_j}{h_j}\right) - E_1\left(\frac{r_M + z_{j+1}}{h_j}\right)\right],\end{aligned} \tag{8.27}$$

and the partial derivative to n_{j+1}

$$\begin{aligned}\frac{\partial \Delta p_j}{\partial n_{j+1}} =& \frac{\Delta p_j}{n_{j+1}} \frac{r_M + z_j}{(z_{j+1} - z_j)} \\ &- \frac{n_j}{n_{j+1}} \frac{m_a\, g_0\, r_M^2}{(z_{j+1} - z_j)} \exp\left(\frac{r_M + z_j}{h_j}\right) \left[E_1\left(\frac{r_M + z_j}{h_j}\right) - E_1\left(\frac{r_M + z_{j+1}}{h_j}\right)\right].\end{aligned} \tag{8.28}$$

The two last terms in 8.27 represent 24% of $\partial \Delta p_j / \partial n_j$ and cannot be neglected in practice.

The uncertainties on the pressure profile depend on the uncertainty on p_{top} and the uncertainties on Δp_i. The variable p_{top} is independent of all Δp_i but the Δp_i are not independent of each other so we need to take into account their covariances

$$\delta p_i = \sqrt{\delta p_{top}^2 + \sum_{j=i}^{N} \delta \Delta p_j^2 + 2 \sum_{j=i}^{N} \sum_{k=i}^{N} \sigma_{\Delta p_j \Delta p_k}} \tag{8.29}$$

where the uncertainty δp_i correspond to the altitude z_i.

In matrix notation, we find the covariance matrix for the pressure retrieved

$$\boldsymbol{S_p} = \boldsymbol{K_p}\, \boldsymbol{S_{\Delta p}}\, \boldsymbol{K_p^T} \tag{8.30}$$

and the δp_i are the square roots of the diagonal elements of $\boldsymbol{S_p}$. Due to the $\boldsymbol{K_p}$ matrix, $\boldsymbol{S_p}$ is a full matrix.

To understand how the uncertainty ratio evolves from $\delta n/n$ to $\delta t/t$, let's consider $\delta p_{top} = 0$, a constant ratio $\delta n/n$ and we also neglect the last two terms in 8.27 and 8.28. Those terms almost compensate each other in the computation of δp provided that $\delta n_i \approx \delta n_{i+1}$, which is fine for small steps in altitudes ($z_{i+1} - z_i << h_i$). By first propagating the uncertainties from $\delta n/n$ to $\delta \Delta p_j / \Delta p_j$, we find

$$\frac{\delta \Delta p_j}{\Delta p_j} \approx \frac{1}{\Delta p_j} \frac{\Delta p_j}{n_j} \delta n_j = \frac{\delta n_j}{n_j}. \tag{8.31}$$

and the uncertainty ratio did not change when passing from density to increments of pressure. Continuing for $\delta p/p$ using 8.30,

$$\frac{\delta p_j}{p_j} = \frac{\sqrt{\sum_{i=j}^{N} \delta \Delta p_i^2}}{\sum_{i=j}^{N} \Delta p_i} = \frac{\sqrt{\sum_{i=j}^{N} \left(\frac{\Delta p_i\, \delta n_i}{n_i}\right)^2}}{\sum_{i=j}^{N} \Delta p_i} = \frac{\delta n_j}{n_j} \sqrt{\frac{\sum_{i=j}^{N} (\Delta p_i)^2}{\left(\sum_{i=j}^{N} \Delta p_i\right)^2}} \tag{8.32}$$

and the ratio $\delta p_j / p_j$ is smaller than the ratio $\delta n_j / n_j$ as $\sum_{i=j}^{N} (\Delta p_i)^2 \leq \left(\sum_{i=j}^{N} \Delta p_i \right)^2$ as the pressure is computed as a sum of the Δp_j.

Finally, we derive in a similar manner the ratio $\delta t / t$ where the t is computed from the n and p, the latter being computed from n. It is easier to derive the temperature formula directly from the density. We then construct a vector Δt containing the differences in temperature

$$\Delta t_i = \frac{\Delta p_i}{k_B \, n_i} \tag{8.33}$$

and the associated covariance matrix is

$$\boldsymbol{S_{\Delta t}} \; = \; \boldsymbol{J_{\Delta t}} \, \boldsymbol{S_n} \, \boldsymbol{J_{\Delta t}^T} \tag{8.34}$$

where $\boldsymbol{J_{\Delta p}}$ is again a bi-diagonal matrix containing the partial derivatives $\partial \Delta t_i / \partial n_i$ elements on the diagonal and the $\partial \Delta t_i / \partial n_{i+1}$ on the first diagonal above. The partial derivative to n_j is

$$\frac{\partial \Delta t_j}{\partial n_j} = \frac{1}{k_B \, n_j} \left(\frac{\partial \Delta p_j}{\partial \, n_j} - \frac{\Delta p_j}{n_j} \right) \tag{8.35}$$

and the partial derivative with respect to n_{j+1} is

$$\frac{\partial \Delta t_j}{\partial n_{j+1}} = \frac{1}{k_B \, n_j} \left(\frac{\partial \Delta p_j}{\partial \, n_j} \right) \tag{8.36}$$

As for the pressure profile, we have a matrix formulation

$$\boldsymbol{t} = \boldsymbol{K_p} \, \boldsymbol{\Delta t}, \tag{8.37}$$

and the covariance matrix associated with the temperature profile

$$\boldsymbol{S_t} \; = \; \boldsymbol{K_p} \, \boldsymbol{S_{\Delta t}} \, \boldsymbol{K_p^T}. \tag{8.38}$$

Roughly, the relative uncertainties over the temperature are close to the relative uncertainties over the pressure as

$$\begin{aligned} \delta t_i &= \sqrt{\left(\frac{\partial t}{\partial p} \right)^2 \delta p_i^2 + \left(\frac{\partial t}{\partial n_i} \right)^2 \delta n_i^2} = \sqrt{\frac{\delta p_i^2}{k_B^2 \, n_i^2} + \frac{\delta n_i^2}{k_B^2 \, n^4}} \\ &\approx \frac{\delta p_i}{k_B \, n} = \frac{t_i}{p_i} \delta p_i. \end{aligned} \tag{8.39}$$

In practice, the Monte Carlo method with 20000 samples and the covariance method retrieve uncertainties that are different by 0.08%. This value is fairly acceptable and the covariance method will be used in the following as the Monte Carlo analysis is much more time-consuming as we need to compute 20000 operations while the moment method takes only a few operations.

8.3 Iteration over the retrieved temperature profile

As seen in section 3.1.2, the CO_2 spectral lines intensities are sensitive to temperature. Thus, we need a first guess of temperature as close as possible to the correct one for the fitting of the CO_2 lines. This first guess is provided by simulations from GEM-Mars for the location and time of the tangent points of the solar occultation. As we are using simulation and not the direct temperature of the atmosphere at the tangent points, the fit of the lines can be improved by iterating the retrievals over the temperature.

In practice, for the diffraction orders treated in this work, there is not a lot of improvement of the fit with the loop over the temperature and one loop over the temperature is sufficient for convergence. An example is provided in Figures 8.13 for fits of spectra and 8.14 for retrieved profiles. The first profile (blue) is already very close to the ones of the next iterations. The profiles for iterations 1 to 3 are almost similar. Another example is provided in Figure 8.15 where again the second retrieved temperature is already very close to the fifth one.

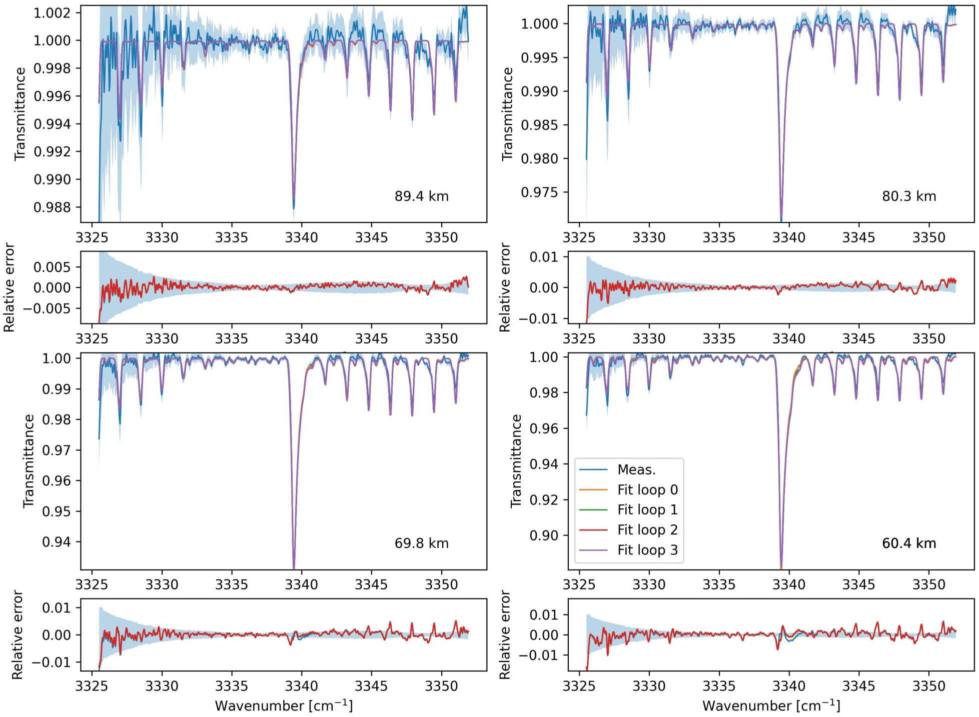

Figure 8.13: Fit of the profiles along three loops over the temperature. The blue spectrum is the measured one. The other spectra are the fits and the iteration number is given in the lower right panel. The sub-panels contain the residuals. Those spectra are from the occultation 20200824_020917_1p0a_SO_A_I_148.

The convergence criteria of this iteration are simply that the last temperature profile t_i must be within the uncertainties of the previous one.

$$(\boldsymbol{t_i} - \boldsymbol{t_{i-1}})^T S_i^{-1} (\boldsymbol{t_i} - \boldsymbol{t_{i-1}}) < n. \tag{8.40}$$

where $\boldsymbol{t_{i-1}}$ and $\boldsymbol{t_i}$ are the penultimate and last temperature profiles, S_i is the covariance matrix over $\boldsymbol{t_i}$, and n is the number of values in the temperature profile.

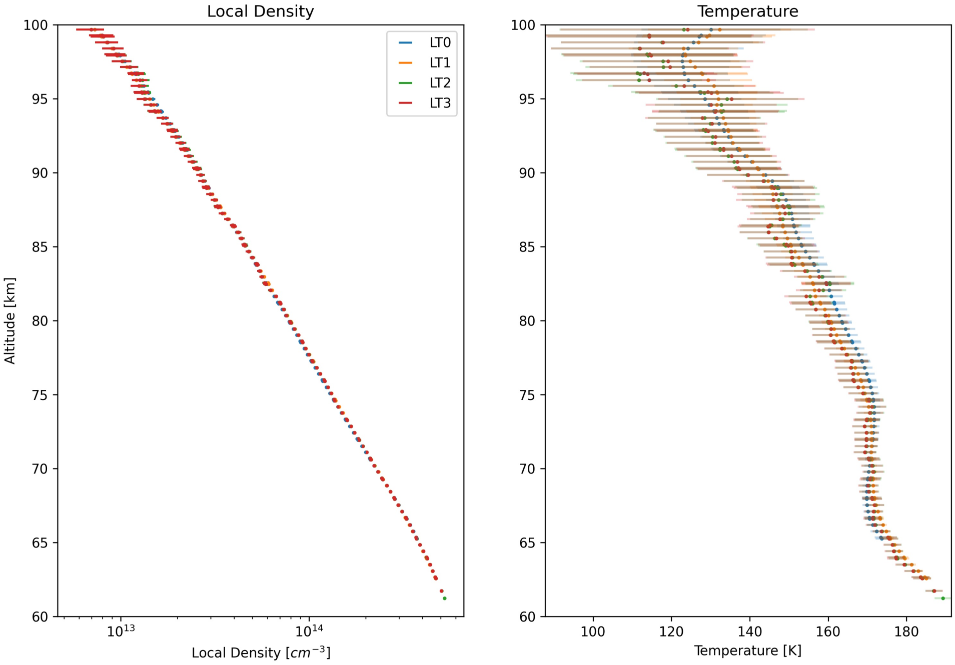

Figure 8.14: Profiles of density in the left panel and temperature in the right panel for occultation 20200824_020917_1p0a_SO_A_I_148 and for three loops over the temperature.

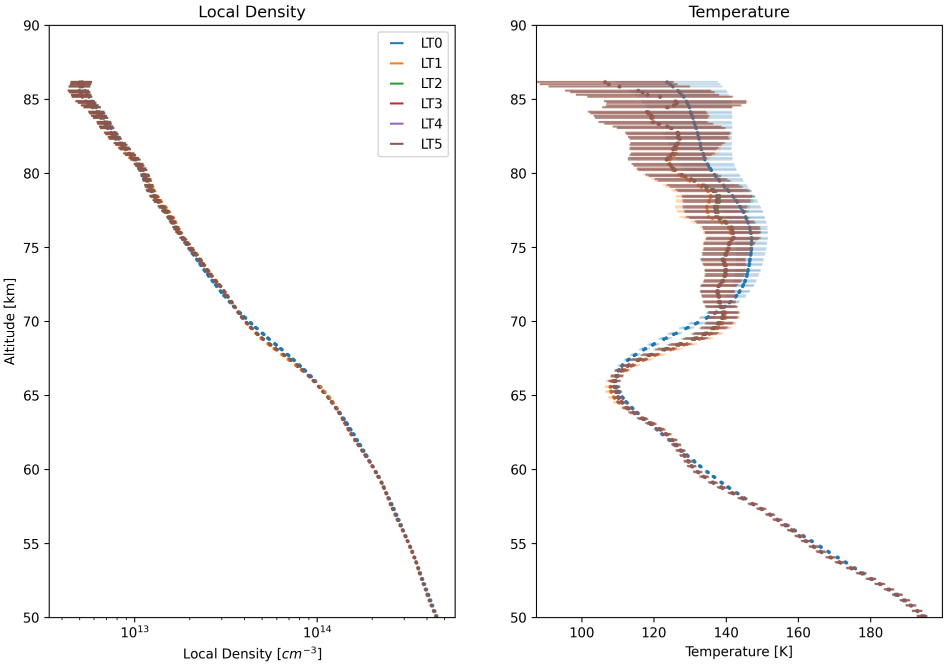

Figure 8.15: Profiles of density in the left panel and temperature in the right panel for occultation 20191216_222753_1p0a_SO_A_I_148 and for five loops over the temperature.

The algorithm described in this part is fast and robust. It takes usually 10 minutes to perform one loop over the temperature, meaning that four (the number of bins) times 100 spectra are inverted to CO_2 density and temperature profiles within that time. The inversion of each spectrum is independent and done in parallel on ten threads.

8.4 Uncertainties on the profiles

The computation of the uncertainties over NOMAD-SO transmittance spectra was described in section 6.2.1. The uncertainties on the slant column and the density profiles are provided in section 4.1.3 and equation 4.27 respectively while the uncertainties on the pressure and temperature profiles are computed from a Monte Carlo analysis (see section 8.2.5). Figure 8.16 present the relative error of the slant column (panel a), density (panel b), and temperature (panel c). The relative uncertainties over the transmittance spectra are of the order of 0.1% while the uncertainties on the slant column, local density, and temperature profiles are of the order of 1% with slightly increasing relative errors along the retrieved products. The increase of the relative error on the temperature profiles is due to the error on p_{top} which affects the highest altitudes. On average for the profiles from diffraction order 148, the uncertainties are $5.0 \pm 1.7\,K$ but with $10.2 \pm 3.6\,K$ at top of profile ($2 \times 10^{-2}\,Pa$) and $2.1 \pm 0.8\,K$ at bottom of profile ($4 \times 10^{-1}\,Pa$).

8.5 Vertical resolution

The vertical resolution of a profile depends on the field of view (FOV), the vertical sampling, and the regularisation applied. Figure 8.17 shows those three parameters for the occultations with diffraction order 148 in MY 35.

The vertical sampling of the NOMAD-SO spectra has an averaged value of $250\,m$ and varies between 0.1 and $1.0\,km$. This variation depends on the β-angle as there is an apparent higher vertical sampling for occultations where the LoS spans broader latitude-longitude ranges.

The FOV has an averaged value of $1.8\,km$ and it changes by a maximum of $100\,m$ as the orbit of TGO is quasi-circular. The displacement of the FOV along the measurement of a spectrum was taken into account. The FOV values have a clear dependence on a latitude which is in fact dependent on the orbit of TGO.

The regularisation depends on the noise and the vertical sampling and has already been discussed in section 4.2.6. The vertical resolution has an averaged value of $1.6\,km$[5] and varies between 1.2 and $3.0\,km$. The most important constraint on the vertical resolution is the broad FOV which is much higher than the vertical sampling.

We only consider the averaging kernels from the vertical inversion and neglect the regularisation from the spectral inversion as we kept only slant columns with a DOF higher than 0.99. The corresponding averaging kernels matrix of the spectral inversion is close to the identity matrix.

8.6 Combination of the pressure and temperature profiles with GEM-Mars simulated data

A goal of temperature profile retrievals is to provide those profiles for the density retrieval of other species such as carbon monoxide and water which also have line intensities sensitive to temperature. Those other species are retrieved in the troposphere and the mesosphere and the

---

[5] Caution is needed as sometimes the resolution is misinterpreted as the full-width at half maximum of the averaging kernels.

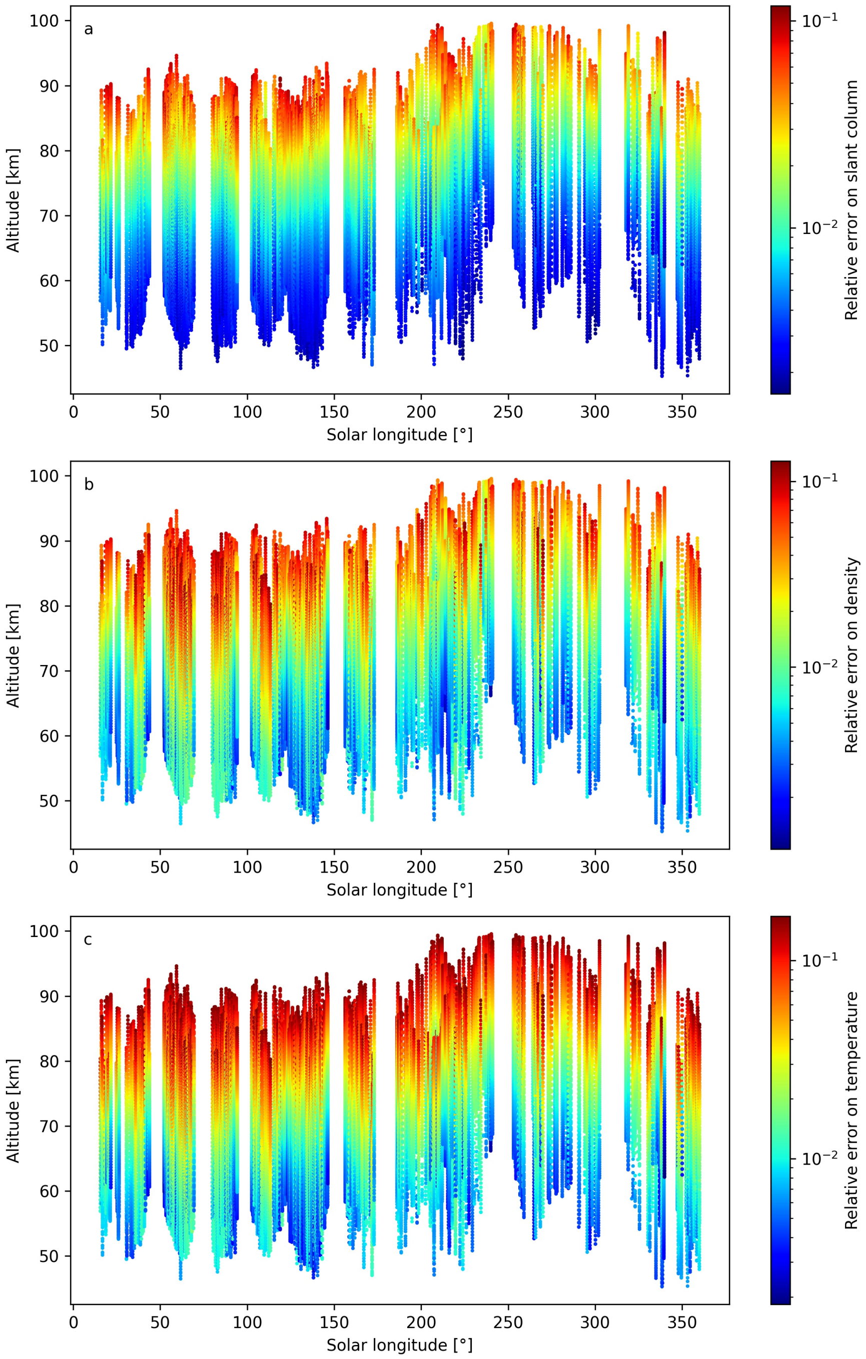

Figure 8.16: Relative error on the profiles for diffraction order 148 and MY 35. Profiles of slant column, density, and temperature in panels a, b, and c respectively.

a) FOV

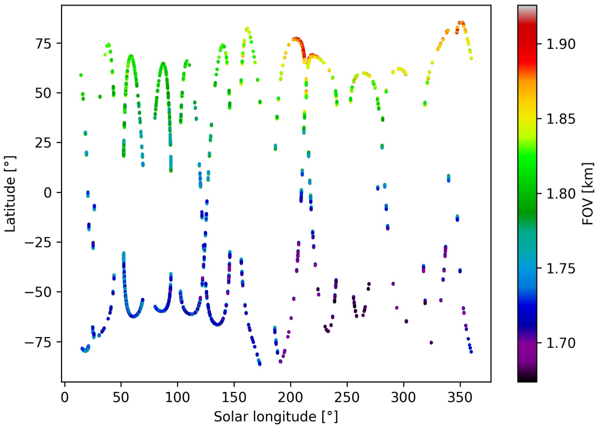

b) Vertical sampling

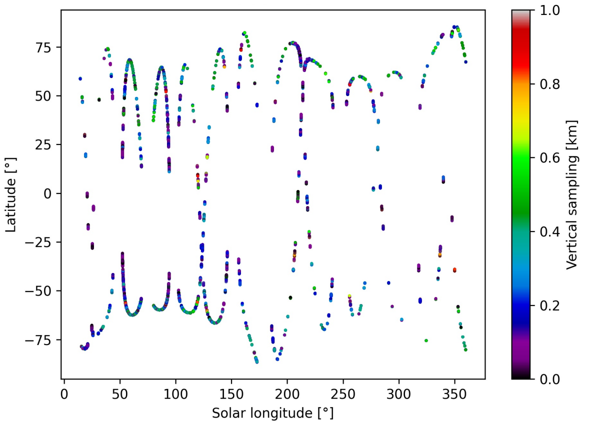

c) Vertical resolution

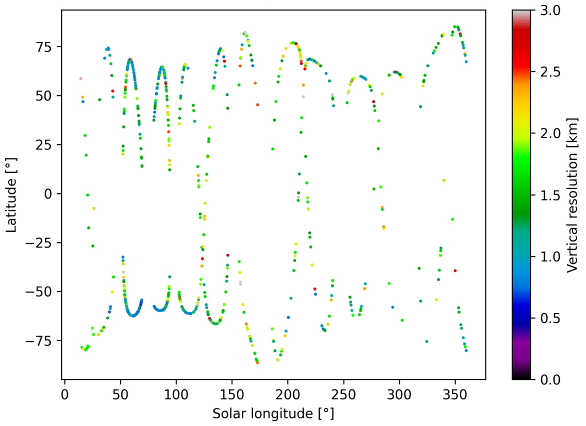

Figure 8.17: Field of view (FOV), vertical sampling, and resolution for occultations where diffraction order 148 was scanned in MY 35.

corresponding altitudes are covered by diffraction orders 132 and 148 (see section 5.3). When combining the profiles from different diffraction orders scanned during the same occultation, there can be a gap in altitude in-between them. A smooth combination of those profiles is implemented in an inverse problem background with the formula (Calisesi et al., 2005; Ceccherini, 2012)

$$\hat{\boldsymbol{x}} = \boldsymbol{x_a} + \boldsymbol{A}\left(\boldsymbol{x} - \boldsymbol{x_a}\right) \tag{8.41}$$

where, here, $\hat{\boldsymbol{x}}$ is the smoothed profile, $\boldsymbol{x_a}$ the profile from GEM-Mars, $\boldsymbol{x}$ the retrieved profile, and $\boldsymbol{A}$ is a matrix build with triangular functions

$$A_{ij} = \begin{cases} 0_{ij} & \text{if } z_i > z_{top} \text{ or } z_i < z_{bot} \\ \delta_{ij} & \text{if } z_{bot} + h < z_i < z_{top} - h \\ max\left(0, \frac{1}{a_i}\left(1 - \left|\frac{z_j - z_i}{a_i}\right|\right)\right) & \text{if } z_{bot} < z_i < z_{bot} + h \\ max\left(0, \frac{1}{b_i}\left(1 - \left|\frac{z_j - z_i}{b_i}\right|\right)\right) & \text{if } z_{top} - h < z_i < z_{top} \end{cases} \tag{8.42}$$

where z_i is the altitude corresponding to x_i, $a_i = z_i - z_{bot}$, $b_i = z_{top} - z_i$, and h is a constant controlling the smoothness of the combination of the profiles. By try-error, the best value was found as 10 km. Figure 8.18 shows three examples of a combination of vertical profiles of temperature. The combined profile (green) and the initial SO profile (blue) are almost similar.

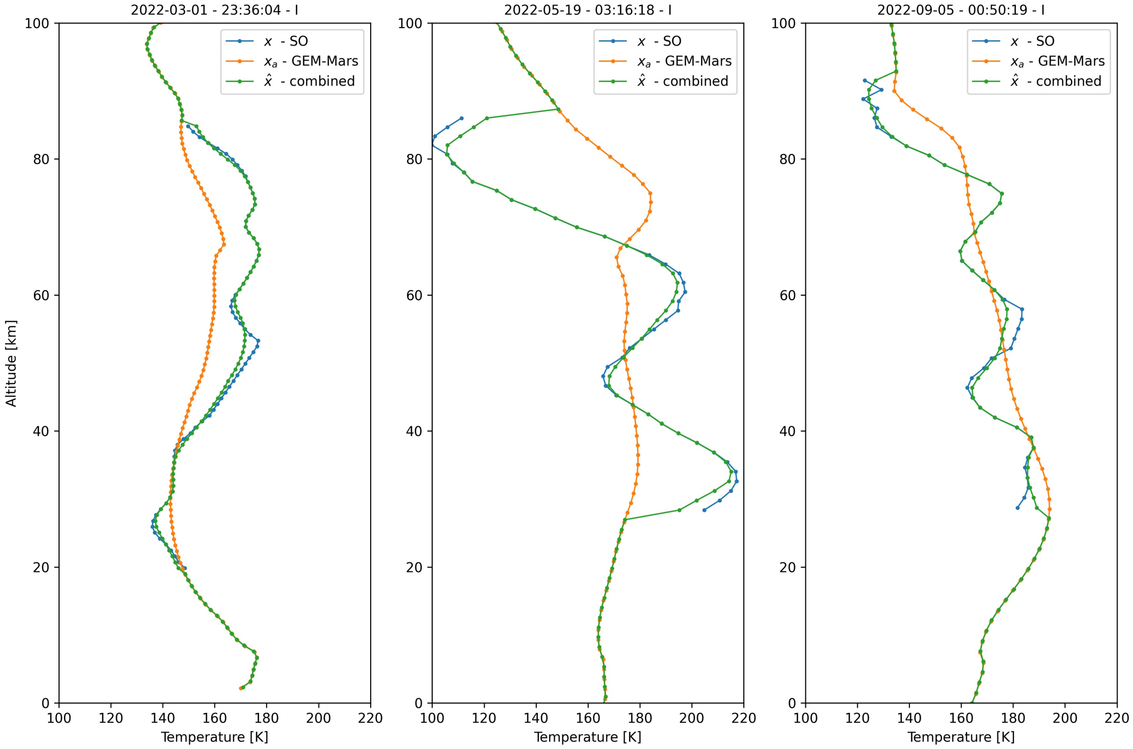

Figure 8.18: Three examples of vertical profiles of temperature. Orange profile for the simulation from GEM-Mars, the blue curve for a combination of profiles from diffraction order 132 and 148, and the green curve for the combination with GEM-Mars.

The pressure profile can also be provided by dividing the retrieved CO_2 partial pressure by the CO_2 VMR provided by GEM-Mars. Its importance in the computation of the radiative transfer happens in the collisional broadening of the line shape. Instead of the formula 8.41, the pressure profile is combined with the formula

$$\hat{x}_i = \exp\left(ln(x_{ai}) + \sum_j A_{ij} ln\left(\frac{x_j}{x_{aj}}\right)\right). \tag{8.43}$$

The creation of those files is automatically launched each day. A cron scheduler runs the retrievals of diffraction orders 132 and 148 and creates those atmosphere files. Those profiles can then be used the same day as when the level 1.0a files (transmittance calibrated) are produced.

8.7 summary

This chapter described the retrieval algorithm to derive carbon dioxide density, pressure, and temperature from the transmittance spectra of the SO channel. This algorithm is divided into three main steps: 1) a spectral inversion to derive a slant column from a transmittance spectrum, 2) a vertical inversion to derive the carbon dioxide local density at the terminator from the slant column, and 3) the use of the hydrostatic equilibrium equation and the ideal gas law to derive the carbon dioxide partial pressure and the temperature profiles from the local density profile. The first step is performed with the ASIMUT radiative transfer code and no regularisation is applied at this point. The regularisation is applied in the second step with an iterated-Tikhonov regularisation. Several methods developed to find the best regularisation were compared with a synthetic test and the best one is the Expected Error Estimation. This fine-tuning requires the computation of many local density profiles and then selecting the one that minimises the total error. For the derivation of the pressure and temperature profiles, several formulae are compared with a synthetic test. The analytical and numerical computation of the hydrostatic equilibrium equation provides the best results. An extended analysis of the error was provided. This includes the errors due to the pressure guess at the top of the profile, the discretisation, and the assumption of a constant scale height in between the grid-step. We have also seen that if we consider an error on the first pressure guess, only the downward method prevents a rapid increase in the errors. The retrieved pressure and temperature profiles are then fed back to the first step as the line shape and intensity are a function of those parameters and it usually takes less than three iterations until the profiles converge. The last section explained the merging of profiles from different diffraction orders with the GEM-Mars profile.

Chapter 9

Comparisons

Before describing the variabilities in the retrieved dataset, this section shows some comparisons to highlight possible biases of the retrieved profiles. Those comparisons are an important step for the validation of the profiles.

We compare simulations from the GEM-Mars GCM but also to datasets available online from other instruments.

9.1 Comparison to simulations from the GEM-Mars general circulation model

The GEM-Mars general circulation model (GCM) simulates densities of various species as well as temperature on a three-dimensional mesh of 4° by 4° (horizontal grid of 45 by 90 points) and 103 vertical levels from the surface to around 150 km. The time step is $1/48^{\text{th}}$ of a sol (30.8246 minutes). Details on the GEM-Mars GCM can be found in Daerden et al. (2019) and Neary et al. (2020). The GEM-Mars data shown in this section was derived with the model version a731 and GEM-Mars data were provided up to November, 30^{th} 2021 (MY 36 L_S 135°).

It is important to remind that the SO profiles retrieved in this work do not contain any information from the *a priori* (which is a GEM-Mars profile averaged for all seasons, latitudes, longitudes, and local solar times) as only retrieved values with a DOF higher than 0.99 are kept.

The comparison to GEM-Mars is shown in Figures 9.1 and 9.2 for averaged profiles in seasons and latitudes for, respectively, dawn and dusk profiles in MY 35. The same datasets were presented in (Trompet et al., 2023a) but the profiles there are still those before the reprocessing of the altitude grid of late 2021. Over all, the agreement between the two datasets is fairly good with averaged absolute differences of 15.8 K and 11.4 K for, respectively, dawn and dusk. The SO profiles in Figure 9.1 (Dawn) in L_S 0°-120° all show a distinct pattern as a cold layer below 0.1 Pa, even more evident in the Southern hemisphere. The profiles in L_S 120°-240° are in good agreement and the profiles in L_S 240°-360° show some warm layer around 0.02 Pa in panels 11 and 12 with, appearing still stronger for SO. The dusk profiles show similar trends except that no warm layer is seen in L_S 240°-360° and the cold layers in L_S 0°-60° for the SO profiles have higher amplitudes.

All the individual profiles are presented as well in Figures 9.3 and 9.4 but for MY 35 and 36.

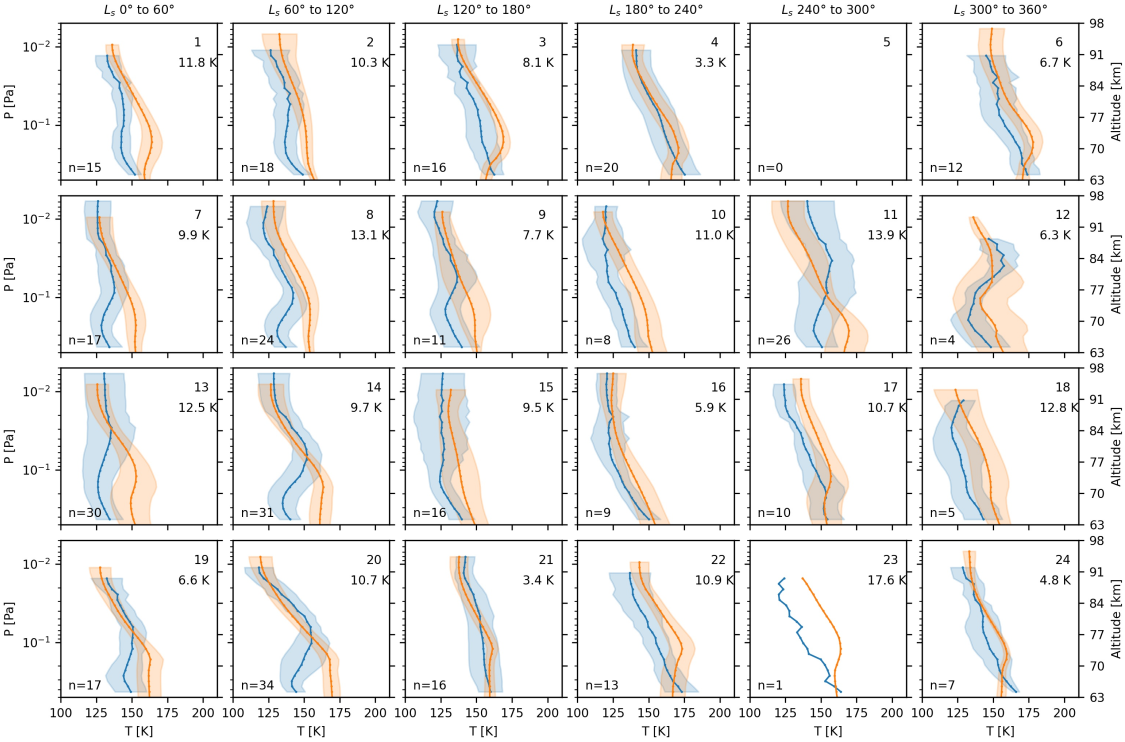

Figure 9.1: Averaged profiles of GEM-Mars in orange and NOMAD-SO in blue for Martian year 35 and only dawns (0 hr < LST <12 hr). The shaded areas indicate the 1-sigma variability in the L_S-lat bins. The number below the panel number is the weighted absolute difference between the GEM-Mars and NOMAD-SO profiles. Approximated altitudes are provided as the second Y-axis.

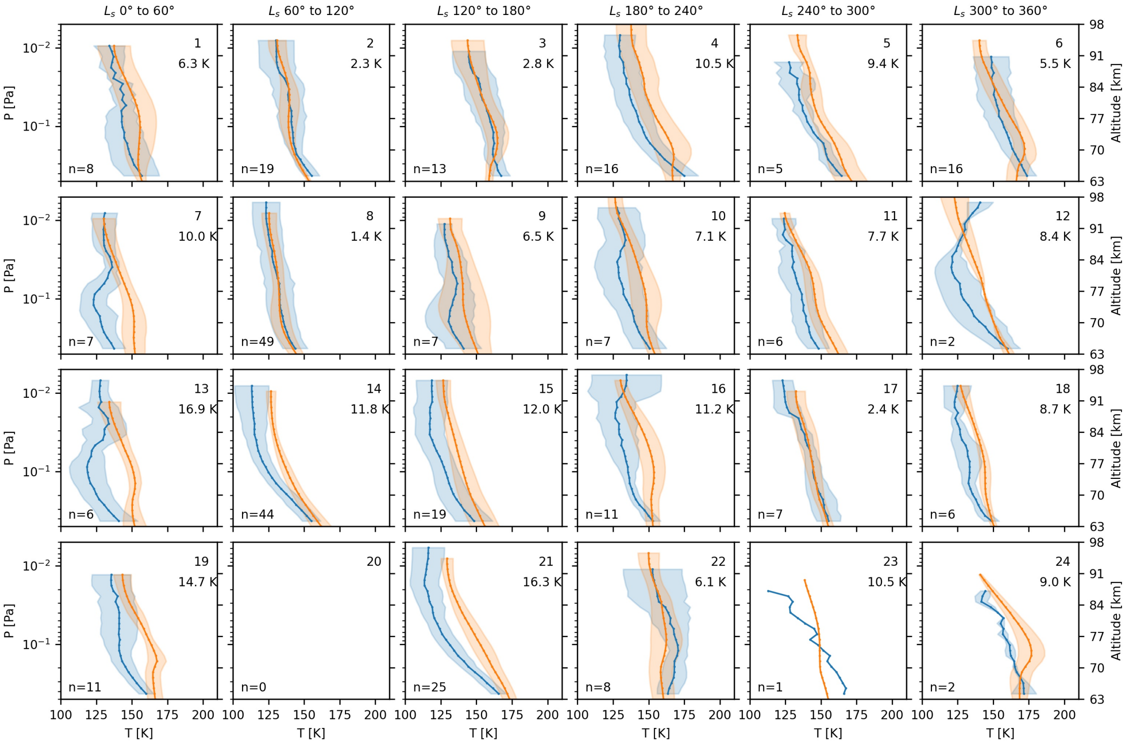

Figure 9.2: Averaged profiles of GEM-Mars in orange and NOMAD-SO in blue for Martian year 35 and only dusks (12 hr < LST < 24 hr). The shaded areas indicate the 1-sigma variability in the L_S-lat bins. The number below the panel number is the weighted absolute difference between the GEM-Mars and NOMAD-SO profiles. Approximated altitudes are provided as the second Y-axis.

The weighted average difference (SO - GEM-Mars) over the two Martian years is -5.1 K. This value is similar to the average uncertainties on the SO profiles. This value seems relatively small with respect to the differences seen in the figures. It is due compensation of the positive and negative biases. A better value to represent the disparities between the dataset is the weighted absolute difference which is 12.1 K.

The higher temperature values in SO profiles at pressures above 0.3 Pa and around L_S 200° is some reminiscent effect due to saturation of the CO_2 lines. For both dawn and dusk, in the Southern hemisphere and around L_S 40° to 120°, we see some warmer temperatures in SO profiles above 0.1 Pa and colder temperatures in SO profiles below 0.1 Pa, both in MY 35 and 36. Between L_S 120° to 240°, two dataset shows a good agreement with the same recurrences of temperature variations. The most important bias seen in this dataset is the warmer layers in SO between L_S 250° to 280° at both dawn and dusk, and at pressures below 0.1 Pa. The two datasets between L_S 280° to 360° in MY 35 shows a good agreement as well but with some higher SO temperature at pressures below 0.1 Pa in the Northern mid-latitudes.

The differences around aphelion in the Southern hemisphere might be explained by thermal tides being out of phase (F. Daerden, private communication). More details are provided in Trompet et al. (2023b).

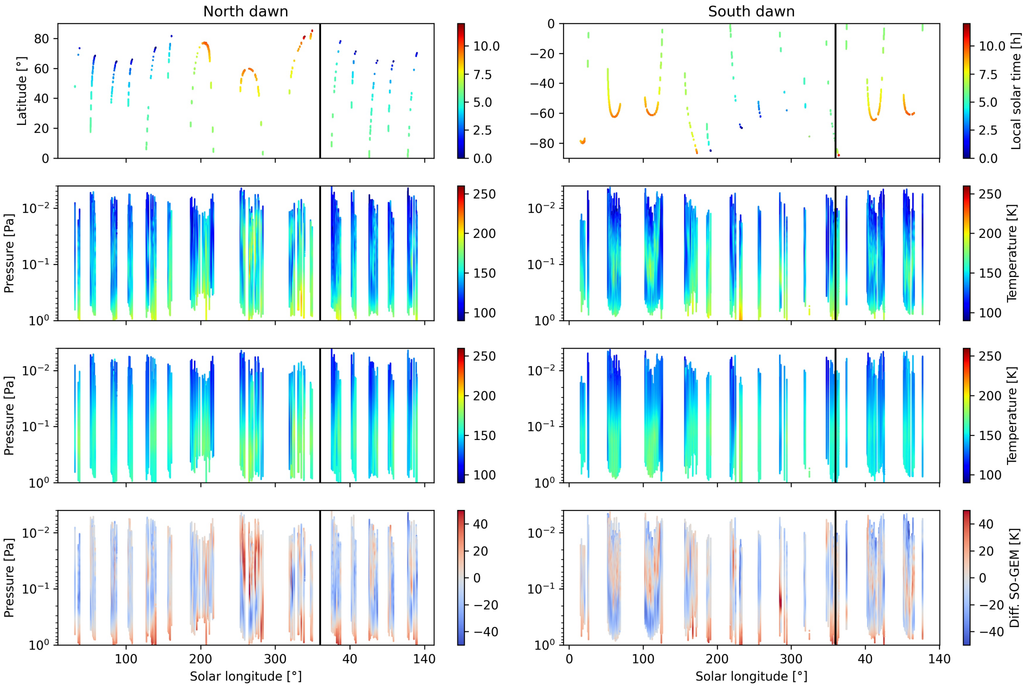

Figure 9.3: Maps of profiles from SO (second line), GEM-Mars (third line), and their difference (fourth line - SO-GEM) at dawn. The first line provides the coverage of the profiles. The left panels are for the Northern hemisphere and the right panels are for the Southern hemisphere. The black vertical line separates MY 35 and 36.

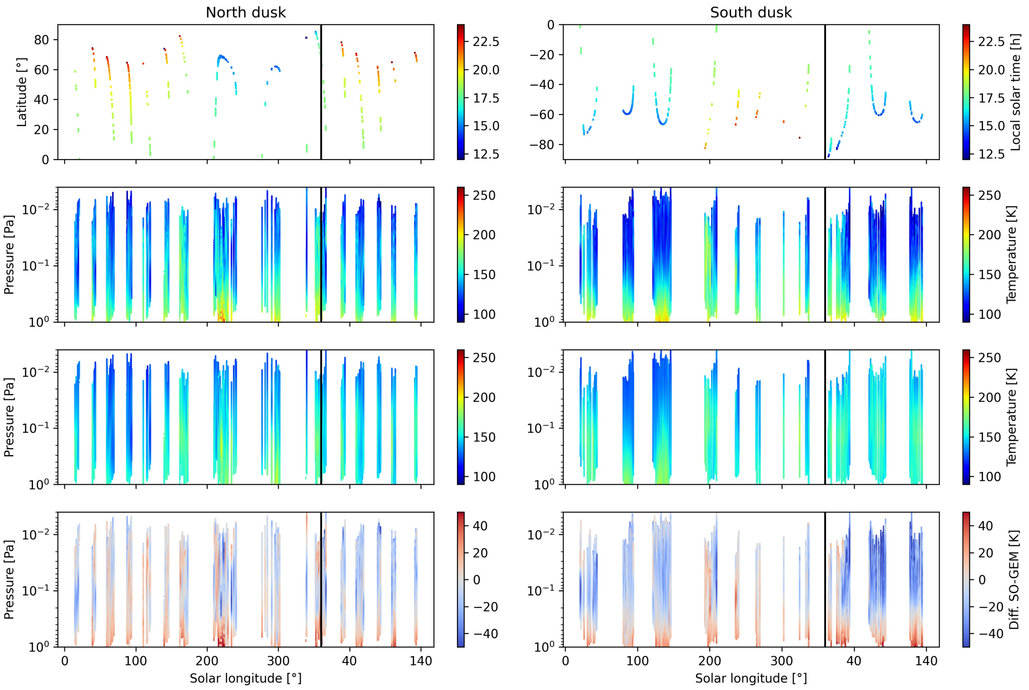

Figure 9.4: Maps of profiles from SO (second line), GEM-Mars (third line), and their difference (fourth line - SO-GEM) at dusk. The first line provides the coverage of the profiles. The left panels are for the Northern hemisphere and the right panels are for the Southern hemisphere. The black vertical line separates MY 35 and 36.

9.2 Comparison to other instruments sounding the atmosphere of Mars

9.2.1 Comparison to MRO-MCS

The Mars Climate Sounder (MCS) is a spectrometer measuring the thermal emission in limb, nadir, and off-nadir McCleese et al. (2007). MCS is one of the instruments onboard the Mars Reconnaissance Orbiter (MRO) which is on a Sun-synchronous polar orbit and crosses the equator at local times of 3 h and 15 h (Zurek and Smrekar, 2007). Those local times are scanned by SO when its LoS reaches high latitudes around 70° (see Figure 10.1 panel b).

The MCS team provides profiles of temperature, dust, and water vapour from the surface to 90 km altitude Kleinböhl et al. (2009). Their vertical resolution corresponds to a FWHM of 5 to 6 km and the average uncertainty is 0.5 K at low altitudes and up to 3 K above 65 km Kleinböhl et al. (2009, p. 13).

The comparison of SO temperature profiles against those of MCS is interesting as the latter have already been compared against those of the Thermal Emission Spectrometer (TES) and Radio Science onboard Mars Global Surveyor (MGS). Their average difference was lower than 2 K (Shirley et al., 2015). MCS temperature profiles of Mars atmosphere can be considered as the most reliable ones nowadays.

The retrieved SO profiles for diffraction order 148 are compared to MCS ones using a co-location criterion similar to the one proposed in Guerlet et al. (2022): the maximum difference must be 0.5° in solar longitude, 0.5 h in local solar time, 3° in latitude, and 6° in longitude. There are often several MCS profiles matching with an SO one and we select the closest MCS profile as the one which minimizes the weighted Eulerian distance over the differences in solar longitude, local solar time, latitude, and longitude. For each parameter, the weight is the inverse of the maximum difference, thus 2, 2, 1/3, 1/6.

The compared time range extended from the beginning of the TGO science operation till October 2022 (MY 36 L_S 330°). A total of 117 co-located profiles were found within that time range. Forty-seven of them (until only November 2021 and before reprocessing of the dataset with the SPICE kernel issue) are shown in Figure 2 in Trompet et al. (2023a). As explained above, due to the coverage of NOMAD-SO, all profiles except one occurred at a latitude above 45°. The limits in altitude of this comparison are due, at the top ($\sim 90\,km$), to the MCS profiles and, at the bottom ($\sim 50\,km$), to the saturation of the CO_2 lines in NOMAD-SO spectra.

To reduce the biases due to the difference in vertical resolution, the SO profiles have been smoothed with the same method as the one described in Guerlet et al. (2022). The equation 8.41 is used where the averaging kernel matrix $\boldsymbol{A}$ is built with normalized Gaussian functions and with a full-width at half-maximum of 5 km. The *a priori* profile is the MCS profile. The choice of the *a priori* has very limited importance to the edges of the profile. The uncertainties on the smoothed profile are the square roots of the diagonal elements of the matrix $\boldsymbol{(1-A)U_a(1-A)^T + AUA^T}$ where $\boldsymbol{U_a}$ and $\boldsymbol{U}$ are, respectively, the covariance matrix over the SO and MCS profile. The average uncertainties on the smoothed SO profiles and the MCS profiles are respectively 5.1 K and 6.4 K.

Figures 9.5 and 9.6 show all the 117 profiles. Many values are within the uncertainties (1-σ) of each other dataset and they show very similar curvatures with sometimes different amplitudes, as for instance in panel 33 of Figure 9.5 around 55 km. Starting in the end of MY 36 L_S 224° (panel 18 in Figure 9.6), we see some higher differences but still with similar curvatures.

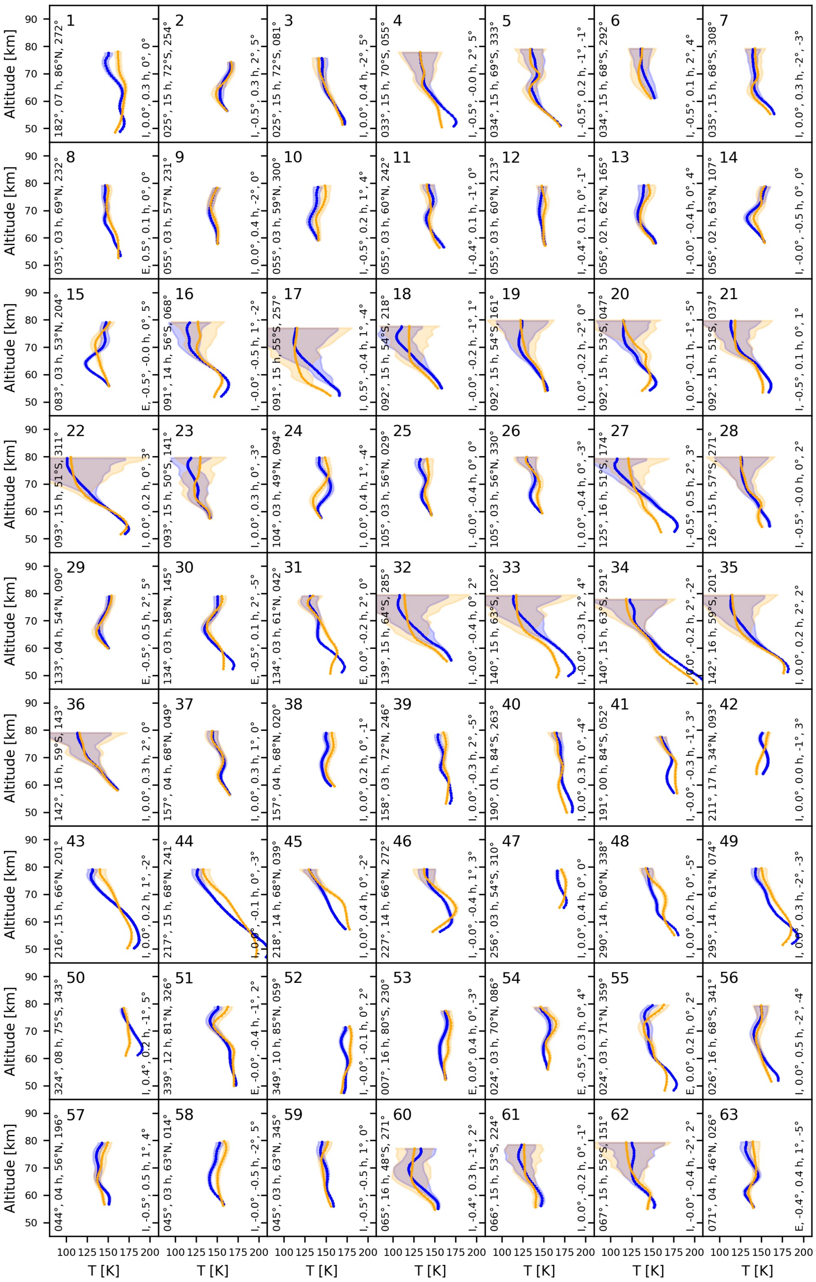

Figure 9.5: The 65 first co-located profiles of temperature from MCS (in orange) and NOMAD-SO (in blue). On the left of each panel are provided the solar longitude, local solar time, latitude and longitude of the NOMAD-SO profile and on the right are provided the ingress (I) or egress (E) case and the differences then the differences in solar longitude, local time, latitude, and longitude of the NOMAD-SO profile to the MCS.

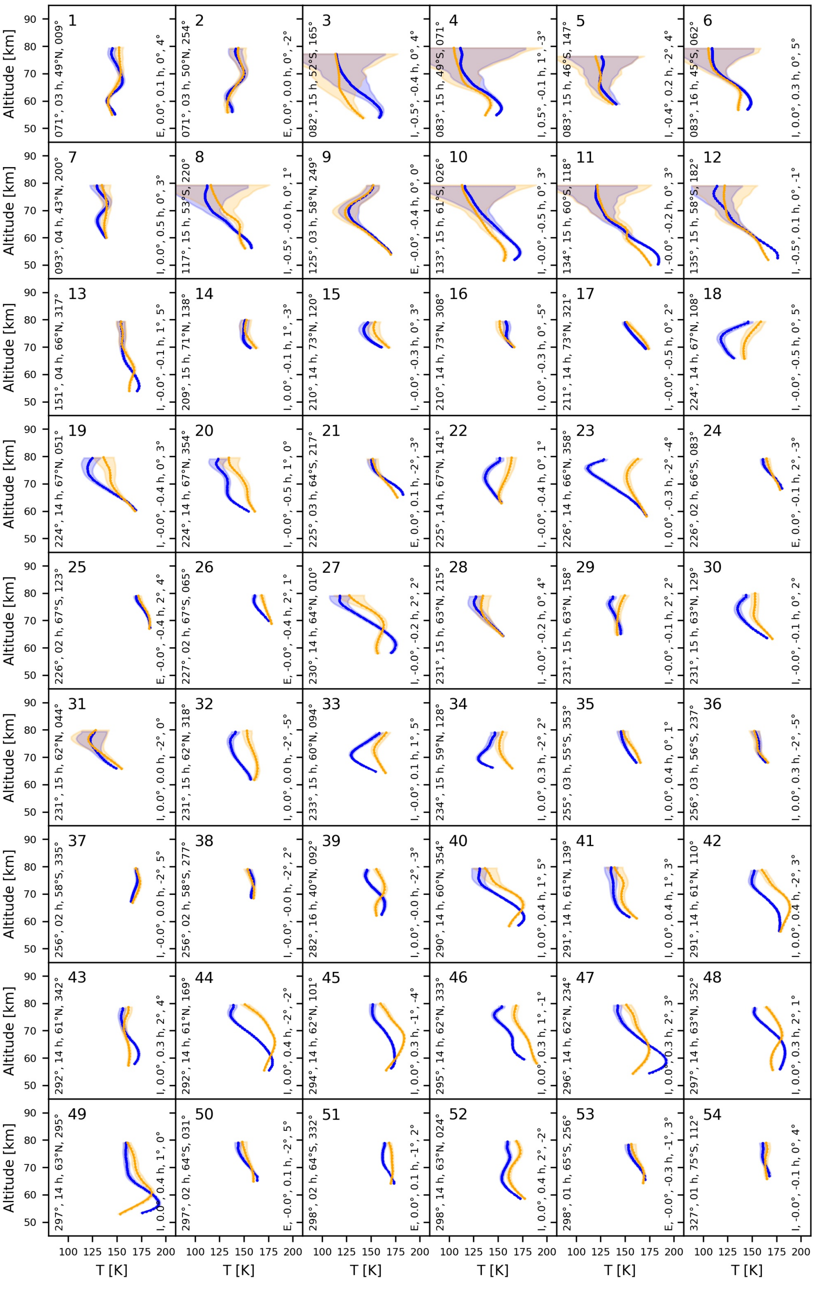

Figure 9.6: The 52 last co-located profiles of temperature from MCS (in orange) and NOMAD-SO (in blue). On the left of each panel are provided the solar longitude, local solar time, latitude and longitude of the NOMAD-SO profile and on the right are provided the ingress (I) or egress (E) case and the differences then the differences in solar longitude, local time, latitude, and longitude of the NOMAD-SO profile to the MCS.

The weighted average difference between the 117 sets of profiles is 0.1 K but the weighted average absolute difference is 8.5 K. The first value represents an overall good match between the two datasets. The second value represents some remaining disparities within the profiles. They show the same variations along altitudes but the SO profiles still show some stronger variabilities than the MCS ones. This can be due to a still better vertical resolution in SO profiles as they were smoothed considering the average MCS vertical resolution of 5 km while the true vertical resolution at those high altitudes might be worse. Another reason for the discrepancy might be the difference in airmass scanned as the LoS of both instruments crosses each other close to the tangent point but are not parallel. A last possibility might be the natural variability of the temperature profiles which is more important in the mesosphere then the troposphere where strong thermal tides and gravity waves are known to occur.

Figure 9.7 shows the average difference on the profiles (NOMAD-SO - MCS) in green. The difference is within the 1-σ standard deviation variabilities of both datasets (blue for SO and orange for MCS). The SO profiles have on average higher values around 60 km which is explained by a reminiscence of some effects from the saturation of the CO_2 lines. The SO profiles are on average lower than the MCS ones at around 85 km. This bias could be explained by a reminiscence of lower values due to the pressure taken at the top of the profile P_{top} (see section 8.2.4) which is a value taken from GEM-Mars. (Neary and Daerden, 2018) made a comparison between the data from GEM-Mars and MCS and found on average a slightly lower value in GEM-Mars.

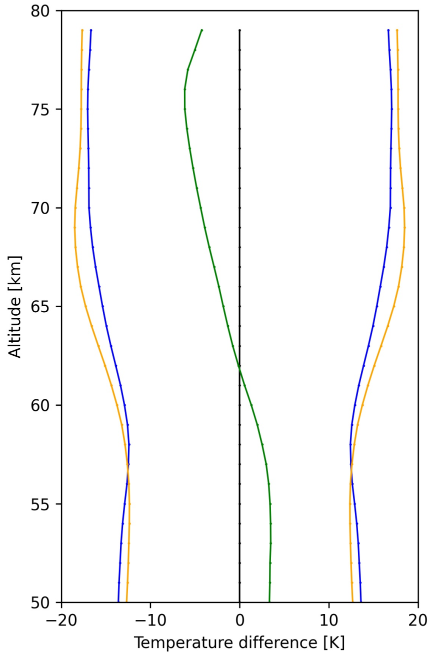

Figure 9.7: Weighted average difference between the 117 co-located profiles (NOMAD-SO - MCS) in green. The blue and orange curves are the variabilities on, respectively, SO and MCS profiles.

9.2.2 Comparison to TGO-ACS-MIR

The Mid-InfraRed (MIR) channel of the Atmospheric Chemistry Suite (ACS) instrument is also measuring at the terminator and has a spectral range of 2.3 to 4.3 µm, similar to NOMAD-SO. It is composed of two gratings. The secondary grating sweeps across a dozen of diffraction orders to be recorded. The resolving power ($\lambda/\Delta\lambda$) is reported as 30000 (Alday et al., 2021). The SNR is reported to be between 2500 and 5000 (Korablev et al., 2018).

The channels ACS-MIR and NOMAD-SO are never switched on together as the angle between their respective pointing is too important. Nevertheless, datasets from both channels can be compared. Alday et al. (2021) used data from the secondary grating position number four which covers ten diffraction orders (215 to 224) in a spectral range between 2.65 and 2.77 µm (3600 to 3770 cm^{-1}).

For the retrieval of CO_2, they used only the diffraction order 223 corresponding to a spectral range covering partly the highest wavenumber range in diffraction order 165 and the lowest wavenumber range in diffraction order 166. They are using the optimal estimation method and their *a priori* and first guess are provided by the Mars Climate Database (MCD) GCM (Forget et al., 1999; Millour et al., 2012). Alday et al. (2021) derived the temperature from the CO_2 density profile using the hydrostatic equilibrium equation.

A comparison between SO and MIR retrieved data is presented in Figures 9.8 and 9.9 with SO data in orange and MIR data in blue. The datasets are split into ingress and egress cases to better follow the variations in latitudes and time as described in section 10.1. Quantifying this comparison is impossible due to the variations in the distributions of the measurements of both channels.

Figure 9.8 shows the CO_2 density at altitudes of 60, 70, and 80 km retrieved from the SO and MIR channels. Both datasets show very similar variations except at 60 km after L_S 250° where the density from SO is lower due to the saturation of the CO_2 lines. The effect of saturation is more important in that season as the density increases. There is also some difference around L_S 210° for both ingress and egress cases. This difference is difficult to understand without knowing the averaging kernels from the MIR dataset.

Figure 9.9 represents the temperature retrieved from the SO and MIR channels. The temperature datasets show more variabilities than for the CO_2 density but the same trends are seen in both datasets with, again some differences after L_S 250° due to the saturation of the CO_2 lines. Another difference is the level of uncertainties between the two datasets. Even if the method to retrieve the data is the same, the averaged relative uncertainties on the CO_2 density and the temperature values are 1.5% and 3.0% on SO data while they are 1.0% and 0.8% for MIR data. While the uncertainties on the CO_2 density are similar, those on the temperature are almost four times lower for the MIR dataset.

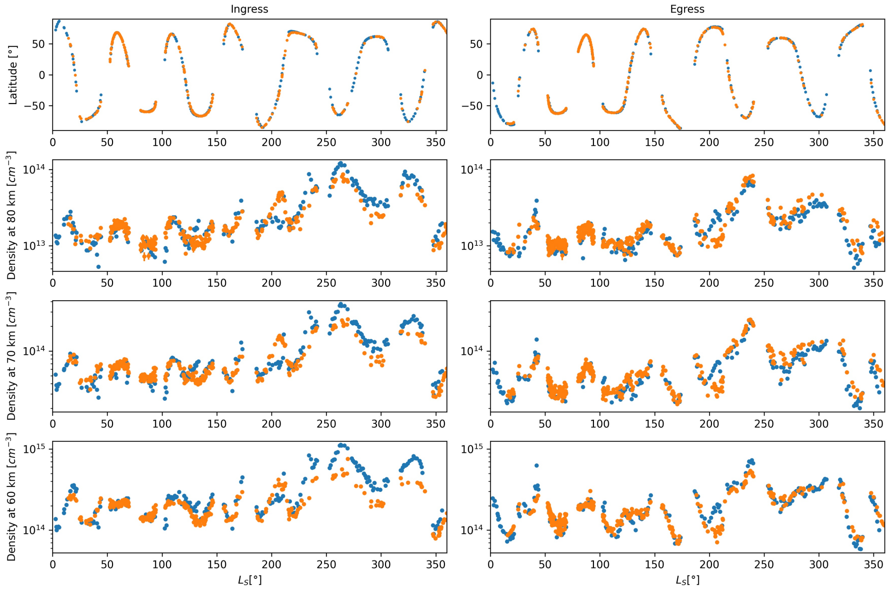

Figure 9.8: Carbon dioxide density retrieved at three altitudes: 60, 70, 80 km in MY 35. Orange points for NOMAD-SO and blue points for ACS-MIR. The datasets are split into ingress and egress cases. The panels on the first line show the coverage.

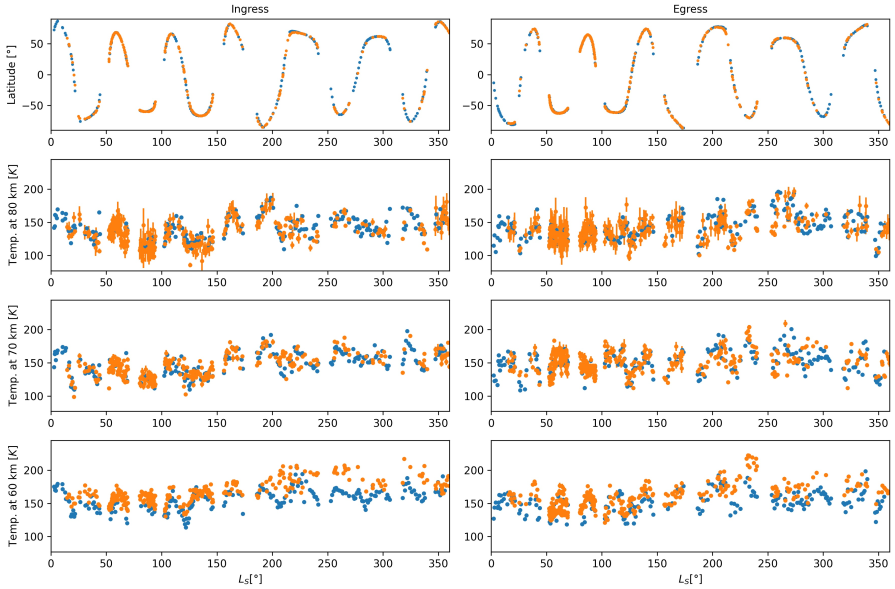

Figure 9.9: Temperature retrieved at three altitudes: 60, 70, 80 km in MY 35. Orange points for NOMAD-SO and blue points for ACS-MIR. The datasets are split for ingress and egress cases. The panels on the first line show the coverage.

9.2.3 Comparison to TGO-ACS-NIR

The NIR channel from the ACS instrument is very similar to NOMAD-SO. It also uses solar occultation measurements but covers the 0.7 to 1.7 µm spectral range with a spectral power of 28 000 (Fedorova et al., 2023). What is interesting about the NIR channel is that it is pointing almost in the same direction as NOMAD-SO and they are sometimes switched on together allowing to compare some simultaneous profiles of temperature. Temperature and CO_2 are retrieved from the CO_2 bands at 1.43 µm and 1.57 µm. The temperature is retrieved from both the rotational structure of the CO_2 band and the hydrostatic equilibrium law (Fedorova et al., 2023).

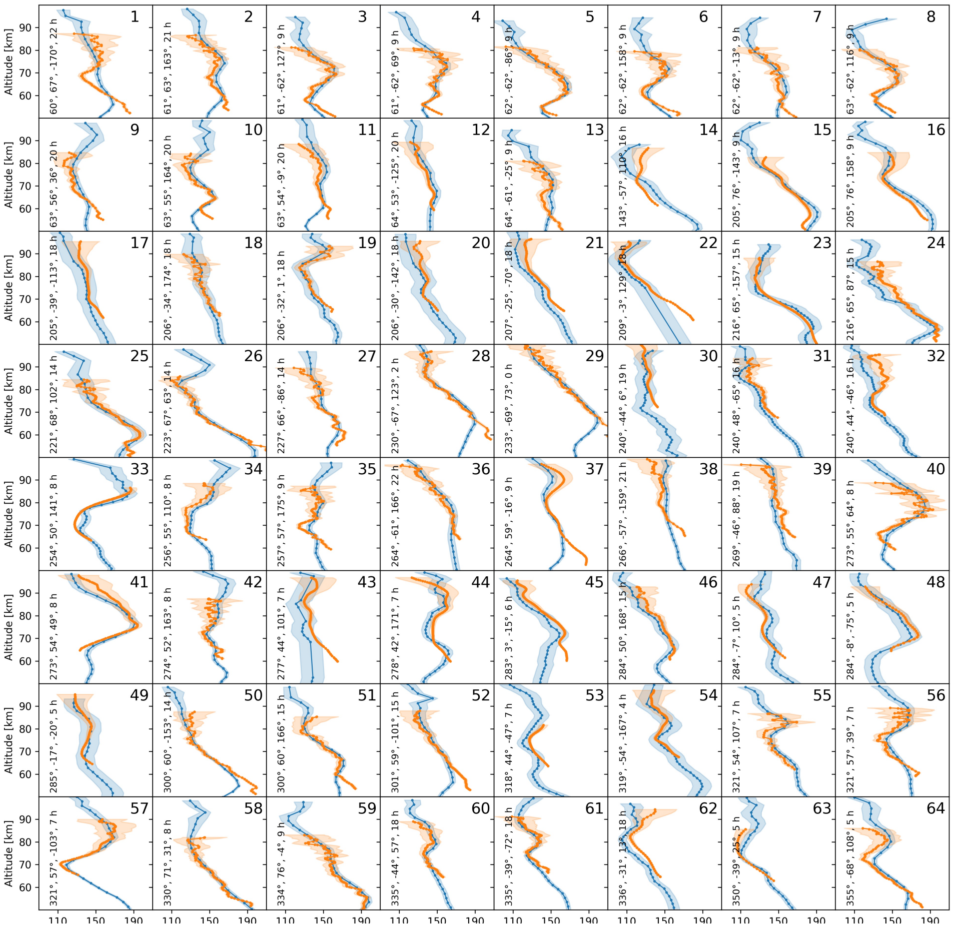

Figure 9.10: Temperature retrieved from ACS-NIR (Fedorova et al., 2023) in blue and NOMAD-SO in orange for simultaneous measurements. The number on the upper right side of each panel is the panel number and the numbers on the left side of each panel provide the solar longitude, latitude, longitude, and local solar time corresponding to the profiles.

The average difference (NIR - SO) is -4.7 K while the absolute difference is 6.7 K. The difference between those two numbers leads to think that most of the differences within the comparison of the datasets of NOMAD-SO to MCS (section 9.2.1) are due to differences in co-locations.

9.3 summary

The dataset of temperature profiles in the mesosphere was compared to simulations from the GEM-Mars model. The average difference was around 5 K but some differences are found especially when warm layers (around Northern dawn around perihelion) or very cold layers (around Southern dusk around aphelion) are seen in the SO dataset. The GEM-Mars profiles also show warm or cold layers but of weaker amplitude. This dataset was also compared to measured temperature from the Mars Climate Sounder (MCS) on-board Mars Reconnaissance Orbiter. The vertical resolution had to be degraded to the one of MCS. Within the co-location criteria, 117 profiles could be compared. On average the difference between the two datasets is very small (0.1 K) but the average of the absolute differences is quite high (8.5 K) meaning that there are some disparities within the variabilities of the compared profiles. Those disparities can be due to a remaining difference in vertical resolution or co-location. A comparison to the dataset of ACS-MIR on-board TGO shows a fairly good agreement. However, as ACS-MIR and NOMAD-SO are never switched on together, we cannot compare some corresponding profiles and it is difficult to provide an average value for the difference between the two datasets. Finally, the NOMAD-SO dataset was compared to the one of ACS-NIR on-board TGO. Contrary to the comparison to ACS-MIR, ACS-NIR and NOMAD-SO are sometimes switched on together, they have a similar vertical resolution and they are pointing in almost the same direction. The average difference is quite small with a value of 4.7 K while the average absolute difference is only 6.7 K. This means that the variability between the two datasets is rather small with a value around 2 K. These results suggest that the average absolute difference in the comparison with MCS is due to differences in vertical resolution and co-locations.

Chapter 10

Mars climatology - Thermal structure at the terminator

This chapter details the main trends present in the datasets of CO_2 density and temperature derived from order 148 and thus focuses on the mesosphere. First, section 10.1 describes the coverage of the datasets. Then the seasonal, inter-annual, latitudinal, and longitudinal trends are presented. The diurnal trends are shown across latitudinal trend as it is tightly related to latitude (see section 10.1) in solar occultation measurements. The dataset shown here is mainly derived from diffraction order 148. The two last sections provide the distribution of cold layers and strong warm layers present in this dataset.

10.1 Coverage

Figure 10.1 depicts an example of coverage, for diffraction order 148 along MY 35 and 36. Panel a shows the latitudes scanned along those two Martian years. Panel b shows that there is a dependence between local solar time and latitudes. Due to the inclination of Mars rotation axis, the local solar times between 6 h and 18 h are scanned in the atmosphere which is closer to its winter solstice (in the southern hemisphere from L_S 0° to 180° and the northern hemisphere from L_S 180° to 360°). The opposite happens for the local solar times between 18 h and 6 h. The local solar times 6 h and 18 h are scanned only at the equator.

The panels are split for ingress and egress cases in figure 10.2 and the latitude to solar longitude curves are continuous functions. The ingress and egress cases mainly scan respectively the afternoons and the mornings. There is also a bias inducing that LST corresponding to late evening and early mornings are scanned in the Northern hemisphere in Northern spring and summer (first half year) and in the Southern hemisphere in Southern spring and summer (second half year). On the opposite, the LST corresponding to late morning and early afternoon are scanned in the hemisphere in autumn and winter.

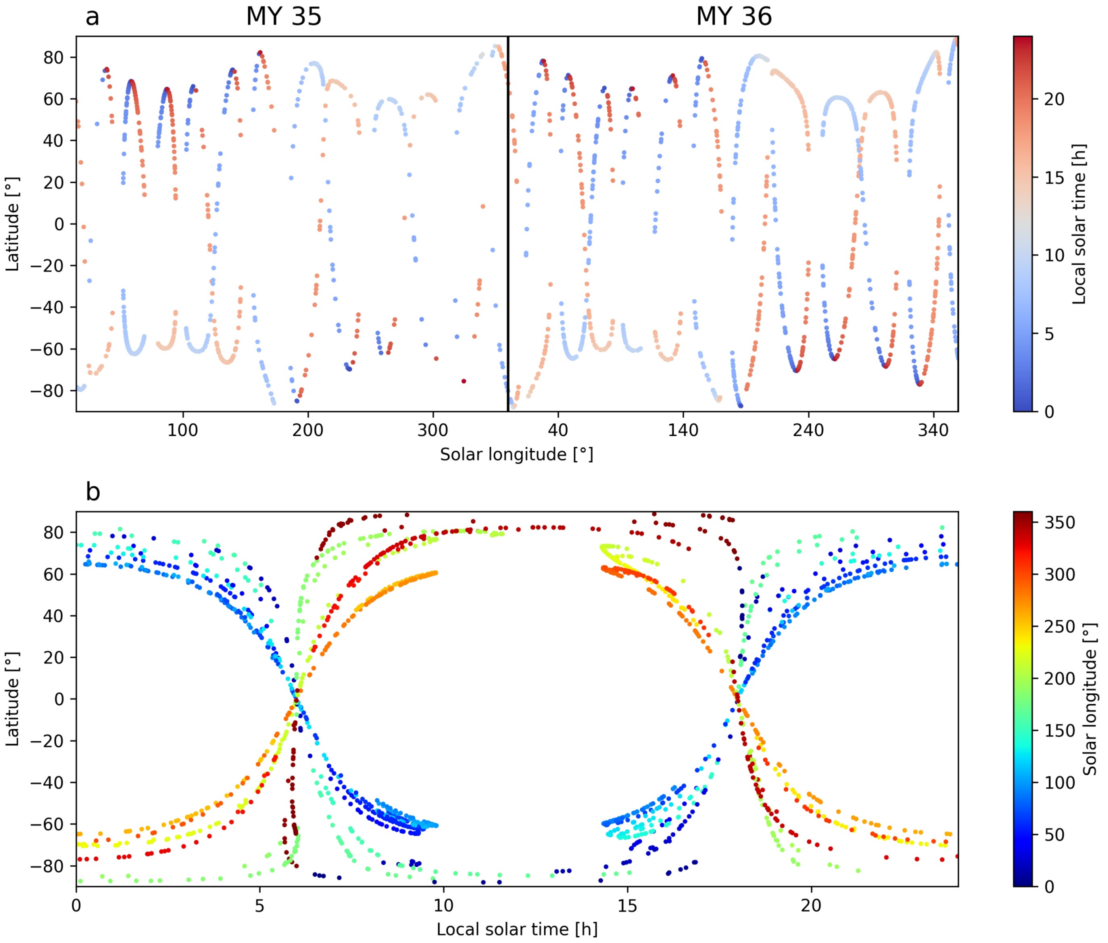

Figure 10.1: Coverage for diffraction order 148 in MY 35 and 36. Panel a is for the latitude coverage as a function of solar longitude and the colours are for the local solar time. Panel b is for the latitude coverage as a function of the local solar time and the colours are for the solar longitude.

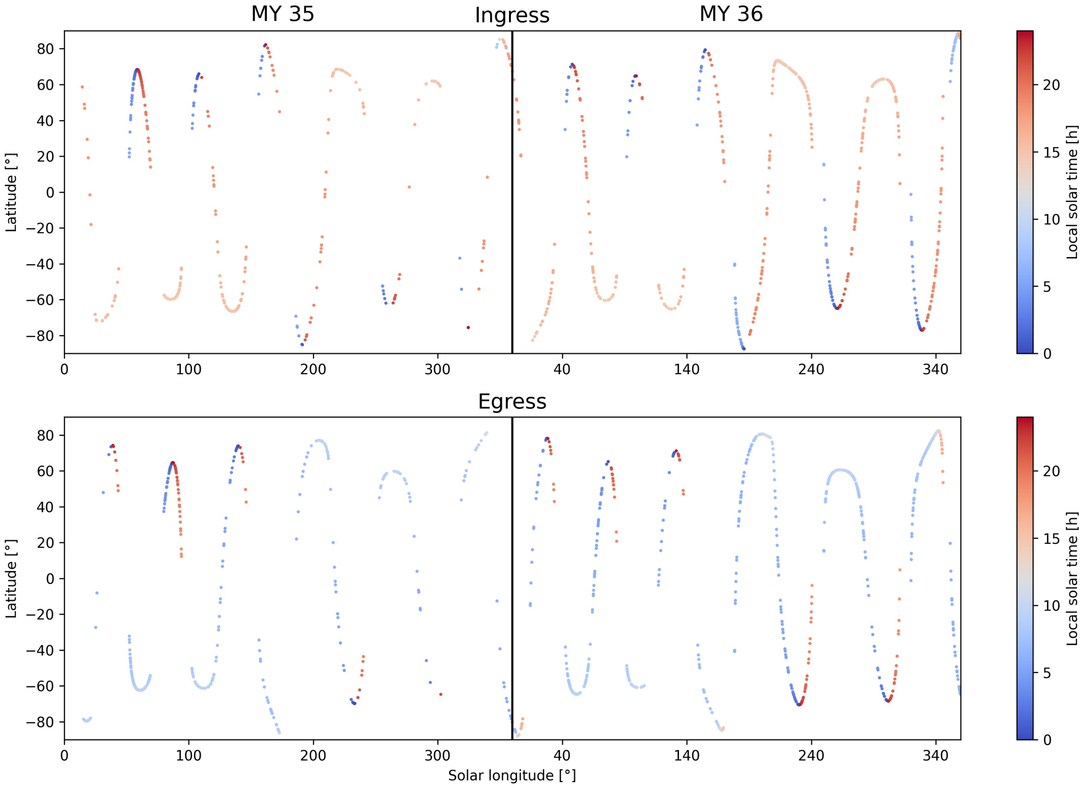

Figure 10.2: Coverage for diffraction order 148 in MY 35 and 36 splits for ingress (upper panel) and egress (lower panel) occultations.

10.2 Seasonal variations

Figures 10.3 to 10.6 show all 1748 vertical profiles of temperature retrieved from diffraction order 148 (mesosphere) in MY 35 and 36. Those figures are split for dawn/dusk and North/South profiles. The latitude and local solar time coverage are provided in the corresponding panel *a* in each Figure. As noted in section 10.1, the latitude and local solar time covered varies rapidly over time and the coverage is almost similar in MY 35 and 36.

We can notice that several warmer layers appear around 0.1 Pa in the dawn profiles in both northern and southern hemispheres but only in the northern profiles at dusk. Those warm layers appear to be stronger in the southern hemisphere at dawn and around aphelion while the southern dusk profiles appear much colder with temperature as low as around 120 K. A strong increase in the temperatures can also be seen in both MY in the Northern winter hemisphere (around perihelion). Those features are also visible in the datasets shown in Belyaev et al. (2021, Figure 2 panel b) and in Alday et al. (2021, Figure 2 panel b) which are both covering MY 35.

Seasonal trends are better seen when considering some specific altitudes and Figure 10.7 presents the CO_2 density at 75 km. We see some seasonal variations with much higher density around L_S 240° in MY 35 and around L_S 280° in MY 36. It is known that the seasonal trend of density in Mars atmosphere is a sinusoidal-like function with two peaks, an important one around perihelion and a weaker one around aphelion (e.g. Forget et al. (2009)). The solar longitudes of both maxima are around 50° and 260° (Smith et al., 2017). The reason for those seasonal variations of density is the variation of the temperature in the lower atmosphere. A higher temperature in the lower atmosphere induces a higher scale height and thus the density increases for the same altitude. This increase of the temperature in the lower atmosphere is due to the presence of more dust heating the atmosphere. The reason for a higher peak around perihelion than at aphelion is the increase in the incoming solar flux as Mars is closer to the Sun (Forget et al., 2009) around perihelion. In the dataset presented here, the peak at aphelion does not appear clearly. The likely reason is that the variations in latitudes and local solar time overwhelm the presence of this peak.

Nevertheless, we can still see an increase in the density during the B storm at L_S 240-270° and the C storm at L_S 320-330° both in the Southern hemisphere in MY 35 that were also present in ACS-MIR profiles (Belyaev et al., 2022). Similar increases are found in MY 36.

Figure 10.8 shows the variation of temperature at 75 km. There are strong variations of temperature with seasons but there is also more disparity in the temperature values that are uneasy to follow on this plot but will be easier to follow while checking for the latitudinal and longitudinal variations in the next sections.

The distribution of temperature is very similar in Figures 10.8 and 10.9 except that the variation of temperature along season is much reduced while looking at the temperature on the same pressure level. Thus this seasonal variation of temperature is explained by the seasonal density variation.

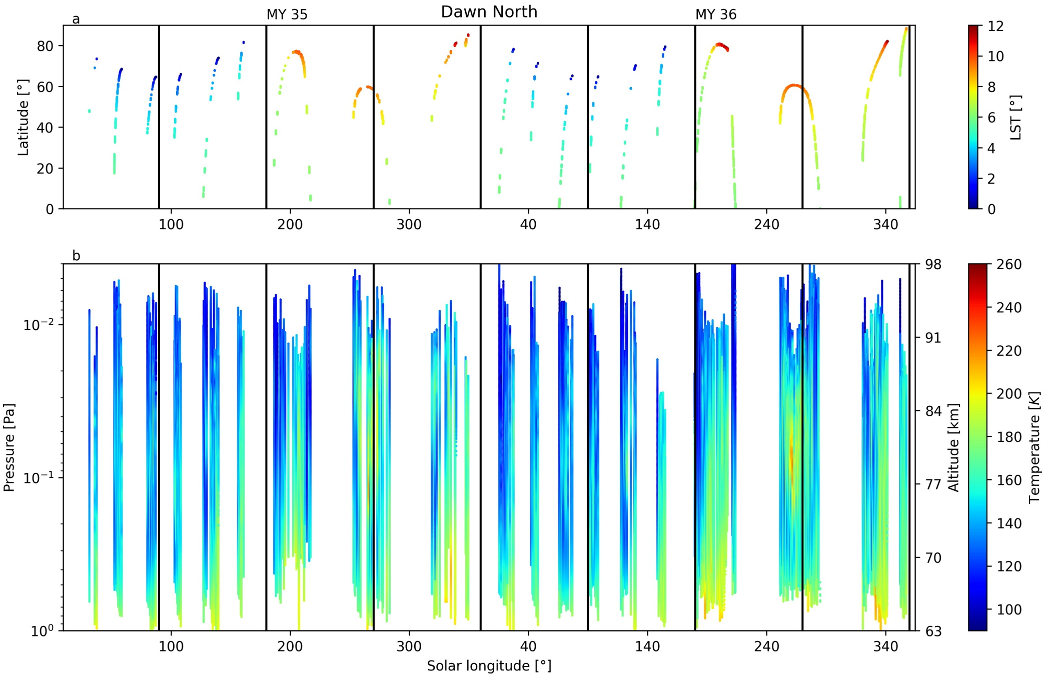

Figure 10.3: Map of vertical profiles of temperature retrieved from diffraction order 148 in MY 35 and 36 for dawn and northern measurements in panel b. Panel a provides the corresponding coverage in latitude in Y-axis and local solar time as a colourbar. A second Y-axis in panel b provides the corresponding rough altitudes to the pressure scale.

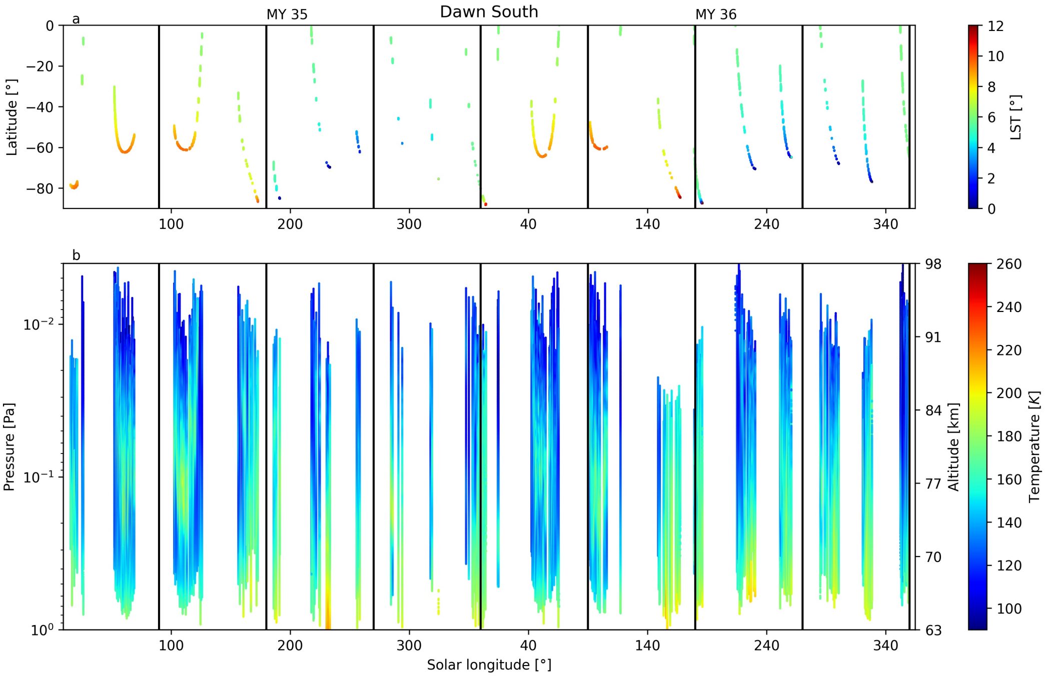

Figure 10.4: Same as Figure 10.3 but for dawn and southern measurements.

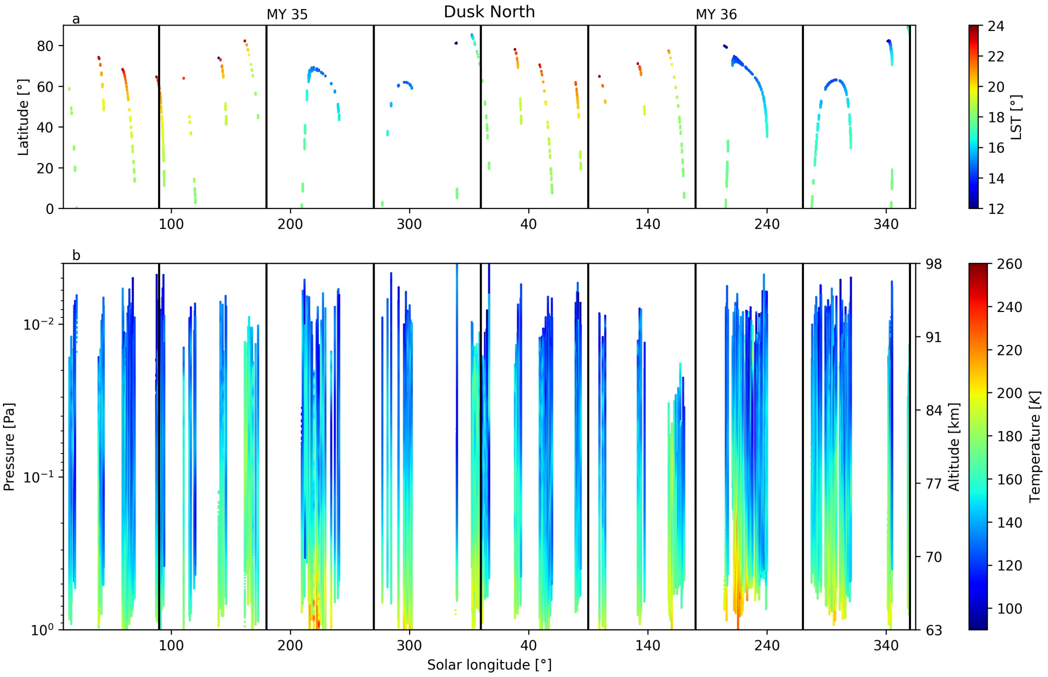

Figure 10.5: Same as Figure 10.3 but for dusk and northern measurements.

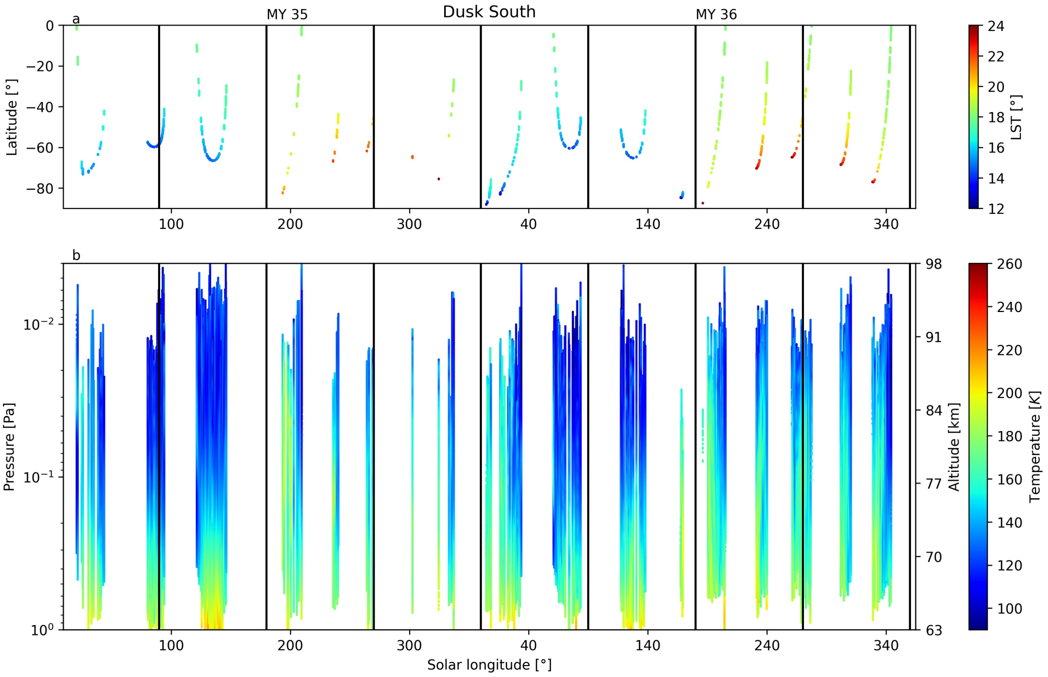

Figure 10.6: Same as Figure 10.3 but for dusk and southern measurements.

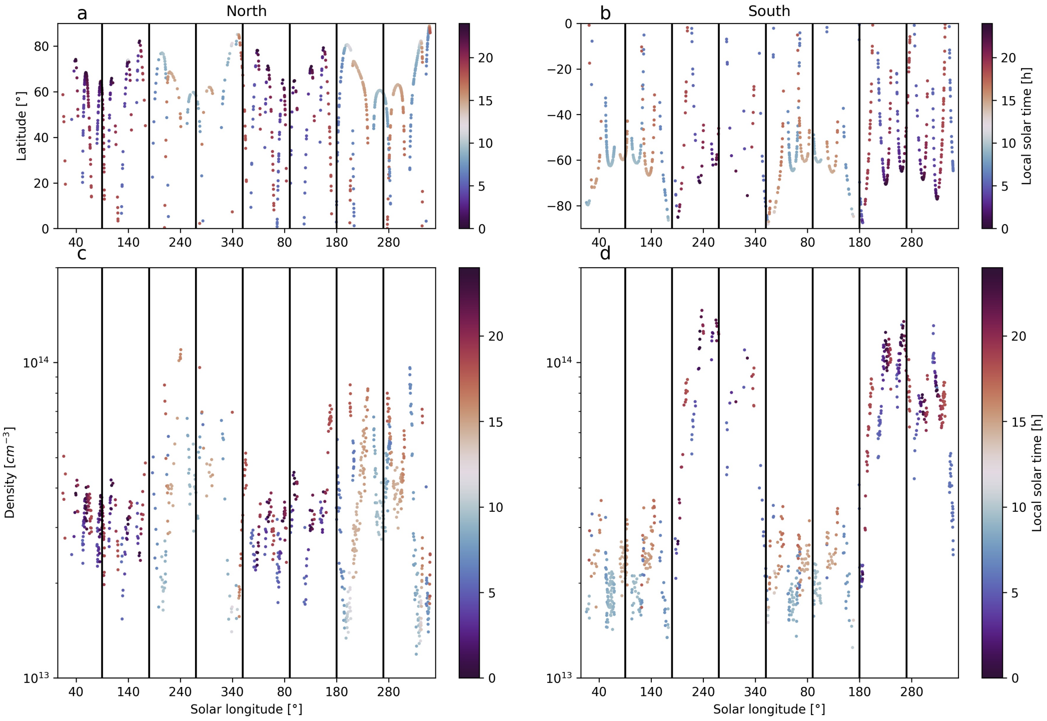

Figure 10.7: Retrieved CO_2 density in MY 35 and 36 at 75 km from diffraction order 148 in panels b and d as a function of solar longitude. Panels a and b provide the latitude in Y-axis and the local solar time as colour-bar. Panels a and c are for the northern hemisphere and panels b and d are for the Southern hemisphere. The vertical lines mark the solstices and equinoxes.

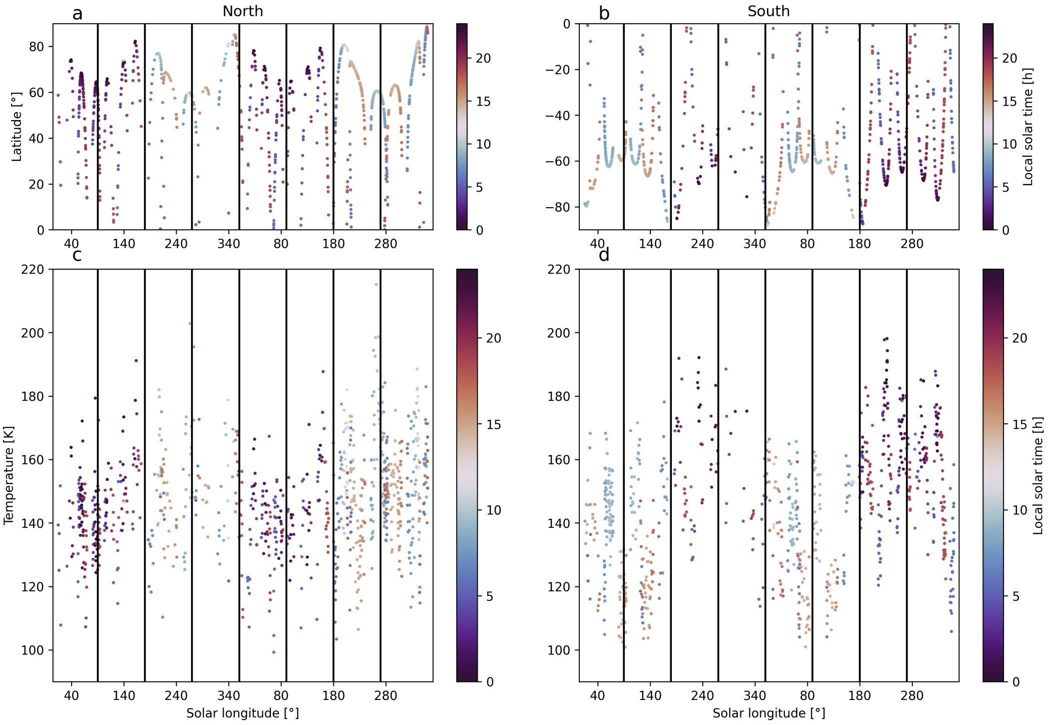

Figure 10.8: Same as Figure 10.7 but panels c and d present the retrieved temperature.

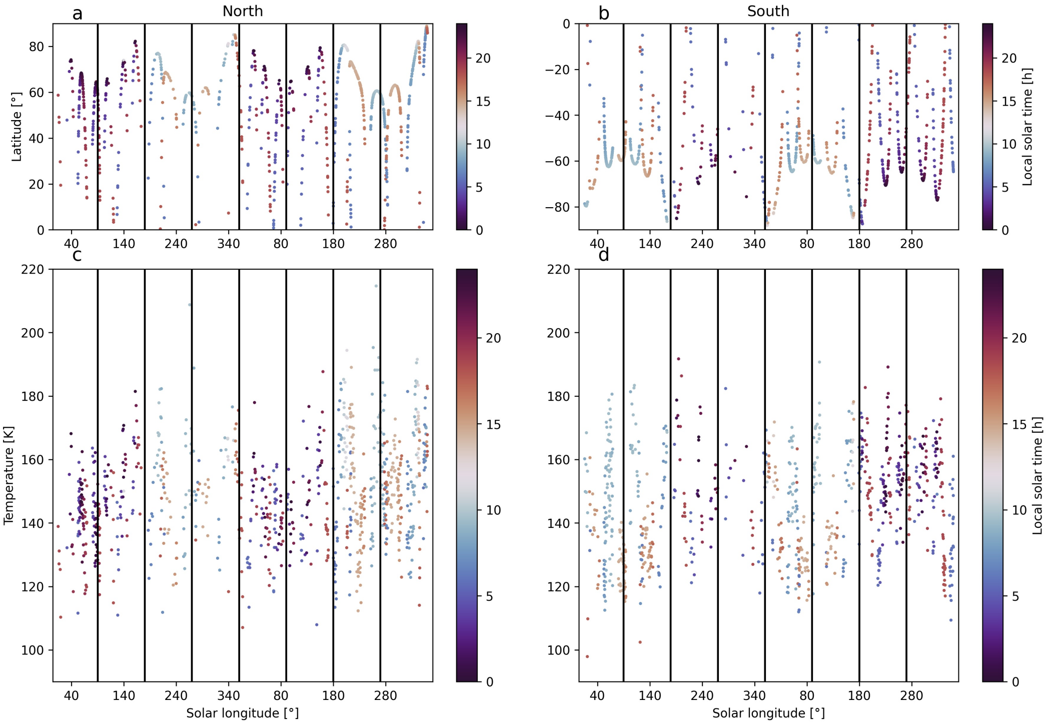

Figure 10.9: Same as Figure 10.8 but for a pressure of 0.1 Pa.

10.3 Inter-annual variations

A comparison of the retrieved CO_2 density and temperature values at 75 km for MY 35 and 36 are presented in Figures 10.10 and 10.11. During both years, the orbit of TGO was similar, in particular in the second half year ($L_S > 180°$) meaning that an inter-annual comparison can be easily done with this dataset. In particular, the amplitude of the increase in the density within each hemisphere was very similar for both years. Concerning density and temperature, MY 35 and 36 are very similar Martian years.

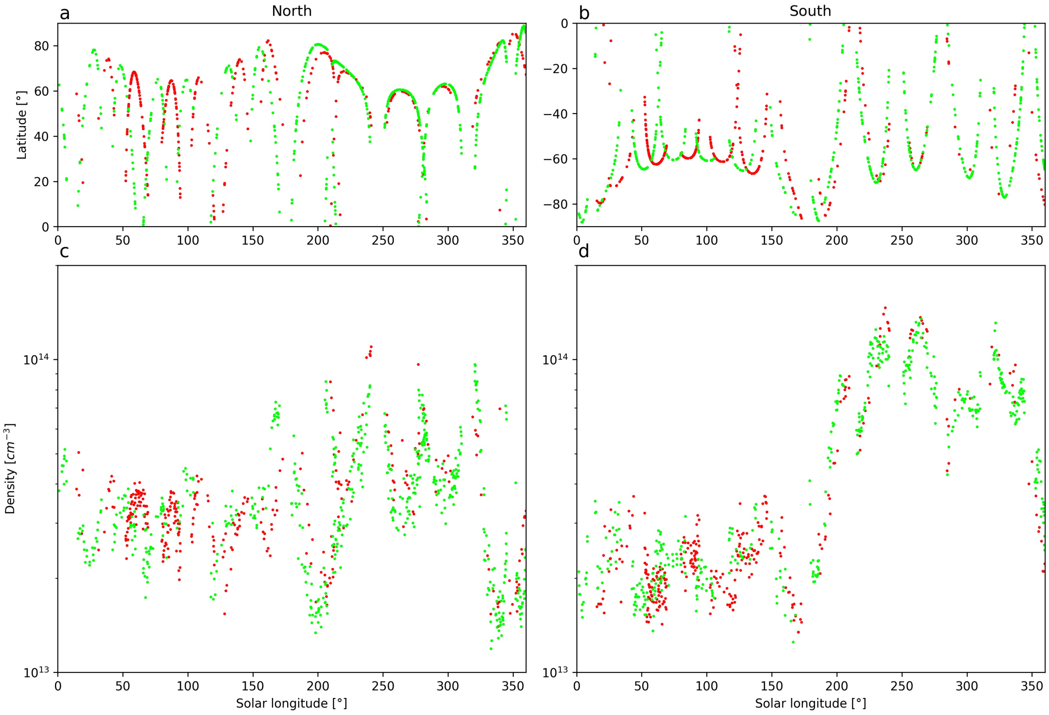

Figure 10.10: Retrieved CO_2 density at 75 km in MY 35 in red and MY 36 in green as a function of solar longitude.

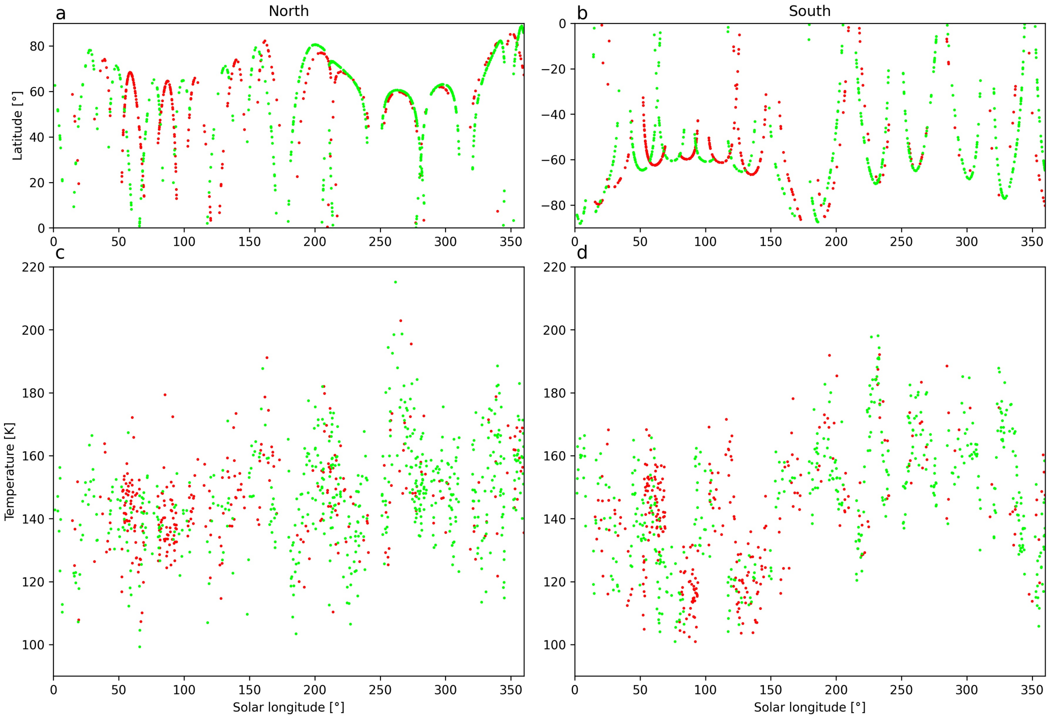

Figure 10.11: Same as Figure 10.10 but for temperature.

10.4 Latitudinal variations

Figure 10.12 highlights the variation of the density along latitudes throughout solar longitudes. There is a symmetrical distribution of density to latitudes equinoxes (L_S ~0° - black and grey - and ~180° - dark green) where the Hadley cell (McCleese et al., 2010) is split into two branches lifting air at the equator and the descending branches are at high latitudes in both hemispheres. The solstices (L_S ~90° - blue - and ~270° - yellow and orange) have an asymmetrical distribution of density with higher values towards the Summer hemisphere.

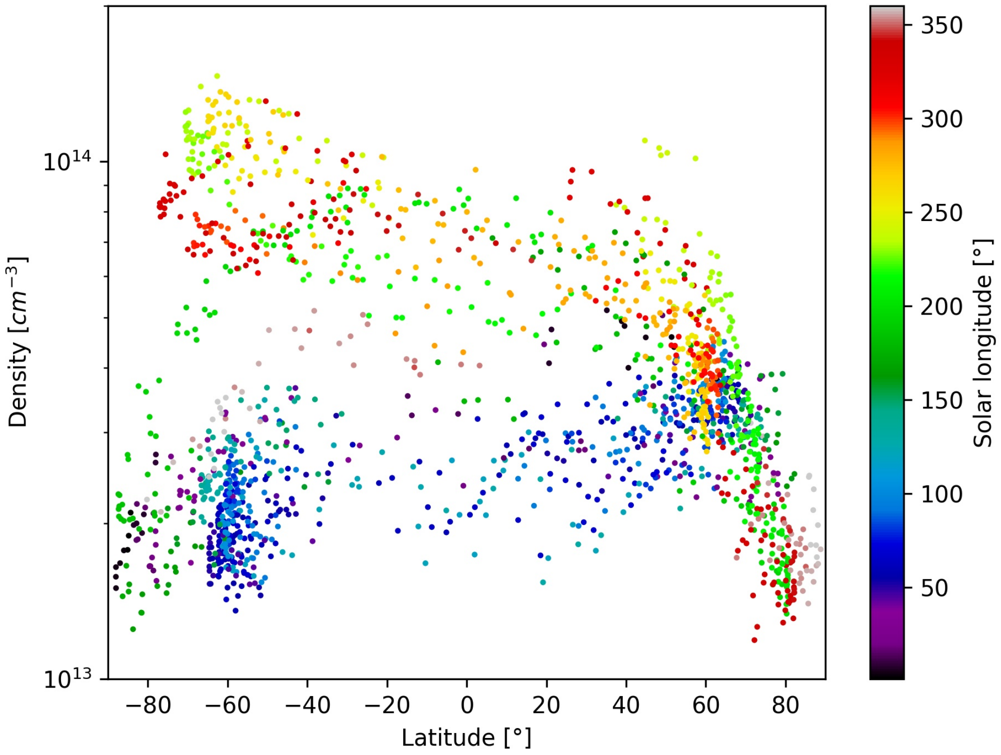

Figure 10.12: Retrieved CO_2 density at 75 km in MY 35 and 36 as a function of latitude and the colour-bar for solar longitude.

The local solar times are tightly correlated to latitudes and we see some patterns in Figure 10.13 that are mainly due to the latitudinal variations. The main results from this figure is that diurnal variations cannot be inferred from solar occultation except for the morning-evening distinction. The conclusions are the same for Figure 10.15.

In Figure 10.14, we see an increase of the temperature towards the poles for all times of the year but still with a striking higher increase in the Northern hemisphere around perihelion (L_S 250° - yellow points) with a few temperatures even higher than 200 K around perihelion (late northern fall). This polar warming results from the adiabatic compression induced by the descending branch of the mean meridional circulation (e.g. McDunn et al. (2013); McCleese et al. (2010)).

Figure 10.16 compares the retrieved temperature profiles between MY 35 and 36 up to around L_S 180°. The local solar time and solar longitudes roughly match from one year to another.

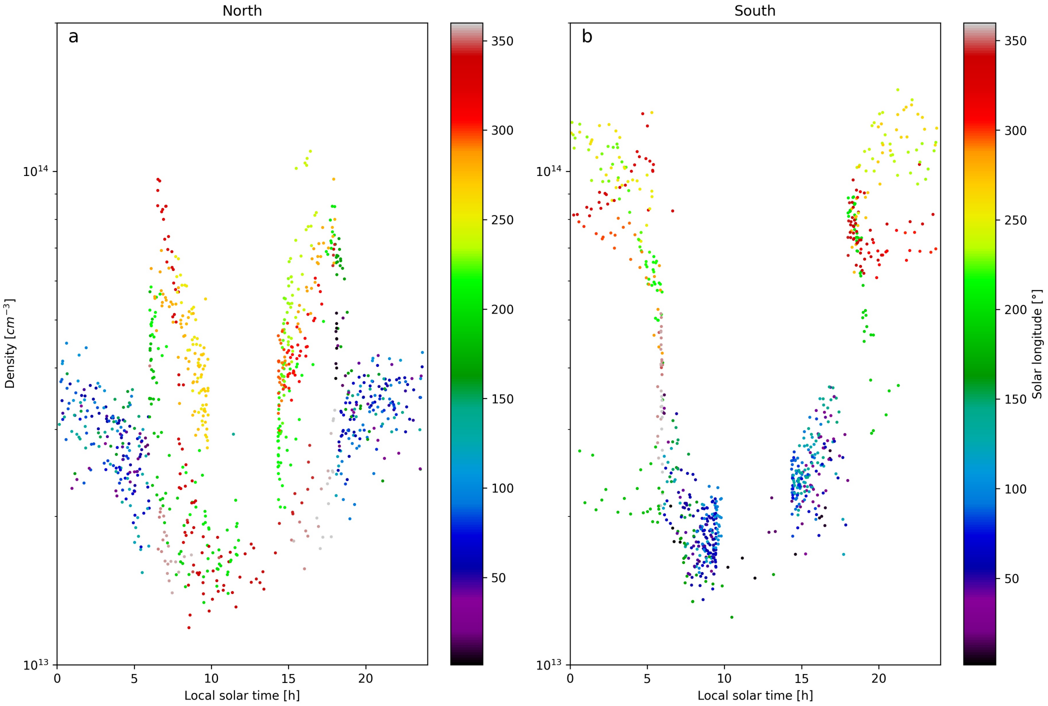

Figure 10.13: Retrieved CO_2 density at 75 km in MY 35 and 36 as a function of local solar time and the colour-bar for solar longitude. Panel a and b are, respectively, for the northern and southern hemispheres.

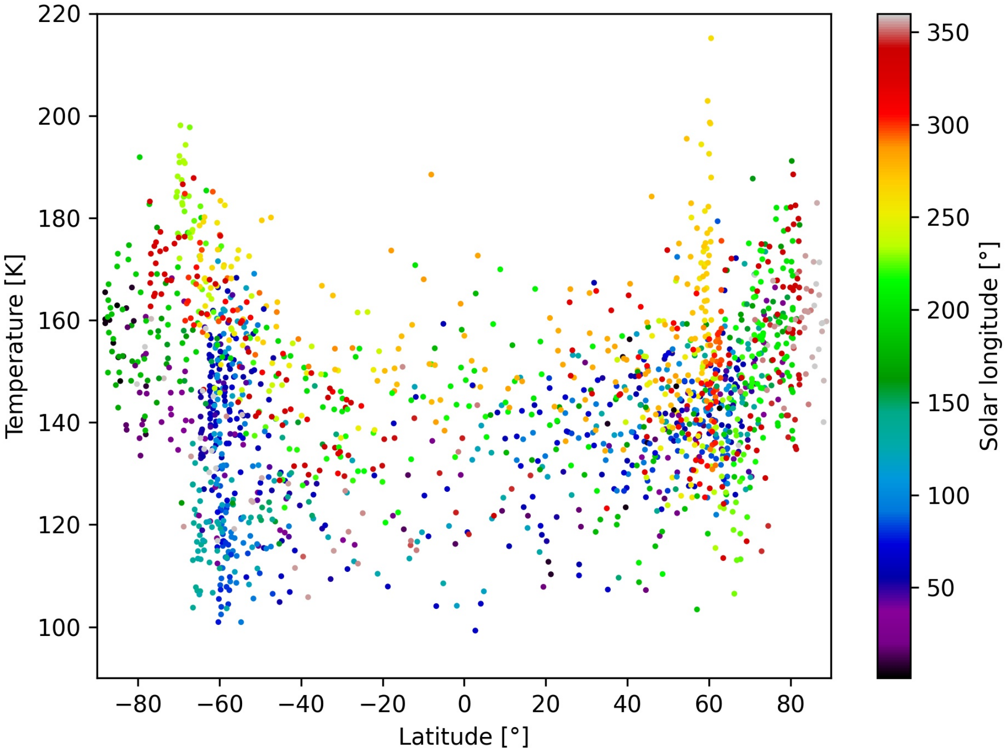

Figure 10.14: Same as Figure 10.12 but for temperature.

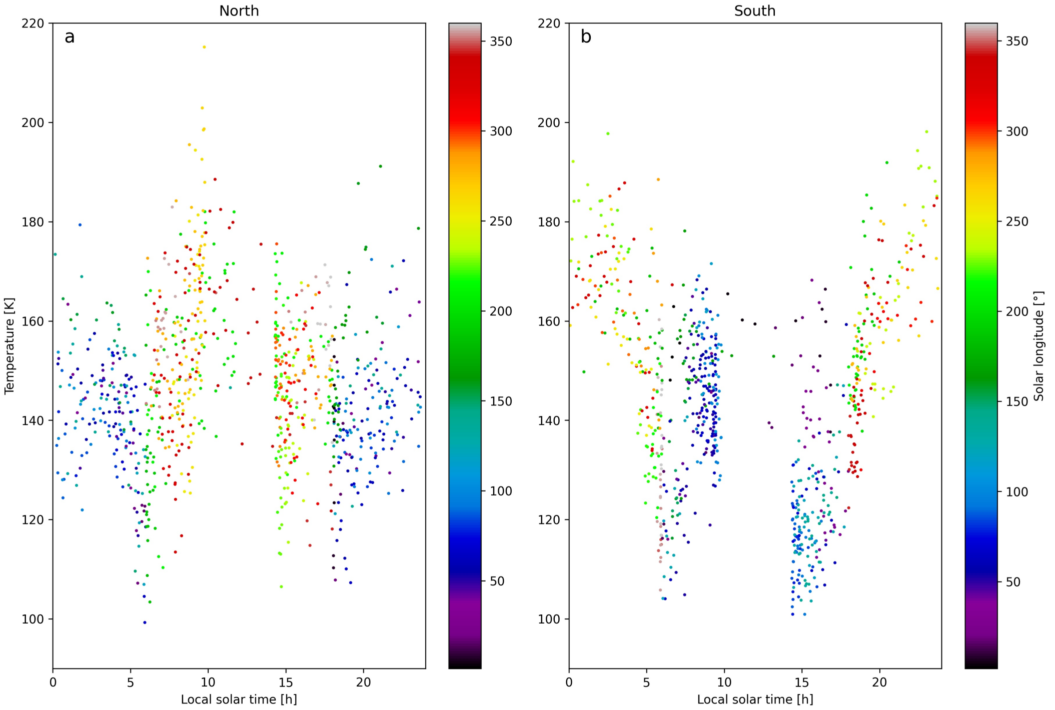

Figure 10.15: Same as Figure 10.13 but presenting the retrieved temperature at 75 km.

Similar features are found in the datasets of both MY. In particular, in panels 8 and 20 (L_S 30°-60°), a similar tongue of higher temperature of around 170 K stretches from southern high latitudes towards 40°S and to higher altitudes. From the comparable latitudes in L_S 50°-140° (panels 9 to 11 and 21 to 23), warmer layers are seen at very similar altitudes across MY. The last panels, 12 and 24 (L_S 130°-180°), both cover very high latitudes and have higher temperatures reaching 200 K.

Figure 10.17 is the same than Figure 10.16 but presents the second half year (L_S 180° to 360°). An important difference is that MY 36 was better covered by scans of diffraction order 148. MY 35 and 36 contain respectively 404 and 392 occultations in the first half of the year while the second half contains respectively 202 and 703 occultations.

Nevertheless, the profiles that can be compared show similar features. In particular, panels 8 and 20 show very similar warmer temperatures around latitudes of 0° to 50°N from the higher pressure to 0.1 Pa and a warmer layer stretching from the southern latitudes towards the 20°S. A general increase of the temperature at most latitudes is seen in L_S 230° to 340° (panels 3-5 and 21-23).

Figures 10.18 and 10.19 shows the latitudinal trends in the retrieved temperature profiles at dusk. Those profiles show similar trends in both MY when the corresponding profiles can be compared. The temperature in the dusk profiles are very cold ($\sim$100 K) compared to dawn profiles in the southern hemisphere during the first part of the Martian years (L_S 30° to 150°) which appears to be featureless, especially above 0.1 Pa. The second part of the MYs has higher temperatures up to 170 K along all latitudes from (L_S 180° to 310°). An interesting feature in panel 21 (L_S 38° to 76°) in Figure 10.18 is a warm layer appearing around the equator. A similar feature was reported in Lee et al. (2009); McCleese et al. (2010) at close pressure levels and might

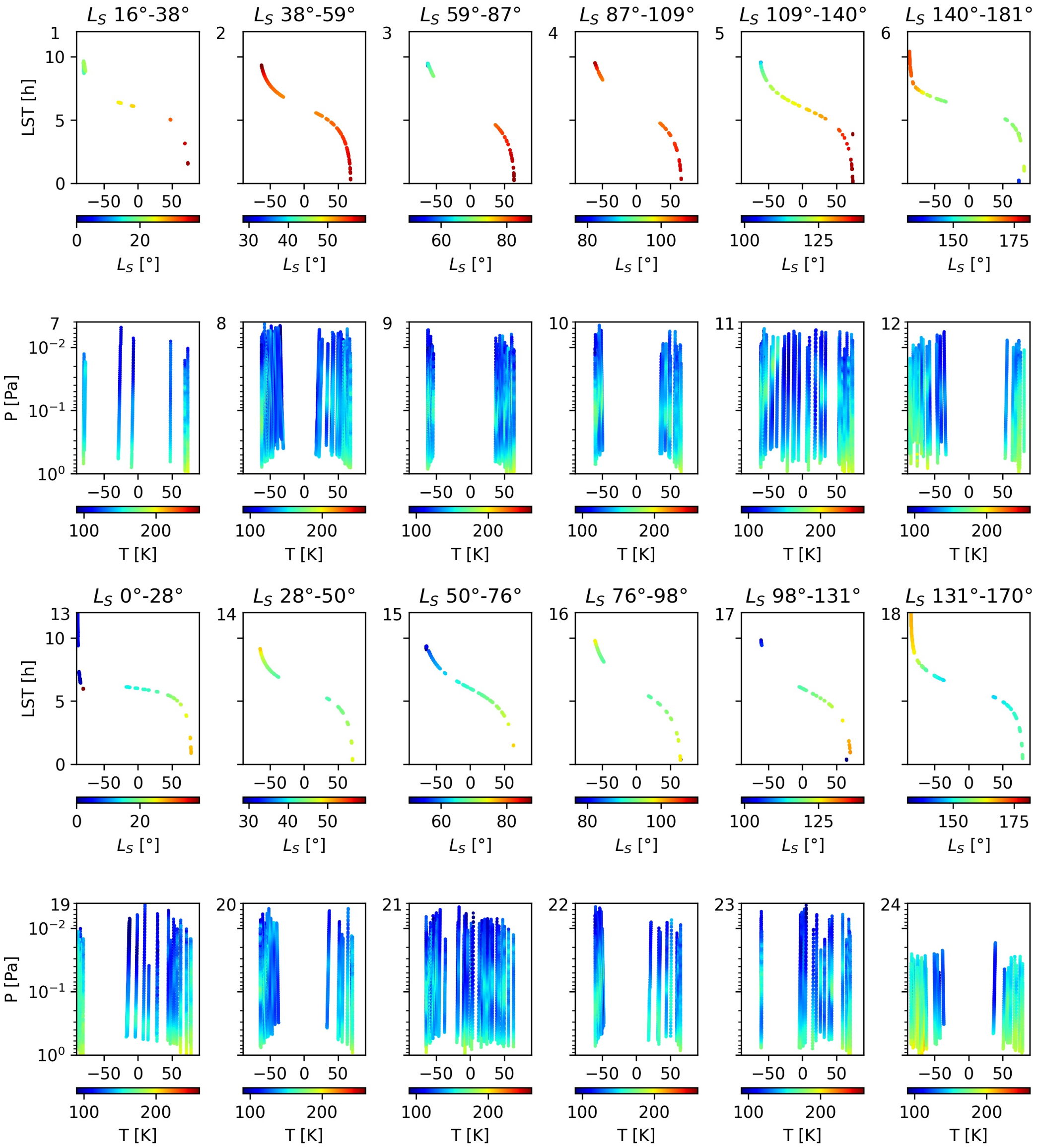

Figure 10.16: Retrieved temperature profiles at dawn for the first half year in panels 7 to 12 and 19 to 24. Panels 1 to 12 for MY 35 and panels 13 to 24 for MY36. Panels 1 to 6 and 13 to 18 provide the latitudes (x-axis), local solar times (y-axis), and solar longitude (colour-bar).

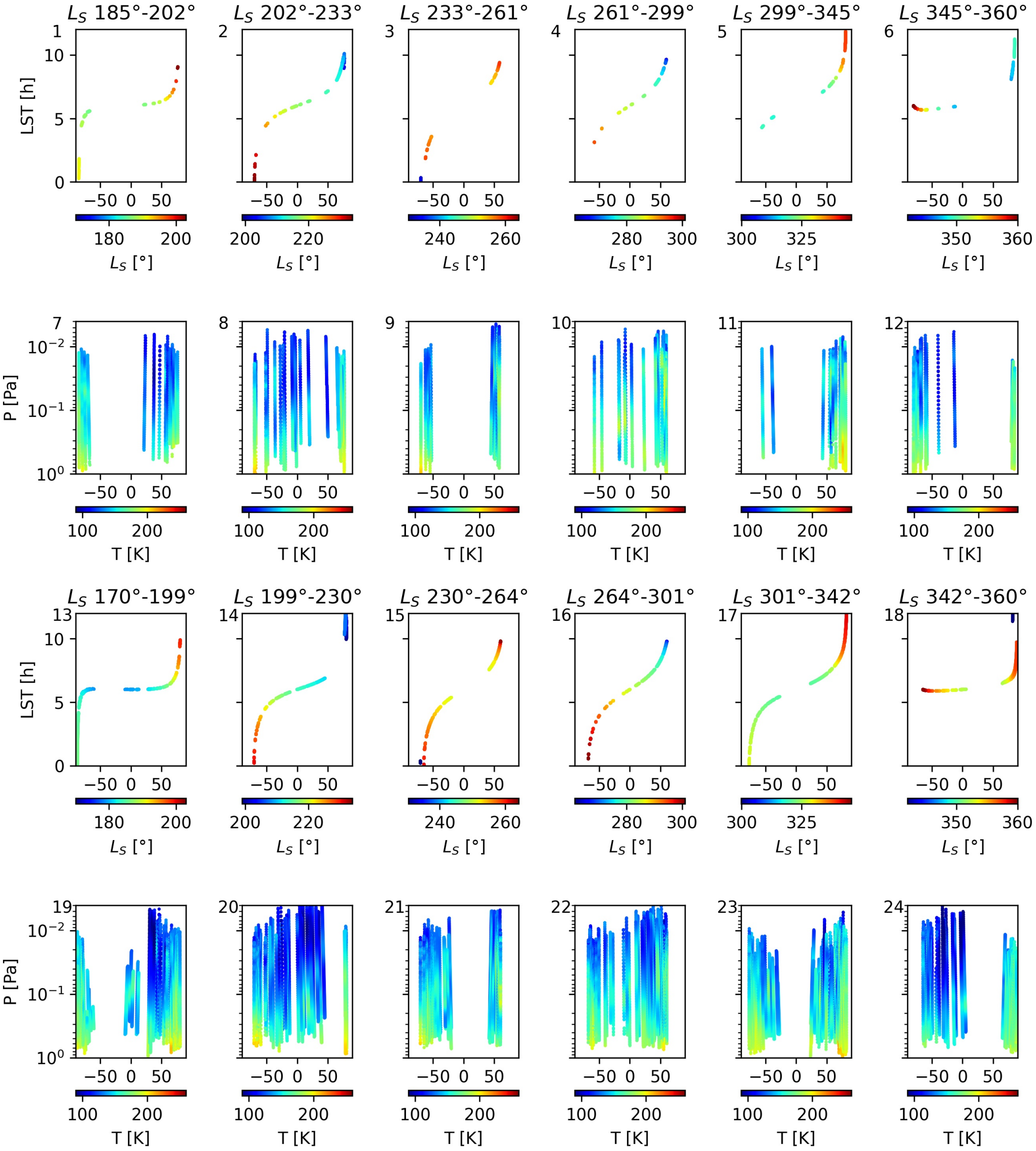

Figure 10.17: Same as for figure 10.16 but for the second half year.

be related to thermal tides.

Inter-annual variations of temperature are mainly related to differences in dust content (Giuranna et al., 2021). MY 35 and 36 had a close dust activity favouring a similar temperature distribution.

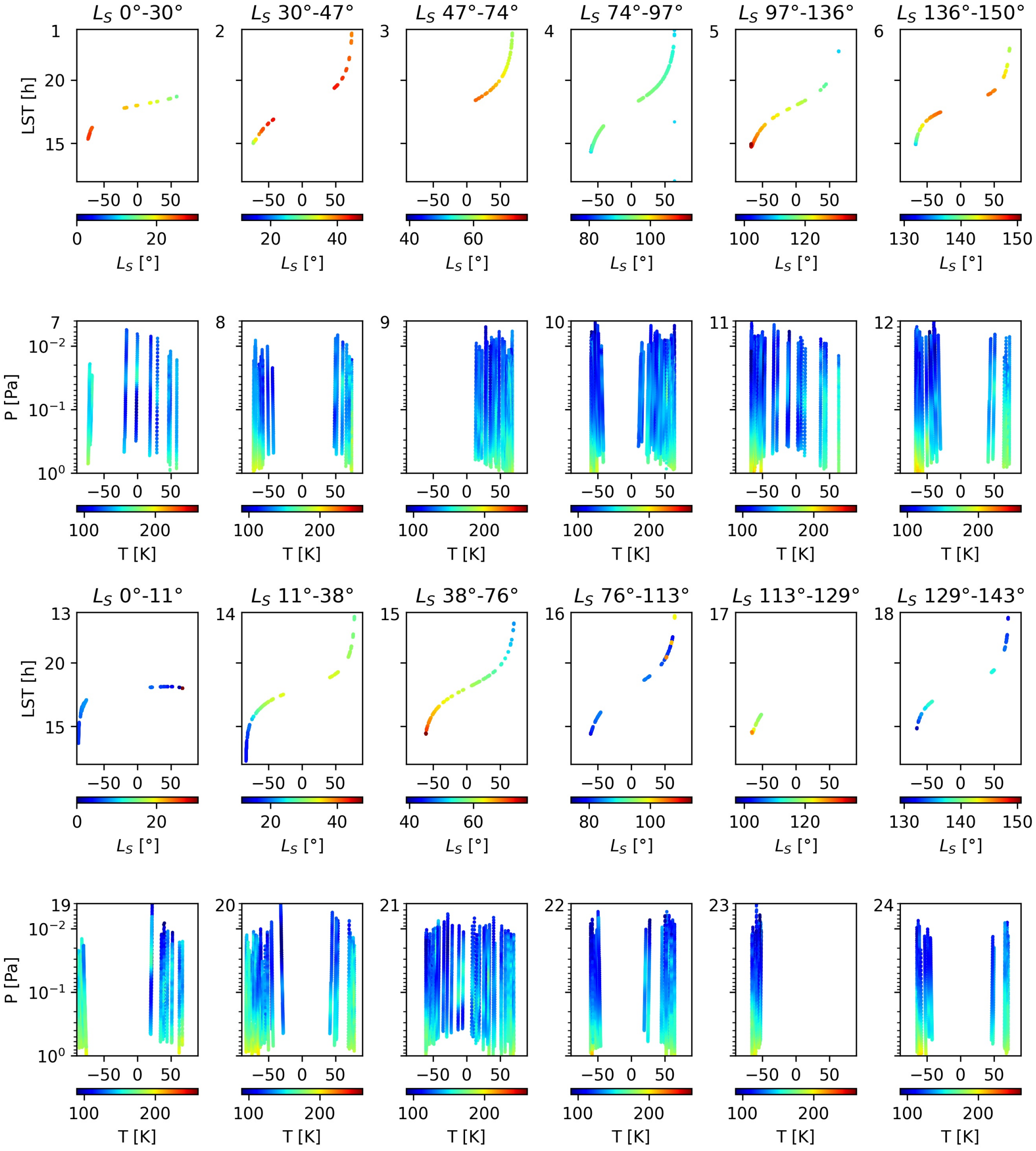

Figure 10.18: Retrieved temperature profiles at dusk for the first half year in panels 7 to 12 and 19 to 24. Panels 1 to 12 for MY 35 and panels 13 to 24 for MY36. Panels 1 to 6 and 13 to 18 provide the latitudes (x-axis), local solar times (y-axis), and solar longitude (colour-bar).

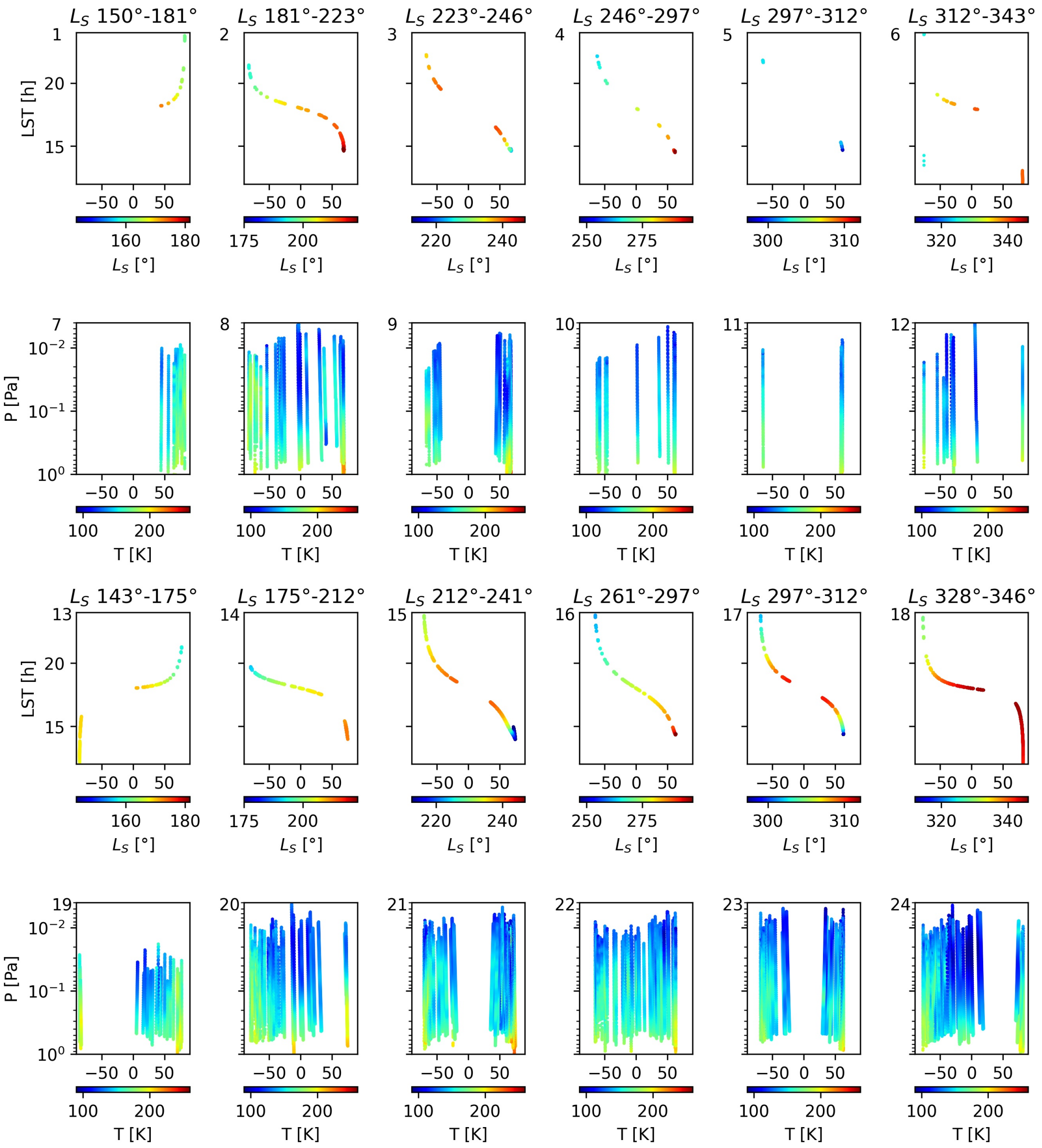

Figure 10.19: Same as for figure 10.18 but for the second half year.

10.5 Longitudinal variations

Some TGO occultation periods are appropriate to derive the longitude variations. When looking at Figure 10.2, those periods mainly appear at the peaks of the L_S to latitude curves. Those peaks mainly happen at high latitudes around 60° here thermal tides have a weaker amplitude (González-Galindo et al., 2011). To check for longitudinal variations, we would prefer to analyse them at low latitudes. Unfortunately, the curves in Figure 10.2 are rapidly sweeping across the equator. Nevertheless, we will see in this section that some longitudinal variations can be seen at those high latitudes.

The maximum ranges of solar longitude, latitude, and local solar time are set to 30°, 10°, and 1.5 h to avoid to mixing different possible phenomena in the longitudinal variations. Figure 10.20 shows the profiles in those specific ranges in MY 35. The mean solar longitude and local solar time are provided above the panels and can be compared to Figure 10.2. We need to keep in mind that those ranges are not equivalently spread in local solar time and seasons as the ingress and egress cases mainly scan respectively the afternoons and the mornings while they scan the night times in the hemisphere which is in summer. There are clear variations of a temperature inversion in the morning around 7 and 10 h (panels b, h, i, k, and m) around 65 km, and smooth profiles in the afternoon around 14 h (panels e, g, j, l, and p). The main parameter changing is the local solar time as the longitudinal variations within one panel are equivalently distributed along hemispheres and seasons. No information can be given on the latitudinal variations as those ranges are all located around 60°. Some of those longitudinal variations might be related to the polar warming phenomenon (e.g. McDunn et al. (2013)) happening in the lower mesosphere at latitudes in the polar night but most of those profiles are not located in the polar night.

The diurnal variation of the Solar radiant flux produces planetary-wide thermal tides (Haberle et al., 2017, section 9.5) which have higher amplitudes around the equator than at high latitudes (González-Galindo et al., 2011) and vary in amplitude and phase with height (e.g. Lee et al. (2009)). Thermal tides are split into migrating and non-migrating tides which are, respectively, synchronous and asynchronous with the position of the Sun around Mars. For the sets of profiles presented in Figure 10.20 only non-migrating tides can be derived as the local solar time is fixed. For a specific altitude and a fixed local solar time, the amplitudes A_k and the corresponding phases ϕ_k of the wavenumbers k are fitted with the formula

$$T(\lambda) = \sum_k A_k \cos(k\,\lambda - \phi_k) \tag{10.1}$$

where k is positive integer, and λ is the longitude. There are thus six (eight) parameters fitted if we consider the three (four) first wavenumbers. We need to have much more profiles than the number of fitted parameters to avoid any over-fitting of the data. This formula is a simplification where k is the difference of the westward propagating zonal wavenumber s minus a harmonic of the diurnal period m (England et al., 2016). With a fixed local solar time, we cannot derive any knowledge about s or m nor derive migrating tides for which s is a multiple of m. The fit is performed with a Levenberg-Marquardt least square algorithm from the MINPACK library (Moré, 1977) through the SciPy module (Virtanen et al., 2020). No bounds are applied to the fitted parameters A_k and ϕ_k and their initial values are set to zero to avoid forcing any particular solution. The uncertainties are computed with a Monte Carlo analysis with a thousand of samples.

Some results were already provided in Trompet et al. (2023a) for MY 35 L_S 100°–125°, Lat 63°S–56°S, LST 8.5–10 h and MY 35 L_S 126°–146°, Lat 70°S–64°S, LST 14.5–16 h. In the first case corresponding to the southern hemisphere in the morning was found around 65 km a WN-1 with an amplitude of 10% of the averaged temperature in addition to a 5% WN-3. In the afternoon case corresponding to the southern hemisphere too but 20° in L_S later, was found a 5% amplitude

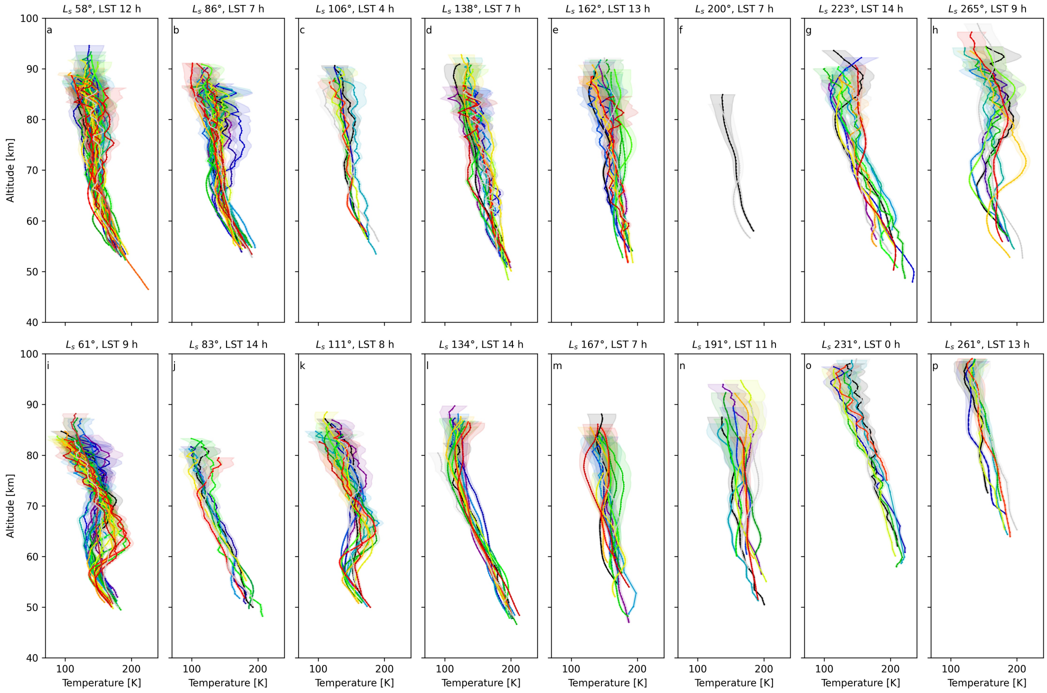

Figure 10.20: Profiles of temperature for specific solar longitude, latitude, and local solar time ranges in MY 35. Upper panels (a to h) for the northern hemisphere and lower panels (i to p) for the southern hemisphere. The mean solar longitude and local solar time are provided above the panels. The shaded area represents the uncertainty on the profiles.

for WN-1 around 65 km. For other altitudes, it is difficult to provide any information about longitudinal variations as the uncertainties on the amplitudes are important. In addition, when the uncertainties on the amplitude increase, those on the corresponding phase are important too, indicating an unsteady fit on the phase. We need also to note that only the tidal activity is fitted here while the variations of temperature might be due in addition to variations due to circulation or gravity waves, the latter mainly happening where Mars topography contains large variations.

Those results of stronger tidal activities in the morning and lower tidal activities in the afternoon were already reported in (Jain et al., 2021) although their results were reported for the 90-105 km altitude range.

10.6 CO_2 condensation temperature limit

Tropospheric CO_2 ice clouds were already reported from the MOLA instrument onboard MGS in the polar night (Ivanov and Muhleman, 2001; Pettengill and Ford, 2000). Mesospheric CO_2 ice clouds were reported from Mariner 6 and 7 from a spectral signature at 4.2 µm (Herr and Pimentel, 1970) but later attributed to CO_2 fluorescence (Lellouch et al., 2000; Piccialli et al., 2016). During the entry of Pathfinder in the Martian atmosphere, temperature in the mesosphere was found lower than the limit for CO_2 condensation (Schofield et al., 1997). Earth ground measurements also detected some locations in Mars mesosphere where the temperature was lower than this limit (Clancy and Sandor, 1998). When Mars Express (MEx) started its science operations, several instruments identified the presence of CO_2 ice clouds. First, the Planetary Fourier Spectrometer (PFS) reported the detection of a CO_2 ice spectral signature at L_S 135°, LST 11h30 and at 80-85 km altitude (Formisano et al., 2006). Then the SPectroscopy for the Investigation of the Characteristics of the Atmosphere of Mars (SPICAM) instrument detected very high clouds at $\sim$100 km on the nightside in the Southern winter subtropical region (Montmessin et al., 2006; Forget et al., 2009). Other measurements with the Observatoire pour la Minéralogie, l'Eau, les Glaces et l'Activité (OMEGA) instrument detected the CO_2 ice spectral signature at 4.26 µm before and after the northern summer solstice (L_S 45° and 135°) (Montmessin et al., 2007). Other super cold pockets were reported from the Thermal Emission Spectrometer (TES) and the Radio Sounder experiment onboard MGS (Colaprete et al., 2008) as well as from MCS onboard MRO (Sefton-Nash et al., 2013).

The mechanisms producing those cold pockets are involving thermal tides (González-Galindo et al., 2011) where the minima of temperature are further amplified with gravity waves (Spiga et al., 2012; Listowski et al., 2014). The nucleation of CO_2 ice clouds cannot be solely homogeneous as it would require temperature minima 50 K lower than the limit for CO_2 condensation, and this temperature has never been reported in Mars atmosphere (González-Galindo et al., 2011). It might be initiated by dust or water ice but this heterogeneous nucleation still needs a temperature 8-18 K lower than the limit for CO_2 condensation (Nachbar et al., 2016).

Those mechanisms are not yet fully understood and more reports of CO_2 ice clouds were provided from TES and Mars Orbiter Camera onboard MGS (Clancy et al., 2007), OMEGA and High Resolution Stereo Camera (HSRC) onboard MEx (Scholten et al., 2010; Määttänen et al., 2010), Thermal Emission Imaging System (THEMIS) onboard Mars Odyssey (Inada et al., 2007; McConnochie et al., 2010), OMEGA and Compact Reconnaissance Imaging Spectrometer for Mars (CRISM) (Vincendon et al., 2011), Imaging Ultraviolet Spectrograph (IUVS) onboard Mars Atmosphere and Volatile EvolutioN (MAVEN) (Jiang et al., 2019; Stevens et al., 2017), PFS and OMEGA (Aoki et al., 2018), CRISM, MCS and Mars Color Imager (MARCI) onboard MRO (Clancy et al., 2019). All those datasets have time and location biases but most of the reported presence of CO_2 ice clouds are at the equator (20°S-20°N) in-between Meridiani (0° longitude) and the extent of Valles Marineris (150°W) around northern summer and at mid-latitudes in the southern hemisphere east of Hellas Bassin around L_S perihelion (200°-300°).

Liuzzi et al. (2021) already reported the presence of CO_2 ice clouds in 26 occultations from NOMAD-SO using three criteria: the broadband reduction of the signal due to scattering of the sunlight by the cloud, a temperature lower than the limit for CO_2 condensation, and the spectral signature of CO_2 ice clouds at $3820\,\mathrm{cm}^{-1}$, in diffraction order 169. Amongst those 26 occultations, there were five occultations where diffraction order 148 was scanned. They correspond to the timestamps:

- 2019-05-05 07:00:03 ingress,
- 2019-07-15 16:23:35 egress,
- 2019-11-05 16:20:06 egress,
- 2019-12-16 14:35:36 ingress,
- 2019-12-16 22:27:53 ingress.

From this analysis on diffraction order 148 from MY 34 to MY 36, we found eight over 1811 temperature profiles with values lower than the limit for CO_2 condensation in the mesosphere:

- 2018-05-04 14:10:44 ingress,
- 2019-05-05 07:00:03 ingress,
- 2019-10-13 04:31:21 ingress,
- 2019-12-16 14:35:36 ingress,
- 2021-07-01 05:49:15 egress,
- 2022-03-06 12:23:50 egress,
- 2022-05-14 17:08:26 ingress
- 2022-12-16 13:50:50 egress,

The second and third ones in the list from Liuzzi et al. (2021) could not be found here as the CO_2 ice cloud was found at too low altitudes for this dataset (respectively 45 and 55 km). The last one in the list from Liuzzi et al. (2021) could not be found here as the temperature profile does not reach the limit for CO_2 condensation but is as close as 2 K from it at the altitude reported in Liuzzi et al. (2021) (65 km). The four last ones in the second list could not be reported in Liuzzi et al. (2021) as the time range of this study stopped at the end of 2020.

Those eight profiles are gathered in Figure 10.21. The ordering in the legend is the same as in the list above. The temperature limit is computed from the formula provided in Sánchez-Lavega et al. (2004). We see that the reduction of the transmittance, which is here just the value at pixel 180, is happening at tangent altitudes lower than the temperature minimum. This height difference depends on the position of the cloud along the line of sight. For the same reason, the decrease in transmittance is broader in height if the cloud is horizontally broad and covers more tangent heights. The two profiles in MY 35 and for L_S 20° ad 121° were already presented in Liuzzi et al. (2021). A strong decrease in transmittance is visible for MY 34 L_S 170°, MY 35 L_S 20°, MY 35 L_S 121°, MY 36 L_S 66°, MY 36 L_S 355° which are all happening at latitudes lower than 40°.

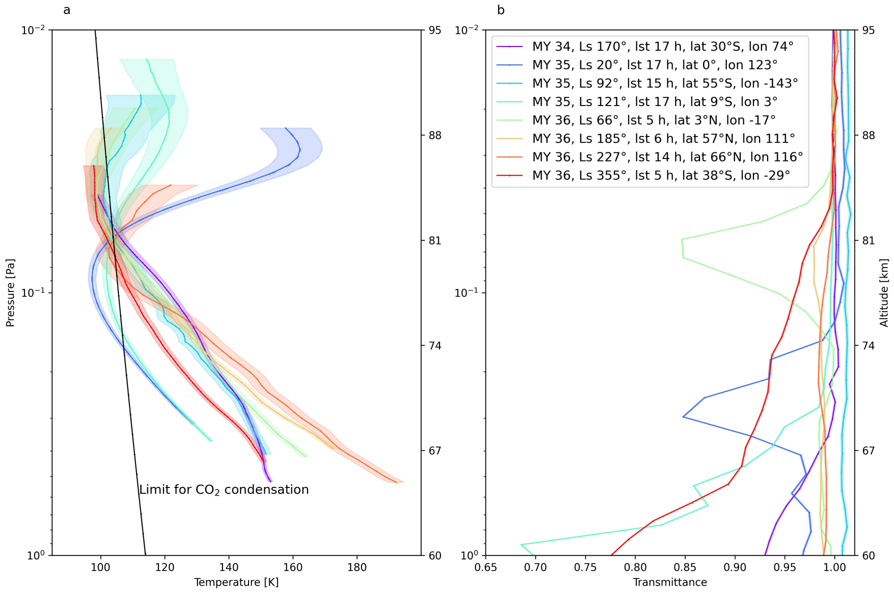

Figure 10.21: The possible presence of CO_2 ice clouds in the dataset of temperature retrieved from NOMAD-SO for diffraction order 148 in MY 34 to MY 36. Panel a for the temperature profiles and panel b for the transmittance at pixel 180. The second Y-axis provides rough altitude values.

Mesospheric CO_2 ice clouds are reported either closer to the equator (Aoki et al., 2018; Liuzzi et al., 2021) in L_S 0°-140° and in L_S 200°-300° at midlatitudes in the Southern hemisphere.

The three profiles at high Northern latitudes, MY 35 L_S 92° (light blue), MY 36 L_S 185° (yellow), and MY 36 L_S 227° (orange) do not have a clear reduction of the baseline meaning that a CO_2 ice cloud is less likely to be effectively present in those occultations.

The two occultations with a reduction of the transmittance over only a few kilometers, MY 35 L_S 20° (dark blue) and MY 36 L_S 66° (light green), are located at the equator. A third profile, MY 35 L_S 121°, is close to the equator (9°S) and contains a long reduction of the baseline possibly due to the presence of the cloud further away from the tangent point combined with a long extends. MY 36 L_S 355° (red) at mid-latitudes in the southern hemisphere contains a reduction of the baseline at an altitude well below the temperature minimum. This profile is close to the season for CO_2 ice clouds but further away from the equator. The last profile with a reduction of the baseline is MY 34 L_S 170° (purple) at mid-latitudes in the Southern hemisphere. All those profiles are located where CO_2 ice clouds were already previously reported.

Interestingly, we can see that there are two different sets of temperature minima: two happening at 0.1 Pa and those happening at 0.7 Pa. The first ones happens in the morning and the second ones happen in the afternoon.

10.7 Mesospheric inversion layers

The previous section reported some strong cold pockets in the mesosphere but this dataset contains as well some strong warm layers. Nakagawa et al. (2020a) already reported those strong warm layers in the nightside and some warm layers are also noticeable in the datasets presented in Belyaev et al. (2022) and López Valverde et al. (2022). I adopted a similar method than the one implemented in Nakagawa et al. (2020a) to infer their presence in this dataset:

- 1. I compute a linear regression on the temperature profile to derive a background temperature profile

- 2. A profile contains a warm layer if some of its values are 20 K higher than this background.

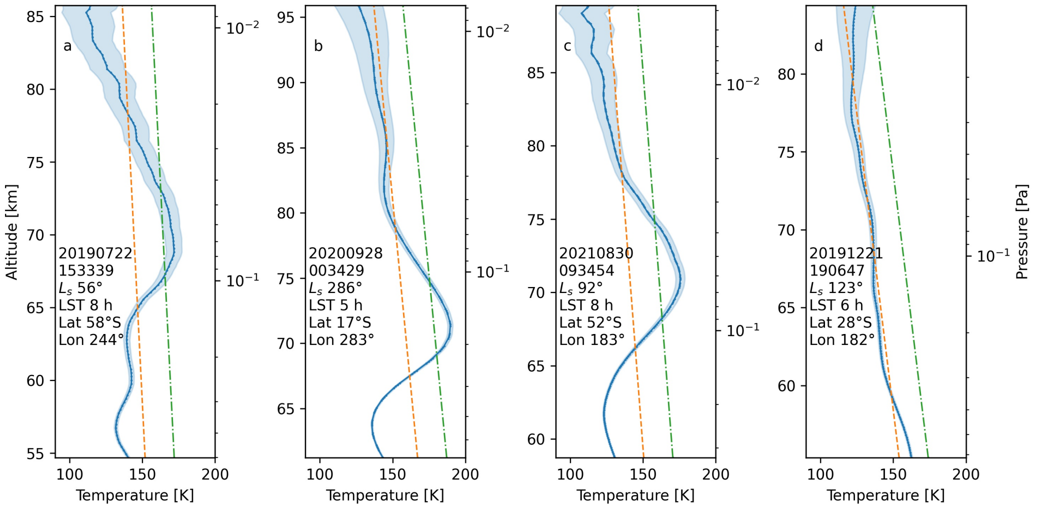

Figure 10.22: Four examples of temperature profiles in blue where the fitted background is plotted in dashed orange, and the limit of background plus 20 K is plotted in dot-dash green. Panels a to c contain a warm layer but not panel d. The dates, times, solar longitudes, local solar times, latitudes, and longitudes are reported on the left side of each panel.

Figure 10.22 shows some examples of profiles with the background in dashed orange and the +20 K limit in dash-dot green. Panels a to c thus contain a warm layer but not panel d.

The detected warm layers for the dataset in MY 35 and 36 are presented in Figure 10.23 in orange while the blue dots are the mean position of all occultations reported here. As already reported in section 10.1, we notice some important biases in the distribution of occultations and this dataset is represented in histograms in Figures 10.24 and 10.25. The histogram on solar longitude in Figure 10.24 is split for North (panel a) and South (panel b). There is an important seasonal trend with most of the warm layers found in the Southern hemisphere around Southern winter solstice (L_S 90°) while around Northern winter solstice (L_S 180°) most of them are found in the Northern hemisphere. The times and locations of the warm layers are similar to the "polar warming" happening in the mesosphere in the polar night. This warming is due to adiabatic heating from the downward flux of the Hadley cell (Forget et al., 1999; Wilson, 1997).

Coming back to the paper from Nakagawa et al. (2020a), they reported the presence of warm layers in the nightside in the mesosphere in a dataset covering L_S 0° to 180°. During those solar longitudes, the warm layers were present at mid-latitudes in the Northern hemisphere as well as at high latitudes in the Southern hemisphere but absent in the Southern mid-latitudes. Panels a and g (for L_S 0° to 180°) in Figure 10.25 show very similar results at the terminator.

From panels b, e, h, and k, no clear longitudinal trend can be seen but from panels c, f, i, l we note a strong dependence with local solar time. Almost all warm layers are seen between 8 h and 10 h with most of the remaining ones between 14 h and 16 h.

Amongst the 1848 profiles used for this section 86 (4.7%) of them contains a warm layer. This value is lower than those reported in Trompet et al. (2023a) as the dataset in this manuscript has been reprocessed due to a problem with the clock time in the SPICE kernels in the previous version. But the conclusions remains the same. The number of warm layers for each half year is provided in table 10.1.

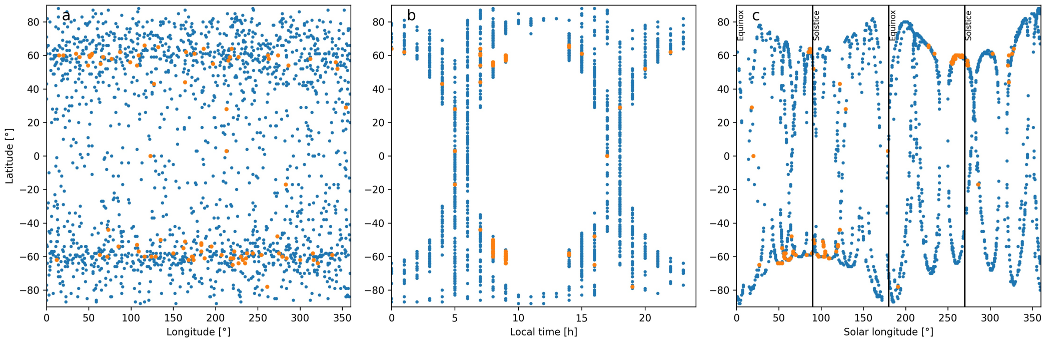

Figure 10.23: Location and time of all retrieved temperature profiles in MY 35 and 36 in blue and those with a warm layer in orange. All y-axis are latitudes and x-axes are longitudes (panel a), local solar times (panel b) and solar longitudes (panel c). In panel c, the vertical lines indicate the solstices and equinoxes. Note that the y-axis is in log scale to better see the warm layers distributions.

Time range	# of profiles	# warm layers	Ratio [%]
MY 35 L_S 0°-180°	454	34	7.5
MY 35 L_S 180°-360°	202	11	5.4
MY 36 L_S 0°-180°	403	20	5.0
MY 36 L_S 180°-360°	789	21	2.7
Total	1848	86	4.7

Table 10.1: Number of temperature profiles retrieved in half a year, the number of strong warm layer found amongst them and the ratio of warm layer to the total number of profiles.

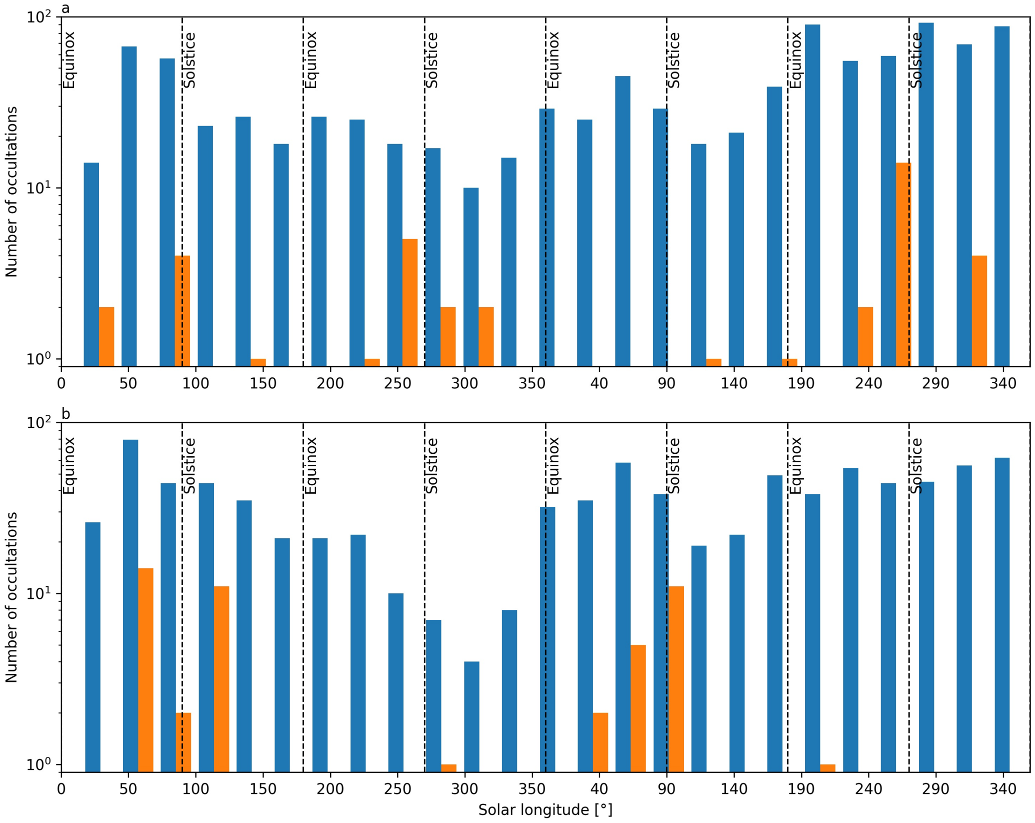

Figure 10.24: Histograms on solar longitudes of all retrieved temperature profiles in MY 35 and 36 in blue and those with a warm layer in orange.

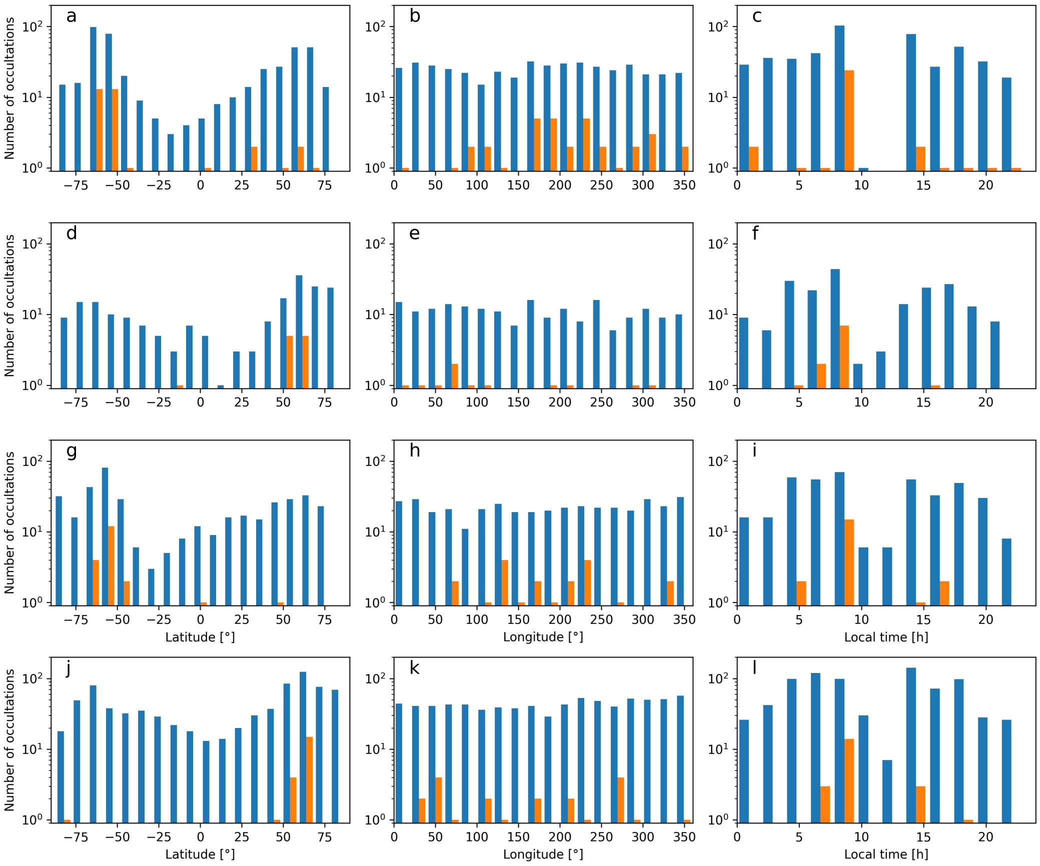

Figure 10.25: Histograms on latitude, longitude and local solar time for all retrieved temperature profiles in MY 35 and 36 in blue and those with a warm layer in orange. Panels a, b, c for MY 35 L_S 0° to 180°, panels d, e, f for MY 35 L_S 180° to 360°, panels g, h, i for MY 36 L_S 0° to 180°, and panels j, k, l for MY 36 L_S 180° to 360°. Note that the y-axis is in log scale to better see the warm layers distributions.

10.8 summary

This chapter gathered the main results from the carbon dioxide density and temperature profiles at the terminator and in the mesosphere retrieved from the SO channel of NOMAD. First, the coverage in space and time is described. For solar occultation measurements, there is a correlation between latitudes and the local solar times (LST). Most of the latitudes scanned are around 60°. The LST around midday are scanned in the hemisphere in spring or summer and the LST around midnight are scanned in the hemisphere in autumn and winter.

This dataset shows a clear seasonal variation of the carbon dioxide density in the mesosphere following the known dust cycle. Warm layers are present in the morning and appear stronger in the Southern Hemisphere. This dataset spans Martian years 35 and 36 and very similar variations of carbon dioxide are seen in both years.

The latitudinal variations highlight the seasonal change in circulation as the Hadley cells pass from symmetrical cells around equinoxes to asymmetrical cells around solstices. There is an enhanced cell in the hemisphere close to summer and a weaker cell in the other hemisphere with still a stronger cell in the summer hemisphere. This results in an important increase in the density in that hemisphere around the summer solstice. Comparing MY 35 and 36 for specific solar longitude ranges shows very similar temperature values and variations.

Longitudinal variations could be studied for specific solar longitude, latitude, and local solar time ranges. The latitudinal range has to be around 60°. Important longitudinal variations were found around 70 km altitude for local solar times around 7 h to 9 h. An analysis of the non-migrating tides is reported and the main tidal components found are a first component of 10% and a third component of 5% of the background temperature.

Some temperature profiles present some strong cold layers and others some strong warm layers. Concerning the temperature with a cold layer, some of them have values lower than the limit for carbon dioxide condensation and match a substantial decrease in the baseline of the spectra. This translates to the presence of an important layer of aerosols likely to be some carbon dioxide ice clouds. Most of them are in the first half year close to the equator at longitudes where the topography of Mars has many important variations. The times and locations of the warm layers are also presented and compared to a previous study concerning the nightside of the Mars mesosphere. Those warm layers are mainly seen in the late morning at high latitudes in the hemisphere closer to winter and mid-latitudes closer to summer.

In conclusion, the mesosphere of Mars comprises important density and temperature variations. Some seasonal and latitudinal temperature variations were related to known phenomena. This analysis first focussed on longitudinal variations. Due to the typical coverage of solar occultation measurements, this analysis can be done only for particular ranges in time and location. However, some important longitudinal variations were found at 70 km altitude. A second part of this analysis focussed on the very cold and very warm layers in the mesosphere and similar results were found in the literature. Continuing the comparison with general circulation models will allow us to learn more about the atmospheric mechanism behind those results.

Chapter 11

Conclusions and outlook

The SO channel of the NOMAD instrument benefits from the legacy of the SOIR instrument (2005-2014) and its calibration stands on the preliminary work made for SOIR (Mahieux, 2011). One major difference with the calibration for SOIR is the presence of an asymmetrical ILS for SO. Special attention was given to the transmittance calibration (see chapter 6) which is not as simple as one would first think due to instrumental variations, spacecraft pointing, and possibly limb darkening (Trompet et al., 2016). This work also focussed on the pixel-to-wavenumber calibration and its variation with the instrument temperature. The parameters for the pixel to wavenumber calibration are provided in section 5.2.1. Concerning the outlook for the calibration of NOMAD-SO spectra, still, some artefacts remain with the current transmittance calibration. One of those artefacts is a curvy baseline of the transmittance spectra probably due to a modification of the instrument function along an occultation. This artefact is now simply removed by fitting the baseline with a polynomial but in the future, we could investigate a possible improvement by using a wider pixel grid using zero-padding, providing the wavenumber range for each spectrum that varies with the instrument temperature and computing the transmittance on the wavenumber grid instead of the pixel grid.

Before the launch of ESA's TGO mission, claims of methane detection in Mars atmosphere were reported from Earth ground observation (Krasnopolsky et al., 2004; Mumma et al., 2009), orbiter (Formisano et al., 2004), as well as from a rover (Webster et al., 2015) with quantifications in the order of $1\,ppb$. The detection of this molecule in the atmosphere could have important consequences concerning astrobiological possibilities. A primary objective of the NOMAD instrument was to detect and quantify the presence of methane in the Martian atmosphere. However, no trace of the spectral signature of methane around $3020\,\mathrm{cm}^{-1}$ could be found from both the ACS and NOMAD instruments (both onboard TGO). The detection limits reported from both ACS and NOMAD are at least an order of magnitude lower than the detections reported before the Science phase of TGO. But the altitudes with the highest sensitivity of those instruments to methane is around $10\,km$ while the measurements of the rover are made at the surface.

This work mainly focussed on the retrievals of CO_2 density and temperature profiles. It has been known for a long time that the retrieval of atmospheric parameters from remote sensing is an ill-posed problem (e.g. Phillips (1962)). This ill-posedness is translated here into an important impact on the inverted parameters of any error or uncertainty on the measurement. The presence of noise in the data, an extended field of view, and a vertical sampling leads to the presence of some spurious features in the retrieved solution. Many methods have been proposed to "regularise" the solution. Amongst them, there is the Monte Carlo method, the Optimal Estimation method (Rodgers, 2000), or the Tikhonov method (Tikhonov, 1963). In practice, the two last methods are similar if one chooses carefully the regularisation term in the Optimal Estimation method (see section 4.2.3). In this work, we have chosen to split the spectral inversion and the vertical inversion to be able to fine-tune the regularisation. We have made tests with seven known methods and found that the best one is the expected error estimation (see sections 4.2.5 and 8.1.2). We have also shown that the regularisation matrix in the Tikhonov method corresponds to the Cholesky factorization of the inverse of the covariance matrix used in the statistical method (see section 4.2.3). Retrievals were performed mainly in the mesosphere (approx. 50-100 km altitude) with spectra from diffraction order 148 and we are starting to retrieve CO_2 and temperature profiles in the troposphere ($\approx 0 - 50\,km$ altitude) with diffraction order 132. However, some diffraction orders contain stronger CO_2 lines to infer CO_2 density and temperature in the thermosphere ($\approx 100 - 200\,km$ altitude). Those altitudes correspond to very low pressures ($< 10^{-3}\,Pa$) and we would need to check if non-local thermodynamic equilibrium might play a role there.

The results of this work have been compared with datasets from co-located measurements or simulations to validate these retrievals. The focus was given to MCS datasets as it has been previously validated towards other datasets (Shirley et al., 2015). A proper comparison requires taking into account the possible presence of bias from the instrument, and/or from the retrievals. We have seen that too high regularisation is capable to biasing the solution towards the *a priori*. This clearly needs to be taken into account. A quantification of the comparison can be computed only for co-located profiles. The comparison with MCS gave an average difference of $0.1\,K$ with an average absolute difference of $8.5\,K$. A comparison to simultaneous measurements from the ACS-NIR channel gave an average difference of $-4.7\,K$ while the average absolute difference is $6.7\,K$. A comparison of those numbers leads to thinking that most of the absolute difference with the MCS dataset might come from the difference in co-location. In addition, the datasets compared can have different vertical resolutions leading to differences as some variabilities can be seen in the dataset with a better vertical resolution. Also, some differences might be from bias toward the *a priori*. In the method used in this work, this *a priori* can be considered as the null vector. A proper comparison must consider the averaging kernels, the *a priori*, and the regularisation operator. Unfortunately, none of the datasets available in the literature provide those data.

The results found in this work and partly reported in Trompet et al. (2023a,b) are supporting previous results, in particular, concerning the CO_2 seasonal variation. The solar longitudes and latitudes probed in MY 35 and 36 were close enough and we found very similar temperature variations comparing those two Martian years. Some cold pockets that could bear the presence of CO_2 ice clouds were found with a decrease of the corresponding transmittance inducing the presence of a cloud or an extended object able to scatter or absorb most of the light. The corresponding locations match the previously reported presence of CO_2 ice clouds. We also checked for the presence of longitudinal variations and found important variations around 65 km in the morning terminator while the evening terminator was much smoother. Concerning this last analysis, only two ranges in solar longitude, local solar time, and latitudes were reported here. Those ranges are always located around 60° latitude (north or south) due to the orbit of TGO. In the case of the morning terminator, an analysis of the amplitude and phase showed mainly a wavenumber-1 with a 10% amplitude with a wavenumber-3 with a 5% amplitude with respect to the background temperature. This analysis could be extended to a dozen of other adequate ranges. An analysis of the vertical variabilities in the profiles showed that amongst the 1848 profiles used for this work, 86 (4.7%) of them contains a warm layer.

The data reported in this work is available on the VESPA portal (https://vespa.obspm.fr) as well as all profiles derived from the SOIR measurements (Trompet et al., 2018).

Appendix A

Recall on simple linear regression

The simple linear regression is described in detail in Taylor (1997, chap. 8). The main formulas are reproduced hereafter as they are used in several part of this manuscript.

We want to fit the vector y as a linear function of the vector x, both containing N values

$$y = A + Bx. \tag{A.1}$$

where A and B are the coefficients to fit. Deriving $\sum_{i=0}^{N} y_i - A - Bx_i$ with respect to A and B and solving the equations, we find

$$\begin{aligned} A &= \frac{\sum x^2 \sum y - \sum x \sum xy}{\Delta}, \\ B &= \frac{N \sum xy - \sum x \sum xy}{\Delta}, \\ \Delta &= N \sum x^2 - \left(\sum x\right)^2. \end{aligned} \tag{A.2}$$

The interpolated values of y will be different from the measured ones except if all measured values are strictly linear along x. The uncertainties on the interpolated y and the coefficients A and B are

$$\begin{aligned} \sigma_y &= \sqrt{\frac{1}{N-2} \sum_{i=0}^{N} (y_i - A - Bx_i)^2}, \\ \sigma_A &= \sigma_y \sqrt{\frac{\sum x^2}{\Delta}}, \\ \sigma_B &= \sigma_y \sqrt{\frac{N}{\Delta}} \end{aligned} \tag{A.3}$$

where σ_A and σ_B are computed by error propagation from the uncertainties on the measurements x and y. All those values are standard deviations. The standard error are then found as $s = \sigma/\sqrt{N}$. Those uncertainties considered that all uncertainties on the measured y are similar and that the uncertainties on x are negligible.

The uncertainty on any extrapolated value Y(X) is (Casella and Berger, 2002)

$$\sigma_Y(X) = \sigma_y \sqrt{N + 1 + \frac{NX - \sum x}{\Delta}}. \tag{A.4}$$

Appendix B

Analytical integration of the hydrostatic equilibrium equation

This appendix details the analytical integration of equation 8.5 using equations 2.2, 2.22 and 8.7. Replacing 2.2 and 2.22 in 8.5, we find

$$\Delta p_i = -m_a\, n_i g_0 r_M^2 \exp\left(\frac{z_i}{h_i}\right) \int_{z_i}^{z_{i+1}} \frac{exp\left(\frac{-z}{h_i}\right)}{(r_M+z)^2} \mathrm{d}z. \tag{B.1}$$

Now substituting $x = (r_M + z)/h_i$,

$$\Delta p_i = -\frac{m_a\, n_i g_0 r_M^2}{h_i} \exp\left(\frac{r_M + z_i}{h_i}\right) \int_{(r_M+z_i)/h_i}^{(r_M+z_{i+1})/h_i} \frac{exp(-x)}{x^2} \mathrm{d}x. \tag{B.2}$$

This last integral is a close form of the exponential integral (Zhang and Jin, 1996, eq. 19.1.1) defined as

$$E_n(x) = x^{n-1} \int_x^{\infty} \frac{exp(-y)}{y^n} \mathrm{d}y. \tag{B.3}$$

Recognizing indeed $\frac{E_2(x)}{x}$ in the integral in B.2,

$$\Delta p_i = \frac{m_a\, n_i g_0 r_M^2}{h_i} \exp\left(\frac{r_M + z_i}{h_i}\right) \left[\frac{E_2\left(\frac{r_M+z_i}{h_i}\right)}{\frac{r_M+z_i}{h_i}} - \frac{E_2\left(\frac{r_M+z_{i+1}}{h_i}\right)}{\frac{r_M+z_{i+1}}{h_i}} \right]. \tag{B.4}$$

Appendix C

Derivation of the scale height from a linear interpolation on the natural logarithm of the density

Considering a density profile with a finite number of values n_i, we want to find a linear interpolation of the natural logarithm of this density profile. The formula for the linear interpolation gives

$$\ln(n) = \ln(n_i) + (z - z_i)\frac{\ln(n_{i+1}) - \ln(n_i)}{z_{i+1} - z_i}. \tag{C.1}$$

Rearranging it as

$$n = n_i \exp\left(\frac{z_i - z}{\frac{z_{i+1}-z_i}{\ln\left(\frac{n_i}{n_{i+1}}\right)}}\right). \tag{C.2}$$

This equation is similar to 2.22 if we pose

$$h_i = \frac{z_{i+1} - z_i}{\ln\left(\frac{n_i}{n_{i+1}}\right)}. \tag{C.3}$$

The formula 2.22 can be used only if the scale height and the temperature can be considered as constant with altitude, i.e. the altitude step must be small with respect to the scale height.

List of Tables

2.1 Earth and Mars main parameters comparison (Haberle et al., 2017). 21

3.1 The five most important isotopologues for CO_2 with their three digit code and their abundances for Earth and Mars (Shved, 2016). 36
3.2 Main solar lines in the NOMAD-SO spectral range. 42

5.1 Table of coefficients F_i corresponding to different polynomial orders n with i an integer in $[0, n]$. Those coefficients are in units of cm^{-1}. 75
5.2 Diffraction orders and altitude for the retrievals of CO_2 density profiles. The first column provides the isotopologue number as defined in the AFGL notation (Mcclatchey et al., 1973): 626 for $^{12}C^{16}O^2$, 636 for $^{13}C^{16}O^2$, 628 for $^{16}O^{12}C^{18}O$, ... 82
5.3 Parameters of the five most abundant CO_2 isotopologues. The Earth abundance are those provided in HITRAN and used in ASIMUT. The Mars abundances are those provide in (Shved, 2016). 83
5.4 The main CO_2 bands regularly scanned by NOMAD-SO. The AFGL code for CO_2 (Rothman and Young, 1981; Esplin et al., 1988; Mcclatchey et al., 1973) rovibrational energy levels is $\nu_1\nu_2 l\nu_3 r$ (see section 3.1.1). The fundamental modes are those described in Figure 3.1. The diffraction orders correspond to spectral ranges specific to the NOMAD-SO channel and are explained in chapter 5. The last column gives the corresponding CO_2 isotopologue. 83

6.1 Table of S_{min}: the tangent altitudes separating the atmosphere region T and the Sun region U. 94

8.1 Relative error on Δp for $z_i = 50\,\text{km}$ from the different methods. The methods are sorted in ascending order of absolute relative error on Δp. 120

10.1 Number of temperature profiles retrieved in half a year, the number of strong warm layer found amongst them and the ratio of warm layer to the total number of profiles. 176

List of Figures

2.1 Topography of Mars from Mars Orbiter Laser Altimeter on board Mars Global Surveyor (image from NASA/JPL, downloaded at https://www.planetary.org/space-images/mars-orbiter-laser-altimeter). O the upper panels, the Southern hemisphere is on the left and the Northern hemisphere is on the right. 20

2.2 Relative error on g_0 as computed by equation 2.3 and 2.1 as a function of longitude and latitude at solstices (L_S 90° and 270°) and equinoxes (L_S 0° and 180°). . . . 23

2.3 Representation of the vertical forces (black) acting on a portion of the atmosphere (blue) in hydrostatic equilibrium. 24

2.4 Viking Landers pressure curves measured on the landed surface (image downloaded from https://www.planetary.org/space-images/atmospheric-pressure-data-viking-landers). 28

2.5 In situ measurements of temperature from different landers. The lower, middle and upper atmospheres correspond respectively to the troposphere, mesosphere and thermosphere. Image credits: Haberle et al. (2017) 29

3.1 Representation of the three fundamental vibration modes of CO_2. The black and red circles represent respectively the carbon and oxygen atoms. 36

3.2 The intensity of the lines for transition $2\nu_1 + \nu 2$ (AFGL code 21102-00001) of CO_2 as a function of temperature and computed with equation 3.8. This band contains a Q branch around $3340\,cm^{-1}$. 38

3.3 The intensity of lines of different molecules reported in Mars atmosphere and in the mid-infrared. The values are taken from the HITRAN database. 39

3.4 Geometry of an occultation. 43

3.5 Discretization of the atmosphere for the Abel transform. 45

3.6 Relative error on c due to the discretisation of the atmosphere. The density used here is the GEM-Mars averaged CO_2 density profile from version a585. 45

3.7 Example of K matrix where the y-axis corresponds to the i index and the x-axis corresponds to the j index. Those index correspond to around 60 km for index 0 to around 100 km for index 36. The colour bar provides the values of the matrix in meter. We see that the K matrix is an upper triangular matrix with values decreasing with off-diagonal terms. 46

4.1 Example of $\boldsymbol{G_0}$ matrix. 53

4.2 Example of slant columns (upper left panel) and local densities (upper right panel). From the local density $\boldsymbol{n}$, a slant column $\boldsymbol{c}$ is computed. Some random noise is added from a Gaussian distribution with $\sigma = 0.1$ to get $\hat{\boldsymbol{c}}$ (see the ratio $\hat{\boldsymbol{c}}/\boldsymbol{c}$ in the lower left panel). A local density $\hat{\boldsymbol{n}}$ is retrieved from $\hat{\boldsymbol{c}}$ using the non-regularised least square formula (see the ratio $\hat{\boldsymbol{n}}/\boldsymbol{n}$ in the lower right panel). 54

4.3 Same as figure 4.2 but with added noise by considering a standard deviation of 0.01. 55
4.4 Values for the middle row of the $\boldsymbol{S_a}$ matrix obtained by inverting different combinations of differential operators. The orange and blue curves are the Markovian covariance matrices. The green curve is the identity matrix. The red, purple and brown curves correspond, respectively, to the $\boldsymbol{L_0} + \boldsymbol{L_1}$, $\boldsymbol{L_0} + \boldsymbol{L_1} + \boldsymbol{L_2}$ and $\boldsymbol{L_0} + \boldsymbol{L_2}$ differential operators. 58

5.1 The NOMAD instrument (Vandaele et al., 2015a) with (1) the SO channel, (2) the LNO channel; (3) the UVIS channel; (4) the electronics SINBAD. 64
5.2 NOMAD-SO base plate (Neefs et al., 2015): 1) Entrance consisting of three flat mirrors, 3) AOTF entrance optics, 4) diaphragm, 6) the AOTF, 7) AOTF exit optics, 8) folding mirror, 9) spectrometer entrance slit, 10) off-axis parabolic mirror, 11) the echelle grating, 12) folding mirror, 13) detector optics, 14) the detector. . 64
5.3 Mean SNR in the Sun region for on-board background subtraction (green), background subtraction (orange), and no background subtraction (blue). 68
5.4 Example of refined and normalized line for 20180502_130154_0p3k_SO_A_I_149, bin 1. The initial spectrum is in blue, the refined one with zero padding is in green and the minimum of the line is the orange dot. The black curve in the left panel is the baseline fitted with the asymmetric least-square method. The curves in the right panel have been normalized by dividing the curves in the left panel by the black curve. 71
5.5 Example of fitted wavenumber shift for the CO$_2$ lines in the dataset 20180626_182155_1p0a_SO_A_E_14 bin 2. The shift computed here is with respect to the previous calibration. 72
5.6 Coefficients of the shift with respect to pixels and computed from a linear regression on the coefficients computed along the spectra for 20181231_210823_1p0a_SO_A_I_123. 73
5.7 Example of corrected spectrum for 20180502_130154_0p3k_SO_A_I_149, bin 1 at 60 km. The initial spectrum is in black, and the new one is in red. The main theoretical CO$_2$ lines positions are marked with vertical lines. The green lines are those used for the correction. 74
5.8 Variation of the position of the line on the detector as a function of temperature for diffraction order 116 and all datasets until August 2021. 74
5.9 Pixel to wavenumber for diffraction order 116 and all datasets until August 2021. 75
5.10 Variation of the position of the line on the detector as a function of temperature for diffraction order 116 and all datasets until August 2021. 76
5.11 Minimum and maximum spectral sampling within diffraction orders. 77
5.12 Spectral resolution computed from the model 5.11 and 5.12 in black for all diffraction orders and pixels referred on the right of each curve. The minimum and maximum spectral resolution computed from the detector array is provided, respectively, in red and blue. The green, orange and purple curves are the width and the opposite of the displacement for the first and last pixels, respectively. 79
5.13 Blaze function for different diffraction orders in the range 110-115, 145-150, and 185-190. 81
5.14 Simulated transmittance of CO$_2$ five main isotopologues at an altitude of 5 km with GEM-Mars version a585 (Erwin et al., 2018) and convolved with an ILS consisting of one Gaussian with a width of $0.15 cm^{-1}$. The spectral range of the main diffraction order where CO$_2$ density is retrieved are shown in grey. 85
5.15 Line intensities for CO$_2$ (orange), H$_2$O (blue) and CO (green) in NOMAD-SO spectral range. Examples of extension of diffraction orders 132, 140, 148, and 165 are represented in black. 86

5.16 Example of curves of growth for order 149 and dataset 20180502_130154_1p0a_SO_A I. 87
5.17 Example of curves of growth for order 165 and dataset 20180611_201459_1p0a_SO_H I. 88

6.1 Comparison of the variations of the background (blue) and the signal for order 164 (red) at pixel 180 for dataset 20180521_195114_0p3k_SO_A_E_164. 92
6.2 Example of the signal recorded on pixel 180, bin 1 for the dataset 20180820_094517_0p3a_SO_A_E_134. For diffraction order 134, the top of the atmosphere is 120 km. 93
6.3 Example of variation of the signal over six pixels (numbers 20, 80, 140, 160, 200, 260) for bin 1 of dataset 20180528_004211_0p3j_SO_A_I_168. The linear regression is in green and the extrapolated values are in red and purple. 94
6.4 Signal for pixels 160 to 240 for dataset 20180607_140558_0p3a_SO_A_I_133. . 95
6.5 Example of occultation (20180729_032027_0p3j_SO_1_I_121 bin 3) where there was a movement of the High Gain Antenna (HGA). The selected solar region for the transmittance calibration is represented in green. The region with the drop in the signal recorded was avoided by the algorithm. 98
6.6 Mean signal (top), mean uncertainty on the signal(middle) and mean signal-to-noise ratio (bottom) in the S region for all datasets for diffraction order 168. Orange points are for datasets where the background is subtracted on-board TGO (before binning) while the blue points are for datasets with the background subtracted in the pipeline. 100

7.1 Example of NOMAD-SO spectra in black for occultation 20180823_063314_1p0a_SO_A_E, left panel for diffraction order 134 and right panel for diffraction order 135. Simulations of spectra containing 0.1 ppb and 1 ppb of methane are plotted in red and green respectively and a water spectrum in cyan (those spectra are simulated but not fitted to the experimental spectra). 102
7.2 Detection limits as a function of altitude for occultations in Martian year 34. The colour bars in the left and right panels represent respectively the solar longitude on the latitude. 104

8.1 Diagram of the retrieval of vertical profiles of CO_2 density, CO_2 partial pressure and temperature. Once retrieved, pressure (computed from the CO_2 partial pressure) and temperature are provided fir another loop on the retrieval until convergence. 108
8.2 Example of fit for order 165, dataset 20200806_074733_1p0a_SO_A I for four altitudes. The residuals are provided in the lower panels and compared to the $1-\sigma$ standard deviation on the spectra. 110
8.3 Example of fit for order 148, dataset 20200824_020917_1p0a_SO_A I for four altitudes. The residuals are provided in the lower panels and compared to the $1-\sigma$ standard deviation on the spectra. 111
8.4 Example of fit for order 132, dataset 20200622_155025_1p0a_SO_A I for four altitudes. The residuals are provided in the lower panels and compared to the $1-\sigma$ standard deviation on the spectra. There are also some strong water lines fitted as the water line at $2973.25\,cm^{-1}$. 112
8.5 Ratio of slant column below the altitude to the slant column above that altitude for different limits of the atmosphere considered (space). 114
8.6 Relative error with respect to n_{true} from the synthetic tests for different noise levels. 114

8.7 Inverted density profile for different λ_0 values for occultation 20200824_020917_1p0a_SO_A_I, diffraction order 148. The best λ_0 is 0.73 from the expected error estimation method. The first panel provides the density profiles and the second panel provides the corresponding relative uncertainties. The vertical line in the second panel corresponds to 1/6. The third panel provides the vertical resolution corresponding to each λ_0 with the Backus-Gilbert spread formula. The last panel represents the corresponding temperature profiles. 115

8.8 Retrieved profiles of CO_2 density in MY 35 with NOMAD-SO. 116

8.9 Relative error on Δp with respect to the number of points interpolated within each altitude z to compute the numerical integration of 8.5. As the integrand in 8.8 is concave up, the numerical integration slightly overestimates the value of the integral and the relative error is negative. The opposite of the relative error is shown here as we used a logarithmic scale. The curves are the same for all altitudes. 119

8.10 Relative error on the derived pressure(up) and temperature (down) profiles for the synthetic case. The left panels are for the upward case and the right panel are for the downward case. The colours are passing from dark blue to dark red corresponding to 0.99 to 1.01 times the density profile by step of 0.001. 121

8.11 Derived pressure profiles for the synthetic case with different values for the lapse rate Γ. 122

8.12 Convergence of the $\delta t/t$ values computed with the Monte Carlo method to the number of samples N_s. 125

8.13 Fit of the profiles along three loops over the temperature. The blue spectrum is the measured one. The other spectra are the fits and the iteration number is given in the lower right panel. The sub-panels contain the residuals. Those spectra are from the occultation 20200824_020917_1p0a_SO_A_I_148. 128

8.14 Profiles of density in the left panel and temperature in the right panel for occultation 20200824_020917_1p0a_SO_A_I_148 and for three loops over the temperature. 129

8.15 Profiles of density in the left panel and temperature in the right panel for occultation 20191216_222753_1p0a_SO_A_I_148 and for five loops over the temperature. 130

8.16 Relative error on the profiles for diffraction order 148 and MY 35. Profiles of slant column, density, and temperature in panels a, b, and c respectively. 132

8.17 Field of view (FOV), vertical sampling, and resolution for occultations where diffraction order 148 was scanned in MY 35. 133

8.18 Three examples of vertical profiles of temperature. Orange profile for the simulation from GEM-Mars, the blue curve for a combination of profiles from diffraction order 132 and 148, and the green curve for the combination with GEM-Mars. 134

9.1 Averaged profiles of GEM-Mars in orange and NOMAD-SO in blue for Martian year 35 and only dawns (0 hr < LST <12 hr). The shaded areas indicate the 1-sigma variability in the L_S-lat bins. The number below the panel number is the weighted absolute difference between the GEM-Mars and NOMAD-SO profiles. Approximated altitudes are provided as the second Y-axis. 138

9.2 Averaged profiles of GEM-Mars in orange and NOMAD-SO in blue for Martian year 35 and only dusks (12 hr < LST < 24 hr). The shaded areas indicate the 1-sigma variability in the L_S-lat bins. The number below the panel number is the weighted absolute difference between the GEM-Mars and NOMAD-SO profiles. Approximated altitudes are provided as the second Y-axis. 139

9.3 Maps of profiles from SO (second line), GEM-Mars (third line), and their difference (fourth line - SO-GEM) at dawn. The first line provides the coverage of the profiles. The left panels are for the Northern hemisphere and the right panels are for the Southern hemisphere. The black vertical line separates MY 35 and 36. 140
9.4 Maps of profiles from SO (second line), GEM-Mars (third line), and their difference (fourth line - SO-GEM) at dusk. The first line provides the coverage of the profiles. The left panels are for the Northern hemisphere and the right panels are for the Southern hemisphere. The black vertical line separates MY 35 and 36. 141
9.5 The 65 first co-located profiles of temperature from MCS (in orange) and NOMAD-SO (in blue). On the left of each panel are provided the solar longitude, local solar time, latitude and longitude of the NOMAD-SO profile and on the right are provided the ingress (I) or egress (E) case and the differences then the differences in solar longitude, local time, latitude, and longitude of the NOMAD-SO profile to the MCS. 143
9.6 The 52 last co-located profiles of temperature from MCS (in orange) and NOMAD-SO (in blue). On the left of each panel are provided the solar longitude, local solar time, latitude and longitude of the NOMAD-SO profile and on the right are provided the ingress (I) or egress (E) case and the differences then the differences in solar longitude, local time, latitude, and longitude of the NOMAD-SO profile to the MCS. 144
9.7 Weighted average difference between the 117 co-located profiles (NOMAD-SO - MCS) in green. The blue and orange curves are the variabilities on, respectively, SO and MCS profiles. 145
9.8 Carbon dioxide density retrieved at three altitudes: 60, 70, 80 km in MY 35. Orange points for NOMAD-SO and blue points for ACS-MIR. The datasets are split into ingress and egress cases. The panels on the first line show the coverage. 147
9.9 Temperature retrieved at three altitudes: 60, 70, 80 km in MY 35. Orange points for NOMAD-SO and blue points for ACS-MIR. The datasets are split for ingress and egress cases. The panels on the first line show the coverage. 147
9.10 Temperature retrieved from ACS-NIR (Fedorova et al., 2023) in blue and NOMAD-SO in orange for simultaneous measurements. The number on the upper right side of each panel is the panel number and the numbers on the left side of each panel provide the solar longitude, latitude, longitude, and local solar time corresponding to the profiles. 148

10.1 Coverage for diffraction order 148 in MY 35 and 36. Panel a is for the latitude coverage as a function of solar longitude and the colours are for the local solar time. Panel b is for the latitude coverage as a function of the local solar time and the colours are for the solar longitude. 152
10.2 Coverage for diffraction order 148 in MY 35 and 36 splits for ingress (upper panel) and egress (lower panel) occultations. 153
10.3 Map of vertical profiles of temperature retrieved from diffraction order 148 in MY 35 and 36 for dawn and northern measurements in panel b. Panel a provides the corresponding coverage in latitude in Y-axis and local solar time as a colourbar. A second Y-axis in panel b provides the corresponding rough altitudes to the pressure scale. 155
10.4 Same as Figure 10.3 but for dawn and southern measurements. 155
10.5 Same as Figure 10.3 but for dusk and northern measurements. 156
10.6 Same as Figure 10.3 but for dusk and southern measurements. 156

10.7 Retrieved CO_2 density in MY 35 and 36 at 75 km from diffraction order 148 in panels b and d as a function of solar longitude. Panels a and b provide the latitude in Y-axis and the local solar time as colour-bar. Panels a and c are for the northern hemisphere and panels b and d are for the Southern hemisphere. The vertical lines mark the solstices and equinoxes. 157
10.8 Same as Figure 10.7 but panels c and d present the retrieved temperature. 158
10.9 Same as Figure 10.8 but for a pressure of 0.1 Pa. 159
10.10 Retrieved CO_2 density at 75 km in MY 35 in red and MY 36 in green as a function of solar longitude. 160
10.11 Same as Figure 10.10 but for temperature. 161
10.12 Retrieved CO_2 density at 75 km in MY 35 and 36 as a function of latitude and the colour-bar for solar longitude. 162
10.13 Retrieved CO_2 density at 75 km in MY 35 and 36 as a function of local solar time and the colour-bar for solar longitude. Panel a and b are, respectively, for the northern and southern hemispheres. 163
10.14 Same as Figure 10.12 but for temperature. 164
10.15 Same as Figure 10.13 but presenting the retrieved temperature at 75 km. 165
10.16 Retrieved temperature profiles at dawn for the first half year in panels 7 to 12 and 19 to 24. Panels 1 to 12 for MY 35 and panels 13 to 24 for MY36. Panels 1 to 6 and 13 to 18 provide the latitudes (x-axis), local solar times (y-axis), and solar longitude (colour-bar). 166
10.17 Same as for figure 10.16 but for the second half year. 167
10.18 Retrieved temperature profiles at dusk for the first half year in panels 7 to 12 and 19 to 24. Panels 1 to 12 for MY 35 and panels 13 to 24 for MY36. Panels 1 to 6 and 13 to 18 provide the latitudes (x-axis), local solar times (y-axis), and solar longitude (colour-bar). 168
10.19 Same as for figure 10.18 but for the second half year. 169
10.20 Profiles of temperature for specific solar longitude, latitude, and local solar time ranges in MY 35. Upper panels (a to h) for the northern hemisphere and lower panels (i to p) for the southern hemisphere. The mean solar longitude and local solar time are provided above the panels. The shaded area represents the uncertainty on the profiles. 171
10.21 The possible presence of CO_2 ice clouds in the dataset of temperature retrieved from NOMAD-SO for diffraction order 148 in MY 34 to MY 36. Panel a for the temperature profiles and panel b for the transmittance at pixel 180. The second Y-axis provides rough altitude values. 174
10.22 Four examples of temperature profiles in blue where the fitted background is plotted in dashed orange, and the limit of background plus 20 K is plotted in dot-dash green. Panels a to c contain a warm layer but not panel d. The dates, times, solar longitudes, local solar times, latitudes, and longitudes are reported on the left side of each panel. 175
10.23 Location and time of all retrieved temperature profiles in MY 35 and 36 in blue and those with a warm layer in orange. All y-axis are latitudes and x-axes are longitudes (panel a), local solar times (panel b) and solar longitudes (panel c). In panel c, the vertical lines indicate the solstices and equinoxes. Note that the y-axis is in log scale to better see the warm layers distributions. 176
10.24 Histograms on solar longitudes of all retrieved temperature profiles in MY 35 and 36 in blue and those with a warm layer in orange. 177

10.25 Histograms on latitude, longitude and local solar time for all retrieved temperature profiles in MY 35 and 36 in blue and those with a warm layer in orange. Panels a, b, c for MY 35 L_S 0° to 180°, panels d, e, f for MY 35 L_S 180° to 360°, panels g, h, i for MY 36 L_S 0° to 180°, and panels j, k, l for MY 36 L_S 180° to 360°. Note that the y-axis is in log scale to better see the warm layers distributions. 178

Bibliography

N. H. Abel. 15. Auflösung einer mechanischen Aufgabe. *Journal fur die Reine und Angewandte Mathematik*, 1826(1):153–157, jan 1826. ISSN 14355345. doi: 10.1515/crll.1826.1.153. URL `https://www.degruyter.com/view/journals/crll/1826/1/article-p153.xml`.

Juan Alday, Alexander Trokhimovskiy, Patrick G.J. Irwin, Colin F. Wilson, Franck Montmessin, Franck Lefévre, Anna A. Fedorova, Denis A. Belyaev, Kevin S. Olsen, Oleg Korablev, Margaux Vals, Loïc Rossi, Lucio Baggio, Jean Loup Bertaux, Andrey Patrakeev, and Alexey Shakun. Isotopic fractionation of water and its photolytic products in the atmosphere of Mars. *Nature Astronomy*, 5(9):943–950, jun 2021. ISSN 23973366. doi: 10.1038/s41550-021-01389-x. URL `https://www.nature.com/articles/s41550-021-01389-x`.

S. Aoki, Y. Sato, M. Giuranna, P. Wolkenberg, T. M. Sato, H. Nakagawa, and Y. Kasaba. Mesospheric CO2 ice clouds on Mars observed by Planetary Fourier Spectrometer onboard Mars Express. *Icarus*, 302:175–190, mar 2018. ISSN 10902643. doi: 10.1016/j.icarus.2017.10.047.

S. Aoki, Ann Carine Vandaele, F. Daerden, G. L. Villanueva, G. Liuzzi, I. R. Thomas, J. T. Erwin, L. Trompet, S. Robert, L. Neary, S. Viscardy, R. T. Clancy, M. D. Smith, Miguel López-Valverde, B. Hill, B. Ristic, M. R. Patel, G. Bellucci, Jose Juan López-Moreno, Gustavo Alonso-Rodrigo, Francesca Altieri, Sophie Bauduin, David Bolsée, Giacomo Carrozzo, Edward Cloutis, Matteo Crismani, Fabiana Da Pieve, Emiliano D'aversa, Cédric Depiesse, Giuseppe Etiope, Anna A. Fedorova, Bernd Funke, Didier Fussen, Maia Garcia-Comas, Anna Geminale, Jean Claude Gérard, Marco Giuranna, Leo Gkouvelis, Francisco Gonzalez-Galindo, James Holmes, Benoît Hubert, Nicolay I. Ignatiev, Jacek Kaminski, Ozgur Karatekin, Yasumasa Kasaba, David Kass, Armin Kleinböhl, Orietta Lanciano, Franck Lefèvre, Stephen Lewis, Manuel López-Puertas, Arnaud Mahieux, Jon Mason, Daniel Mege, Michael J. Mumma, Hiromu Nakagawa, Eddy Neefs, Robert E. Novak, Fabrizio Oliva, Arianna Piccialli, Etienne Renotte, Birgit Ritter, Frédéric Schmidt, Nick Schneider, Giuseppe Sindoni, Nicholas A. Teanby, Ed Thiemann, Alexander Trokhimovskiy, Jean Vander Auwera, James Whiteway, Valerie Wilquet, Yannick Willame, Michael J. Wolff, Paulina Wolkenberg, Roger Yelle, Aparicio Del Moral Beatriz, Pascal Barzin, Bram Beeckman, Ali Benmoussa, Sophie Berkenbosch, David Biondi, Sabrina Bonnewijn, Gian Paolo Candini, Roland Clairquin, Javier Cubas, Boris Giordanengo, Samuel Gissot, Alejandro Gomez, Brijen Hathi, Jose Jeronimo Zafra, Mark Leese, Jeroen Maes, Emmanuel Mazy, Alexandra Mazzoli, Jose Meseguer, Rafael Morales, Anne Orban, M. Pastor-Morales, Isabel Perez-Grande, Claudio Queirolo, Julio Rodriguez Gomez, Bortolino Saggin, Valérie Samain, Angel Sanz Andres, Rosario Sanz, Juan Felipe Simar, Tanguy Thibert, M. A. Lopez-Valverde, B. Hill, B. Ristic, M. R. Patel, G. Bellucci, J. J. Lopez-Moreno, Jose Juan López-Moreno, Gustavo Alonso-Rodrigo, Francesca Altieri, Sophie Bauduin, David Bolsée, Giacomo Carrozzo, Edward Cloutis, Matteo Crismani, Fabiana Da Pieve, Emiliano D'aversa, Cédric Depiesse, Giuseppe Etiope, Anna A. Fedorova, Bernd Funke, Didier Fussen, Maia Garcia-Comas, Anna Geminale, Jean Claude Gérard, Marco Giuranna, Leo Gkouvelis, Francisco Gonzalez-Galindo, James Holmes, Benoît Hubert, Nicolay I. Ignatiev, Jacek Kaminski, Ozgur Karatekin, Yasumasa Kasaba, David Kass, Armin Kleinböhl, Orietta Lanciano, Franck Lefèvre, Stephen Lewis, Manuel López-Puertas, Miguel López-Valverde, Arnaud Mahieux, Jon Mason, Daniel Mege, Michael J. Mumma, Hiromu Nakagawa, Eddy Neefs, Robert E. Novak, Fabrizio Oliva, Arianna Piccialli, Etienne Renotte, Birgit Ritter, Frédéric Schmidt, Nick Schneider, Giuseppe Sindoni, Nicholas A. Teanby, Ed Thiemann, Alexander Trokhimovskiy, Jean Vander Auwera, James Whiteway, Valerie Wilquet, Yannick Willame, Michael J. Wolff, Paulina Wolkenberg, Roger Yelle, Aparicio Del Moral Beatriz, Pascal Barzin, Bram Beeckman, Ali Benmoussa, Sophie Berkenbosch, David Biondi, Sabrina Bonnewijn, Gian Paolo Candini, Roland Clairquin, Javier Cubas, Boris Giordanengo, Samuel Gissot, Alejandro Gomez, Brijen Hathi, Jose Jeronimo Zafra, Mark Leese, Jeroen Maes, Emmanuel Mazy, Alexandra Mazzoli, Jose Meseguer, Rafael Morales, Anne Orban, M. Pastor-Morales, Isabel Perez-Grande, Claudio Queirolo, Julio Rodriguez Gomez, Bortolino Saggin, Valérie Samain, Angel Sanz Andres, Rosario Sanz, Juan Felipe Simar, and Tanguy Thibert. Water Vapor Vertical Profiles on Mars in Dust Storms Observed by TGO/NOMAD. *Journal of Geophysical Research: Planets*, 124(12):3482–3497, 2019. ISSN 21699100. doi: 10.1029/2019JE006109. URL `https://doi.org/10.1029/`.

S. Aoki, F. Daerden, S. Viscardy, I. R. Thomas, J. T. Erwin, S. Robert, L. Trompet, L. Neary, G. L. Villanueva, G. Liuzzi, M. M.J. J. Crismani, R. T. Clancy, J. Whiteway, F. Schmidt, M. A. Lopez-Valverde, B. Ristic, M. R. Patel, G. Bellucci, J. J. Lopez-Moreno, K. S. Olsen, F. Lefèvre, F. Montmessin, A. Trokhimovskiy, A. A. Fedorova, O. Korablev, A. C. Vandaele, M. A. Lopez-Valverde, B. Ristic, M. R. Patel, G. Bellucci, J.-J. Lopez-Moreno, K. S. Olsen, F. Lefèvre, F. Montmessin, A. Trokhimovskiy, A. A. Fedorova, O. Korablev, and A. C. Vandaele. Annual Appearance of Hydrogen Chloride on Mars and a Striking Similarity With the Water Vapor Vertical Distribution Observed by TGO/NOMAD. *Geophysical Research Letters*, 48(11):e2021GL092506, jun 2021. ISSN 0094-8276. doi: 10.1029/2021GL092506. URL `https://onlinelibrary.wiley.com/doi/10.1029/2021GL092506https://doi.`

S. Aoki, A. C. Vandaele, F. Daerden, G. L. Villanueva, G. Liuzzi, R. T. Clancy, M. A. Lopez-Valverde, A. Brines, I. R. Thomas, L. Trompet, J. T. Erwin, L. Neary, S. Robert, A. Piccialli, J. A. Holmes, M. R. Patel, N. Yoshida, J. Whiteway, M. D. Smith, B. Ristic, G. Bellucci, J. J. Lopez-Moreno, and A. A. Fedorova. Global Vertical Distribution of Water Vapor on Mars: Results From 3.5 Years of ExoMars-TGO/NOMAD Science Operations. *Journal of Geophysical Research: Planets*, 127(9):e2022JE007231, sep 2022a. ISSN 2169-9100. doi: 10.1029/2022JE007231. URL `https://onlinelibrary.wiley.com/doi/full/10.1029/2022JE007231https://onlinelibrary.wiley.com/doi/abs/10.1029/2022JE007231https://agupubs.onlinelibrary.wiley.com/doi/10.1029/2022JE007231`.

Shohei Aoki, L Gkouvelis, J.-C Gérard, L Soret, B Hubert, M. A. Lopez-Valverde, F. González-Galindo, H Sagawa, I R Thomas, B Ristic, Y Willame, C Depiesse, J Mason, M R Patel, G Bellucci, J.-J. Lopez-Moreno, F Daerden, and A C Vandaele. Density and temperature of the upper mesosphere and lower thermosphere of Mars retrieved from the OI 557.7 nm dayglow measured by TGO/NOMAD. *Journal of Geophysical Research: Planets*, page e2022JE007206, may 2022b. ISSN 2169-9097. doi: 10.1029/2022JE007206. URL `https://onlinelibrary.wiley.com/doi/full/10.1029/2022JE007206https://onlinelibrary.wiley.com/doi/abs/10.1029/2022JE007206https://agupubs.onlinelibrary.wiley.com/doi/10.1029/2022JE007206https://onlinelibrary.wiley.com/doi/10.1029/2022JE007206`.

G Backus and F Gilbert. Uniqueness in the inversion of inaccurate gross Earth data. *Philosophical*

Transactions of the Royal Society of London. Series A, Mathematical and Physical Sciences, 266(1173):123–192, mar 1970. ISSN 0080-4614. doi: 10.1098/rsta.1970.0005. URL `https://royalsocietypublishing.org/doi/10.1098/rsta.1970.0005`.

D. A. Belyaev, A. A. Fedorova, A. Trokhimovskiy, J. Alday, O. I. Korablev, F. Montmessin, E. D. Starichenko, K. S. Olsen, and A. S. Patrakeev. Thermal Structure of the Middle and Upper Atmosphere of Mars From ACS/TGO CO2 Spectroscopy. *Journal of Geophysical Research: Planets*, 127(10):e2022JE007286, oct 2022. ISSN 2169-9100. doi: 10.1029/2022JE007286. URL `https://onlinelibrary.wiley.com/doi/full/10.1029/2022JE007286https://onlinelibrary.wiley.com/doi/abs/10.1029/2022JE007286https://agupubs.onlinelibrary.wiley.com/doi/10.1029/2022JE007286`.

Denis A. Belyaev, Anna A. Fedorova, Alexander Trokhimovskiy, Juan Alday, Franck Montmessin, Oleg I. Korablev, Franck Lefèvre, Andrey S. Patrakeev, Kevin S. Olsen, and Alexey V. Shakun. Revealing a High Water Abundance in the Upper Mesosphere of Mars With ACS Onboard TGO. *Geophysical Research Letters*, 48(10):e2021GL093411, may 2021. ISSN 19448007. doi: 10.1029/2021GL093411. URL `https://onlinelibrary.wiley.com/doi/full/10.1029/2021GL093411https://onlinelibrary.wiley.com/doi/abs/10.1029/2021GL093411https://agupubs.onlinelibrary.wiley.com/doi/10.1029/2021GL093411`.

Peter Bernath. *Spectra of Atoms and Molecules.* Oxford University Press, 3rd edition, 2005.

Jean Loup Bertaux, O. Korablev, D. Fonteyn, S. Guibert, E. Chassefière, F. Lefèvre, E. Dimarellis, J. P. Dubois, A. Hauchecorne, M. Cabane, P. Rannou, A. C. Levasseur-Regourd, G. Cernogora, E. Quémerais, C. Hermans, G. Kockarts, C. Lippens, M. De Maziere, D. Moreau, C. Muller, E. Neefs, P. C. Simon, F. Forget, F. Hourdin, O. Talagrand, V. I. Moroz, A. Rodin, B. Sandel, and A. Stern. Global structure and composition of the martian atmosphere with SPICAM on Mars express. *Advances in Space Research*, 35(1):31–36, 2005. ISSN 02731177. doi: 10.1016/j.asr.2003.09.055.

Bipm. *Bureau international des poids et mesures.* 2018. ISBN 9789282222768. URL `https://www.bipm.org/documents/20126/17314988/CGPM26.pdf/9db96c32-a986-e32a-09f9-3ed7e6c77cf7`.

J. E. Blamont, E. Chassefiere, J. P. Goutail, B. Mege, M. Nunes-Pinharanda, G. Souchon, V. A. Krasnopolsky, A. A. Krysko, and V. I. Moroz. Vertical profiles of dust and ozone in the martian atmosphere deduced from solar occultation measurements. *Nature*, 341(6243):600–603, 1989. ISSN 00280836. doi: 10.1038/341600a0.

Yasmine Calisesi, Vincent T. Soebijanta, and Roeland van Oss. Regridding of remote soundings: Formulation and application to ozone profile comparison. *Journal of Geophysical Research Atmospheres*, 110(23):1–8, dec 2005. ISSN 01480227. doi: 10.1029/2005JD006122. URL `http://doi.wiley.com/10.1029/2005JD006122`.

George. Casella and Roger L. Berger. *Statistical inference.* Thomson Learning, 2nd editio edition, 2002. ISBN 978-0-534-24312-8.

Simone Ceccherini. Analytical determination of the regularization parameter in the retrieval of atmospheric vertical profiles. *Optics Letters*, 30(19):2554, 2005. ISSN 0146-9592. doi: 10.1364/ol.30.002554. URL `https://www.osapublishing.org/abstract.cfm?uri=OL-30-19-2554`.

Simone Ceccherini. A generalization of optimal estimation for the retrieval of atmospheric vertical profiles. *Journal of Quantitative Spectroscopy and Radiative Transfer*, 113(12):1437–1440, aug 2012. ISSN 00224073. doi: 10.1016/j.jqsrt.2012.03.021. URL http://dx.doi.org/10.1016/j.jqsrt.2012.03.021https://www.sciencedirect.com/science/article/pii/S0022407312001446?casa{_}token=4c9K7h9KjEgAAAAA:jbDerUAOxMMRCDIJzDbSuSRjhFUfrEkEQFbzbnOeTKN3JERT7V4jRpLilQd8ybl06DKLKUj-mQ.

S Chandrasekhar. *Radiative transfer*. Dover Publications, New York, 1960. ISBN 9780486605906.

S. Chapman. The absorption and dissociative or ionizing effect of monochromatic radiation in an atmosphere on a rotating earth part II. Grazing incidence. *Proceedings of the Physical Society*, 43(5):483–501, sep 1931. ISSN 0959-5309. doi: 10.1088/0959-5309/43/5/302. URL https://iopscience.iop.org/article/10.1088/0959-5309/43/5/302.

R. T. Clancy, B. J. Sandor, M. J. Wolff, P. R. Christensen, M. D. Smith, J. C. Pearl, B. J. Conrath, and R. J. Wilson. An intercomparison of ground-based millimeter, MGS TES, and Viking atmospheric temperature measurements: Seasonal and interannual variability of temperatures and dust loading in the global Mars atmosphere. *Journal of Geophysical Research E: Planets*, 105(E4):9553–9571, 2000. ISSN 01480227. doi: 10.1029/1999JE001089.

R. Todd Clancy and Brad J. Sandor. CO2 ice clouds in the upper atmosphere of Mars. *Geophysical Research Letters*, 25(4):489–492, feb 1998. ISSN 00948276. doi: 10.1029/98GL00114. URL https://onlinelibrary.wiley.com/doi/full/10.1029/98GL00114https://onlinelibrary.wiley.com/doi/abs/10.1029/98GL00114https://agupubs.onlinelibrary.wiley.com/doi/10.1029/98GL00114.

R Todd Clancy, Michael J Wolff, Barbara A Whitney, Bruce A Cantor, and Michael D Smith. Mars equatorial mesospheric clouds: Global occurrence and physical properties from Mars Global Surveyor Thermal Emission Spectrometer and Mars Orbiter Camera limb observations. *Journal of Geophysical Research: Planets*, 112(4):4004, apr 2007. ISSN 01480227. doi: 10.1029/2006JE002805. URL https://onlinelibrary.wiley.com/doi/full/10.1029/2006JE002805https://onlinelibrary.wiley.com/doi/abs/10.1029/2006JE002805https://agupubs.onlinelibrary.wiley.com/doi/10.1029/2006JE002805.

R. Todd Clancy, Michael J. Wolff, Michael D. Smith, Armin Kleinböhl, Bruce A. Cantor, Scott L. Murchie, Anthony D. Toigo, Kim Seelos, Franck Lefèvre, Franck Montmessin, Frank Daerden, and Brad J. Sandor. The distribution, composition, and particle properties of Mars mesospheric aerosols: An analysis of CRISM visible/near-IR limb spectra with context from near-coincident MCS and MARCI observations. *Icarus*, 328:246–273, aug 2019. ISSN 10902643. doi: 10.1016/j.icarus.2019.03.025.

Anthony Colaprete, Jeffrey R. Barnes, Robert M. Haberle, and Franck Montmessin. CO2 clouds, CAPE and convection on Mars: Observations and general circulation modeling. *Planetary and Space Science*, 56(2):150–180, 2008. ISSN 00320633. doi: 10.1016/j.pss.2007.08.010.

Analytical Methods Committee. Recommendations for the definition, estimation and use of the detection limit. *The Analyst*, 112(2):199–204, jan 1987. ISSN 00032654. doi: 10.1039/AN9871200199. URL https://pubs.rsc.org/en/content/articlehtml/1987/an/an9871200199https://pubs.rsc.org/en/content/articlelanding/1987/an/an9871200199.

Barney J. Conrath. Vertical Resolution of Temperature Profiles Obtained from Remote Radiation Measurements, 1972. ISSN 0022-4928.

Charles-P. Courtoy. SPECTRES DE VIBRATION-ROTATION DE MOLECULES SIMPLES DIATOMIQUES OU POLYATOMIQUES AVEC LONG PARCOURS D'ABSORPTION: XII. LE SPECTRE DE C 12 O 16 2 ENTRE 3500 ET 8000 CM -1 ET LES CONSTANTES MOLECULAIRES DE CETTE MOLECULE. *Canadian Journal of Physics*, 35(5):608–648, may 1957. ISSN 0008-4204. doi: 10.1139/p57-068. URL `https://cdnsciencepub.com/doi/abs/10.1139/p57-068`.

R Curtis, A. Discussion of a statistical model for water vapour absorption. *Q. J. R. Meteorol. Soc.*, 78:638–640, 1952.

F. Daerden, L. Neary, S. Viscardy, A. García Muñoz, R. T. Clancy, M. D. Smith, T. Encrenaz, and A. Fedorova. Mars atmospheric chemistry simulations with the GEM-Mars general circulation model. *Icarus*, 326:197–224, jul 2019. ISSN 10902643. doi: 10.1016/j.icarus.2019.02.030.

Emmanuel Dekemper. *Development of an AOTF-based hyperspectral imager for atmospheric remote sensing*. PhD thesis, Université Catholique de Louvain, 2014. URL `https://pul.uclouvain.be/book/?gcoi=29303100818980`.

Adrian Doicu, Thomas Trautmann, and Franz Schreier. Tikhonov regularization for linear problems. In *Numerical Regularization for Atmospheric Inverse Problems*, pages 39–106. Springer Berlin Heidelberg, 2010a. doi: 10.1007/978-3-642-05439-6_3.

Adrian Doicu, Thomas Trautmann, and Franz Schreier. *Numerical Regularization for Atmospheric Inverse Problems*. Springer Berlin Heidelberg, 2010b. doi: 10.1007/978-3-642-05439-6.

D. P. Edwards, M. López-Puertas, and R. R. Gamache. The non-LTE correction to the vibrational component of the internal partition sum for atmospheric calculations. *Journal of Quantitative Spectroscopy and Radiative Transfer*, 59(3-5):423–436, 1998. ISSN 00224073. doi: 10.1016/S0022-4073(97)00125-8.

Paul H.C. Eilers. A perfect smoother, 2003. ISSN 00032700. URL `http://www.science.uva.nl/{~}hboelens/publications/draftpub/Eilers{_}2005.pdf`.

Scott L. England, Guiping Liu, Paul Withers, Erdal Yiğit, Daniel Lo, Sonal Jain, Nicholas M. Schneider, Justin Deighan, William E. McClintock, Paul R. Mahaffy, Meredith Elrod, Mehdi Benna, and Bruce M. Jakosky. Simultaneous observations of atmospheric tides from combined in situ and remote observations at Mars from the MAVEN spacecraft. *Journal of Geophysical Research E: Planets*, 121(4):594–607, apr 2016. ISSN 21699100. doi: 10.1002/2016JE004997. URL `https://onlinelibrary.wiley.com/doi/full/10.1002/2016JE004997https://onlinelibrary.wiley.com/doi/abs/10.1002/2016JE004997https://agupubs.onlinelibrary.wiley.com/doi/10.1002/2016JE004997`.

Scott L. England, Guiping Liu, Aishwarya Kumar, Paul R. Mahaffy, Meredith Elrod, Mehdi Benna, Sonal Jain, Justin Deighan, Nicholas M. Schneider, William E. McClintock, and J. Scott Evans. Atmospheric Tides at High Latitudes in the Martian Upper Atmosphere Observed by MAVEN and MRO. *Journal of Geophysical Research: Space Physics*, 124(4):2943–2953, apr 2019. ISSN 21699402. doi: 10.1029/2019JA026601. URL `https://onlinelibrary.wiley.com/doi/full/10.1029/2019JA026601https://onlinelibrary.wiley.com/doi/abs/10.1029/2019JA026601https://agupubs.onlinelibrary.wiley.com/doi/10.1029/2019JA026601`.

Sonja Engman and Peter Lindblom. Blaze characteristics of echelle gratings. *Applied Optics*, 21(23):4356, dec 1982. ISSN 0003-6935. doi: 10.1364/ao.21.004356. URL `https://www.osapublishing.org/viewmedia.cfm?uri=ao-21-23-4356{&}seq=0{&}html=truehttps://www.osapublishing.org/abstract.cfm?uri=ao-21-23-4356https://www.osapublishing.org/ao/abstract.cfm?uri=ao-21-23-4356`.

Patrick Eriksson. Analysis and comparison of two linear regularization methods for passive atmospheric observations, jul 2000. ISSN 01480227.

Patrick Eriksson, Carlos Jiménez, and Stefan A. Buehler. Qpack, a general tool for instrument simulation and retrieval work. *Journal of Quantitative Spectroscopy and Radiative Transfer*, 91(1):47–64, feb 2005. ISSN 00224073. doi: 10.1016/j.jqsrt.2004.05.050. URL `www.elsevier.com/locate/jqsrt`.

Justin Erwin, Lori Neary, Frank Daerden, Sébastien Viscardy, and Ann Carine Vandaele. Creating high-spatial resolution atmospheric profiles from the GEM-Mars GCM for the investigation of Mars. In *EPSC 2018*, page 2, 2018. doi: 10.1016/j.icarus.2017.09.028. URL `https://doi.org/10.1016/j.icarus.2017.09.028`.

Mark P Esplin, William M Barowy, Ronald J Huppi, Laurence S Rothman, and George A Vanasse. High Resolution Infrared Spectroscopy of Carbon Dioxide and Nitrous Oxide at Elevated Temperatures. Technical report, 1988. URL `https://apps.dtic.mil/dtic/tr/fulltext/u2/a196317.pdf`.

Giuseppe Etiope and Dorothy Z. Oehler. Methane spikes, background seasonality and non-detections on Mars: A geological perspective, apr 2019. ISSN 00320633.

J. S. Evans, E. Soto, S. K. Jain, J. Deighan, M. H. Stevens, M. S. Chaffin, D. Y. Lo, S. Gupta, N. M. Schneider, and S. Curry. Dayside temperature maps of the upper mesosphere and lower thermosphere of Mars retrieved from MAVEN IUVS observations of O I 297 . 2 nm emission. *Journal of Geophysical Research: Planets*, 128(2):e2022JE007325, feb 2023. ISSN 2169-9097. doi: 10.1029/2022je007325. URL `https://onlinelibrary.wiley.com/doi/full/10.1029/2022JE007325https://onlinelibrary.wiley.com/doi/abs/10.1029/2022JE007325https://agupubs.onlinelibrary.wiley.com/doi/10.1029/2022JE007325`.

A. A. Fedorova, O. I. Korablev, J. L. Bertaux, A. V. Rodin, F. Montmessin, D. A. Belyaev, and A. Reberac. Solar infrared occultation observations by SPICAM experiment on Mars-Express: Simultaneous measurements of the vertical distributions of H2O, CO2 and aerosol. *Icarus*, 200 (1):96–117, mar 2009. ISSN 00191035. doi: 10.1016/j.icarus.2008.11.006.

Anna Fedorova, Oleg Korablev, Jean Loup Bertaux, Alexander Rodin, Alexander Kiselev, and Seyerine Perrier. Mars water vapor abundance from SPICAM IR spectrometer: Seasonal and geographic distributions. *Journal of Geophysical Research: Planets*, 111(9):9–17, sep 2006. ISSN 01480227. doi: 10.1029/2006JE002695. URL `https://onlinelibrary.wiley.com/doi/full/10.1029/2006JE002695https://onlinelibrary.wiley.com/doi/abs/10.1029/2006JE002695https://agupubs.onlinelibrary.wiley.com/doi/10.1029/2006JE002695`.

Anna Fedorova, Jean Loup Bertaux, Daria Betsis, Franck Montmessin, Oleg Korablev, Luca Maltagliati, and John Clarke. Water vapor in the middle atmosphere of Mars during the 2007 global dust storm. *Icarus*, 300:440–457, 2018. ISSN 10902643. doi: 10.1016/j.icarus.2017.09.025. URL `https://doi.org/10.1016/j.icarus.2017.09.025`.

Anna Fedorova, Franck Montmessin, Alexander Trokhimovskiy, Mikhail Luginin, Oleg Korablev, Juan Alday, Denis Belyaev, James Holmes, Franck Lefevre, Kevin Olsen, Andrey Patrakeev, and Alexey Shakun. A Two-Martian Years Survey of the Water Vapor Saturation State on Mars Based on ACS NIR/TGO Occultations. *Journal of Geophysical Research: Planets*, 128(1):e2022JE007348, jan 2023. ISSN 2169-9100. doi: 10.1029/2022JE007348. URL `https://onlinelibrary.wiley.com/doi/full/10.1029/2022JE007348https://onlinelibrary.wiley.com/doi/abs/10.1029/2022JE007348https://agupubs.onlinelibrary.wiley.com/doi/10.1029/2022JE007348`.

François Forget, Frédéric Hourdin, Richard Fournier, Christophe Hourdin, Olivier Talagrand, Matthew Collins, Stephen R. Lewis, Peter L. Read, and Jean Paul Huot. Improved general circulation models of the Martian atmosphere from the surface to above 80 km. *Journal of Geophysical Research E: Planets*, 104(E10):24155–24175, oct 1999. ISSN 01480227. doi: 10.1029/1999JE001025. URL `https://onlinelibrary.wiley.com/doi/full/10.1029/1999JE001025https://onlinelibrary.wiley.com/doi/abs/10.1029/1999JE001025https://agupubs.onlinelibrary.wiley.com/doi/10.1029/1999JE001025`.

François Forget, Aymeric Spiga, Bastien Dolla, Sandrine Vinatier, Riccardo Melchiorri, Pierre Drossart, Aline Gendrin, Jean-Pierre Bibring, Yves Langevin, and Brigitte Gondet. Remote sensing of surface pressure on Mars with the Mars Express/OMEGA spectrometer: 1. Retrieval method. *Journal of Geophysical Research: Planets*, 112(E8):8–15, aug 2007. ISSN 01480227. doi: 10.1029/2006JE002871. URL `https://onlinelibrary.wiley.com/doi/full/10.1029/2006JE002871https://onlinelibrary.wiley.com/doi/abs/10.1029/2006JE002871https://agupubs.onlinelibrary.wiley.com/doi/10.1029/2006JE002871http://doi.wiley.com/10.1029/2006JE002871`.

François Forget, Franck Montmessin, Jean Loup Bertaux, Francisco González-Galindo, Sébastien Lebonnois, Eric Quémerais, Aurélie Reberac, Emmanuel Dimarellis, and Miguel A. López-Valverde. Density and temperatures of the upper Martian atmosphere measured by stellar occultations with Mars Express SPICAM. *Journal of Geophysical Research E: Planets*, 114(1):1004, jan 2009. ISSN 01480227. doi: 10.1029/2008JE003086. URL `https://agupubs.onlinelibrary.wiley.com/doi/full/10.1029/2008JE003086https://agupubs.onlinelibrary.wiley.com/doi/abs/10.1029/2008JE003086https://agupubs.onlinelibrary.wiley.com/doi/10.1029/2008JE003086https://onlinelibrary.wiley.com/doi/full/10.1029/20`.

V. Formisano, A. Maturilli, M. Giuranna, E. D'Aversa, and M. A. Lopez-Valverde. Observations of non-LTE emission at 4-5 microns with the planetary Fourier spectrometer abord the Mars Express mission. *Icarus*, 182(1):51–67, 2006. ISSN 00191035. doi: 10.1016/j.icarus.2005.12.022.

Vittorio Formisano, Sushil Atreya, Thérèse Encrenaz, Nikolai Ignatiev, and Marco Giuranna. Detection of methane in the atmosphere of Mars. *Science*, 306(5702):1758–1761, dec 2004. ISSN 00368075. doi: 10.1126/science.1101732.

Bengt Fornberg. Generation of Finite Difference Formulas on Arbitrarily Spaced Grids. *Mathematics of Computation*, 51(184):699, 1988. ISSN 00255718. doi: 10.2307/2008770.

Heather B Franz, Melissa G Trainer, Charles A Malespin, Paul R Mahaffy, Sushil K Atreya, Richard H Becker, Mehdi Benna, Pamela G Conrad, Jennifer L Eigenbrode, Caroline Freissinet, Heidi L.K. Manning, Benito D Prats, Eric Raaen, and Michael H Wong. Initial SAM calibration gas experiments on Mars: Quadrupole mass spectrometer results and implications. *Planetary and Space Science*, 138:44–54, 2017. ISSN 00320633. doi: 10.1016/j.pss.2017.01.014. URL `http://dx.doi.org/10.1016/j.pss.2017.01.014`.

Louis Galatry. Simultaneous effect of doppler and foreign gas broadening on spectral lines. *Physical Review*, 122(4):1218–1223, 1961. ISSN 0031899X. doi: 10.1103/PhysRev.122.1218.

Robert R. Gamache, Bastien Vispoel, Michaël Rey, Vladimir Tyuterev, Alain Barbe, Andrei Nikitin, Oleg L. Polyansky, Jonathan Tennyson, Sergei N. Yurchenko, Attila G. Császár, Tibor Furtenbacher, Valery I. Perevalov, and Sergei A. Tashkun. Partition sums for non-local thermodynamic equilibrium conditions for nine molecules of importance in planetary atmospheres. *Icarus*, 378:114947, may 2022. ISSN 10902643. doi: 10.1016/j.icarus.2022.114947.

Fuchang Gao and Lixing Han. Implementing the Nelder-Mead simplex algorithm with adaptive parameters. *Computational Optimization and Applications*, 51(1):259–277, 2012. ISSN 09266003. doi: 10.1007/s10589-010-9329-3.

A. Geminale, V. Formisano, and M. Giuranna. Methane in Martian atmosphere: Average spatial, diurnal, and seasonal behaviour. *Planetary and Space Science*, 56(9):1194–1203, jul 2008. ISSN 00320633. doi: 10.1016/j.pss.2008.03.004. URL `www.elsevier.com/locate/pss`.

A. Geminale, V. Formisano, and G. Sindoni. Mapping methane in Martian atmosphere with PFS-MEX data. *Planetary and Space Science*, 59(2-3):137–148, feb 2011. ISSN 00320633. doi: 10.1016/j.pss.2010.07.011.

Antonio Genova, Sander Goossens, Frank G. Lemoine, Erwan Mazarico, Gregory A. Neumann, David E. Smith, and Maria T. Zuber. Seasonal and static gravity field of Mars from MGS, Mars Odyssey and MRO radio science. *Icarus*, 272:228–245, jul 2016. ISSN 10902643. doi: 10.1016/j.icarus.2016.02.050.

J. C. Gérard, S. Aoki, Y. Willame, L. Gkouvelis, C. Depiesse, I. R. Thomas, B. Ristic, A. C. Vandaele, F. Daerden, B. Hubert, J. Mason, M. R. Patel, J. J. López-Moreno, G. Bellucci, M. A. López-Valverde, and B. Beeckman. Detection of green line emission in the dayside atmosphere of Mars from NOMAD-TGO observations. *Nature Astronomy*, 4(11):1049–1052, 2020. ISSN 23973366. doi: 10.1038/s41550-020-1123-2. URL `http://dx.doi.org/10.1038/s41550-020-1123-2`.

J. C. Gérard, S. Aoki, L. Gkouvelis, L. Soret, Y. Willame, I. R. Thomas, C. Depiesse, B. Ristic, A. C. Vandaele, B. Hubert, F. Daerden, M. R. Patel, J. J. López-Moreno, G. Bellucci, J. P. Mason, and M. A. López-Valverde. First Observation of the Oxygen 630 nm Emission in the Martian Dayglow. *Geophysical Research Letters*, 48(8):e2020GL092334, apr 2021. ISSN 19448007. doi: 10.1029/2020GL092334. URL `https://onlinelibrary.wiley.com/doi/full/10.1029/2020GL092334https://onlinelibrary.wiley.com/doi/abs/10.1029/2020GL092334https://agupubs.onlinelibrary.wiley.com/doi/10.1029/2020GL092334`.

Marco Giuranna, Sébastien Viscardy, Frank Daerden, Lori Neary, Giuseppe Etiope, Dorothy Oehler, Vittorio Formisano, Alessandro Aronica, Paulina Wolkenberg, Shohei Aoki, Alejandro Cardesín-Moinelo, Julia Marín-Yaseli de la Parra, Donald Merritt, and Marilena Amoroso. Independent confirmation of a methane spike on Mars and a source region east of Gale Crater. *Nature Geoscience*, 12(5):326–332, may 2019. ISSN 17520908. doi: 10.1038/s41561-019-0331-9.

Marco Giuranna, Paulina Wolkenberg, Davide Grassi, Alessandro Aronica, Shohei Aoki, Diego Scaccabarozzi, Bortolino Saggin, and V. Formisano. The current weather and climate of Mars: 12 years of atmospheric monitoring by the Planetary Fourier Spectrometer on Mars Express. *Icarus*, 353:113406, jan 2021. ISSN 10902643. doi: 10.1016/j.icarus.2019.113406.

W. L. Godson. The evaluation of infra-red radiative fluxes due to atmospheric water vapour. *Quarterly Journal of the Royal Meteorological Society*, 80(346):644–646, 1953. ISSN 1477870X. doi: 10.1002/qj.49708034621.

Gene H. Golub, Michael Heath, and Grace Wahba. Generalized Cross-Validation as a Method for Choosing a Good Ridge Parameter. *Technometrics*, 21(2):215, may 1979. ISSN 00401706. doi: 10.2307/1268518.

Francisco González-Galindo, Anni Määttänen, François Forget, and Aymeric Spiga. The martian mesosphere as revealed by CO2 cloud observations and General Circulation Modeling. *Icarus*, 216(1):10–22, nov 2011. ISSN 10902643. doi: 10.1016/J.ICARUS.2011.08.006.

R. M. Goody and Y. L. Yung. *Atmospheric Radiation*. Oxford University Press, jun 1989. ISBN 9780195051346. doi: 10.1093/oso/9780195051346.001.0001.

I. E. Gordon, L. S. Rothman, C. Hill, R. V. Kochanov, Y. Tan, P. F. Bernath, M. Birk, V. Boudon, A. Campargue, K. V. Chance, B. J. Drouin, J. M. Flaud, R. R. Gamache, J. T. Hodges, D. Jacquemart, V. I. Perevalov, A. Perrin, K. P. Shine, M. A.H. Smith, J. Tennyson, G. C. Toon, H. Tran, V. G. Tyuterev, A. Barbe, A. G. Császár, V. M. Devi, T. Furtenbacher, J. J. Harrison, J. M. Hartmann, A. Jolly, T. J. Johnson, T. Karman, I. Kleiner, A. A. Kyuberis, J. Loos, O. M. Lyulin, S. T. Massie, S. N. Mikhailenko, N. Moazzen-Ahmadi, H. S.P. Müller, O. V. Naumenko, A. V. Nikitin, O. L. Polyansky, M. Rey, M. Rotger, S. W. Sharpe, K. Sung, E. Starikova, S. A. Tashkun, J. Vander Auwera, G. Wagner, J. Wilzewski, P. Wcisło, S. Yu, and E. J. Zak. The HITRAN2016 molecular spectroscopic database. *Journal of Quantitative Spectroscopy and Radiative Transfer*, 203:3–69, dec 2017. ISSN 00224073. doi: 10.1016/j.jqsrt.2017.06.038.

I.E. Gordon, L.S. Rothman, R.J. Hargreaves, R. Hashemi, E.V. Karlovets, F.M. Skinner, E.K. Conway, C. Hill, R.V. Kochanov, Y. Tan, P. Wcisło, A.A. Finenko, K. Nelson, P.F. Bernath, M. Birk, V. Boudon, A. Campargue, K.V. Chance, A. Coustenis, B.J. Drouin, J.–M. Flaud, R.R. Gamache, J.T. Hodges, D. Jacquemart, E.J. Mlawer, A.V. Nikitin, V.I. Perevalov, M. Rotger, J. Tennyson, G.C. Toon, H. Tran, V.G. Tyuterev, E.M. Adkins, A. Baker, A. Barbe, E. Canè, A.G. Császár, A. Dudaryonok, O. Egorov, A.J. Fleisher, H. Fleurbaey, A. Foltynowicz, T. Furtenbacher, J.J. Harrison, J.–M. Hartmann, V.–M. Horneman, X. Huang, T. Karman, J. Karns, S. Kassi, I. Kleiner, V. Kofman, F. Kwabia–Tchana, N.N. Lavrentieva, T.J. Lee, D.A. Long, A.A. Lukashevskaya, O.M. Lyulin, V.Yu. Makhnev, W. Matt, S.T. Massie, M. Melosso, S.N. Mikhailenko, D. Mondelain, H.S.P. Müller, O.V. Naumenko, A. Perrin, O.L. Polyansky, E. Raddaoui, P.L. Raston, Z.D. Reed, M. Rey, C. Richard, R. Tóbiás, I. Sadiek, D.W. Schwenke, E. Starikova, K. Sung, F. Tamassia, S.A. Tashkun, J. Vander Auwera, I.A. Vasilenko, A.A. Vigasin, G.L. Villanueva, B. Vispoel, G. Wagner, A. Yachmenev, and S. N. Yurchenko. The HITRAN2020 molecular spectroscopic database. *Journal of Quantitative Spectroscopy and Radiative Transfer*, 277:107949, 2022. ISSN 00224073. doi: 10.1016/j.jqsrt.2021.107949. URL `https://doi.org/10.1016/j.jqsrt.2021.107949`.

H. Gröller, F. Montmessin, R. V. Yelle, F. Lefèvre, F. Forget, N. M. Schneider, T. T. Koskinen, J. Deighan, and S. K. Jain. MAVEN/IUVS Stellar Occultation Measurements of Mars Atmospheric Structure and Composition. *Journal of Geophysical Research: Planets*, 123(6):1449–1483, jun 2018. ISSN 21699100. doi: 10.1029/2017JE005466. URL `https://onlinelibrary.wiley.com/doi/full/10.1029/2017JE005466https://onlinelibrary.wiley.com/doi/abs/10.1029/2017JE005466https://agupubs.onlinelibrary.wiley.com/doi/10.1029/2017JE005466`.

S. Guerlet, N. Ignatiev, F. Forget, T. Fouchet, P. Vlasov, G. Bergeron, R. M.B. Young, E. Millour, S. Fan, H. Tran, A. Shakun, A. Grigoriev, A. Trokhimovskiy, F. Montmessin, and O. Korablev. Thermal Structure and Aerosols in Mars' Atmosphere From TIRVIM/ACS Onboard the ExoMars Trace Gas Orbiter: Validation of the Retrieval Algorithm. *Journal of Geophysical Research: Planets*, 127(2):e2021JE007062, feb 2022. ISSN 21699100. doi: 10.1029/2021JE007062. URL `https://onlinelibrary.wiley.com/doi/full/10.1029/2021JE007062https://onlinelibrary.wiley.com/doi/abs/10.1029/2021JE007062https://agupubs.onlinelibrary.wiley.com/doi/10.1029/2021JE007062`.

R. M. Haberle. *Solar System/Sun, Atmospheres, Evolution of Atmospheres: Planetary Atmospheres: Mars*, volume 5. Elsevier, second edi edition, jan 2015. ISBN 9780123822260. doi: 10.1016/B978-0-12-382225-3.00312-1. URL `http://dx.doi.org/10.1016/B978-0-12-382225-3.00312-1`.

Robert M. Haberle, R. Todd Clancy, François Forget, Michael D. Smith, and Richard W. Zurek. *The atmosphere and climate of mars*. Cambridge University Press, jun 2017. ISBN 9781139060172. doi: 10.1017/9781139060172. URL `https://www.cambridge.org/core/books/atmosphere-and-climate-of-mars/CA5316BF24A89891563B2E17EF185E19`.

Jacques Hadamard. *Lectures on Cauchy's Problem in Linear Partial Differential Equations*. Yale University Press, New Haven, 1923. URL `https://archive.org/details/lecturesoncauchy00hadauoft/page/26/mode/2up`.

Per Christian Hansen. Analysis of Discrete Ill-Posed Problems by Means of the L-Curve. *SIAM Review*, 34(4):561–580, dec 1992a. ISSN 0036-1445. doi: 10.1137/1034115. URL `http://www.siam.org/journals/ojsa.php`.

Per Christian Hansen. Numerical tools for analysis and solution of Fredholm integral equations of the first kind. *Inverse Problems*, 8(6):849–872, dec 1992b. ISSN 02665611. doi: 10.1088/0266-5611/8/6/005. URL `https://iopscience.iop.org/article/10.1088/0266-5611/8/6/005https://iopscience.iop.org/article/10.1088/0266-5611/8/6/005/meta`.

Per Christian Hansen and Dianne Prost O'Leary. The Use of the L-Curve in the Regularization of Discrete Ill-Posed Problems. *SIAM Journal on Scientific Computing*, 14(6):1487–1503, nov 1993. ISSN 1064-8275. doi: 10.1137/0914086. URL `http://www.siam.org/journals/ojsa.php`.

Frank Hase, Lloyd Wallace, Sean D. McLeod, Jeremy J Harrison, and Peter F Bernath. The ACE-FTS atlas of the infrared solar spectrum. *Journal of Quantitative Spectroscopy and Radiative Transfer*, 111(4):521–528, 2010. ISSN 00224073. doi: 10.1016/j.jqsrt.2009.10.020. URL `www.elsevier.com/locate/jqsrt`.

P. B. Hays and R. G. Roble. Atmospheric properties from the inversion of planetary occultation data. *Planetary and Space Science*, 16(9):1197–1198, sep 1968. ISSN 00320633. doi: 10.1016/0032-0633(68)90131-1. URL `https://linkinghub.elsevier.com/retrieve/pii/0032063368901311`.

Kenneth C. Herr and George C. Pimentel. Evidence for solid carbon dioxide in the upper atmosphere of Mars. *Science*, 167(3914):47–49, jan 1970. ISSN 00368075. doi: 10.1126/science.167.3914.47. URL `https://www.science.org/doi/10.1126/science.167.3914.47`.

Gerhard Herzberg. *Molecular Spectra and Molecular Structure. I. Spectra of Diatomic Molecules*, volume 1. D. VAN MOSTRAND COMPANY, INC., 1950. ISBN 978-0-442-03385-9.

Gerhard Herzberg and Bryce L. Crawford. Infrared and Raman Spectra of Polyatomic Molecules. *The Journal of Physical Chemistry*, 50(3):288–288, mar 1946. ISSN 0092-7325. doi: 10.1021/j150447a021.

C. Hirt, S. J. Claessens, M. Kuhn, and W. E. Featherstone. Kilometer-resolution gravity field of Mars: MGM2011. *Planetary and Space Science*, 67(1):147–154, jul 2012. ISSN 00320633. doi: 10.1016/j.pss.2012.02.006.

Michael Hollas. *Modern Spectroscopy*. Wiley, 4th editio edition, 2004.

Jack J. Horvath, L. H. Brace, and R. W. Simmons. Theory and implementation of the Pitot-static technique for upper atmospheric measurements. 1962. URL `http://deepblue.lib.umich.edu/handle/2027.42/5603`.

Frédéric Hourdin, François Forget, and Olivier Talagrand. The sensitivity of the Martian surface pressure and atmospheric mass budget to various parameters: A comparison between numerical simulations and Viking observations. *Journal of Geophysical Research*, 100(E3):5501, 1995. ISSN 0148-0227. doi: 10.1029/94je03079.

Aapo Hyvärinen. Independent component analysis: Recent advances, feb 2013. ISSN 1364503X. URL `/pmc/articles/PMC3538438//pmc/articles/PMC3538438/?report=abstracthttps://www.ncbi.nlm.nih.gov/pmc/articles/PMC3538438/`.

Ai Inada, Mark I. Richardson, Timothy H. McConnochie, Melissa J. Strausberg, Huiqun Wang, and James F. Bell. High-resolution atmospheric observations by the Mars Odyssey Thermal Emission Imaging System. *Icarus*, 192(2):378–395, 2007. ISSN 00191035. doi: 10.1016/j.icarus.2007.07.020.

P. G.J. Irwin, N. A. Teanby, R. de Kok, L. N. Fletcher, C. J.A. Howett, C. C.C. Tsang, C. F. Wilson, S. B. Calcutt, C. A. Nixon, and P. D. Parrish. The NEMESIS planetary atmosphere radiative transfer and retrieval tool. *Journal of Quantitative Spectroscopy and Radiative Transfer*, 109(6):1136–1150, apr 2008. ISSN 00224073. doi: 10.1016/j.jqsrt.2007.11.006.

Anton B. Ivanov and Duane O. Muhleman. Cloud reflection observations: Results from the Mars Orbiter Laser Altimeter. *Icarus*, 154(1):190–206, 2001. ISSN 00191035. doi: 10.1006/icar.2001.6686.

S. K. Jain, E. Soto, J. S. Evans, J. Deighan, N. M. Schneider, and S. W. Bougher. Thermal structure of Mars' middle and upper atmospheres: Understanding the impacts of dynamics and solar forcing. *Icarus*, 393:114703, mar 2021. ISSN 10902643. doi: 10.1016/j.icarus.2021.114703. URL `https://doi.org/10.1016/j.icarus.2021.114703`.

B. M. Jakosky, R. P. Lin, J. M. Grebowsky, J. G. Luhmann, D. F. Mitchell, G. Beutelschies, T. Priser, M. Acuna, L. Andersson, D. Baird, D. Baker, R. Bartlett, M. Benna, S. Bougher, D. Brain, D. Carson, S. Cauffman, P. Chamberlin, J. Y. Chaufray, O. Cheatom, J. Clarke, J. Connerney, T. Cravens, D. Curtis, G. Delory, S. Demcak, A. Dewolfe, F. Eparvier, R. Ergun, A. Eriksson, J. Espley, X. Fang, D. Folta, J. Fox, C. Gomez-Rosa, S. Habenicht, J. Halekas, G. Holsclaw, M. Houghton, R. Howard, M. Jarosz, N. Jedrich, M. Johnson, W. Kasprzak, M. Kelley, T. King, M. Lankton, D. Larson, F. Leblanc, F. Lefevre, R. Lillis, P. Mahaffy, C. Mazelle, W. McClintock, J. McFadden, D. L. Mitchell, F. Montmessin, J. Morrissey, W. Peterson, W. Possel, J. A. Sauvaud, N. Schneider, W. Sidney, S. Sparacino, A. I.F. Stewart, R. Tolson, D. Toublanc, C. Waters, T. Woods, R. Yelle, and R. Zurek. The mars atmosphere and volatile evolution (MAVEN) mission. *Space Science Reviews*, 195(1-4):3–48, dec 2015. ISSN 15729672. doi: 10.1007/s11214-015-0139-x.

José M. Jerónimo Zafra, Rosario Sanz Mesa, Juan M. Gómez López, Julio F. Rodríguez Gómez, Beatriz Aparicio del Moral, Rafael Morales Muñoz, Gian Paolo Candini, M. Carmen Pastor Morales, Nicolás Robles Muñoz, José Juan López-Moreno, Ann Carine Vandaele, Eddy Neefs, Rachel Drummond, Sofie Delanoye, Sophie Berkenbosch, Roland Clairquin, Bojan Ristic, Jeroen Maes, Sabrina Bonnewijn, Manish R. Patel, and Mark Leese. SINBAD electronic models of the interface and control system for the NOMAD spectrometer on board of ESA ExoMars Trace Gas Orbiter mission. In *Space Telescopes and Instrumentation 2016: Optical, Infrared, and Millimeter Wave*, volume 9904, page 99045B. SPIE, jul 2016. ISBN 9781510601871. doi: 10.1117/12.2233353.

F. Y. Jiang, Roger V. Yelle, S. K. Jain, J. Cui, F. Montmessin, N. M. Schneider, J. Deighan, H. Gröller, and L. Verdier. Detection of Mesospheric CO2 Ice Clouds on Mars in Southern Summer. *Geophysical Research Letters*, 46(14):7962–7971, jul 2019. ISSN 19448007. doi: 10.1029/2019GL082029. URL `https://onlinelibrary.wiley.com/doi/full/10.1029/2019GL082029https://onlinelibrary.wiley.com/doi/abs/10.1029/2019GL082029https://agupubs.onlinelibrary.wiley.com/doi/10.1029/2019GL082029`.

L. M. Jones, J. W. Peterson, E. J. Schaefer, and H. F. Schulte. Upper-air density and temperature: some variations and an abrupt warming in the mesosphere. *Journal of Geophysical Research*, 64(12):2331–2340, dec 1959. doi: 10.1029/jz064i012p02331. URL `https://agupubs.onlinelibrary.wiley.com/doi/full/10.1029/JZ064i012p02331https://agupubs.onlinelibrary.wiley.com/doi/abs/10.1029/JZ064i012p02331https://agupubs.onlinelibrary.wiley.com/doi/10.1029/JZ064i012p02331`.

M. Kaula, William. *Theory of Satellite Geodesy: Applications of Satellites to Geodesy.* Dovers Publications, Inc., Mineola, New York, 2000.

Gerald M. Keating, S. W. Bougher, R. W. Zurek, R. H. Tolson, G. J. Cancro, S. N. Noll, J. S. Parker, T. J. Schellenberg, R. W. Shane, B. L. Wilkerson, J. R. Murphy, J. L. Hollingsworth, R. M. Haberle, M. Joshi, J. C. Pearl, B. J. Conrath, M. D. Smith, R. T. Clancy, R. C. Blanchard, R. G. Wilmoth, D. F. Rault, T. Z. Martin, D. T. Lyons, P. B. Esposito, M. D. Johnston, C. W. Whetzel, C. G. Justus, and J. M. Babicke. The structure of the upper atmosphere of Mars: In situ accelerometer measurements from Mars Global Surveyor. *Science*, 279(5357):1672–1676, 1998. ISSN 00368075. doi: 10.1126/science.279.5357.1672. URL `http://science.sciencemag.org/`.

V. V. Kerzhanovich. Mars 6: Improved analysis of the descent module measurements. *Icarus*, 30 (1):1–25, 1977. ISSN 10902643. doi: 10.1016/0019-1035(77)90117-8.

Alain S.J. Khayat, Michael D. Smith, Michael Wolff, Frank Daerden, Lori Neary, Manish R. Patel, Arianna Piccialli, Ann C. Vandaele, Ian Thomas, Bojan Ristic, Jon Mason, Yannick Willame, Cedric Depiesse, Giancarlo Bellucci, and José Juan López-Moreno. ExoMars TGO/NOMAD-UVIS Vertical Profiles of Ozone: 2. The High-Altitude Layers of Atmospheric Ozone. *Journal of Geophysical Research: Planets*, 126(11):e2021JE006834, nov 2021. ISSN 21699100. doi: 10.1029/2021JE006834. URL `https://onlinelibrary.wiley.com/doi/full/10.1029/2021JE006834https://onlinelibrary.wiley.com/doi/abs/10.1029/2021JE006834https://agupubs.onlinelibrary.wiley.com/doi/10.1029/2021JE006834`.

Andreas Kirsch. *An Introduction to the Mathematical Theory of Inverse Problems*, volume 120 of *Applied Mathematical Sciences.* Springer International Publishing, Cham, 1996. ISBN 978-0387945309.

Armin Kleinböhl, John T. Schofield, David M. Kass, Wedad A. Abdou, Charles R. Backus, Bhaswar Sen, James H. Shirley, W. Gregory Lawson, Mark I. Richardson, Fredric W. Taylor, Nicholas A. Teanby, and Daniel J. McCleese. Mars Climate Sounder limb profile retrieval of atmospheric temperature, pressure, and dust and water ice opacity. *Journal of Geophysical Research E: Planets*, 114(10):1–30, oct 2009. ISSN 01480227. doi: 10.1029/2009JE003358. URL `https://agupubs.onlinelibrary.wiley.com/doi/full/10.1029/2009JE003358https://agupubs.onlinelibrary.wiley.com/doi/abs/10.1029/2009JE003358https://agupubs.onlinelibrary.wiley.com/doi/10.1029/2009JE003358`.

Elise W. Knutsen, Geronimo L. Villanueva, Giuliano Liuzzi, Matteo M.J. Crismani, Michael J. Mumma, Michael D. Smith, Ann Carine Vandaele, Shohei Aoki, Ian R. Thomas, Frank Daerden, Sébastien Viscardy, Justin T. Erwin, Loic Trompet, Lori Neary, Bojan Ristic, Miguel Angel Lopez-Valverde, Jose Juan Lopez-Moreno, Manish R. Patel, Ozgur Karatekin, and Giancarlo Bellucci. Comprehensive investigation of Mars methane and organics with ExoMars/NOMAD. *Icarus*, 357(August 2020):114266, mar 2021. ISSN 10902643. doi: 10.1016/j.icarus.2020.114266. URL `https://doi.org/10.1016/j.icarus.2020.114266https://linkinghub.elsevier.com/retrieve/pii/S001910352030587X`.

Nils König, Peter Braesicke, and Thomas Von Clarmann. Tropopause altitude determination from temperature profile measurements of reduced vertical resolution. *Atmospheric Measurement Techniques*, 12(7):4113–4129, jul 2019. ISSN 18678548. doi: 10.5194/amt-12-4113-2019. URL `https://amt.copernicus.org/articles/12/4113/2019/`.

O. Korablev, F. Montmessin, A. Trokhimovskiy, A. A. Fedorova, A. V. Shakun, A. V. Grigoriev, B. E. Moshkin, N. I. Ignatiev, F. Forget, F. Lefèvre, K. Anufreychik, I. Dzuban, Y. S. Ivanov, Y. K. Kalinnikov, T. O. Kozlova, A. Kungurov, V. Makarov, F. Martynovich, I. Maslov, D. Merzlyakov, P. P. Moiseev, Y. Nikolskiy, A. Patrakeev, D. Patsaev, A. Santos-Skripko, O. Sazonov, N. Semena, A. Semenov, V. Shashkin, A. Sidorov, A. V. Stepanov, I. Stupin, D. Timonin, A. Y. Titov, A. Viktorov, A. Zharkov, Francesca Altieri, G. Arnold, D. A. Belyaev, J. L. Bertaux, D. S. Betsis, N. Duxbury, T. Encrenaz, T. Fouchet, J. C. Gérard, D. Grassi, S. Guerlet, P. Hartogh, Y. Kasaba, I. Khatuntsev, V. A. Krasnopolsky, R. O. Kuzmin, E. Lellouch, M. A. Lopez-Valverde, M. Luginin, A. Määttänen, E. Marcq, J. Martin Torres, A. S. Medvedev, Ehouarn Millour, K. S. Olsen, M. R. Patel, C. Quantin-Nataf, A. V. Rodin, V. I. Shematovich, I. Thomas, N. Thomas, L. Vazquez, M. Vincendon, V. Wilquet, C. F. Wilson, L. V. Zasova, L. M. Zelenyi, and M. P. Zorzano. The Atmospheric Chemistry Suite (ACS) of Three Spectrometers for the ExoMars 2016 Trace Gas Orbiter, feb 2018. ISSN 15729672.

Oleg Korablev, Jean Loup Bertaux, Anna Fedorova, D. Fonteyn, A. Stepanov, Y. Kalinnikov, A. Kiselev, A. Grigoriev, V. Jegoulev, S. Perrier, E. Dimarellis, J. P. Dubois, A. Reberac, E. Van Ransbeeck, B. Gondet, F. Montmessin, and A. Rodin. SPICAM IR acousto-optic spectrometer experiment on Mars Express. *Journal of Geophysical Research: Planets*, 111(9):9–12, sep 2006. ISSN 01480227. doi: 10.1029/2006JE002696. URL `https://onlinelibrary.wiley.com/doi/full/10.1029/2006JE002696https://onlinelibrary.wiley.com/doi/abs/10.1029/2006JE002696https://agupubs.onlinelibrary.wiley.com/doi/10.1029/2006JE002696`.

Oleg Korablev, Ann Carine Vandaele, Franck Montmessin, Anna A. Fedorova, Alexander Trokhimovskiy, François Forget, Franck Lefèvre, Frank Daerden, Ian R. Thomas, Loïc Trompet, Justin T. Erwin, Shohei Aoki, Séverine Robert, Lori Neary, Sébastien Viscardy, Alexey V. Grigoriev, Nikolay I. Ignatiev, Alexey Shakun, Andrey Patrakeev, Denis A. Belyaev, Jean Loup

Bertaux, Kevin S. Olsen, Lucio Baggio, Juan Alday, Yuriy S. Ivanov, Bojan Ristic, Jon Mason, Yannick Willame, Cédric Depiesse, Laszlo Hetey, Sophie Berkenbosch, Roland Clairquin, Claudio Queirolo, Bram Beeckman, Eddy Neefs, Manish R. Patel, Giancarlo Bellucci, Jose Juan López-Moreno, Colin F. Wilson, Giuseppe Etiope, Lev Zelenyi, Håkan Svedhem, Jorge L. Vago, Gustavo Alonso-Rodrigo, Francesca Altieri, Konstantin Anufreychik, Gabriele Arnold, Sophie Bauduin, David Bolsée, Giacomo Carrozzo, R. Todd Clancy, Edward Cloutis, Matteo Crismani, Fabiana Da Pieve, Emiliano D'Aversa, Natalia Duxbury, Therese Encrenaz, Thierry Fouchet, Bernd Funke, Didier Fussen, Maia Garcia-Comas, Jean Claude Gérard, Marco Giuranna, Leo Gkouvelis, Francisco Gonzalez-Galindo, Davide Grassi, Sandrine Guerlet, Paul Hartogh, James Holmes, Benoît Hubert, Jacek Kaminski, Ozgur Karatekin, Yasumasa Kasaba, David Kass, Igor Khatuntsev, Armin Kleinböhl, Nikita Kokonkov, Vladimir Krasnopolsky, Ruslan Kuzmin, Gaétan Lacombe, Orietta Lanciano, Emmanuel Lellouch, Stephen Lewis, Mikhail Luginin, Giuliano Liuzzi, Manuel López-Puertas, Miguel López-Valverde, Anni Määttänen, Arnaud Mahieux, Emmanuel Marcq, Javier Martin-Torres, Igor Maslov, Alexander Medvedev, Ehouarn Millour, Boris Moshkin, Michael J J. Mumma, Hiromu Nakagawa, Robert E. Novak, Fabrizio Oliva, Dmitry Patsaev, Arianna Piccialli, Cathy Quantin-Nataf, Etienne Renotte, Birgit Ritter, Alexander Rodin, Frédéric Schmidt, Nick Schneider, Valery Shematovich, Michael D D. Smith, Nicholas A. Teanby, Ed Thiemann, Nicolas Thomas, Jean Vander Auwera, Luis Vazquez, Geronimo Villanueva, Matthieu Vincendon, James Whiteway, Valérie Wilquet, Michael J. Wolff, Paulina Wolkenberg, Roger Yelle, Roland Young, Ludmila Zasova, Maria Paz Zorzano, AA Fedorova Nature, Undefined 2019, Anna A. Fedorova, Alexander Trokhimovskiy, François Forget, Franck Lefèvre, Frank Daerden, Ian R. Thomas, Loïc Trompet, Justin T. Erwin, Shohei Aoki, Séverine Robert, Lori Neary, Sébastien Viscardy, Alexey V. Grigoriev, Nikolay I. Ignatiev, Alexey Shakun, Andrey Patrakeev, Denis A. Belyaev, Jean Loup Bertaux, Kevin S. Olsen, Lucio Baggio, Juan Alday, Yuriy S. Ivanov, Bojan Ristic, Jon Mason, Yannick Willame, Cédric Depiesse, Laszlo Hetey, Sophie Berkenbosch, Roland Clairquin, Claudio Queirolo, Bram Beeckman, Eddy Neefs, Manish R. Patel, Giancarlo Bellucci, Jose Juan López-Moreno, Colin F. Wilson, Giuseppe Etiope, Lev Zelenyi, Håkan Svedhem, Jorge L. Vago, Gustavo Alonso-Rodrigo, Francesca Altieri, Konstantin Anufreychik, Gabriele Arnold, Sophie Bauduin, David Bolsée, Giacomo Carrozzo, R. Todd Clancy, Edward Cloutis, Matteo Crismani, Fabiana Da Pieve, Emiliano D'Aversa, Natalia Duxbury, Therese Encrenaz, Thierry Fouchet, Bernd Funke, Didier Fussen, Maia Garcia-Comas, Jean Claude Gérard, Marco Giuranna, Leo Gkouvelis, Francisco Gonzalez-Galindo, Davide Grassi, Sandrine Guerlet, Paul Hartogh, James Holmes, Benoît Hubert, Jacek Kaminski, Ozgur Karatekin, Yasumasa Kasaba, David Kass, Igor Khatuntsev, Armin Kleinböhl, Nikita Kokonkov, Vladimir Krasnopolsky, Ruslan Kuzmin, Gaétan Lacombe, Orietta Lanciano, Emmanuel Lellouch, Stephen Lewis, Mikhail Luginin, Giuliano Liuzzi, Manuel López-Puertas, Miguel López-Valverde, Anni Määttänen, Arnaud Mahieux, Emmanuel Marcq, Javier Martin-Torres, Igor Maslov, Alexander Medvedev, Ehouarn Millour, Boris Moshkin, Michael J J. Mumma, Hiromu Nakagawa, Robert E. Novak, Fabrizio Oliva, Dmitry Patsaev, Arianna Piccialli, Cathy Quantin-Nataf, Etienne Renotte, Birgit Ritter, Alexander Rodin, Frédéric Schmidt, Nick Schneider, Valery Shematovich, Michael D D. Smith, Nicholas A. Teanby, Ed Thiemann, Nicolas Thomas, Jean Vander Auwera, Luis Vazquez, Geronimo Villanueva, Matthieu Vincendon, James Whiteway, Valérie Wilquet, Michael J. Wolff, Paulina Wolkenberg, Roger Yelle, Roland Young, Ludmila Zasova, and Maria Paz Zorzano. No detection of methane on Mars from early ExoMars Trace Gas Orbiter observations. *Nature*, 568(7753):517–520, apr 2019. ISSN 14764687. doi: 10.1038/s41586-019-1096-4. URL `https://doi.org/10.1038/s41586-019-1096-4https://idp.nature.com/authorize/casa?redirect{_}uri=https://www.nature.com/articles/s41586-019-1096-4{&}casa{_}token=thR6MhDzPMIAAAAA:`

Z8Tc6dwzW8pjoSTDqtfPkfzY0JaaHnMxWesWtw7vuKvpaBiMx{_}THV{_}IIlJrgYl7rpNXUMlJyiQM911kUF7o.

T. T. Koskinen, B. R. Sandel, R. V. Yelle, F. J. Capalbo, G. M. Holsclaw, W. E. McClintock, and S. Edgington. The density and temperature structure near the exobase of Saturn from Cassini UVIS solar occultations. *Icarus*, 226(2):1318–1330, nov 2013. ISSN 00191035. doi: 10.1016/j.icarus.2013.07.037.

V. A. Krasnopolsky and V. A. Parshev. Chemical composition of the atmosphere of Venus. *Nature*, 292(5824):610–613, 1981. ISSN 00280836. doi: 10.1038/292610a0. URL `https://www.nature.com/articles/292610a0`.

Vladimir A. Krasnopolsky, Jean Pierre Maillard, and Tobias C. Owen. Detection of methane in the martian atmosphere: Evidence for life? *Icarus*, 172(2):537–547, dec 2004. ISSN 00191035. doi: 10.1016/j.icarus.2004.07.004.

Gerard P. Kuiper. Carbon Dioxide on Mars. *Harvard College Observatory Announcement Card*, 851, 1947.

Ludivine Leclercq, Hayley N Williamson, Robert E Johnson, Orenthal J Tucker, Lucia Tian, and Darci Snowden. Molecular kinetic simulations of transient perturbations in a planet's upper atmosphere. *Icarus*, 335:113394, 2020. ISSN 00191035. doi: 10.1016/j.icarus.2019.113394. URL `https://doi.org/10.1016/j.icarus.2019.113394`.

C. Lee, W. G. Lawson, M. I. Richardson, N. G. Heavens, A. Kleinböhl, D. Banfield, D. J. McCleese, R. Zurek, D. Kass, J. T. Schofield, C. B. Leovy, F. W. Taylor, and A. D. Toigo. Thermal tides in the Martian middle atmosphere as seen by the Mars Climate Sounder. *Journal of Geophysical Research: Planets*, 114(E3):3005, mar 2009. ISSN 2156-2202. doi: 10.1029/2008JE003285. URL `https://onlinelibrary.wiley.com/doi/full/10.1029/2008JE003285https://onlinelibrary.wiley.com/doi/abs/10.1029/2008JE003285https://agupubs.onlinelibrary.wiley.com/doi/10.1029/2008JE003285`.

Franck Lefèvre and François Forget. Observed variations of methane on Mars unexplained by known atmospheric chemistry and physics. *Nature*, 460(7256):720–723, aug 2009. ISSN 00280836. doi: 10.1038/nature08228. URL `https://www.nature.com/articles/nature08228`.

E. Lellouch, T. Encrenaz, T. De Graauw, S. Erard, P. Morris, J. Crovisier, H. Feuchtgruber, T. Girard, and M. Burgdorf. The 2.4-45 μm spectrum of Mars observed with the Infrared Space Observatory. *Planetary and Space Science*, 48(12-14):1393–1405, 2000. ISSN 00320633. doi: 10.1016/s0032-0633(00)00118-5.

F G Lemoine, S. Bruinsma, D. S. Chinn, and J. M. Forbes. Thermospheric studies with Mars global surveyor. In *Collection of Technical Papers - AIAA/AAS Astrodynamics Specialist Conference, 2006*, volume 2, pages 993–1005, 2006. ISBN 1563478226. doi: 10.2514/6.2006-6395.

Jacqueline Lenoble. *Atmospheric Radiative Transfer*. A. Deepak Publishing, 1993. ISBN 0-937194-21-2.

Kenneth Levenberg. A method for the solution of certain non-linear problems in least squares. *Quarterly of Applied Mathematics*, 2(2):164–168, 1944. ISSN 0033-569X. doi: 10.1090/qam/10666. URL `https://about.jstor.org/terms`.

C. Listowski, A. Määttänen, F. Montmessin, A. Spiga, and F. Lefèvre. Modeling the microphysics of CO2 ice clouds within wave-induced cold pockets in the martian mesosphere. *Icarus*, 237: 239–261, jul 2014. ISSN 10902643. doi: 10.1016/j.icarus.2014.04.022.

Giuliano Liuzzi, Geronimo L. Villanueva, Michael J. Mumma, Michael D. Smith, Frank Daerden, Bojan Ristic, Ian Thomas, Ann Carine Vandaele, Manish R. Patel, José Juan Lopez-Moreno, Giancarlo Bellucci, Mark Allen, Gustavo Alonso-Rodrigo, Francesca Altieri, Shohei Aoki, Sophie Bauduin, David Bolsée, Todd Clancy, Edward Cloutis, Emiliano D'Aversa, Cédric Depiesse, Justin Erwin, Anna Fedorova, Vittorio Formisano, Bernd Funke, Didier Fussen, Maia Garcia-Comas, Anna Geminale, Jean Claude Gérard, Didier Gillotay, Marco Giuranna, Francisco Gonzalez-Galindo, Will Hewson, James Homes, Nicolai Ignatiev, Jacek Kaminski, Ozgur Karatekin, Yasumasa Kasaba, Orietta Lanciano, Franck Lefèvre, Stephen Lewis, Manuel López- Puertas, Miguel López-Valverde, Arnaud Mahieux, Jon Mason, Jack Mc Connell, Lori Hiromu Neary Nakagawa, Eddy Neefs, R. Novak, Fabrizio Oliva, Arianna Piccialli, Etienne Renotte, Severine Robert, Giuseppe Sindoni, Arnaud Stiepen, Alexander Trokhimovskiy, Jean Vander Auwera, Sébastien Viscardy, Jim Whiteway, Yannick Willame, Valérie Wilquet, Michael Wolff, Paulina Wolkenberg, Gustavo Alonso-Rodrigo, Beatriz Aparicio del Moral, Pascal Barzin, Bram Beeckman, Ali BenMoussa, Sophie Berkenbosch, David Biondi, Sabrina Bonnewijn, Gian Paolo Candini, Roland Clairquin, Javier Cubas, Boris Giordanengo, Samuel Gissot, Alejandro Gomez, Brijen Hathi, Jose Jeronimo Zafra, Mark Leese, Jeroen Maes, Emmanuel Mazy, Alexandra Mazzoli, Jose Meseguer, Rafael Morales, Anne Orban, M. Pastor-Morales, Isabel Perez-grande, Claudio Queirolo, Julio Rodriguez Gomez, Bortolino Saggin, Valérie Samain, Angel Sanz Andres, Rosario Sanz, Juan Felipe Simar, and Tanguy Thibert. Methane on Mars: New insights into the sensitivity of CH 4 with the NOMAD/ExoMars spectrometer through its first in-flight calibration. *Icarus*, 321:671–690, mar 2019. ISSN 10902643. doi: 10.1016/j.icarus.2018.09.021. URL `https://doi.org/10.1016/j.icarus.2018.09.021`.

Giuliano Liuzzi, Geronimo L. Villanueva, Loïc Trompet, Matteo M. J. Crismani, Arianna Piccialli, Shohei Aoki, Miguel Angel Lopez-Valverde, Aurélien Stolzenbach, Frank Daerden, Lori Neary, Michael D. Smith, Manish R. Patel, Stephen R. Lewis, R. Todd Clancy, Ian R. Thomas, Bojan Ristic, Giancarlo Bellucci, Jose-Juan Lopez-Moreno, and Ann Carine Vandaele. First Detection and Thermal Characterization of Terminator CO 2 Ice Clouds with ExoMars/NOMAD. *Geophysical Research Letters*, 48(22):e2021GL095895, nov 2021. ISSN 0094-8276. doi: 10.1029/2021gl095895. URL `https://onlinelibrary.wiley.com/doi/full/10.1029/2021GL095895https://onlinelibrary.wiley.com/doi/abs/10.1029/2021GL095895https://agupubs.onlinelibrary.wiley.com/doi/10.1029/2021GL095895`.

Gary L. Long and J. D. Winefordner. Limit of Detection A Closer Look at the IUPAC Definition. *Analytical Chemistry*, 55(07):712A–724A, jun 1983. ISSN 0003-2700. doi: 10.1021/ac00258a724. URL `https://pubs.acs.org/doi/abs/10.1021/ac00258a724`.

Miguel A López-Valverde, Jean Claude Gerard, Francisco González-Galindo, Ann Carine Vandaele, Ian Thomas, Oleg Korablev, Nikolai Ignatiev, Anna Fedorova, Franck Montmessin, Anni Määttänen, Sabrina Guilbon, Franck Lefevre, Manish R Patel, Sergio Jiménez-Monferrer, Maya García-Comas, Alejandro Cardesin, Colin F Wilson, R. T. Clancy, Armin Kleinböhl, Daniel J. McCleese, David M Kass, Nick M Schneider, Michael S Chaffin, José Juan López-Moreno, and Julio Rodríguez. Investigations of the Mars Upper Atmosphere with ExoMars Trace Gas Orbiter, 2018. ISSN 15729672. URL `https://doi.org/10.1007/s11214-017-0463-4`.

Miguel-Angel López Valverde, Bernd Funke, Adrian Brines, Aurèlien Aurlien Stolzenbach, Ashimananda Modak, Brittany Hill, Francisco González-Galindo, Ian Thomas, Loic Trompet, Shohei Aoki, Gerónimo Gernimo Gerónimo Villanueva, Giuliano Liuzzi, Justin Erwin, Udo Grabowski, Francois Forget, José Juan Lopez Moreno, Julio Rodriguez-Gómez, Bojan Ristic, Frank Daerden, Giancarlo Bellucci, Manish Patel, Ann-Carine Ann-Carine

Ann-Carine Vandaele, Miguel-Angel Lopez-Valverde, Bernd Funke, Adrian Brines, Aurèlien Aurlien Stolzenbach, Ashimananda Modak, Brittany Hill, Gonzlez-Galindo Francisco, Ian Thomas, Loic Trompet, Shohei Aoki, Gerónimo Gernimo Gerónimo Villanueva, Giuliano Liuzzi, Justin Erwin, Ann-Carine Ann-Carine Ann-Carine Vandaele, Udo Grabowski, Francois Forget, Jose Juan Lopez Moreno, Julio Rodriguez, Bojan Ristic, Frank Daerden, Giancarlo Bellucci, and Manish Patel. Martian atmospheric temperature and density profiles during the 1st year of NOMAD/TGO solar occultation measurements. *Journal of Geophysical Research: Planets*, 128(2):e2022JE007278, nov 2022. ISSN 2169-9097. doi: 10.1029/2022je007278. URL `https://onlinelibrary.wiley.com/doi/full/10.1029/2022JE007278https://onlinelibrary.wiley.com/doi/abs/10.1029/2022JE007278https://agupubs.onlinelibrary.wiley.com/doi/10.1029/2022JE007278`.

A. Määttänen, F. Montmessin, B. Gondet, F. Scholten, H. Hoffmann, F. González-Galindo, A. Spiga, F. Forget, E. Hauber, G. Neukum, J. P. Bibring, and J. L. Bertaux. Mapping the mesospheric CO2 clouds on Mars: MEx/OMEGA and MEx/HRSC observations and challenges for atmospheric models. *Icarus*, 209(2):452–469, oct 2010. ISSN 10902643. doi: 10.1016/j.icarus.2010.05.017.

Julio A Magalhses, John T. Schofield, Alvin Seiff, Julio A. Magalhães, John T. Schofield, and Alvin Seiff. Results of the Mars Pathfinder atmospheric structure investigation. *Journal of Geophysical Research E: Planets*, 104(E4):8943–8955, apr 1999. ISSN 01480227. doi: 10.1029/1998JE900041. URL `https://agupubs.onlinelibrary.wiley.com/doi/10.1029/1998JE900041`.

P. R. Mahaffy, M. Benna, M. Elrod, R. V. Yelle, S. W. Bougher, S. W. Stone, and B. M. Jakosky. Structure and composition of the neutral upper atmosphere of Mars from the MAVEN NGIMS investigation. *Geophysical Research Letters*, 42(21):8951–8957, nov 2015. ISSN 19448007. doi: 10.1002/2015GL065329. URL `https://onlinelibrary.wiley.com/doi/full/10.1002/2015GL065329https://onlinelibrary.wiley.com/doi/abs/10.1002/2015GL065329https://agupubs.onlinelibrary.wiley.com/doi/10.1002/2015GL065329`.

Paul R. Mahaffy, Christopher R. Webster, Michel Cabane, Pamela G. Conrad, Patrice Coll, Sushil K. Atreya, Robert Arvey, Michael Barciniak, Mehdi Benna, Lora Bleacher, William B. Brinckerhoff, Jennifer L. Eigenbrode, Daniel Carignan, Mark Cascia, Robert A. Chalmers, Jason P. Dworkin, Therese Errigo, Paula Everson, Heather Franz, Rodger Farley, Steven Feng, Gregory Frazier, Caroline Freissinet, Daniel P. Glavin, Daniel N. Harpold, Douglas Hawk, Vincent Holmes, Christopher S. Johnson, Andrea Jones, Patrick Jordan, James Kellogg, Jesse Lewis, Eric Lyness, Charles A. Malespin, David K. Martin, John Maurer, Amy C. McAdam, Douglas McLennan, Thomas J. Nolan, Marvin Noriega, Alexander A. Pavlov, Benito Prats, Eric Raaen, Oren Sheinman, David Sheppard, James Smith, Jennifer C. Stern, Florence Tan, Melissa Trainer, Douglas W. Ming, Richard V. Morris, John Jones, Cindy Gundersen, Andrew Steele, James Wray, Oliver Botta, Laurie A. Leshin, Tobias Owen, Steve Battel, Bruce M. Jakosky, Heidi Manning, Steven Squyres, Rafael Navarro-González, Christopher P. McKay, Francois Raulin, Robert Sternberg, Arnaud Buch, Paul Sorensen, Robert Kline-Schoder, David Coscia, Cyril Szopa, Samuel Teinturier, Curt Baffes, Jason Feldman, Greg Flesch, Siamak Forouhar, Ray Garcia, Didier Keymeulen, Steve Woodward, Bruce P. Block, Ken Arnett, Ryan Miller, Charles Edmonson, Stephen Gorevan, and Erik Mumm. The sample analysis at mars investigation and instrument suite. *Space Science Reviews*, 170 (1-4):401–478, sep 2012. ISSN 00386308. doi: 10.1007/s11214-012-9879-z. URL `https://link.springer.com/article/10.1007/s11214-012-9879-z`.

A. Mahieux, A. C. Vandaele, E. Neefs, S. Robert, V. Wilquet, R. Drummond, A. Federova, and

J. L. Bertaux. Densities and temperatures in the Venus mesosphere and lower thermosphere retrieved from SOIR on board Venus Express: Retrieval technique. *Journal of Geophysical Research E: Planets*, 115(12), 2010. ISSN 01480227. doi: 10.1029/2010JE003589.

A. Mahieux, A. C. Vandaele, S.W. Bougher, R. Drummond, S. Robert, V. Wilquet, S. Chamberlain, A. Piccialli, F. Montmessin, S. Tellmann, M. Pätzold, B. Häusler, and J.L. Bertaux. Update of the Venus density and temperature profiles at high altitude measured by SOIR on board Venus Express. *Planetary and Space Science*, 113-114:309–320, aug 2015. ISSN 00320633. doi: 10.1016/j.pss.2015.02.002. URL `https://linkinghub.elsevier.com/retrieve/pii/S0032063315000343`.

Arnaud Mahieux. *Inversion of the infrared spectra recorded by the SOIR instrument on board VenusExpress*. PhD thesis, Université Libre de Bruxelles, 2011. URL `http://planetary.aeronomie.be/multimedia/pdf/These{_}ArnaudMahieux{_}2011.pdf`.

Arnaud Mahieux, Sophie Berkenbosch, Roland Clairquin, Didier Fussen, Nina Mateshvili, Eddy Neefs, Dennis Nevejans, Bojan Ristic, Ann Carine Vandaele, Valérie Wilquet, Denis Belyaev, Anna Fedorova, Oleg Korablev, Eric Villard, Franck Montmessin, and Jean Loup Bertaux. In-flight performance and calibration of SPICAV SOIR onboard Venus Express. *Applied Optics*, 47(13):2252–2265, may 2008. ISSN 15394522. doi: 10.1364/AO.47.002252. URL `https://www.osapublishing.org/abstract.cfm?uri=ao-47-13-2252`.

Donald W Marquardt. An Algorithm for Least-Squares Estimation of Nonlinear Parameters. *Journal of the Society for Industrial and Applied Mathematics*, 11(2):431–441, 1963. ISSN 0368-4245. doi: 10.1137/0111030.

R A Mcclatchey, W S Benedict, S A Clough, D E Burch, and R F Calfee. AFCRL Atmospheric Absorption Line Parameters\Compilation. Technical report, AIR FORCE CAMBRIDGE RESEARCH LABORATORIES, 1973. URL `https://apps.dtic.mil/dtic/tr/fulltext/u2/762904.pdf`.

Daniel J. McCleese, J. T. Schofield, F. W. Taylor, S. B. Calcutt, M. C. Foote, D. M. Kass, C. B. Leovy, D. A. Paige, P. L. Read, and R. W. Zurek. Mars Climate Sounder: An investigation of thermal and water vapor structure, dust and condensate distributions in the atmosphere, and energy balance of the polar regions. *Journal of Geophysical Research E: Planets*, 112(5):1–16, may 2007. ISSN 01480227. doi: 10.1029/2006JE002790. URL `https://onlinelibrary.wiley.com/doi/full/10.1029/2006JE002790https://onlinelibrary.wiley.com/doi/abs/10.1029/2006JE002790https://agupubs.onlinelibrary.wiley.com/doi/10.1029/2006JE002790`.

Daniel J. McCleese, N. G. Heavens, J. T. Schofield, W. A. Abdou, J. L. Bandfield, S. B. Calcutt, P. G.J. Irwin, D. M. Kass, A. Kleinböhl, S. R. Lewis, D. A. Paige, P. L. Read, M. I. Richardson, J. H. Shirley, F. W. Taylor, N. Teanby, and R. W. Zurek. Structure and dynamics of the Martian lower and middle atmosphere as observed by the Mars Climate Sounder: Seasonal variations in zonal mean temperature, dust, and water ice aerosols. *Journal of Geophysical Research E: Planets*, 115(12):12016, dec 2010. ISSN 01480227. doi: 10.1029/2010JE003677. URL `https://onlinelibrary.wiley.com/doi/full/10.1029/2010JE003677https://onlinelibrary.wiley.com/doi/abs/10.1029/2010JE003677https://agupubs.onlinelibrary.wiley.com/doi/10.1029/2010JE003677`.

T. H. McConnochie, J. F. Bell, D. Savransky, M. J. Wolff, A. D. Toigo, H. Wang, M. I. Richardson, and P. R. Christensen. THEMIS-VIS observations of clouds in the martian mesosphere:

Altitudes, wind speeds, and decameter-scale morphology. *Icarus*, 210(2):545–565, dec 2010. ISSN 00191035. doi: 10.1016/j.icarus.2010.07.021.

M. Patrick McCormick. SAGE AEROSOL MEASUREMENTS. Technical report, 1987.

T. McDunn, S Bougher, J Murphy, A. Kleinböhl, F Forget, and M Smith. Characterization of middle-atmosphere polar warming at Mars. *Journal of Geophysical Research E: Planets*, 118(2):161–178, 2013. ISSN 21699100. doi: 10.1002/jgre.20016. URL `https://hal.archives-ouvertes.fr/hal-01091228`.

M. Meftah, L. Damé, D. Bolsée, A. Hauchecorne, N. Pereira, D. Sluse, G. Cessateur, A. Irbah, J. Bureau, M. Weber, K. Bramstedt, T. Hilbig, R. Thiéblemont, M. Marchand, F. Lefèvre, A. Sarkissian, and S. Bekki. SOLAR-ISS: A new reference spectrum based on SOLAR/SOLSPEC observations. *Astronomy and Astrophysics*, 611:A1, mar 2018. ISSN 14320746. doi: 10.1051/0004-6361/201731316. URL `https://public.wmo.int/en/programmes/`.

E Millour, A Spiga, A Colaitis, T Navarro, J.-B. Madeleine, J.-Y. Chauffray, L Montabone, M.~A. Lopez-valverde, F Gonzalez-Galindo, F Lefèvre, F Montmessin, S.~R. Lewis, L.~P. Read, M.-C. Desjean, and J.-P. Huot. Mars Climate Database Version 5. In *European Planetary Science Congress 2012*, volume 1, pages 2012–302. European Planetary Science Congress, 2012. URL `http://www-mars.lmd.jussieu.fr`.

Luca Montabone, Aymeric Spiga, David M. Kass, Armin Kleinböhl, François Forget, and Ehouarn Millour. Martian Year 34 Column Dust Climatology from Mars Climate Sounder Observations: Reconstructed Maps and Model Simulations. *Journal of Geophysical Research: Planets*, 125(8):e2019JE006111, aug 2020. ISSN 21699100. doi: 10.1029/2019JE006111. URL `https://onlinelibrary.wiley.com/doi/full/10.1029/2019JE006111https://onlinelibrary.wiley.com/doi/abs/10.1029/2019JE006111https://agupubs.onlinelibrary.wiley.com/doi/10.1029/2019JE006111`.

F. Montmessin, O. Korablev, F. Lefèvre, J. L. Bertaux, A. Fedorova, A. Trokhimovskiy, J. Y. Chaufray, G. Lacombe, A. Reberac, L. Maltagliati, Y. Willame, S. Guslyakova, J. C. Gérard, A. Stiepen, D. Fussen, N. Mateshvili, A. Määttänen, F. Forget, O. Witasse, F. Leblanc, A. C. Vandaele, E. Marcq, B. Sandel, B. Gondet, N. Schneider, M. Chaffin, and N. Chapron. SPICAM on Mars Express: A 10 year in-depth survey of the Martian atmosphere. *Icarus*, 297:195–216, nov 2017. ISSN 10902643. doi: 10.1016/j.icarus.2017.06.022.

F. Montmessin, O. I. Korablev, A. Trokhimovskiy, F. Lefèvre, A. A. Fedorova, L. Baggio, A. Irbah, G. Lacombe, K. S. Olsen, A. S. Braude, D. A. Belyaev, Juan Alday, F. Forget, F. Daerden, J. Pla-Garcia, S. Rafkin, C. F. Wilson, A. Patrakeev, A. Shakun, and J. L. Bertaux. A stringent upper limit of 20 pptv for methane on Mars and constraints on its dispersion outside Gale crater. *Astronomy & Astrophysics*, 650:A140, jun 2021. ISSN 0004-6361. doi: 10.1051/0004-6361/202140389. URL `https://www.aanda.org/articles/aa/full{_}html/2021/06/aa40389-21/aa40389-21.htmlhttps://www.aanda.org/articles/aa/abs/2021/06/aa40389-21/aa40389-21.html`.

Franck Montmessin, Jean Loup Bertaux, Eric Quémerais, Oleg Korablev, Pascal Rannou, François Forget, Séverine Perrier, Didier Fussen, Sébastien Lebonnois, Aurélie Rébérac, and Emmanuel Dimarellis. Subvisible CO2 ice clouds detected in the mesosphere of Mars. *Icarus*, 183(2): 403–410, aug 2006. ISSN 00191035. doi: 10.1016/j.icarus.2006.03.015.

Franck Montmessin, B. Gondet, J. P. Bibring, Y. Langevin, P. Drossart, F. Forget, and T. Fouchet. Hyperspectral imaging of convective CO2 ice clouds in the equatorial mesosphere of Mars. *Journal of Geophysical Research E: Planets*, 112(11):11–90, nov 2007. ISSN 01480227. doi: 10.1029/2007JE002944. URL `https://onlinelibrary.wiley.com/doi/full/10.1029/2007JE002944https://onlinelibrary.wiley.com/doi/abs/10.1029/2007JE002944https://agupubs.onlinelibrary.wiley.com/doi/10.1029/2007JE002944`.

John E. Moores, Penelope L. King, Christina L. Smith, German M. Martinez, Claire E. Newman, Scott D. Guzewich, Pierre Yves Meslin, Christopher R. Webster, Paul R. Mahaffy, Sushil K. Atreya, and Andrew C. Schuerger. The Methane Diurnal Variation and Microseepage Flux at Gale Crater, Mars as Constrained by the ExoMars Trace Gas Orbiter and Curiosity Observations. *Geophysical Research Letters*, 46(16):9430–9438, aug 2019. ISSN 19448007. doi: 10.1029/2019GL083800. URL `https://doi.org/10.1029/https://onlinelibrary.wiley.com/doi/10.1029/2019GL083800`.

J. Moré. Lecture Notes in Mathematics 630. Technical report, 1977.

V. Morozov. On the solution of functional equations by the method of regularization. *Dokl. Akad. Nauk SSSR*, 167(3):510–512, 1966. URL `http://www.mathnet.ru/php/archive.phtml?wshow=paper{&}jrnid=dan{&}paperid=32161{&}option{_}lang=eng`.

Michael J. Mumma, Geronimo L. Villanueva, Robert E. Novak, Tilak Hewagama, Boncho P. Bonev, Michael A. DiSanti, Avi M. Mandell, and Michael D. Smith. Strong release of methane on Mars in northern summer 2003. *Science*, 323(5917):1041–1045, feb 2009. ISSN 00368075. doi: 10.1126/science.1165243.

Mario Nachbar, Denis Duft, Thomas Peter Mangan, Juan Carlos Gomez Martin, John M.C. Plane, and Thomas Leisner. Laboratory measurements of heterogeneous CO2 ice nucleation on nanoparticles under conditions relevant to the Martian mesosphere. *Journal of Geophysical Research: Planets*, 121(5):753–769, may 2016. ISSN 21699100. doi: 10.1002/2015JE004978.

Hiromu Nakagawa, Sonal K. Jain, Nicholas M. Schneider, Franck Montmessin, Roger V. Yelle, Fayu Jiang, Loic Verdier, Takeshi Kuroda, Nao Yoshida, Hitoshi Fujiwara, Takeshi Imamura, Naoki Terada, Kaori Terada, Kanako Seki, Hannes Gröller, and Justin I. Deighan. A Warm Layer in the Nightside Mesosphere of Mars. *Geophysical Research Letters*, 47(4):1–10, 2020a. ISSN 19448007. doi: 10.1029/2019GL085646.

Hiromu Nakagawa, Naoki Terada, Sonal K. Jain, Nicholas M. Schneider, Franck Montmessin, Roger V. Yelle, Fayu Jiang, Loic Verdier, Scott L. England, Kanako Seki, Hitoshi Fujiwara, Takeshi Imamura, Nao Yoshida, Takeshi Kuroda, Kaori Terada, Hannes Gröller, Justin Deighan, and Bruce M. Jakosky. Vertical Propagation of Wave Perturbations in the Middle Atmosphere on Mars by MAVEN/IUVS. *Journal of Geophysical Research: Planets*, 125(9):e2020JE006481, sep 2020b. ISSN 21699100. doi: 10.1029/2020JE006481. URL `https://onlinelibrary.wiley.com/doi/full/10.1029/2020JE006481https://onlinelibrary.wiley.com/doi/abs/10.1029/2020JE006481https://agupubs.onlinelibrary.wiley.com/doi/10.1029/2020JE006481`.

L. Neary and F. Daerden. The GEM-Mars general circulation model for Mars: Description and evaluation. *Icarus*, 300:458–476, jan 2018. ISSN 10902643. doi: 10.1016/j.icarus.2017.09.028. URL `https://linkinghub.elsevier.com/retrieve/pii/S0019103517302270`.

L. Neary, F. Daerden, S. Aoki, J. Whiteway, R. T. Clancy, M. Smith, S. Viscardy, J. T. Erwin, I. R. Thomas, G. Villanueva, G. Liuzzi, M. Crismani, M. Wolff, S. R. Lewis, J. A. Holmes, M. R. Patel, M. Giuranna, C. Depiesse, A. Piccialli, S. Robert, L. Trompet, Y. Willame, B. Ristic, and A. C. Vandaele. Explanation for the Increase in High-Altitude Water on Mars Observed by NOMAD During the 2018 Global Dust Storm. *Geophysical Research Letters*, 47(7), apr 2020. ISSN 19448007. doi: 10.1029/2019GL084354. URL `https://onlinelibrary.wiley.com/doi/abs/10.1029/2019GL084354https://doi.org/10.1029/2019GL084354`.

Eddy Neefs, Ann Carine Vandaele, Rachel Drummond, Ian R. Thomas, Sophie Berkenbosch, Roland Clairquin, Sofie Delanoye, Bojan Ristic, Jeroen Maes, Sabrina Bonnewijn, Gerry Pieck, Eddy Equeter, Cédric Depiesse, Frank Daerden, Emiel Van Ransbeeck, Dennis Nevejans, Julio Rodriguez-Gómez, José-Juan López-Moreno, Rosario Sanz, Rafael Morales, Gian Paolo Candini, M. Carmen Pastor-Morales, Beatriz Aparicio del Moral, José-Maria Jeronimo-Zafra, Juan Manuel Gómez-López, Gustavo Alonso-Rodrigo, Isabel Pérez-Grande, Javier Cubas, Alejandro M. Gomez-Sanjuan, Fermín Navarro-Medina, Tanguy Thibert, Manish R. Patel, Giancarlo Bellucci, Lieve De Vos, Stefan Lesschaeve, Nico Van Vooren, Wouter Moelans, Ludovic Aballea, Stijn Glorieux, Ann Baeke, Dave Kendall, Jurgen De Neef, Alexander Soenen, Pierre-Yves Puech, Jon Ward, Jean-François Jamoye, David Diez, Ana Vicario-Arroyo, and Michel Jankowski. NOMAD spectrometer on the ExoMars trace gas orbiter mission: part 1—design, manufacturing and testing of the infrared channels. *Applied Optics*, 54(28):8494, oct 2015. ISSN 0003-6935. doi: 10.1364/ao.54.008494. URL `http://dx.doi.org/10.1364/AO.54.008494`.

A O Nier and M. B. McElroy. Composition and structure of Mars' Upper atmosphere: Results from the neutral mass spectrometers on Viking 1 and 2. *Journal of Geophysical Research*, 82(28):4341–4349, sep 1977. ISSN 01480227. doi: 10.1029/js082i028p04341. URL `http://doi.wiley.com/10.1029/JS082i028p04341`.

Gerald R. North, John A. Pyle, and Fuqing Zhang, editors. *Encyclopedia of Atmospheric Sciences*. Academic Press, 2014. ISBN 9780123822253.

Tobias Owen, K. Biemann, D. R. Rushneck, J. E. Biller, D. W. Howarth, and A. L. Lafleur. The composition of the atmosphere at the surface of Mars. *Journal of Geophysical Research*, 82(28):4635–4639, sep 1977. ISSN 0148-0227. doi: 10.1029/js082i028p04635. URL `https://agupubs.onlinelibrary.wiley.com/doi/full/10.1029/JS082i028p04635https://agupubs.onlinelibrary.wiley.com/doi/abs/10.1029/JS082i028p04635https://agupubs.onlinelibrary.wiley.com/doi/10.1029/JS082i028p04635`.

C. Harvey Palmer, Jr. Diffraction Grating Handbook. *Journal of the Optical Society of America*, 46(1):271, 2005. ISSN 0030-3941. URL `http://www.gratinglab.com/http://www.gratinglab.com/library/handbook5/handbook.asphttp://www.amazon.com/Diffraction-Grating-Handbook-Christopher-Palmer/dp/B000XLMD60http://www.opticsinfobase.org/abstract.cfm?URI=josa-46-1-50`.

Ant. Pannekoek. Über die Erscheinungen, welche bei einer Sternbedeckung durch einen Planeten auftreten. *Astronomische Nachrichten*, 164(1):5–10, 1903. ISSN 00046337. doi: 10.1002/asna.19031640103. URL `https://onlinelibrary.wiley.com/doi/10.1002/asna.19031640103`.

M. C. Pastor-Morales, Julio F. Rodríguez-Gómez, Rafael Morales-Muñoz, Juan M. Gómez-López, Beatriz Aparicio-del Moral, Gian Paolo Candini, Jose M. Jerónimo-Zafra, Jose J. López-Moreno, Nicolás F. Robles-Muñoz, Rosario Sanz-Mesa, Eddy Neefs, Ann Carine Vandaele, Rachel Drummond, Ian R. Thomas, Sophie Berkenbosch, Roland Clairquin, Sofie Delanoye, Bojan Ristic, Jeroen Maes, Sabrina Bonnewijn, Manish R. Patel, Mark Leese, and Jon P.

Mason. SINBAD flight software, the on-board software of NOMAD in ExoMars 2016. In *Software and Cyberinfrastructure for Astronomy IV*, volume 9913, page 99133I. SPIE, jul 2016. ISBN 9781510602052. doi: 10.1117/12.2230760.

M. R. Patel, G. Sellers, J. P. Mason, J. A. Holmes, M. A.J. Brown, S. R. Lewis, K. Rajendran, P. M. Streeter, C. Marriner, B. G. Hathi, D. J. Slade, M. R. Leese, M. J. Wolff, A. S.J. Khayat, M. D. Smith, S. Aoki, A. Piccialli, A. C. Vandaele, S. Robert, F. Daerden, I. R. Thomas, B. Ristic, Y. Willame, C. Depiesse, G. Bellucci, and J. J. Lopez-Moreno. ExoMars TGO/NOMAD-UVIS Vertical Profiles of Ozone: 1. Seasonal Variation and Comparison to Water. *Journal of Geophysical Research: Planets*, 126(11):e2021JE006837, nov 2021. ISSN 21699100. doi: 10.1029/2021JE006837. URL `https://onlinelibrary.wiley.com/doi/full/10.1029/2021JE006837https://onlinelibrary.wiley.com/doi/abs/10.1029/2021JE006837https://agupubs.onlinelibrary.wiley.com/doi/10.1029/2021JE006837`.

Manish R. Patel, Philippe Antoine, Jonathon Mason, Mark Leese, Brijen Hathi, Adam H. Stevens, Daniel Dawson, Jason Gow, Timothy Ringrose, James Holmes, Stephen R. Lewis, Didier Beghuin, Philip van Donink, Renaud Ligot, Jean-Luc Dewandel, Daohua Hu, Doug Bates, Richard Cole, Rachel Drummond, Ian R. Thomas, Cédric Depiesse, Eddy Neefs, Eddy Equeter, Bojan Ristic, Sophie Berkenbosch, David Bolsée, Yannick Willame, Ann Carine Vandaele, Stefan Lesschaeve, Lieve De Vos, Nico Van Vooren, Tanguy Thibert, Emmanuel Mazy, Julio Rodriguez-Gomez, Rafael Morales, Gian Paolo Candini, M. Carmen Pastor-Morales, Rosario Sanz, Beatriz Aparicio del Moral, José-Maria Jeronimo-Zafra, Juan Manuel Gómez-López, Gustavo Alonso-Rodrigo, Isabel Pérez-Grande, Javier Cubas, Alejandro M. Gomez-Sanjuan, Fermín Navarro-Medina, Ali BenMoussa, Boris Giordanengo, Samuel Gissot, Giancarlo Bellucci, and Jose Juan Lopez-Moreno. NOMAD spectrometer on the ExoMars trace gas orbiter mission: part 2—design, manufacturing, and testing of the ultraviolet and visible channel. *Applied Optics*, 56(10):2771, apr 2017. ISSN 0003-6935. doi: 10.1364/ao.56.002771. URL `https://www.osapublishing.org/abstract.cfm?uri=ao-54-28-8494`.

M. Pätzold, B. Häusler, G. L. Tyler, T. Andert, S. W. Asmar, M. K. Bird, V. Dehant, D. P. Hinson, P. Rosenblatt, R. A. Simpson, S. Tellmann, P. Withers, M. Beuthe, A. I. Efimov, M. Hahn, D. Kahan, S. Le Maistre, J. Oschlisniok, K. Peter, and S. Remus. Mars Express 10 years at Mars: Observations by the Mars Express Radio Science Experiment (MaRS), aug 2016. ISSN 00320633.

Gordon H. Pettengill and Peter G. Ford. Winter clouds over the North Martian polar cap. *Geophysical Research Letters*, 27(5):609–612, 2000. ISSN 00948276. doi: 10.1029/1999GL010896.

Grant W. Petty. *A First Course in Atmospheric Thermodynamics.* Sundog Publishing, Madison, Wisconsin, 2008. ISBN 978-0972903325.

David L. Phillips. A Technique for the Numerical Solution of Certain Integral Equations of the First Kind. *Journal of the ACM (JACM)*, 9(1):84–97, jan 1962. ISSN 1557735X. doi: 10.1145/321105.321114.

A. Piccialli, A. C. Vandaele, Y. Willame, Anni Määttänen, L. Trompet, J. T. Erwin, F. Daerden, L. Neary, S. Aoki, S. Viscardy, I. R. Thomas, C. Depiesse, B. Ristic, J. P. Mason, M. R. Patel, M.J. J. Wolff, A.S.J. S.J. Khayat, G. Bellucci, and J.-J. J. Lopez-Moreno. Ozone observed by TGO/NOMAD-UVIS solar occultation: an inter-comparison of three retrieval methods. *Earth and Space Science*, in rev.(2), 2022. ISSN 23335084. doi: 10.1029/2022EA002429. URL `https://agupubs.onlinelibrary.wiley.com/doi/10.1029/2022EA002429`.

Arianna Piccialli, M. A. López-Valverde, Anni Määttänen, F. González-Galindo, J. Audouard, Francesca Altieri, François Forget, P. Drossart, Brigitte Gondet, and J. P. Bibring. CO2 non-LTE limb emissions in Mars' atmosphere as observed by OMEGA/Mars Express. *Journal of Geophysical Research: Planets*, 121(6):1066–1086, jun 2016. ISSN 21699100. doi: 10.1002/2015JE004981.

William H. Press, Saul A. Teukolsky, William T. Vetterling, and Brian P. Flannery. *Numerical Recipes 3rd Edition: The Art of Scientific Computing.* Cambridge University Press, 2007. ISBN 0521880688.

R. J. Purser and H. L. Huang. Estimating effective data density in a satellite retrieval or an objective analysis. *Journal of Applied Meteorology*, 32(6):1092–1107, jun 1993. ISSN 08948763. doi: 10.1175/1520-0450(1993)032<1092:EEDDIA>2.0.CO;2. URL `http://journals.ametsoc.org/jamc/article-pdf/32/6/1092/3896439/1520-0450`.

Tae-Soo Pyo. IRCS Echelle spectrograph and Data Handling. Technical report, Subaru Telescope, National Astronomical Observatory, 2003.

Eric Quémerais, Jean Loup Bertaux, Oleg Korablev, Emmanuel Dimarellis, Charles Cot, Bill R Sandel, and Didier Fussen. Stellar occultations observed by SPICAM on Mars Express. *Journal of Geophysical Research E: Planets*, 111(9):9–13, 2006. ISSN 01480227. doi: 10.1029/2005JE002604.

Sergei G Rautian and Igor I Sobel'man. THE EFFECT OF COLLISIONS ON THE DOPPLER BROADENING OF SPECTRAL LINES. *Soviet Physics Uspekhi*, 9(5):701–716, 1967. ISSN 0038-5670. doi: 10.1070/pu1967v009n05abeh003212.

S. Robert, A. C. Vandaele, I. R. Thomas, Y. Willame, F. Daerden, S. Delanoye, C. Depiesse, R. Drummond, E. Neefs, L. Neary, B. Ristic, J. Mason, J. J. Lopez-Moreno, J. Rodriguez-Gomez, M. R. Patel, G. Bellucci, M. Patel, M. Allen, F. Altieri, S. Aoki, D. Bolsée, T. Clancy, E. Cloutis, A. Fedorova, V. Formisano, B. Funke, D. Fussen, M. Garcia-Comas, A. Geminale, J. C. Gérard, D. Gillotay, M. Giuranna, F. Gonzalez-Galindo, N. Igna-Tiev, J. Kaminski, O. Karatekin, Y. Kasaba, F. Lefèvre, S. Lewis, M. López-Puertas, M. López-Valverde, A. Mahieux, J. McConnell, M. Mumma, R. Novak, E. Renotte, G. Sindoni, M. Smith, A. Trokhimovskiy, Auwera J. Vander, G. Villanueva, S. Viscardy, J. Whiteway, V. Wilquet, M. Wolff, G. Alonso-Rodrigo, B. Aparicio Del Moral, P. Barzin, A. Benmoussa, S. Berkenbosch, D. Biondi, S. Bonnewijn, G. Candini, R. Clairquin, J. Cubas, B. Giordanengo, S. Gissot, A. Gomez, J. J. Zafra, M. Leese, J. Maes, E. Mazy, A. Mazzoli, J. Meseguer, R. Morales, A. Orban, M. Pastor-Morales, I. Perez-Grande, B. Saggin, V. Samain, Andres A. Sanz, R. Sanz, J. F. Simar, and T. Thibert. Expected performances of the NOMAD/ExoMars instrument. *Planetary and Space Science*, 124:94–104, may 2016. ISSN 00320633. doi: 10.1016/j.pss.2016.03.003.

Clive D Rodgers. *Inverse methods for atmospheric sounding*, volume 2 of *Series on Atmospheric, Oceanic and Planetary Physics.* WORLD SCIENTIFIC, jul 2000. ISBN 978-981-02-2740-1. doi: 10.1142/3171. URL `https://www.worldscientific.com/worldscibooks/10.1142/3171http://books.google.com/books/about/Inverse{_}methods{_}for{_}atmospheric{_}sounding.html?id=dW-0QgAACAAJ`.

Laurence S. Rothman and Louise D.G. Young. Infrared energy levels and intensities of carbon dioxide-II. *Journal of Quantitative Spectroscopy and Radiative Transfer*, 25(6):505–524, jun 1981. ISSN 00224073. doi: 10.1016/0022-4073(81)90026-1.

Agustı´n Sánchez-Lavega, Santiago Pérez-Hoyos, and Ricardo Hueso. Clouds in planetary atmospheres: A useful application of the Clausius–Clapeyron equation. *American Journal of Physics*, 72(6):767–774, jun 2004. ISSN 0002-9505. doi: 10.1119/1.1645279. URL `https://aapt.scitation.org/doi/abs/10.1119/1.1645279http://aapt.scitation.org/doi/10.1119/1.1645279`.

B. R. Sandel, H. Gröller, R. V. Yelle, T. Koskinen, N. K. Lewis, J. L. Bertaux, F. Montmessin, and E. Quémerais. Altitude profiles of O2 on Mars from SPICAM stellar occultations. *Icarus*, 252:154–160, may 2015. ISSN 10902643. doi: 10.1016/j.icarus.2015.01.004.

Frédéric Schmidt, Guillaume Cruz Mermy, Justin Erwin, Séverine Robert, Lori Neary, Ian R. Thomas, Frank Daerden, Bojan Ristic, Manish R. Patel, Giancarlo Bellucci, Jose-Juan Juan Lopez-Moreno, and Ann Carine Vandaele. Machine Learning for automatic identification of new minor species. *Journal of Quantitative Spectroscopy and Radiative Transfer*, 259:107361, sep 2020. ISSN 00224073. doi: 10.1016/j.jqsrt.2020.107361. URL `https://doi.org/10.1016/j.jqsrt.2020.107361`.

J. T. Schofield, J. R. Barnes, D. Crisp, R. M. Haberle, S. Larsen, J. A. Magalhães, J. R. Murphy, A. Seiff, and G. Wilson. The Mars Pathfinder atmospheric structure investigation/meteorology (ASI/MET) experiment, dec 1997. ISSN 00368075. URL `https://www.science.org/doi/10.1126/science.278.5344.1752`.

Frank Scholten, Harald Hoffmann, Anni Mttnen, Franck Montmessin, Brigitte Gondet, and Ernst Hauber. Concatenation of HRSC colour and OMEGA data for the determination and 3D-parameterization of high-altitude CO2 clouds in the Martian atmosphere. *Planetary and Space Science*, 58(10):1207–1214, aug 2010. ISSN 00320633. doi: 10.1016/j.pss.2010.04.015.

E. Sefton-Nash, N. A. Teanby, L. Montabone, P. G.J. Irwin, J. Hurley, and S. B. Calcutt. Climatology and first-order composition estimates of mesospheric clouds from Mars Climate Sounder limb spectra. *Icarus*, 222(1):342–356, 2013. ISSN 00191035. doi: 10.1016/j.icarus.2012.11.012. URL `http://dx.doi.org/10.1016/j.icarus.2012.11.012`.

Alvin Seiff and Donn B. Kirk. Structure of the atmosphere of Mars in summer at mid-latitudes. *Journal of Geophysical Research*, 82(28):4364–4378, 1977. doi: 10.1029/js082i028p04364.

James H. Shirley, Timothy H. McConnochie, David M. Kass, Armin Kleinböhl, John T. Schofield, Nicholas G. Heavens, Daniel J. McCleese, Jennifer Benson, David P. Hinson, and Joshua L. Bandfield. Temperatures and aerosol opacities of the Mars atmosphere at aphelion: Validation and inter-comparison of limb sounding profiles from MRO/MCS and MGS/TES. *Icarus*, 251:26–49, may 2015. ISSN 10902643. doi: 10.1016/j.icarus.2014.05.011.

Alankar Shrivastava and VipinB Gupta. Methods for the determination of limit of detection and limit of quantitation of the analytical methods. *Chronicles of Young Scientists*, 2(1):21, 2011. ISSN 2229-5186. doi: 10.4103/2229-5186.79345. URL `https://www.readcube.com/articles/10.4103{%}2F2229-5186.79345https://www.readcube.com/articles/10.4103/2229-5186.79345`.

G. M. Shved. On the abundances of carbon dioxide isotopologues in the atmospheres of mars and earth. *Solar System Research*, 50(2):161–164, 2016. ISSN 00380946. doi: 10.1134/S0038094616020064.

Marie Šimečková, David Jacquemart, Laurence S Rothman, Robert R Gamache, and Aaron Goldman. Einstein A-coefficients and statistical weights for molecular absorption transitions in the HITRAN database. *Journal of Quantitative Spectroscopy and Radiative Transfer*, 98 (1):130–155, 2006. ISSN 00224073. doi: 10.1016/j.jqsrt.2005.07.003. URL `www.elsevier.com/locate/jqsrt`.

David E. Smith, Maria T. Zuber, Herbert V. Frey, James B. Garvin, James W. Head, Duane O. Muhleman, Gordon H. Pettengill, Roger J. Phillips, Sean C. Solomon, H. Jay Zwally, W. Bruce Banerdt, Thomas C. Duxbury, Matthew P. Golombek, Frank G. Lemoine, Gregory A. Neumann, David D. Rowlands, Oded Aharonson, Peter G. Ford, Anton B. Ivanov, Catherine L. Johnson, Patrick J. McGovern, James B. Abshire, Robert S. Afzal, and Xiaoli Sun. Mars Orbiter Laser Altimeter: Experiment summary after the first year of global mapping of Mars. *Journal of Geophysical Research E: Planets*, 106(E10):23689–23722, oct 2001. ISSN 01480227. doi: 10.1029/2000JE001364. URL `http://doi.wiley.com/10.1029/2000JE001364`.

David E Smith, Maria T Zuber, Mark H Torrence, Peter J Dunn, Gregory A Neumann, Frank G Lemoine, and Susan K Fricke. Time variations of Mars' gravitational field and seasonal changes in the masses of the polar ice caps. *Journal of Geophysical Research E: Planets*, 114(5):5002, 2009. ISSN 01480227. doi: 10.1029/2008JE003267.

Gerald R. Smith and Donald M. Hunten. Study of planetary atmospheres by absorptive occultations. *Reviews of Geophysics*, 28(2):117–143, may 1990. ISSN 19449208. doi: 10.1029/RG028i002p00117. URL `http://doi.wiley.com/10.1029/RG028i002p00117`.

Michael D. Smith. Spacecraft observations of the Martian atmosphere. *Annual Review of Earth and Planetary Sciences*, 36(1):191–219, may 2008. ISSN 00846597. doi: 10.1146/annurev.earth.36.031207.124334. URL `http://www.annualreviews.org/doi/10.1146/annurev.earth.36.031207.124334`.

Michael D. Smith, Stephen W. Bougher, Thérèse Encrenaz, François Forget, and Armin Kleinböhl. Thermal structure and composition. In Robert M. Haberle, R. Todd Clancy, Francois Forget, Michael D. Smith, and Richard W. Zurek, editors, *The Atmosphere and Climate of Mars*, pages 42–75. Cambridge University Press, Cambridge, jun 2017. ISBN 9781139060172. doi: 10.1017/9781139060172.004. URL `https://www.cambridge.org/core/books/atmosphere-and-climate-of-mars/thermal-structure-and-composition/8266BBE551872BE1BDF714211C48CB9Chttps://www.cambridge.org/core/product/identifier/9781139060172{%}23CN-bp-4/type/book{_}part`.

Maarten Sneep and Wim Ubachs. Direct measurement of the Rayleigh scattering cross section in various gases. *Journal of Quantitative Spectroscopy and Radiative Transfer*, 92(3):293–310, 2005. ISSN 00224073. doi: 10.1016/j.jqsrt.2004.07.025. URL `www.elsevier.com/locate/jqsrt`.

D. Snowden, R. V. Yelle, J. Cui, J.-E E. Wahlund, N. J.T. T Edberg, and K. Ågren. The thermal structure of titan's upper atmosphere, I: Temperature profiles from Cassini INMS observations. *Icarus*, 226(1):552–582, sep 2013. ISSN 00191035. doi: 10.1029/2010JA016251. URL `http://dx.doi.org/10.1016/j.icarus.2013.06.006https://arizona.pure.elsevier.com/en/publications/the-thermal-structure-of-titans-upper-atmosphere-i-temperature-pr`.

A. Spiga, F. Gonzlez-Galindo, M. A. López-Valverde, and F. Forget. Gravity waves, cold pockets and CO2 clouds in the Martian mesosphere. *Geophysical Research Letters*, 39(2):2201, jan 2012. ISSN 00948276. doi: 10.1029/2011GL050343. URL `https://onlinelibrary.wiley.com/doi/full/10.1029/2011GL050343https://onlinelibrary.wiley.com/doi/abs/10.1029/2011GL050343https://agupubs.onlinelibrary.wiley.com/doi/10.1029/2011GL050343`.

Tilman Steck. Methods for determining regularization for atmospheric retrieval problems. *Applied Optics*, 41(9):1788, mar 2002. ISSN 0003-6935. doi: 10.1364/ao.41.001788. URL `https://www.osapublishing.org/viewmedia.cfm?uri=ao-41-9-1788{&}seq=0{&}html=truehttps://www.osapublishing.org/abstract.cfm?uri=ao-41-9-1788https://www.osapublishing.org/ao/abstract.cfm?uri=ao-41-9-1788`.

M. H. Stevens, D. E. Siskind, J. S. Evans, S. K. Jain, N. M. Schneider, J. Deighan, A. I.F. Stewart, M. Crismani, A. Stiepen, M. S. Chaffin, W. E. McClintock, G. M. Holsclaw, F. Lefèvre, D. Y. Lo, J. T. Clarke, F. Montmessin, and B. M. Jakosky. Martian mesospheric cloud observations by IUVS on MAVEN: Thermal tides coupled to the upper atmosphere. *Geophysical Research Letters*, 44(10):4709–4715, may 2017. ISSN 19448007. doi: 10.1002/2017GL072717. URL `https://onlinelibrary.wiley.com/doi/full/10.1002/2017GL072717https://onlinelibrary.wiley.com/doi/abs/10.1002/2017GL072717https://agupubs.onlinelibrary.wiley.com/doi/10.1002/2017GL072717`.

Shane W. Stone, Roger V. Yelle, Mehdi Benna, Meredith K. Elrod, and Paul R. Mahaffy. Neutral Composition and Horizontal Variations of the Martian Upper Atmosphere from MAVEN NGIMS. *Journal of Geophysical Research: Planets*, 2022. ISSN 2169-9097. doi: 10.1029/2021je007085.

Keeyoon Sung and Prasad Varanasi. CO2-broadened half-widths and CO2-induced line shifts of 12C16O relevant to the atmospheric spectra of Venus and Mars. *Journal of Quantitative Spectroscopy and Radiative Transfer*, 91(3):319–332, 2005. ISSN 00224073. doi: 10.1016/j.jqsrt.2004.05.063. URL `www.elsevier.com/locate/jqsrt`.

Albert Tarantola. *Inverse Problem Theory and Methods for Model Parameter Estimation*. Society for Industrial and Applied Mathematics, jan 2005. doi: 10.1137/1.9780898717921.

John R. Taylor. *An Introduction to Error Analysis: The Study of Uncertainties in Physical Measurements*. University Science Books,U.S., jul 1997. ISBN 9780935702750.

J. S. Theon and W. Nordberg. On the determination of pressure and density profiles from temperature profiles in the atmosphere. Technical report, 1965. URL `https://ntrs.nasa.gov/api/citations/19650025462/downloads/19650025462.pdf`.

E. M.B. Thiemann, F. G. Eparvier, S. W. Bougher, M. Dominique, L. Andersson, Z. Girazian, M. D. Pilinski, B. Templeman, and B. M. Jakosky. Mars Thermospheric Variability Revealed by MAVEN EUVM Solar Occultations: Structure at Aphelion and Perihelion and Response to EUV Forcing. *Journal of Geophysical Research: Planets*, 123(9):2248–2269, sep 2018. ISSN 21699100. doi: 10.1029/2018JE005550. URL `https://onlinelibrary.wiley.com/doi/full/10.1029/2018JE005550https://onlinelibrary.wiley.com/doi/abs/10.1029/2018JE005550https://agupubs.onlinelibrary.wiley.com/doi/10.1029/2018JE005550`.

I. R. Thomas, A. C. Vandaele, S. Robert, E. Neefs, R. Drummond, F. Daerden, S. Delanoye, B. Ristic, S. Berkenbosch, R. Clairquin, J. Maes, S. Bonnewijn, C. Depiesse, A. Mahieux, L. Trompet, L. Neary, Y. Willame, V. Wilquet, D. Nevejans, Ludovic Aballea, W. Moelans, L. De Vos, S. Lesschaeve, N. Van Vooren, J.-J. Lopez-Moreno, M. R. Patel, G. Bellucci, and the NOMAD Team. Optical and radiometric models of the NOMAD instrument part II: the infrared channels - SO and LNO. *Optics Express*, 24(4):3790, 2016. ISSN 1094-4087. doi: 10.1364/oe.24.003790.

A N Tikhonov. Solution of incorrectly formulated problems and the regularization method. *Soviet Math. Dokl.*, 4:1035–1038, 1963.

Andrey N Tikhonov and Vasiliy Y Arsenin. *Solutions of ill-posed problems.* V. H. Winston & Sons, Washington, D.C.: John Wiley & Sons, New York, 1977.

R. Tolson, E. Betnis, S. Hough, K. Zaleski, G. Keating, J. Shidner, S. Brown, A. Brickler, M. Scher, and P. Thomas. Atmospheric modeling using accelerometer data during mars reconnaissance orbiter aerobraking operations. *Journal of Spacecraft and Rockets*, 45(3):511–518, 2008. ISSN 15336794. doi: 10.2514/1.34301.

L. Trompet, Y. Geunes, T. Ooms, A. Mahieux, V. Wilquet, S. Chamberlain, S. Robert, I. R. Thomas, S. Erard, B. Cecconi, P. Le Sidaner, and A. C. Vandaele. Description, accessibility and usage of SOIR/Venus Express atmospheric profiles of Venus distributed in VESPA (Virtual European Solar and Planetary Access), jan 2018. ISSN 00320633.

L. Trompet, S. Robert, A. Mahieux, F. Schmidt, J. Erwin, and A. C. Vandaele. Phosphine in Venus' atmosphere: Detection attempts and upper limits above the cloud top assessed from the SOIR/VEx spectra. *Astronomy and Astrophysics*, 645:L4, jan 2021. ISSN 0004-6361. doi: 10.1051/0004-6361/202039932. URL `https://www.aanda.org/articles/aa/full{_}html/2021/01/aa39932-20/aa39932-20.htmlhttps://www.aanda.org/articles/aa/abs/2021/01/aa39932-20/aa39932-20.html`.

L. Trompet, A. C. Vandaele, I. Thomas, S. Aoki, F. Daerden, J. Erwin, Z. Flimon, A. Mahieux, L. Neary, S. Robert, G. Villanueva, G. Liuzzi, M. A. López-Valverde, A. Brines, G. Bellucci, J. J. Lopez-Moreno, and M. R. Patel. Carbon Dioxide Retrievals From NOMAD-SO on ESA's ExoMars Trace Gas Orbiter and Temperature Profile Retrievals With the Hydrostatic Equilibrium Equation: 2. Temperature Variabilities in the Mesosphere at Mars Terminator. *Journal of Geophysical Research: Planets*, 128(3):e2022JE007279, mar 2023a. ISSN 2169-9097. doi: 10.1029/2022JE007279. URL `https://onlinelibrary.wiley.com/doi/10.1029/2022JE007279`.

L. Trompet, A. C. Vandaele, I. Thomas, S. Aoki, F. Daerden, J. Erwin, Z. Flimon, A. Mahieux, L. Neary, S. Robert, G. Villanueva, G. Liuzzi, M. A. López-Valverde, A. Brines, G. Bellucci, J. J. López-Moreno, and M. R. Patel. Carbon Dioxide Retrievals From NOMAD-SO on ESA's ExoMars Trace Gas Orbiter and Temperature Profiles Retrievals With the Hydrostatic Equilibrium Equation: 1. Description of the Method. *Journal of Geophysical Research: Planets*, 128(3):e2022JE007277, mar 2023b. ISSN 2169-9097. doi: 10.1029/2022JE007277. URL `https://onlinelibrary.wiley.com/doi/10.1029/2022JE007277`.

Loïc Trompet, Arnaud Mahieux, Bojan Ristic, Séverine Robert, Valérie Wilquet, Ian R. Thomas, Ann Carine Vandaele, and Jean-Loup Bertaux. Improved algorithm for the transmittance estimation of spectra obtained with SOIR/Venus Express. *Applied Optics*, 55(32):9275, nov 2016. ISSN 0003-6935. doi: 10.1364/ao.55.009275.

S. Twomey. On the Numerical Solution of Fredholm Integral Equations of the First Kind by the Inversion of the Linear System Produced by Quadrature. *Journal of the ACM (JACM)*, 10(1): 97–101, jan 1963. ISSN 1557735X. doi: 10.1145/321150.321157. URL `https://dl.acm.org/doi/10.1145/321150.321157`.

S. Twomey. *Inversion Methods in Atmospheric Remote Sounding.* Elsevier, 1977. doi: 10.1016/b978-0-122-08450-8.x5001-2.

J. Vago, O. Witasse, H. Svedhem, P. Baglioni, A. Haldemann, G. Gianfiglio, T. Blancquaert, D. McCoy, and R. de Groot. ESA ExoMars program: The next step in exploring Mars. *Solar System Research*, 49(7):518–528, dec 2015. ISSN 00380946. doi: 10.1134/S0038094615070199.

A. C. Vandaele, M. Kruglanski, and M. De Mazière. Modeling and retrieval of atmospheric spectra using ASIMUT. In *Proc. of the First 'Atmospheric Science Conference'*, number 618, page 71, Frascati, Italy, 2006.

A. C. Vandaele, M. De Mazière, R. Drummond, A. Mahieux, E. Neefs, V. Wilquet, O. Korablev, A. Fedorova, D. Belyaev, F. Montmessin, and J.-L L. Bertaux. Composition of the Venus mesosphere measured by Solar Occultation at Infrared on board Venus Express. *Journal of Geophysical Research E: Planets*, 113(5):0–23, 2008. ISSN 01480227. doi: 10.1029/2008JE003140. URL `https://agupubs.onlinelibrary.wiley.com/doi/abs/10.1029/2008JE003140@10.1002/(ISSN)2169-9100.VENUSEXP1`.

Ann Carine Vandaele, Arnaud Mahieux, Séverine Robert, Sophie Berkenbosch, Roland Clairquin, Rachel Drummond, Vincent Letocart, Eddy Neefs, Bojan Ristic, Valérie Wilquet, Frédéric Colomer, Denis Belyaev, and Jean-Loup Bertaux. Improved calibration of SOIR/Venus Express spectra. *Optics Express*, 21(18):21148, sep 2013. ISSN 1094-4087. doi: 10.1364/oe.21.021148.

Ann Carine Vandaele, E. Neefs, R. Drummond, I.R. R. Thomas, Frank Daerden, J.-J. J. Lopez-Moreno, J. Rodriguez, M.R. R. Patel, G. Bellucci, Mark Allen, Francesca Altieri, D. Bolsée, T. Clancy, S. Delanoye, C. Depiesse, E. Cloutis, A. Fedorova, V. Formisano, B. Funke, D. Fussen, A. Geminale, J.-C. C. Gérard, M. Giuranna, N. Ignatiev, J. Kaminski, O. Karatekin, F. Lefèvre, M. López-Puertas, M. López-Valverde, A. Mahieux, J. McConnell, M. Mumma, Lori Neary, E. Renotte, B. Ristic, S. Robert, M. Smith, Sacha Trokhimovsky, J. Vander Auwera, G. Villanueva, J. Whiteway, V. Wilquet, M. Wolff, J. Vanderauwera, G. Villanueva, J. Whiteway, V. Wilquet, M. Wolff, Shohei Aoki, Maya Garcia-Comas, Didier Gillotay, Francisco Gonzalez-Galindo, Yasumasa Kasabe, Stephen Lewis, Jon Mason, Giuseppe Sindoni, Yannick Willame, Gustavo Alonso-Rodrigo, Beatriz Aparicio Del Moral, Pascal Barzin, Ali Ben Moussa, Sophie Berkenbosch, David Biondi, Sabrina Bonnewijn, Gian Paolo Candini, Roland Clairquin, Javier Cubas, Boris Giordanengo, Samuel Gissot, Alejandro Gomez, Jose Jeronimo Zafra, Mark Leese, Jeroen Maes, Emmanuel Mazy, Alexandra Mazzoli, Jose Meseguer, Rafael Morales, Anne Orban, Maria Del Carmen Pastor-Morales, Isabel Perez-Grande, Julio Rodriguez-Gomez, Bortolino Saggin, Valérie Samain, Angel Sanz Andres, Rosario Sanz, Juan Felipe Simar, Tanguy Thibert, J. Vander Auwera, G. Villanueva, J. Whiteway, V. Wilquet, and M. Wolff. Science objectives and performances of NOMAD, a spectrometer suite for the ExoMars TGO mission. *Planetary and Space Science*, 119:233–249, dec 2015a. ISSN 00320633. doi: 10.1016/j.pss.2015.10.003. URL `https://linkinghub.elsevier.com/retrieve/pii/S0032063315003025`.

Ann Carine Vandaele, Yannick Willame, Cédric Depiesse, Ian R Thomas, Séverine Robert, David Bolsée, Manish R. Patel, Jon P. Mason, Mark Leese, Stefan Lesschaeve, Philippe Antoine, Frank Daerden, Sofie Delanoye, Rachel Drummond, Eddy Neefs, Bojan Ristic, José-Juan Lopez-Moreno, Giancarlo Bellucci, and Nomad Team. Optical and radiometric models of the NOMAD instrument part I: the UVIS channel. *Optics Express*, 23(23):30028, 2015b. ISSN 1094-4087. doi: 10.1364/oe.23.030028.

Ann Carine Vandaele, Oleg Korablev, Frank Daerden, Shohei Aoki, Ian R. Thomas, Francesca Altieri, Miguel López-Valverde, Geronimo Villanueva, Giuliano Liuzzi, Michael D. Smith, Justin T. Erwin, Loïc Trompet, Anna A. Fedorova, Franck Montmessin, Alexander Trokhimovskiy, Denis A. Belyaev, Nikolay I. Ignatiev, Mikhail Luginin, Kevin S. Olsen, Lucio Baggio, Juan Alday, Jean Loup Bertaux, Daria Betsis, David Bolsée, R. Todd Clancy, Edward Cloutis, Cédric Depiesse, Bernd Funke, Maia Garcia-Comas, Jean Claude Gérard, Marco Giuranna, Francisco Gonzalez-Galindo, Alexey V. Grigoriev, Yuriy S. Ivanov, Jacek Kaminski, Ozgur Karatekin, Franck Lefèvre, Stephen Lewis, Manuel López-Puertas, Arnaud Mahieux, Igor Maslov, Jon Mason, Michael J. Mumma, Lori Neary, Eddy Neefs, Andrey Patrakeev, Dmitry Patsaev, Bojan Ristic, Séverine Robert, Frédéric Schmidt, Alexey Shakun, Nicholas A. Teanby, Sébastien Viscardy, Yannick Willame, James Whiteway, Valérie Wilquet, Michael J. Wolff, Giancarlo Bellucci, Manish R. R. Patel, Jose Juan López-Moreno, François Forget, Colin F. Wilson, Håkan Svedhem, Jorge L. Vago, Daniel Rodionov, Gustavo Alonso-Rodrigo, Sophie Bauduin, Giacomo Carrozzo, Matteo Crismani, Fabiana Da Pieve, Emiliano D'Aversa, Giuseppe Etiope, Didier Fussen, Anna Geminale, Leo Gkouvelis, James Holmes, Benoît Hubert, Yasumasa Kasaba, David Kass, Armin Kleinböhl, Orietta Lanciano, Hiromu Nakagawa, Robert E. Novak, Fabrizio Oliva, Arianna Piccialli, Etienne Renotte, Birgit Ritter, Nick Schneider, Giuseppe Sindoni, Ed Thiemann, Jean Vander Auwera, Paulina Wolkenberg, Roger Yelle, Konstantin Anufreychik, Gabriele Arnold, Jean Loup Bertaux, Natalia Duxbury, Thierry Fouchet, Davide Grassi, Sandrine Guerlet, Paul Hartogh, Igor Khatuntsev, Nikita Kokonkov, Vladimir Krasnopolsky, Ruslan Kuzmin, Gaétan Lacombe, Emmanuel Lellouch, Anni Määttänen, Emmanuel Marcq, Javier Martin-Torres, Alexander Medvedev, Ehouarn Millour, Boris Moshkin, Manish R. R. Patel, Cathy Quantin-Nataf, Alexander Rodin, Valery Shematovich, Nicolas Thomas, Alexander Trokhimovsky, Luis Vazquez, Matthieu Vincendon, Roland Young, Ludmila Zasova, Lev Zelenyi, and Maria Paz Zorzano. Martian dust storm impact on atmospheric H2O and D/H observed by ExoMars Trace Gas Orbiter. *Nature*, 568(7753):521–525, 2019. ISSN 14764687. doi: 10.1038/s41586-019-1097-3. URL `https://idp.nature.com/authorize/casa?redirect{_}uri=https://www.nature.com/articles/s41586-019-1097-3{&}casa{_}token=sOpv6QBLpgIAAAAA:hTAfy-jATpH1xWOKfOjtsRnPs6T6MxSNMsm{_}bKla{_}X8Gh7Lmvh4{_}trJibOGGkDsbBfUev7dPuNd9RvAOeRU`.

Geronimo L Villanueva, Giuliano Liuzzi, Matteo M J Crismani, Shohei Aoki, Ann Carine Vandaele, Frank Daerden, Michael D Smith, Michael J Mumma, Elise W Knutsen, Lori Neary, Sebastien Viscardy, Ian R Thomas, Miguel Angel Lopez-Valverde, Bojan Ristic, Manish R Patel, James A Holmes, Giancarlo Bellucci, and Jose Juan Lopez-Moreno. Water heavily fractionated as it ascends on Mars as revealed by ExoMars/NOMAD. *Sci. Adv*, 7(7):8843, 2021. URL `http://advances.sciencemag.org/`.

Geronimo L. Villanueva, Giuliano Liuzzi, Shohei Aoki, Shane W. Stone, Adrian Brines, Ian R. Thomas, Miguel Angel Lopez-Valverde, Loic Trompet, Justin Erwin, Frank Daerden, Bojan Ristic, Michael D. Smith, Michael J. Mumma, Sara Faggi, Vincent Kofman, Séverine Robert, Lori Neary, Manish Patel, Giancarlo Bellucci, Jose Juan Lopez-Moreno, and Ann Carine Vandaele. The Deuterium Isotopic Ratio of Water Released From the Martian Caps as Measured With TGO/NOMAD. *Geophysical Research Letters*, 49(12), jun 2022. ISSN 0094-8276. doi: 10.1029/2022GL098161. URL `https://onlinelibrary.wiley.com/doi/10.1029/2022GL098161`.

Mathieu Vincendon, Cedric Pilorget, Brigitte Gondet, Scott Murchie, and Jean Pierre Bibring. New near-IR observations of mesospheric CO2 and H2O clouds on Mars. *Journal of Geophysical Research E: Planets*, 116(11):0–02, nov 2011. ISSN 01480227. doi: 10.1029/2011JE003827. URL `https://onlinelibrary.wiley.com/doi/full/10.1029/2011JE003827https://onlinelibrary.wiley.com/doi/abs/10.1029/2011JE003827https://agupubs.onlinelibrary.wiley.com/doi/10.1029/2011JE003827`.

Pauli Virtanen, Ralf Gommers, Travis E. Oliphant, Matt Haberland, Tyler Reddy, David Cournapeau, Evgeni Burovski, Pearu Peterson, Warren Weckesser, Jonathan Bright, Stéfan J. van der Walt, Matthew Brett, Joshua Wilson, K. Jarrod Millman, Nikolay Mayorov, Andrew R.J. Nelson, Eric Jones, Robert Kern, Eric Larson, C. J. Carey, İlhan Polat, Yu Feng, Eric W. Moore, Jake VanderPlas, Denis Laxalde, Josef Perktold, Robert Cimrman, Ian Henriksen,

E. A. Quintero, Charles R. Harris, Anne M. Archibald, Antônio H. Ribeiro, Fabian Pedregosa, Paul van Mulbregt, Aditya Vijaykumar, Alessandro Pietro Bardelli, Alex Rothberg, Andreas Hilboll, Andreas Kloeckner, Anthony Scopatz, Antony Lee, Ariel Rokem, C. Nathan Woods, Chad Fulton, Charles Masson, Christian Häggström, Clark Fitzgerald, David A. Nicholson, David R. Hagen, Dmitrii V. Pasechnik, Emanuele Olivetti, Eric Martin, Eric Wieser, Fabrice Silva, Felix Lenders, Florian Wilhelm, G. Young, Gavin A. Price, Gert Ludwig Ingold, Gregory E. Allen, Gregory R. Lee, Hervé Audren, Irvin Probst, Jörg P. Dietrich, Jacob Silterra, James T. Webber, Janko Slavič, Joel Nothman, Johannes Buchner, Johannes Kulick, Johannes L. Schönberger, José Vinícius de Miranda Cardoso, Joscha Reimer, Joseph Harrington, Juan Luis Cano Rodríguez, Juan Nunez-Iglesias, Justin Kuczynski, Kevin Tritz, Martin Thoma, Matthew Newville, Matthias Kümmerer, Maximilian Bolingbroke, Michael Tartre, Mikhail Pak, Nathaniel J. Smith, Nikolai Nowaczyk, Nikolay Shebanov, Oleksandr Pavlyk, Per A. Brodtkorb, Perry Lee, Robert T. McGibbon, Roman Feldbauer, Sam Lewis, Sam Tygier, Scott Sievert, Sebastiano Vigna, Stefan Peterson, Surhud More, Tadeusz Pudlik, Takuya Oshima, Thomas J. Pingel, Thomas P. Robitaille, Thomas Spura, Thouis R. Jones, Tim Cera, Tim Leslie, Tiziano Zito, Tom Krauss, Utkarsh Upadhyay, Yaroslav O. Halchenko, and Yoshiki Vázquez-Baeza. SciPy 1.0: fundamental algorithms for scientific computing in Python. *Nature Methods*, 17(3):261–272, mar 2020. ISSN 15487105. doi: 10.1038/s41592-019-0686-2. URL `https://doi.org/10.1038/s41592-019-0686-2`.

Christopher R. Webster, Paul R. Mahaffy, Sushil K. Atreya, Gregory J. Flesch, and Kenneth A. Farley. Low upper limit to methane abundance on Mars. *Science*, 342(6156):355–357, 2013. ISSN 10959203. doi: 10.1126/science.1242902.

Christopher R. Webster, Paul R. Mahaffy, Sushil K. Atreya, Gregory J. Flesch, Michael A. Mischna, Pierre Yves Meslin, Kenneth A. Farley, Pamela G. Conrad, Lance E. Christensen, Alexer A. Pavlov, Javier Martín-Torres, María Paz Zorzano, Timothy H. McConnochie, Tobias Owen, Jennifer L. Eigenbrode, Daniel P. Glavin, Andrew Steele, Charles A. Malespin, P. Douglas Archer, Brad Sutter, Patrice Coll, Caroline Freissinet, Christopher P. McKay, John E. Moores, Susanne P. Schwenzer, John C. Bridges, Rafael Navarro-Gonzalez, Ralf Gellert, and Mark T. Lemmon. Mars methane detection and variability at Gale crater. *Science*, 347(6220):415–417, jan 2015. ISSN 10959203. doi: 10.1126/science.1261713.

Christopher R. Webster, Paul R. Mahaffy, Sushil K. Atreya, John E. Moores, Gregory J. Flesch, Charles Malespin, Christopher P. McKay, German Martinez, Christina L. Smith, Javier Martin-Torres, Javier Gomez-Elvira, Maria Paz Zorzano, Michael H. Wong, Melissa G. Trainer, Andrew Steele, Doug Archer, Brad Sutter, Patrice J. Coll, Caroline Freissinet, Pierre Yves Meslin, Raina V. Gough, Christopher H. House, Alexander Pavlov, Jennifer L. Eigenbrode, Daniel P. Glavin, John C. Pearson, Didier Keymeulen, Lance E. Christensen, Susanne P. Schwenzer, Rafael Navarro-Gonzalez, Jorge Pla-García, Scot C.R. Rafkin, Álvaro Vicente-Retortillo, Henrik Kahanpää, Daniel Viudez-Moreiras, Michael D. Smith, Ari Matti Harri, Maria Genzer, Donald M. Hassler, Mark Lemmon, Joy Crisp, Stanley P. Sander, Richard W. Zurek, and Ashwin R. Vasavada. Background levels of methane in Mars' atmosphere show strong seasonal variations. *Science*, 360(6393):1093–1096, jun 2018. ISSN 10959203. doi: 10.1126/science.aaq0131.

Christopher R. Webster, Paul R. Mahaffy, Sushil K. Atreya, Gregory J. Flesch, Charles A. Malespin, and Ashwin R. Vasavada. Curiosity Mars methane measurements are not confused by ozone. *Astronomy and Astrophysics*, 641, sep 2020. ISSN 14320746. doi: 10.1051/0004-6361/202038815. URL `https://www.aanda.org/10.1051/0004-6361/202038815`.

Christopher R. Webster, Paul R. Mahaffy, Jorge Pla-Garcia, Scot C.R. Rafkin, John E. Moores, Sushil K. Atreya, Gregory J. Flesch, Charles A. Malespin, Samuel M. Teinturier, Hemani Kalucha, Christina L. Smith, Daniel Viúdez-Moreiras, and Ashwin R. Vasavada. Day-night differences in Mars methane suggest nighttime containment at Gale crater. *Astronomy and Astrophysics*, 650:A166, jun 2021. ISSN 14320746. doi: 10.1051/0004-6361/202040030. URL `https://www.aanda.org/articles/aa/full{_}html/2021/06/aa40030-20/aa40030-20.htmlhttps://www.aanda.org/articles/aa/abs/2021/06/aa40030-20/aa40030-20.html`.

R. J. Wells. Rapid approximation to the Voigt/Faddeeva function and its derivatives. *Journal of Quantitative Spectroscopy and Radiative Transfer*, 62(1):29–48, may 1999. ISSN 00224073. doi: 10.1016/S0022-4073(97)00231-8.

Yannick Willame. *Aerosol and ozone retrieval in the Martian atmosphere using the SPICAM/UV instrument and algorithm preparation for future missions*. PhD thesis, Université libre de Bruxelles, nov 2015. URL `http://hdl.handle.net/2013/ULB-DIPOT:oai:dipot.ulb.ac.be:2013/219965`.

V. Wilquet, A. Mahieux, A. C. Vandaele, V. I. Perevalov, S. A. Tashkun, A. Fedorova, O. Korablev, F. Montmessin, R. Dahoo, and J. L. Bertaux. Line parameters for the 01111-00001 band of 12C16O18O from SOIR measurements of the Venus atmosphere. *Journal of Quantitative Spectroscopy and Radiative Transfer*, 109(6):895–905, 2008. ISSN 00224073. doi: 10.1016/j.jqsrt.2007.12.021.

R John Wilson. Erratum: A general circulation model simulation of the Martian polar warming (Geophysical Research Letters 24:2 (123-126)), 1997. ISSN 19448007.

Paul Withers. Mars Global Surveyor and Mars Odyssey Accelerometer observations of the Martian upper atmosphere during aerobraking. *Geophysical Research Letters*, 33(2):2201, 2006. ISSN 00948276. doi: 10.1029/2005GL024447. URL `https://agupubs.onlinelibrary.wiley.com/doi/10.1029/2005GL024447`.

Paul Withers and Michael D. Smith. Atmospheric entry profiles from the Mars Exploration Rovers Spirit and Opportunity. *Icarus*, 185(1):133–142, 2006. ISSN 00191035. doi: 10.1016/j.icarus.2006.06.013.

Jian Xu, Franz Schreier, Adrian Doicu, and Thomas Trautmann. Assessment of Tikhonov-type regularization methods for solving atmospheric inverse problems. *Journal of Quantitative Spectroscopy and Radiative Transfer*, 184:274–286, 2016. ISSN 00224073. doi: 10.1016/j.jqsrt.2016.08.003. URL `http://dx.doi.org/10.1016/j.jqsrt.2016.08.003https://www.sciencedirect.com/science/article/pii/S002240731630317X?casa{_}token=Va{_}a4A6Z-HcAAAAA:I0r00BrBu5EoOz5vgXawGYUdyDbGsRuwml0fX5uf{_}G4qJvSjMxOzqjXkqzCXDWlxxC-UDXiKw-L2`.

Jian Xu, Lanlan Rao, Franz Schreier, Dmitry S. Efremenko, Adrian Doicu, and Thomas Trautmann. Insight into construction of tikhonov-type regularization for atmospheric retrievals. *Atmosphere*, 11(10):1052, oct 2020. ISSN 20734433. doi: 10.3390/atmos11101052. URL `https://www.mdpi.com/2073-4433/11/10/1052www.mdpi.com/journal/atmosphere`.

T. Yano and A. Watanabe. Acoustooptic TeO_2 tunable filter using far-off-axis anisotropic Bragg diffraction. *Applied Optics*, 15(9):2250, sep 1976. ISSN 0003-6935. doi: 10.1364/ao.15.002250. URL `https://www.osapublishing.org/viewmedia.cfm?uri=ao-15-9-2250{&}seq=0{&}html=truehttps://www.osapublishing.org/abstract.`

`cfm?uri=ao-15-9-2250https://www.osapublishing.org/ao/abstract.cfm?uri=ao-15-9-2250`.

Nao Yoshida, Hiromu Nakagawa, Shohei Aoki, Justin Erwin, Ann Carine Vandaele, Frank Daerden, Ian Thomas, Loïc Trompet, Shungo Koyama, Naoki Terada, Lori Neary, Isao Murata, Geronimo Villanueva, Giuliano Liuzzi, Miguel Angel Lopez-Valverde, Adrian Brines, Ashimananda Modak, Yasumasa Kasaba, Bojan Ristic, Giancarlo Bellucci, José Juan López-Moreno, and Manish Patel. Variations in Vertical CO/CO2 Profiles in the Martian Mesosphere and Lower Thermosphere Measured by the ExoMars TGO/NOMAD: Implications of Variations in Eddy Diffusion Coefficient. *Geophysical Research Letters*, 49(10):e2022GL098485, may 2022. ISSN 1944-8007. doi: 10.1029/2022GL098485. URL `https://onlinelibrary.wiley.com/doi/full/10.1029/2022GL098485https://onlinelibrary.wiley.com/doi/abs/10.1029/2022GL098485https://agupubs.onlinelibrary.wiley.com/doi/10.1029/2022GL098485`.

Yuk L. Yung, Pin Chen, Kenneth Nealson, Sushil Atreya, Patrick Beckett, Jennifer G. Blank, Bethany Ehlmann, John Eiler, Giuseppe Etiope, James G. Ferry, Francois Forget, Peter Gao, Renyu Hu, Armin Kleinböhl, Ronald Klusman, Franck Lefèvre, Charles Miller, Michael Mischna, Michael Mumma, Sally Newman, Dorothy Oehler, Mitchio Okumura, Ronald Oremland, Victoria Orphan, Radu Popa, Michael Russell, Linhan Shen, Barbara Sherwood Lollar, Robert Staehle, Vlada Stamenković, Daniel Stolper, Alexis Templeton, Ann Carine Vandaele, Sébastien Viscardy, Christopher R. Webster, Paul O. Wennberg, Michael L. Wong, and John Worden. Methane on Mars and Habitability: Challenges and Responses, oct 2018. ISSN 15311074.

Kevin Zahnle. Play it again, SAM. *Science*, 347(6220):370–371, jan 2015. ISSN 0036-8075. doi: 10.1126/science.aaa3687. URL `https://www.science.org/doi/10.1126/science.aaa3687`.

Kevin Zahnle, Richard S. Freedman, and David C. Catling. Is there methane on Mars? *Icarus*, 212(2):493–503, apr 2011. ISSN 00191035. doi: 10.1016/j.icarus.2010.11.027.

Shanjie Zhang and Jian–Ming Jin. *Computation of Special Functions*. Wiley–Blackwell; Har/Dskt edition, aug 1996. ISBN 978-0471119630.

Richard W. Zurek and Suzanne E. Smrekar. An overview of the Mars Reconnaissance Orbiter (MRO) science mission, may 2007. ISSN 01480227. URL `https://onlinelibrary.wiley.com/doi/full/10.1029/2006JE002701https://onlinelibrary.wiley.com/doi/abs/10.1029/2006JE002701https://agupubs.onlinelibrary.wiley.com/doi/10.1029/2006JE002701`.

Nomenclature

ACS	Atmospheric Chemistry Suite
AOTF	Acousto-Optical Tunable Filter
CRISM	Compact Reconnaissance Imaging Spectrometer for Mars
DALR	Dry Adiabatic Lapse Rate
EUVM	Extreme UltraViolet Monitor
FOV	Field Of View
FSR	Free Spectral Range
FWHM	Full-Width at Half-Maximum
GCM	General Circulation Model
GDS	Global Dust Storm
GEM − Mars	Global Environmental Multiscale model adapted to the Martian atmosphere
*GMM*3	Goddard Mars Model 3
HRSC	High Resolution Stereo Camera
HWHM	Half-Width at Half-Maximum
ILS	Instrument Line Shape
IR	Infrared
IUVS	Imaging UltraViolet Spectrograph
L_S	Solar longitude
LNO	Limb, Nadir and Occultation
LoS	Line of Sight
LST	Local Solar Time
MARCI	Mars Color Imager
MAVEN	Mars Atmosphere and Volatile EvolutioN

MCD	Mars Climate Database
MCS	Mars Climate Sounder
MEx	Mars Express
MGS	Mars Global Surveyor
MIR	Mid-InfraRed
MRO	Mars Reconnaissance Orbiter
MY	Martian Year
NIR	Near-InfraRed
NOMAD	Nadir and Occultation for MArs Discoveries
OEM	Optimal Estimation Method
OMEGA	Observatoire pour la Minéralogie, l'Eau, les Glaces et l'Activité
PFS	Planetary Fourier Spectrometer
ppb	part per billion
ppt	part per trillion
SNR	Signal to noise ratio
SO	Solar Occultation
SOIR	Solar Occultation in the InfraRed
SPICAM	SPectroscopy for the Investigation of the Characteristics of the Atmosphere of Mars
TES	Thermal Emission Spectrometer
TGO	Trace Gas Orbiter
THEMIS	Thermal Emission Imaging System
UV	Ultraviolet
UVIS	UltraViolet-VISible
VMR	Volume Mixing Ratio
LTE	Local Thermodynamic Equilibrium